Towards cellular hydrodynamics: Collective migration in artificial microstructures

Matthias Lawrence Zorn

München 2018

Towards cellular hydrodynamics: Collective migration in artificial microstructures

Matthias Lawrence Zorn

Dissertation
an der Fakultät für Physik
der Ludwig–Maximilians–Universität
München

vorgelegt von
Matthias Lawrence Zorn
aus München

München, den 27.03.2018

Erstgutachter: Prof. Dr. Joachim O. Rädler

Zweitgutachter: Prof. Dr. Erwin Frey

Tag der mündlichen Prüfung: 15.05.2018

Zusammenfassung

Die kollektive Migration von Zellen ist maßgeblich für viele biologische Prozesse, darunter Embryogenese, Wundheilung und die Ausbreitung von Krebs. Beobachtete Phänomene lassen sich nicht als Summe der Einzelbewegung vieler isolierter Zellen erklären, sondern sind emergente Eigenschaften, die aus ihren Interaktionen entstehen. Die Bewegung in epitheliale Zellverbänden zeigt eine reiche Phänomenologie, wie das Auftreten von Wirbeln in der Größenordnung mehrerer Zelldurchmesser oder den Übergang von fluidem Verhalten bei niedrigen Zelldichten, hin zu glasartigem Verhalten bei hohen Dichten. In dieser Dissertation wurde die kollektive Invasion epithelialer Zellverbände in Mikrokanäle auf einer phänomenologischen Ebene, im Rahmen von theoretischen Ansätzen zu aktiven Flüssigkeiten, untersucht.

Zunächst wurde das Bewegungsprofil einer Zellmonolage in geraden Kanälen mit Hilfe von Einzelzellverfolgung und "Particle Image Velocimetry" (PIV) an Zeitraff-Mikroskopiedaten untersucht. Quer über den Kanal wurde ein definiertes Pfropfenströmungsprofil beobachtet. Das Dichteprofil der Zellen konnte gut mit Hilfe der Fisher-Kolmogorov Reaktions-Diffusions-Gleichung beschrieben werden, welche aktive Migration der Zellen und den Beitrag von Zellteilung zur Bewegung umfasst. Diese Studie offenbarte eine Veränderung kurzreichweitiger Störungen in Folge der global ausgerichteten Bewegung.

Um die Proliferationskomponente des Systems genauer zu studieren, wurde der Einfluss einer zu Grunde liegenden globalen Migrationsrichtung auf die Ausrichtung der Zellteilungsachsen untersucht. Es konnte eine starke Ausrichtung der Orientierung der Achsen mit der auferlegten Bewegungsrichtung beobachtet werden. Konkret wurde die stärkste Korrelation zwischen der Ausrichtung der Zellteilungsachsen und der Hauptachse des lokalen Dehnungsratentensors gefunden. Diese Ergebnisse sind konsistent mit dem Konzept, dass im migrierenden Zellverband die Spannungen die Zellteilungen ausrichten.

Als Erweiterung der Untersuchung mit geraden Kanälen wurde eine Engstelle eingefügt, die der Zellverband durchqueren musste, um weiter vorzudringen. In der Region vor der Engstelle konnte ein Plateau niedriger Geschwindigkeiten beobachtet werden, welches auf eine lokale Erhöhung der Zelldichte zurück geführt wurde. Diese Ergebnisse wurden mit einem aktiven Isotropen-Nematen-

Mischmodell verglichen. Eine Eignung dieses Modells zur Beschreibung dieses Experiments konnte jedoch ausgeschlossen werden, nachdem es qualitativ ein deutlich anderes Verhalten als das Experiment demonstrierte.

Abschließend wurden in einem minimalen Modellsystem die Häufigkeit topologischer Nächster-Nachbar T1 Übergänge in einem Zellverband untersucht. Um die kleinstmögliche Grundeinheit für solche Übergänge zu untersuchen, wurden Gruppen aus vier Zellen auf ein Kleeblattmuster eingegrenzt, von dem gezeigt werden konnte, dass es das Einsetzen kollektiver Rotationszustände unterdrückt. Die Ergebnisse zeigten, dass T1 Übergänge bei Zellgruppen, deren Länge des im Übergang schrumpfenden Zell-Zell-Kontakts im Mittel kürzer ist, häufiger vorkommen. Diese Resultate sind konsistent mit der Vorstellung, dass die Energiebarriere, die für diese Übergänge überwunden werden muss, mit der ursprünglichen Länge des schrumpfenden Zell-Zell-Kontakts skaliert.

Zusammengefasst tragen die Ergebnisse dieser Dissertation zu einem besseren Verständnis von Strömungsfeldern kollektiver Zellmigrationsprozesse in begrenzenten Geometrien bei. Zusätzlich zu den Erkenntnissen, die die phänomenologischen Beobachtungen dieser Arbeit direkt liefern konnten, werden sie auch als Maßstab zur Bewertung und Plausibilitätsprüfung detaillierter theoretischer Modelle nützlich bleiben.

Abstract

The collective migration of cells governs many biological processes, including embryonic development, wound healing and cancer progression. Observed phenomena are not simply the sum of the individual motion of many isolated cells, but rather emerge as a consequence of their interactions. The movements in epithelial cell sheets display rich phenomenology, such as the occurrence of vortices spanning several cell diameters and the transition from fluid-like behavior at low densities to glass-like behavior at high densities. In this thesis, collective invasion of epithelial cell sheets into microchannels was studied on a phenomenological level within the scope of theoretical approaches to active fluids.

In a first project, the motion profile of a cell layer in straight channels was investigated using single cell tracking and particle image velocimetry (PIV) on time-lapse microscopy data. A defined plug-flow like velocity profile was observed across the channels. The cell density profile is well-described by the Fisher-Kolmogorov reaction-diffusion equation, which includes active migration and the contribution of proliferation. This study revealed a change in the short scale noise behavior in the presence of this global invasion into a channel.

For a closer look at the system's proliferation component, the effect of an underlying global migration direction on the orientation of the cells' division axes was examined. We found strong alignment of the axes' orientation with the imposed movement direction. Specifically, the strongest correlations were observed between the orientation of the cells' division axes and the local strain rate tensor's main axis. This is in agreement with the notion that stresses in the migrating cell sheet orient the cell divisions.

Expanding the assay of invasion into straight channels, we introduced a constriction, which the cell sheet needs to pass through in order to progress. A plateau of low velocities was observed in the region ahead of the constriction, which was attributed to an increase in local cell density accompanied by jamming. These results were compared to an active isotropic-nematic mixture model. The suitability of this model to describe this assay could be ruled out, however, as it showed qualitatively very different behavior than the experiments.

Finally, the frequency of topological nearest-neighbor T1 transitions within a cell sheet was investigated in minimal model systems. In order to study the smallest possible fundamental unit for such transitions, groups of four cells were confined to

cloverleaf patterns, which could be shown to inhibit the onset of collective rotation states. Results showed that T1 transitions occurred more frequently for groups of cells with a lower average length of the cell-cell junction that shrinks in the process of this transition. These results are consistent with the notion that the energy barrier which needs to be overcome by the cells in order to perform this transition, scales with the original length of the shrinking junction.

Taken together, the results of this thesis contribute to a better understanding of the flow fields for collective cell migration processes in confined geometries. In addition to the insights the phenomenological observations in this work could provide directly, they will also continue to prove useful as a standard for validating detailed theoretical models.

Table of Contents

Zusammenfassung v

Abstract vii

Associated Publications xiii

1 Introduction 1

2 Fundamental Concepts 9

2.1 Cell biological aspects . . . 9

2.1.1 Cell migration . . . 9

2.1.2 The role of the T1 transition in tissue development . . . 12

2.2 Soft active matter . . . 15

2.3 Hydrodynamic framework for the description of flow . . . 18

2.3.1 The Navier-Stokes equation . . . 19

2.3.2 Categorizations of fluid flows . . . 21

2.3.3 Poiseuille flow through a pipe . . . 26

2.3.4 Fluid flow through a constriction . . . 28

2.3.5 Diffusion theory . . . 29

2.4 Glass transitions in supercooled liquids and cell collectives . . . 32

2.5 Overview of cell migration models . . . 35

2.5.1 Reaction-diffusion equations: Fisher-Kolmogorov . . . 36

2.5.2 The active isotropic-nematic mixture model . . . 38

2.5.3 Dissipative particle dynamics simulations . . . 43

2.5.4 The vertex model . . . 48

2.5.5 The cellular Potts model . . . 51

2.6 Machine learning for image processing . . . 56

2.6.1 Basic types of machine learning problems . . . 56

2.6.2 General process . . . 57

2.6.3 Supervised and unsupervised learning . . . 58

2.6.4 Decision trees and random forests . . . 59

3 Cellular Hydrodynamics 67

3.1 Flow and diffusion in channel-guided cell migration . . . 69
3.1.1 Cell front velocity and analysis of the flow field . . . 70
3.1.2 Cell density and diffusive flux . . . 77
3.1.3 Reaction-diffusion model . . . 80
3.1.4 Analysis of vorticity in the flow field . . . 83
3.1.5 Single cell motility . . . 90
3.1.6 Discussion . . . 95
3.2 Alignment of cell division axis in directed epithelial cell migration . . . 99
3.2.1 Flow and density profiles in the model . . . 101
3.2.2 Orientation of the cell division axis with respect to global flow . . . 102
3.2.3 Orientation of the cell division axis with respect to local flow . . . 106
3.2.4 Discussion . . . 108
3.3 Collective cell migration through a constricted channel . . . 111
3.3.1 Evolution of the cell front . . . 114
3.3.2 Influx at channel entrance . . . 117
3.3.3 Flow field analysis . . . 121
3.3.4 The detailed velocity profile . . . 126
3.3.5 Comparison with cell migration models . . . 136
3.3.6 Discussion . . . 142
3.4 Hydrodynamics of minimal collective cellular units . . . 147
3.4.1 Cell arrangement and description via the vertex model . . . 150
3.4.2 Stabilization of cell arrangements through choice of the underlying geometry . . . 155
3.4.3 Towards a machine learning algorithm for automated cell-cell junction readout . . . 160
3.4.4 T1 transitions in minimal four cell systems . . . 165
3.4.5 Discussion . . . 170

4 Conclusion and Outlook 175

A Methods and Experimental Protocols 183

A.1 Microstructuring . . . 183
A.1.1 Micromolding in capillaries for 3D structures . . . 183
A.1.2 Microcontact printing of ECM proteins . . . 187

A.2 Evaluation tools for data analysis . . . 190
A.2.1 Particle image velocimetry extracts cellular flow fields . . . 190
A.2.2 Coarse-graining and time averaging . . . 195
A.2.3 Determination of cell density . . . 195
A.2.4 Flux calculation . . . 196
A.2.5 Vorticity calculation . . . 196
A.2.6 Equivalent angle approximation for vorticity . . . 197
A.2.7 Quantitative orientation analysis . . . 198
A.2.8 Single cell tracking and drift correction . . . 202
A.2.9 Automated cell front detection . . . 202
A.2.10 Image stitching . . . 204
A.2.11 Machine learning algorithms for cell-cell junction identification . . . 204
A.3 Experimental protocols . . . 207
A.3.1 Cell culture . . . 207
A.3.2 Microscopy . . . 208

List of Abbreviations **209**

List of Figures **210**

Bibliography **215**

Associated Publications

P1 **Phenomenological approaches to collective behavior in epithelial cell migration**
Matthias L. Zorn, Anna-Kristina Marel, Felix J. Segerer, Joachim O. Rädler
In: *Biochimica et Biophysica Acta*, 1853, 3143-3152, 2015.
https://doi.org/10.1016/j.bbamcr.2015.05.021

P2 **Flow and diffusion in channel-guided cell migration**
Anna-Kristina Marel†, Matthias Zorn†, Christoph Klingner, Roland Wedlich-Söldner, Erwin Frey and Joachim O. Rädler
In: *Biophysical Journal*, 107, 1054-1064, 2014.
https://doi.org/10.1016/j.bpj.2014.07.017

P3 **Alignment of cell division axes in directed epithelial cell migration**
Anna-Kristina Marel, Nils Podewitz, Matthias Zorn, Joachim Oskar Rädler and Jens Elgeti
In: *New Journal of Physics*, 16, 115005, 2014.
https://doi.org/10.1088/1367-2630/16/11/115005

P4 **The actin targeting compound chondramide inhibits breast cancer metastasis via reduction of cellular contractility**
Magdalena H. Menhofer, Rebekka Kubisch, Laura Schreiner, Matthias Zorn, Florian Foerster, Rolf Mueller, Joachim O. Raedler, Ernst Wagner, Angelika M. Vollmar, Stefan Zahler
In:*PLoS ONE*, 9(11), e112542, 2014.
https://doi.org/10.1371/journal.pone.0112542

P5 **Single Cell Microarrays Fabricated by Microscale Plasma-Initiated Protein Patterning (μPIPP)**
Anita Reiser, Matthias Zorn, Alexandra Murschhauser, Joachim O. Rädler
In: *"Cell-Based Microarrays"*, Humana Press, 2018
ISBN 978-1-4939-7791-8

†These authors contributed equally.

Chapter 1

Introduction

Cells are the smallest, most basic structural building block of living matter capable of functioning autonomously. They come in various forms and fulfill a near endless amount of functions necessary for the existence and persistence of life. In recent years, cells and tissues have emerged as prime examples of soft active matter [1–4], a subcategory of condensed matter physics. A key feature of active systems is that they are out of equilibrium due to perpetual energy injection at the sites of the constituent agents [5, 6].

For many of the cells' functions, their ability to achieve locomotion and change shape is crucial. This is, for instance, the case when leukocytes migrate as part of the immune response [7–9], or in the complicated process that allows neurons to reach their destinations in the developing nervous system [10, 11]. These processes, where single cells move on their own, are intriguing in themselves, but in many physiologically relevant scenarios, cells occur in larger groups rather than being isolated. As such, multi-cellular motion is essential in several processes highly relevant to life and disease, most notably morphogenesis [12–16], wound healing [17, 18] and cancer progression [19–22].

Random walk dynamics of networks are of great interest in physics. Unfortunately, even single cell migration is already complex and depends on many factors, such as cell type [23], rigidity of the underlying substrate [24] or the extracellular environment in general [25], as well as molecular expression levels [26]. In addition, collective cell migration is not simply the sum of the individual movement of all the involved single cells, but rather an emergent phenomenon that arises from interactions between the individual agents. The resulting mutli-cellular motion displays rich dynamics and cooperativity with correlations spanning several cell lengths in space, and hours in time [27–29].

Intriguingly, collective cell migration is frequently reminiscent of a fluid flow when examined on sufficiently long time scales. This is the case for the spreading of cellular aggregates on a surface [30], the expansion of circular colonies released from confinement [31, 32] and the wound healing process [33]. By virtue of the complexity of the process and the difficulties of live-cell imaging *in vivo*, much work has gone into creating artificial model

systems to study collective cell migration *in vitro*. In this way, the boundary conditions of the experiment can be defined in a reproducible manner, and imaging can be simplified by designing the samples to be compatible with the desired microscopy setups. The scratch assay represents a very typical example of this sort of experiment [34]. Here, a scratch is created in a monolayer, customarily with a pipette tip, though more advanced setups use laser ablation to produce scratches in a more defined manner and with higher throughput [35]. Collective migration into the wound in response to this injury is then observed and characterized. The recent advent of diverse microstructuring techniques, which can be used to place cells in very well-defined environments, has allowed for even further refinement of *in vitro* assays. For instance, Poujade et al. used thin polydimethylsiloxane (PDMS) films to introduce a model wound into an epithelial monolayer, which allowed studying collective cell migration into an open region without the issue of injured cells at the periphery [17]. This allowed decoupling of some possible reasons for migration (such as cell damage following an injury), and showed that freely available surface is sufficient to trigger migration.

As collective migration *in vivo* frequently occurs in confinement [36], it makes sense to use available microstructuring techniques to introduce geometrical constraints and observe the effect on migrating cells. Following this train of thought, Vedula et al. studied the occurrence of different modes of migration of epithelial sheets migrating into strips with widths ranging from one to several cell diameters [37]. Whereas in wide stripes, they found the occurrence of large scale vortices that are typical of epithelial monolayers [27], a new contraction-elongation type of migration appeared in narrow stripes. These findings highlight the existence of cooperative patterns within collective cell migration, and strikingly, these patterns show noteworthy behavior upon changes in the cell density. Specifically, heterogeneous regions in the velocity field of confluent or advancing monolayers grow in size with increasing density, while, conversely, the velocity decreases [38, 39]. In addition, measurements of the intercellular tension within a monolayer reveal severe fluctuations in space and time, with force clusters over roughly 10-50 cells that pull cohesively and cooperatively [38–41]. Despite these dynamic heterogeneities, local cell migration frequently follows the local orientation of the maximal principal stress. This powerful collective guidance mechanism termed plithotaxis seems to require cooperativity of mechanical stresses across many cell-cell junctions [39, 42].

All these behaviors are the very signatures of a so-called glass transition, leading to a big question: How can collective systems of cells act as fluids in some cases, but like a rigid solid in others? A potential explanation is the notion that these glass transitions are

associated with jamming [41], a phenomenon known (though far from fully understood) from colloidal and granular materials, as well as foams [43]. Recently, much effort has gone towards studying jamming-transitions in collective cell assemblies. For instance, Park et al. showed that in asthmatic airway epithelia, the transition from unjammed, fluid-like phase to a jammed, solid-like phase is significantly delayed compared to healthy tissue. They put forward the hypothesis that fluidization and subsequent re-jamming might function as a mechanism that allows the bronchial epithelium to self-repair from mechanical perturbations in the course of breathing [44]. Meanwhile, Nnetu et al. observed that two collectively migrating monolayers that collide do not mix, even when both consist of the same cell type, and even if this is a type that shows weak cellular interactions. They explain this phenomenon as each of the layer boundaries being in a jammed state [45]. Very recent work by Chepizhko et al., however, showed a jammed monolayer can rapidly transition back to a fluid state in response to a wound [46]. Finally, there is even evidence that mesenchymal tumor cells that normally migrate on their own, migrate collectively as a result of jamming due to confinement [22].

Indeed, the success of a description of collective cell behavior via a jammed system is not entirely surprising, as condensed systems of cells are inhibited by a multitude of the same factors also governing inert systems. These include volume exclusion, size, deformability, mutual crowding and mutual adhesion [41]. As mentioned above, describing dense cellular assemblies via active matter approaches has gained prominence. The term active matter is used to describe a number of systems that share the following characteristics [5, 6]: They consist of a number of self-propelled, interacting particles that can convert free energy into systematic movement. In contrast to other out-of-equilibrium systems, energy is permanently injected into the system locally at each of the constituent units rather than at the system boundaries. Active systems have representatives in living and non-living matter, though the former are far more prevalent. Living active systems encompass, among others, bacteria swimming in suspension [47, 48], *in vitro* mixtures of bio-filaments and associated motor proteins [49], eukaryotic cells [50], as well as flocks of birds, fish or land based animals [51]. Meanwhile non-living systems are often artificial, and include things such as layers of vibrated granular rods [52] or collections of robots [53]. The goal of active matter physics is to find generic behaviors common to the multitude of systems the discipline encompasses, thus helping to understand mechanisms arising *in vivo* [54]. Examples of such behavior include phase transitions or characteristic instabilities. With this notion in mind, and returning specifically to the concept of jamming transitions, one system that can also be considered active matter is particularly noteworthy: traffic flow. The flow of traffic, and the dynamical jamming transition from

free traffic at low densities to traffic jams at high density have been thoroughly studied due to their relevance for humans' everyday lives [55]. Though there are still many open questions, the idea of relating the high density congestion of traffic flow to the high density jamming of cell collectives is compelling, especially since microstructuring allows tailoring the experimental situation for a cell collective to mimic a traffic flow problem, such as the encounter of a bottleneck, where intriguing phenomena such as a density dependent capacity drop-off have been observed [56].

On a more resolved level, fluid regimes and glassy regimes of cell collectives depend on the energy barriers to cell rearrangement. In glassy phases, the energy barriers for cells changing their organization are finite, while in a fluid phase they vanish (or are significantly lower) [57]. Topological rearrangements within a tissue are only possible via cell division, cell extrusion or so-called T1 transitions [58]. Four cells are involved in these transitions, during which two threefold vertices (where three cells meet) degenerate into a single fourfold vertex (where four cells meet), which is not stable and is resolved into two threefold vertices again. T1 transitions have been shown to be relevant in developmental processes [59], but in the theoretical framework of modeling cell collectives as being jammed, they are also relevant in wound healing and cancer invasion [57, 58]. These transitions, in principle, offer direct access to the energy barriers to cell rearrangements, and studying them could thus also be of use in determining where on the fluid to glass phase diagram a cell collective in any given situation falls. A detailed analysis, even *in vitro*, is, however, challenging, given the complexity of even systems such as full scale monolayers. Due to this, these energy barriers have been probed theoretically, finding an exponential distribution and a dependence on number of neighbors [58].

This is only one of many instances, where a theoretical model of cell migration has proven useful in gaining some insight into the mechanisms of collective cell migration behavior. In fact, a vast range of models is available to choose from, though selection of a model appropriate to a given scenario can be difficult. Feasible theoretical frameworks range from the very simple reaction-diffusion models and continuum models, over less coarse-grained particle-based models that describe each constituent agent explicitly, to even more detailed descriptions of cells that include things like area, shape and potentially, to some extent, molecular processes within each cell.

While the complex models are likely the most capable of reproducing intricate migration phenomena if implemented correctly, they can also face computational limitations when applied to systems consisting of very large cell numbers. Here, microstructuring techniques

can offer some aid, reducing the system size to smaller groups of cells, where uncovering molecular details is more feasible. In this context, Segerer et al. studied groups of two to eight collectively rotating cells on small circular micropatterns [60]. With the help of a modified cellular Potts model, they uncovered how crucial the interplay between local cell arrangement and internal cell polarization is for collective migration. Ideally, insights like this, and other molecular details gleaned from various small scale experiments, can be implemented in a coarse-grained manner in the less intricate models, or even in the complex models themselves, where a coarse-grained or rules-based implementation of molecular details can cut down on computation times.

For many-cell systems, the test of whether such an implementation is sufficient comes from examining whether the models correctly reproduce the occurring large scale phenomena. To this end, however, a detailed phenomenological description of collective cell migration in experiments is necessary, in order to give the theoretical implementations a reference for comparison. Thus, the focus of this thesis was to provide such an experimental frame of reference and characterize the collective cell behavior within it. Due to the similarities between migrating cell collectives and flowing fluids already discussed above, phenomenological descriptions in this context can be thought of as a sort of cellular hydrodynamics. In fact, many of the experiments within the scheme of this dissertation were motivated by classical hydrodynamic experiments that had not previously had an equivalent counterpart for collective cell migration, and one of the core analysis tools, particle image velocimetry (PIV), was originally developed for visualization of fluid flows [61, 62].

With this goal in mind, this thesis is structured in the following way:

Chapter 2 introduces the fundamental concepts behind the major components of this work. It gives some background relating to the basic process of cell migration, both on a single cell and a collective level. In addition, the hydrodynamic framework for the description of fluid flows, as well as the theoretical framework for the glass transition are introduced. An overview of the various different theoretical models for describing cell migration is given, with a focus on approaches that were used to some extent within this dissertation. Finally, the chapter gives a brief introduction into machine learning in the context of image processing, a powerful but complex tool for analyzing biological microscopy data.

Chapter 3 contains the results of this thesis and the discussion thereof. Its structure mirrors that of this introduction:

In **section 3.1**, collective migration of an epithelial cell sheet into channels created via micromolding in capillaries (MIMIC) is studied, akin to the flow of a Newtonian fluid through a pipe. The flow profile and the density profile are investigated. A flat, plug-flow like behavior is uncovered for the velocity profile across the channel, in contrast to the parabolic profile a Newtonian liquid would produce as a result of Hagen-Poiseuille's law. Interestingly, an increase of velocity from the back of the cell sheet to the front is uncovered, paired with the reverse trend in density, which decreases upon approaching the leading edge. We could show that on long time scales, the dynamics of this expanding cell layer could be well described by a simple reaction-diffusion theory, and that bursts of collective migration appear to contribute significantly to forward movement, in contrast to confined cell sheets, where these bursts instead cause the formation of vortices. The results of this section are recorded in publication P2 [63], as well as in the review publication P1 [64].
In **section 3.2**, the influence of the emerging flow field on cell division is discussed. Strong alignment between orientation of the division axis and underlying migration direction was uncovered. Specifically, the best correlation was found to exist with local flow gradients. Experimental results were compared to a previously published particle-based model, and both the density and the velocity profiles showed the same characteristic behavior in theory and experiment. Likewise, the strong correlation between division orientation axis and the main axis of the strain rate tensor could also be correctly reproduced. The results of this section are set down in publication P3 [65].
In **section 3.3**, the straight channel assay is expanded, and collective migration of cells through a constriction is examined in analogy the flow of a Newtonian fluid following Bernoulli's principle. The introduction of a constriction in the channel does lead to a reduced velocity prior to the constriction, but from that point forward the velocity increases towards the cell front, and does not drop off again after the bottleneck. Intriguingly, the difference in velocity prior to the constriction does not appear to be the result of cells speeding up in the narrow segment, but rather of cells slowing down in the wide segment over time. This suggests that a buildup in density and potentially a transition to a more jammed state are the dominant mechanisms behind this phenomenon. Results from the experiment are briefly compared with simulations for an active isotropic-nematic mixture model, though both the velocity fields and orientation fields were found to show qualitatively very different behavior, indicating the model is not suitable to these experimental conditions.
In **section 3.4**, in order to study the microscopic rearrangements underlying macroscopic collective cell migration, a novel oligocellular array is presented. Groups of four cells are confined to a cloverleaf pattern created via microcontact printing (μCP) of extracellular

matrix (ECM) proteins. Such a setup presents the minimal system required for undergoing T1 transitions, which represent the major source of rearrangements within a cell layer necessary for collective migration and fluidization. The frequency of T1 transition occurrence was studied for cloverleafs of different sizes, in an attempt to experimentally probe the energy barrier cells need to overcome in order to rearrange. This minimal system has the advantage of decoupling cells from other neighbors not involved in the transition and thus making the energy barrier more easily accessible.

Finally, **chapter 4** summarizes the ideas and results of this dissertation and discusses their implications for the field of cell science. An outlook is given on reasonable follow-up experiments or potential improvements to existing systems that could further the research on collective cell migration. The **appendix A** provides further information on and detailed descriptions of the experimental and data analysis methods used in the course of this thesis.

Chapter 2

Fundamental Concepts

2.1 Cell biological aspects

In order to discuss the rich phenomena associated with collective migration, a basic understanding of the biological processes that are involved is necessary. To this end, this chapter introduces the fundamental concepts of both single cell migration and collective cell migration, before detailing the so-called T1 transitions, by which cells rearrange within the tissue during collective movement.

2.1.1 Cell migration

Cell migration is crucial in many biological phenomena, such as wound healing, embryogenesis or vascularization of tissues, but also pathological processes, in particular cancer metastasis [66]. Cells can migrate either on their own, or in tightly or loosely associated groups. In the latter case, cells are typically linked to their neighbors via various junctions, and, depending on the biological context, can migrate as sheets, clusters, strands or tubes [19, 67]. Due to the interplay between many cells, collective migration is more than just the sum of the single cell migration of each individual cell, but the general principle how individual cells move is still relevant for the emerging behavior.

Single cell migration

Locomotion of individual cells is achieved by turning forces generated within a cell into translational movement of its body. This process is well understood for single, adherent cells and consists of five distinctive steps [68]:

Initially, spatial asymmetries are developed, before the membrane is expanded and new focal adhesions are produced. Then, a contractile force is generated and the old adhesion

sites are released. In more detail, in the first step a front and a rear of the cell develop by morphological polarization that creates spatial asymmetries. As part of this process, the distribution of filamentous actin changes from symmetrical to concentrated regions at the front, and integrin adhesion receptors and integrin-cytoskeleton linkages gather towards the front of the cell. Once the cell is polarized, the migration process continues with expansion of the membrane at the new front of the cell, by extension of broad, flat lamellipodia and thin, cylindrical filopodia. These extensions result from local actin polymerization, likely following a Brownian ratchet mechanism where thermal fluctuations sporadically create enough room between the cell membrane and the actin filament that a new actin monomer has room to be added to the polymer. Once filopodia and lammelipodia protrude out ahead of the cell, new focal adhesions are created, linking cell and substrate. These adhesion sites form primarily at the front of the cell and remain until the locomotion of the cell has moved them towards the rear. Following this, a contraction force is generated that moves the cell forwards, overcoming old adhesions (all other forces, such as viscous drag of the surrounding medium, are negligible). The production of these forces is generally attributed to myosin motor proteins, specifically myosin I and myosin II. Finally, in order for the cell to actually move forward, adhesions at the back of the cell need to be released, a process that leaves a large part of the involved integrins behind. Thus, if a second cell migrates across a surface already traversed by another cell, it likely encounters a modified substrate.

Collective migration

The multitude of interactions taking place between individual cells involved in collective cell migration makes this process more complicated and less well understood. Physical forces, chemical signals and combinations thereof are likely involved in coordinating the separate members of the collective, though there are several options how exactly this might happen. For instance, in the migration of 2D epithelial sheets, evidence has been found supporting several different theories, such as the sheet being pulled by a leader cell, pushed forward by the pressure of cell proliferation farther back, and, most recently, the whole sheet being under tension in a sort of “tug of war” situation [17, 69, 70].

Depending on the situation, further modes of collective migration are possible besides sheet migration. In branching morphogenesis, cells migrate via sprouting of the end bud. Meanwhile, 3D invasion strands or masses consisting of several different cell types are hallmarks of cancer cell migration. Despite superficial differences, all of these migration

modes still share several common features, among them the retention of intercellular cohesion, collective polarization and coordinated cytoskeletal activity [19].

Cohesion is maintained through adherens junctions proteins, such as cadherins and integrins. They couple, directly or indirectly to the actin and/or intermediate filament network, in a robust but dynamic way. The most important of these mediators for collective cell migration appears to be epithelial cadherin (E-cadherin), the loss of which has been shown to promote the onset of the epithelial-mesenchymal transition (EMT), where cells move using a single cell migration mode. Depending on the cell type, loss of E-cadherin may be compensated by the other cell-cell adhesion pathways [19].

Most collectively migrating cell systems described to date develop a front-rear asymmetry by the development of so-called "leader" or "tip" cells. These cells have a very distinct and polarized morphology different from the rest of the collective. Though the mechanism selecting leader cells is still unclear, with both chemical signaling via growth factors [71, 72] and dynamic instabilities [73] having been suggested, it appears that cells that do become leader cells effectively undergo partial EMT [67]. Recent work shows that the selection of leader cells is influenced by the pre-migratory dynamics of the followers immediately behind them. These cells locally unjam long before the actual leaders appear [74]. About one hour after the surrounding area becomes available for migration, the distinct phenotype leaders appear, at which point they typically remain in the leading position for several hours [17, 75, 76]. During this time, they show distinct behavior, such as never dividing [77]. The exact role these "leaders" play has been the subject of much debate, though traction force measurements have now shown they are not solely responsible for pulling the sheet along behind them as originally conceivable [70]. Instead, it seems their role is more the detection of extracellular guidance cues and determining the direction of migration for the followers [71].

Similar to how actin organization and targeted force generation take place in single cell migration, the same principles also apply to cell collectives. In this case, however, the mechanisms are coordinated between the various cells in the group. How this coordination is achieved is still unclear, though it likely involves a combination of cadherin-mediated cell-cell coupling and local release of cytokines or growth factors [19]. Correspondingly, how mechanical forces are transmitted between cells is not entirely understood, though distinct receptor-ligand pairs seem to be responsible in different biological contexts [19].

In this work, sheets of epithelial cells are used as model systems for studying collective migration. Much work has already been done studying these types of systems via

wound healing assays [78–81]. These investigations involve creation of an artificial wound in an epithelial cell layer through scratching and observation of the subsequent motion of epithelial cells while they close this new gap. As there is some concern as to the effect that damaging the cells at the boundary of the scratch might have (such as the release of chemoattractants or other chemical signals) on the migration, in recent years alternative setups have been developed where an artificial wound is created instead. These function, for instance, by removal of a PDMS barrier the cells were grown around [17] or lift-off of a confining poly(ethylene glycol)-dimethacrylate (PEG-DMA) layer [32]. Further refinement allows the dimensionality of the problem to be reduced by confining the collectively migrating cell front to stripes or channels of defined widths [37, 63].

The results from these sorts of experiments reveal that at a coarse-grained level, collective phenomena are well-described by reaction-diffusion type models. At the scale of a few cells, however, collective migration reveals highly intriguing phenomena, such as the formation of vortices or pulsating waves [37, 63, 82]. These properties are interesting to study as they can provide great insight into intercellular coupling.

2.1.2 The role of the T1 transition in tissue development

Collective motion of cells plays an important role in morphogenesis, where it contributes to such things as shape and formation of compartments in an organism [15, 16]. However, the details of how, for instance, tissue shape emerges as a a result of collective mechanical properties and the behavior of individual cells is not well understood. The typical model system for the study of development is the growth of the wing of the *Drosophila melanogaster*'s larval stage [59, 83–85]. In principle, cell divisions, cell shape changes and cell rearrangements are potential contributors to the final result [59]. Shape changes of the *Drosophila* wing blade correspond to elongation along an axis, i.e. pure shear [59]. The pure shear rate tensor $\tilde{v}$ can be decomposed into contributions from the aforementioned processes. Tissue shear is then given by:

$$\tilde{v}_{xx} = \frac{DQ_{xx}}{Dt} + T_{xx} + C_{xx} + E_{xx} + D_{xx} \tag{2.1}$$

Here, $\frac{DQ_{xx}}{Dt}$ characterizes shear by elongation changes of individual cells, T_{xx} the contribution to shear by T1 transitions, C_{xx} the shear contribution resulting from cell divisions, E_{xx} the contribution of cell extrusions (also known as T2 transitions), and D_{xx} the effect

of correlated cell shape changes and cell rotations [59].

It is of particular note that the contribution of topological rearrangements within the cell sheet has been shown to contribute significantly to the resulting tissue flow [59, 86]. As seen in Eq. 2.1, one major possible topological rearrangement is the so-called T1 transition, a process originally introduced in the context of soaps and foams [87, 88].

A classical T1 transition is illustrated in Fig. 2.1. In the minimal case, they require four cells, which are arranged in such a way that they share two threefold vertices, i.e. two of the cells share interfaces with only two other cells, while two of the cells share interfaces with all three other cells. In a T1 transition, the connecting bond between two cells shrink and all cells come together to meet in a single fourfold vertex. Then, a new bond is formed in a manner that has cells switch neighbors from the original configurations. Specifically, the two cells that were initially separated remain together, and the other two are separated. It is also possible for the four way vertex to revert back to its original conformation, or for the neighborhood to fluctuate between both possible confirmations with two three way vertices [83]. Fig 2.2 illustrates how shear can be created by T1 transitions without any change of cell shape.

"Half" T1 transitions in which a bond is lost but no new one is formed can also be defined, but these can also be generated by other events in the cell sheet [86].

It is worth noting that the fourfold vertices that appear temporarily in T1 transitions are unstable in most scenarios [89] and decompose into one of the two possibilities with a pair of threefold vertices. As these two vertices can be shifted against each other, each of these two possibilities has infinite realizations, some of which are energetically more favorable than others if examined by e.g. the vertex model (see chapter 2.5.4) [89].

As it turns out, shear resulting from T1 transitions and shear by cell elongation contribute to total shear in a significant manner, and oppose each other [59]: Early in the process of wing development, T1 transitions cause shear along the anterio-posterior (AP) axis, which is opposed by the increase of cell elongation along the proximal-distal (PD) axis. In intermediate and late stages of the process, the average orientation of T1 transitions shifts, so that they instead cause a PD shear, which is opposed by an AP shear caused by a reduction of cell elongation. Interestingly, upon examining the formation and loss of connections over time as a result of these transitions, even more complex dynamics arise. At early times, when the T1 shear is mainly oriented along the AP axis, connections between cells are typically lost along the PD axis, whereas they are preferentially gained

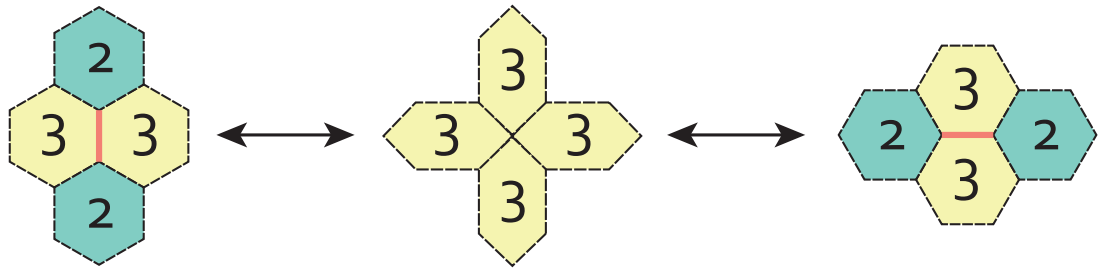

Figure 2.1: Schematic of a T1 transition. This transition occurs at the interface of four cells. Such cells break symmetry in their arrangement (left), with two cells sharing interfaces with two cells (green cells) and two cells sharing interfaces with three cells (yellow cells). In a T1 transition, the two three-neighbored cells lose their shared boundary (indicated in red), and after passing through a perfectly symmetrical configuration where all cells share one common vertex (middle), a new boundary is formed between the two remaining cells (right). This configuration is energetically equivalent to the initial arrangement, though each cell now has a different number of neighbors it shares boundaries with. Despite energetic equivalency, an energy barrier must still be overcome to perform a T1 transition.

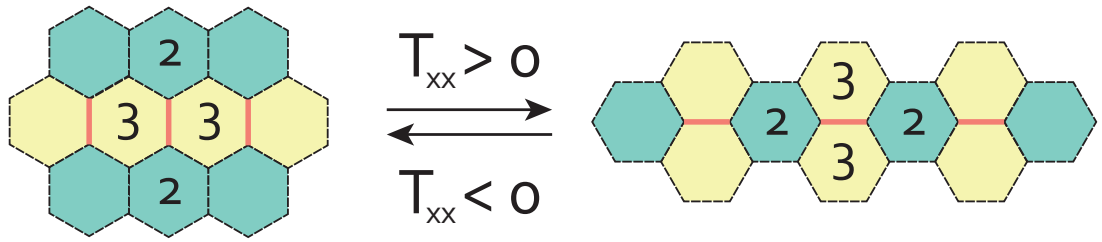

Figure 2.2: Tissue deformation by T1 transition. Multiple T1 transitions can significantly reshape the tissue and create shear. Cells that share interfaces with two cells involved in the rearrangement are highlighted in green, those that share interfaces with three involved cells are highlighted in yellow. The lost and gained shared boundaries are indicated in red.

along the AP axis. At intermediate times, both lost and gained connections are preferentially oriented along the PD axis, and the type of T1 transition where the four way vertex reverts back to two threefold vertices oriented as they were initially is the most common. Finally, at the end of the process, when T1 shear along the PD axis dominates, bonds along the AP axis are preferentially dissolved, while the new ones created are preferentially oriented along the PD axis. This seems to indicate that the PD-oriented epithelial stresses have two threshold values, a lower one at which point they promote expansion of cell boundaries along this axis, and a higher one at which they also block the dissolution of connections in this direction.

Interestingly, PD oriented T1 transitions appear to depend on tissue stresses, whereas AP oriented transitions are driven autonomously, and the rearrangement of T1 transitions depends on external stress, but reacts with a time delay [59].

In general, microscopic rearrangements such as T1 transitions are relevant in allowing cell collectives to become fluid and thus have an influence on resulting migration behavior. Probing these transitions is difficult, however, as they are mostly studied in complex systems with many cells. Thus, in the project detailed in section 3.4, we created a minimal system of four epithelial cells, arranged in the typical geometry with two threefold vertices, which should allow probing such things as the transition frequency between the two possible sets of realization of two threefold vertices.

2.2 Soft active matter

One potential approach to studying collective cell behavior is by accessing it as a subcategory of soft active matter research. Soft matter is a field of study attributed to condensed matter physics that has seen increasing interest in the last twenty-five years. It concerns itself with materials that have important length scales between atomic and macroscopic, and that are easily deformable by thermal fluctuations around room temperature [90]. These types of systems come in both active and inactive form, with the latter typically being more straightforward to describe from a physics perspective. Active systems are out of equilibrium, which is where their allure lies, as this can give rise to a multitude of fascinating phenomena.

Though non-living systems exist, a multitude of biological (living) systems make up a large population of active matter. These include such things as bacteria swimming in

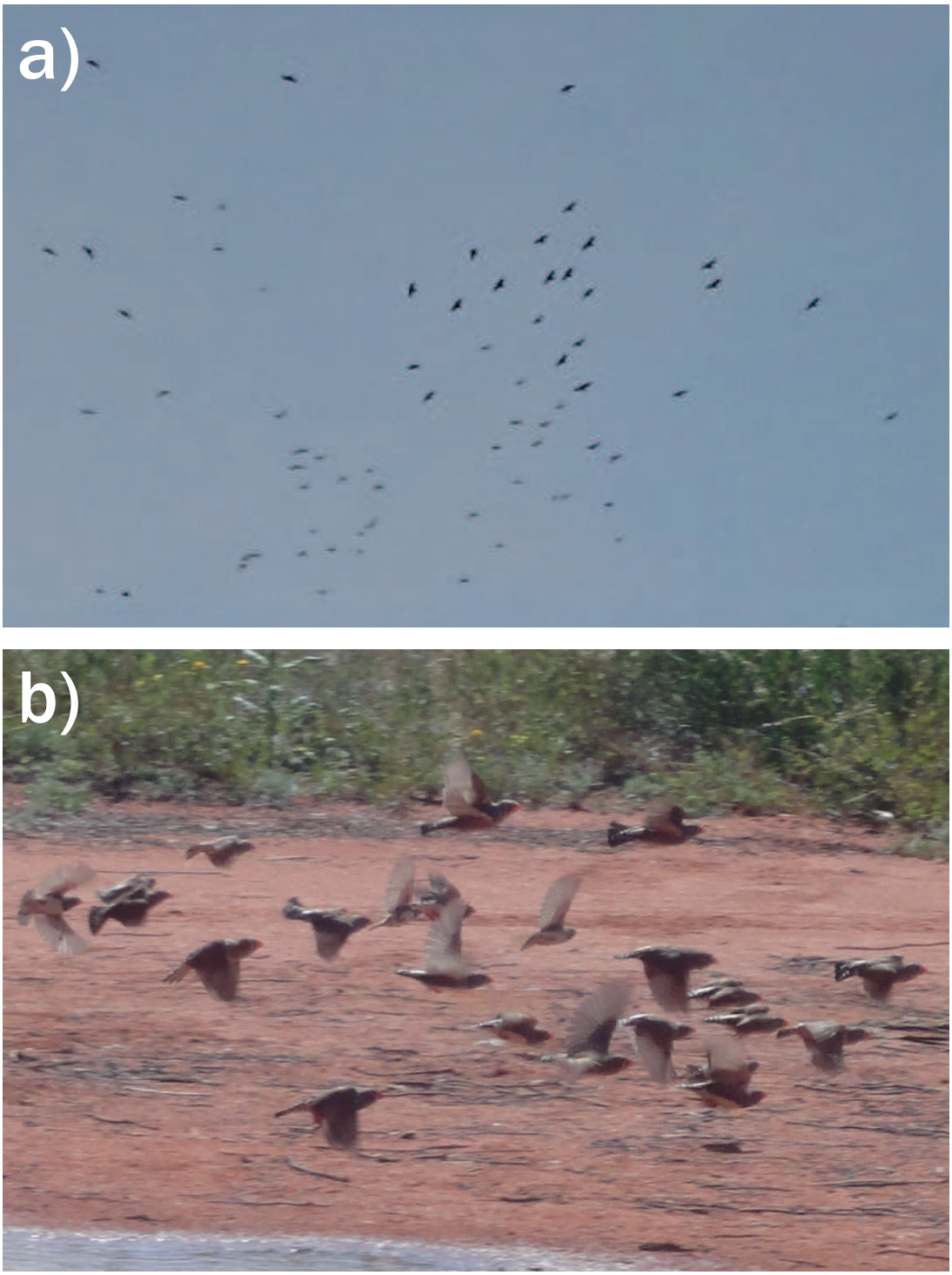

Figure 2.3: Bird flocks as a representative sample of living active matter. **a)** A flock of birds high in the sky, viewed at a coarse-grained level **b)** A flock of birds close to the ground viewed at a much more detailed level, revealing distinctions between the individual components. Image copyrights 2016-2018 Matthias Lawrence Zorn.

suspensions [47, 48], *in vitro* mixtures of bio-filaments and associated motor proteins [49], eukaryotic cells [50], as well as flocks of birds (see Fig. 2.3), fish or land based animals [51]. Thus, they cover an entire range of length scales from microscopic to macroscopic. On the flip side, non-living systems are often artificial, and include things such as layers of vibrated granular rods [52] or collections of robots [53].

All of these diverse materials share some common characteristics that define active matter [5, 6]: Each of these systems consists of a number of self-propelled, interacting particles that can convert free energy into systematic movement. In order to maintain an out-of-equilibrium state, energy needs to constantly be fed into a system from the outside. In contrast to other non-equilibrium systems, in active matter this influx of energy happens directly at each individual self-propelled unit, and not at the system boundaries (as is for example the case for sheared fluids). The resulting motion is thus not defined by an external force or field, but rather by each particle's orientation [54].

The interaction of individual particles with each other highlights the biggest difference to typical equilibrium statistical physics. In particular in biological systems, the energy dissipated into the surrounding medium is non-negligible, so unlike in equilibrium systems, the total momentum of colliding and interacting particles need not be preserved [91].

The goal of (soft) active matter physics is to find generic behaviors common to the multitude of systems the discipline encompasses, such as phase transitions or characteristic instabilities. This knowledge can be used in order to understand mechanisms arising *in vivo* [54] and, ideally, to reproduce biological components for chemomechanical systems artificially [52, 92].

Given the nature of the discipline, a common approach to understanding the complex systems it involves is by borrowing tools from condensed matter physics and statistical mechanics, expanding them to account for the diverging features of active matter [6]. For instance, when only examining systems over large time and length scales, they can be well described with a hydrodynamic theory that only needs to take into account the symmetries of the problem. It does not need to make any assumptions about an underlying microscopic model, and thus the system can be characterized by a few parameters and their relation to one another. A detailed description of all the microscopic interactions taking place between every single self-propelled particle in the system would be much more complicated (especially since the systems in question quite frequently have very large numbers of particles present), but can hereby be avoided [6].

2.3 Hydrodynamic framework for the description of flow

The term fluid dynamics typically refers to the study of a liquid with specified properties in a particular scenario, in particular when such a configuration involves the movement of said fluids [93, 94]. Classical problems might involve the flow of oil through a pipeline, determining the forces acting on an aircraft, or examining the increase of blood pressure as a result of vasoconstriction (blood vessel narrowing). While the well known laws of mechanics govern the behavior of fluids, the consequences of these laws are often exceptionally complex to the point where solving them analytically in order to construct a formalism that predicts fluid behavior is no longer possible.

At any given point in time t, a flow can be quantified at each point (x, y, z) by its velocity $\mathbf{v} = (v_x, v_y, v_z)$, its temperature T, its pressure p and its mass density ρ. Depending on the specific scenario, not all of these state variables will be equally important. For instance, when examining a flowing cell sheet in analogy to a fluid, temperature is rather irrelevant. For collectively migrating cells, active migration of the individual components would take the role of temperature, but when working with a population of only a single type of cell, the energy each of these cells can inject into the system should be identical (assuming a scenario where all cells are healthy and there are no external influences that would cause parts of the population to behave differently). As such, temperature should only play a role when comparing experiments with populations of cells that show a different individual activity.

The issue with calculating fluid flow in a specific scenario (or finding a general solution for fluid flow) is that six (in part) nonlinear differential equations are necessary to determine the state variables:

- Law of conservation of mass
- Law of conservation of momentum (3 equations)
- Law of conservation of energy
- Equation of state (thermodynamic relation between T, p and ρ)

In addition, initial and boundary conditions of specific problems play an important role

and need to be considered. Taken together, it can be hard (or even impossible) to solve these equations mathematically for a given scenario. Thus, in fluid dynamics problems, a formal theory often needs to be supplemented by experimental observation.

Even for simple configurations, complex behavior can emerge for classical fluids. In this work, experiments analogous to "traditional" fluid dynamic experiments are performed with collectively migrating cell sheets. Due to the rich interplay between and the active movement of the individual components of such an active system, the "fluid" in these cases are already different than a straightforward Newtonian liquid, such as water. Accordingly, it is extremely important to understand how more simple fluids would behave in the analogous experiments, and to gain a detailed comprehension of in which aspects they differ from a collectively migrating cell sheet. While many properties cannot be transferred one-to-one from classical liquids to cell sheets, it is worth noting that some of the properties of these actively moving collective systems might fill a role that causes a given phenomenon in a simple fluid.

In consequence, this chapter details the basics of fluid mechanics, highlighting the different classifications of liquids and what differentiates them, as well as discussing where on the spectrum a migrating sheet of epithelial cells would fall in each case. Following this, two classical hydrodynamic problems are examined, flow through a pipe and flow through a constriction. It is these two scenarios that will later be studied analogously for migrating cell sheets.

2.3.1 The Navier-Stokes equation

In classical mechanics, the relationship between the acceleration of an object of mass m and the forces acting upon it is given by Newton's second law:

$$m d_t \mathbf{v} = \sum_j \mathbf{F}_j \tag{2.2}$$

Here, $\sum_j \mathbf{F}_j$ represents the external forces acting upon the particle, and $\mathbf{v}$ describes the particle's velocity. This law can be applied to fluids by means of some conversions, as outlined in reference [95]: In order to apply Eq. 2.2 to fluids, one must divide by the fluid's volume. This leads to the mass being replaced by the density ρ and the forces being replaced by force densities $\mathbf{f}_j$. Replacing the particle's velocity with the Eulerian velocity

field $\mathbf{v}(\mathbf{r}, t)$ and the time derivative d_t with the material time derivative D_t, Newton's second law of motion becomes the so called Navier-Stokes equation:

$$\rho D_t \mathbf{v} = \sum_j \mathbf{f}_j \tag{2.3}$$

Inserting the explicit form of the material time derivative, the Navier-Stokes equation becomes:

$$\rho\Big(\partial_t \mathbf{v} + (\mathbf{v} \cdot \nabla)\mathbf{v}\Big) = \sum_j \mathbf{f}_j \tag{2.4}$$

Finally, the explicit expressions for the force densities $\mathbf{f}_j$ can also be inserted, leading to the full Navier-Stokes equation for compressible fluids:

$$\rho\Big(\partial_t \mathbf{v} + (\mathbf{v} \cdot \nabla)\mathbf{v}\Big) = \underbrace{-\nabla p}_{\substack{\text{pressure-gradient} \\ \text{force density}}} \underbrace{+\eta\nabla^2\mathbf{v} + \Big(\frac{1}{3}\eta + \zeta\Big)\nabla(\nabla \cdot \mathbf{v})}_{\text{viscous force density}} + \underbrace{\rho\mathbf{g} + \rho_{el}\mathbf{E}}_{\text{body force density}} \tag{2.5}$$

Here, ∇p stands for the pressure-gradient, whereas η and ζ represent the viscosity and bulk viscosity (assumed to be constant), respectively. The last two terms of the sum on the right hand side of the equation stem from external forces acting throughout the entire fluid, typically (though not necessarily exclusively) the gravitational force (given by the product of the density ρ and the acceleration of gravity $\mathbf{g}$) and the electrical force (given by the product of the charge density ρ_{el} and the external electric field $\mathbf{E}$).

While the Navier-Stokes equation is not too complicated to write down, solving this non-linear differential equation analytically is a much bigger problem, and only possible for the right circumstances. As a result, whenever possible, special types of fluids, such as incompressible ones, are used as approximation as they allow the equation to be simplified. Numerical solutions of the full equation are possible, but even there, working with a simplified version is preferable.

2.3.2 Categorizations of fluid flows

As mentioned above, analytical solutions to the full Navier-Stokes equation can only be found for a few specific cases. For some special types of fluid flows, however, it can be sufficient to work with a reduced, more simple version. To this end, this chapter examines the different ways fluids and fluid flows can be categorized depending on their characteristics, and discusses how the Navier-Stokes equation can be simplified for some of these cases. Where possible, an assessment is given as to where collectively migrating cell sheets fit on the scale of each classification.

Newtonian vs. non-Newtonian fluids

One of the first distinctions that can be made when characterizing fluids is whether they are Newtoninan or non-Newtonian. The classification depends on the relationship between its strain rate and the resulting viscous stresses. In the most general case, a fluid is considered Newtonian if the viscosity tensor μ_{ij} describing the relationship between stress and strain does not depend on either the strain rate or the velocity of the flow (though a dependence on temperature is still possible).

In the more specific, but very common case that the liquid in question is isotropic (i.e. the mechanical properties of the fluid are the same in any direction) and incompressible (see section 2.3.2), the definition of a Newtonian fluid can be stated in a simple equation [94]:

$$\tau = \mu \frac{dv_x}{dy} \tag{2.6}$$

Here, τ is the shear stress in the fluid, μ is the scalar dynamic viscosity constant, and $\frac{dv_x}{dy}$ is the derivative of the velocity component parallel to the shear with respect to a displacement perpendicular to this direction (i.e. the strain rate).

Some typical examples of fluids that can be considered Newtonian, at least in all typically examined regimes, are water and most gasses [96]. On the other hand, the more

general case

$$\tau = f\left(\frac{dv_x}{dy}\right) \tag{2.7}$$

with f being a nonlinear function, describes all non-Newtonian fluids [94]. Typical examples for these cases include blood and starch suspensions. More generally speaking, emulsions and mixtures are frequently non-Newtonian, as are liquids of complex molecular structure (in particular long-chained molecules), such as polymers [96].

Cell sheets are visco-elastic, showing creep and stress relaxation behavior in response to mechanical loading [97], and as such will likely be more closely described by non-Newtonian liquids.

Incompressible vs. compressible flow

In many flowing fluids, the density of a flowing element of fluid can be seen as constant over the entire motion and in the entire examined volume, i.e. there is no notable expansion or compression of the liquid over the observation period [98]. Such flows are termed incompressible, or flows of incompressible liquids and in many cases the nature of incompressibility significantly simplifies the governing hydrodynamic equations. For instance, the continuity equation [94]

$$\frac{\partial \rho}{\partial t} + \nabla \cdot \mathbf{j} = 0, \tag{2.8}$$

where ρ is the mass density and $\mathbf{j} = \rho\mathbf{v}$ is the mass flux, simplifies to

$$\nabla \cdot \mathbf{v} = 0. \tag{2.9}$$

As $\partial_k v_k = 0$ holds true for incompressible fluids, the Navier-Stokes equation (Eq. 2.5) likewise simplifies to Eq. 2.10.

$$\rho\Big(\partial_t \mathbf{v} + (\mathbf{v} \cdot \nabla)\mathbf{v}\Big) = -\nabla p + \eta \nabla^2 \mathbf{v} + \rho\mathbf{g} + \rho_{el}\mathbf{E} \tag{2.10}$$

Due to the simplification of many of the relevant equations that follows from incompressibility, the question of whether the collective migration of sheets of epithelial cells can be considered an incompressible flow is a very relevant one. In order to answer this question, it is necessary to clarify whether the cell sheets themselves are compressible in general. If they are not compressible in the traditional sense (i.e. force leads to instantaneous deformation), it is important to consider that they might still slowly remodel their shape due to external pressure, by remodeling their cytoskeleton. In terms of flow behavior, such remodeling to adjust for pressure could well take the role of compressibility even if the cells themselves were incompressible. If such a pseudo-compressibility occurs, it then becomes essential to determine whether it happens on a time scale relevant to their migration in a particular scenario. In this scenario, the question of whether or not their migration can nonetheless be modeled as an incompressible flow remains. While compressible fluids generally lead to compressible flows, under the right conditions they can nonetheless be approximated very well by incompressible flows.

In principal, the difference between an incompressible fluid and an incompressible flow is which derivative of the density is required to be zero. An incompressible fluid is one where the partial derivative with respect to time $\frac{\partial \rho}{\partial t} = 0$, i.e. the density of a control volume of the fluid does not change at a fixed point in space. On the other hand, in an incompressible flow, $\frac{\partial \rho}{\partial t}$ can be nonzero, as long as the material derivative $\frac{D\rho}{Dt}$ vanishes [99]. This constraint is the equivalent of saying that the density of a control volume moving at the same velocity as the fluid is constant. It is worth noting that this second, weaker constraint is sufficient to yield the aforementioned simplified continuity equation (Eq. 2.9). Thus, determining whether or not the divergence of the velocity is zero is sufficient to determine whether a flow is incompressible or not. The flow of sheets of epithelial cell sheets (including Madin-Darby Canine Kidney (MDCK) and Michigan Cancer Foundation-10A (MCF10A), the two epithelial cell lines used in this thesis) has been shown to have an average divergence close to zero [100], though the experimental boundary conditions likely play a role in whether or not this holds true in any particular scenario. Thus, while it is possible to treat the flow of migrating cell sheets as incompressible, examining the divergence of the flow for each experiment at hand would be ideal.

Laminar vs. turbulent flows

In fluid dynamics, a flow is considered to be laminar if the liquid can be subdivided into parallel layers that slip past each other at different velocities [101]. In particular, this

means that there is no mixing of these sublayers (i.e. there are no currents perpendicular to the direction of flow). In contrast, in turbulent flows such mixing does occur, typically in the form of so called vortices or swirls. Whether a fluid flows laminarly or turbulent depends on how fast it is flowing relative to how viscous it is. This relation is captured in the dimensionless Reynolds number Re, which varies depending on the boundaries of the examined problem. In the simplest case, for the flow of a fluid through a straight pipe with radius a, it is given by Eq. 2.11 [101].

$$Re = \frac{2\rho a v}{\mu} \tag{2.11}$$

Here ρ represents the density of the fluid, v its velocity, and μ the dynamic viscosity. Though it is not straightforward to determine an exact transition point (due in part to the stability of pipe flow to infinitesimal perturbations and the fact that at low Re turbulence is only transient), a value around $Re = 2000$ is a good approximation [102]. This means that laminar flow generally occurs for liquids that flow slowly or are very viscous.

Still, the concept of the Reynolds number cannot be transferred on a one-to-one basis to the migration of cellular sheets, as it was not conceived for active materials. One striking difference to passive liquids is the fact that individual cells can inject energy into the system, and, in principle, single cells or small groups of cells can temporarily move against the general direction of flow. In addition, cell divisions create new "particles" in the middle of the migrating sheet, and the whole process of rounding up and dividing can also act as a perturbation to the system, whereas for more classical systems such disturbances must be introduced externally. These differences might help explain why despite the fact that generally speaking, migrating cell sheets move slowly (on the scale of tens of micrometers per hour) and viscously (with strong adhesions between the individual cells in the layer), they still tend to behave in a turbulent manner. For instance, the formation of vortices during cell migration is a frequently observed phenomenon [27, 37].

Due to this, the migration of cell sheets is unlikely ever to be entirely reminiscent of a laminar flow. It cannot be ruled out, however, that despite small scale perturbations, on long time scales in the right geometries, the cells' motion can be approximated by a laminar flow. As such, while the default assumption should be that the cell behavior will be turbulent, an investigation on a case-by-case basis is necessary.

Steady vs. unsteady flows

A rather straightforward classification of flows is into steady and unsteady flows. In this context, a steady flow is one that does not change over time, i.e. the flow profile is identical, independently of the time point at which it is examined. Mathematically speaking, a steady flow is one for which $\partial/\partial t = 0$ for any quantity pertaining to flow [93]. An unsteady flow therefore is one that is not constant over time.

Steadiness or unsteadiness always depends on the frame of reference. For instance, flow around an obstacle might be steady, while in a reference frame where the obstacle is instead dragged through the fluid, the motion is not steady [93]. In the case of collectively migrating cells that invade channels (either straight or with a constriction), as were studied in this thesis, the flow is not steady in the reference frame of the observer. Over time, the cell sheet invades deeper into the channel (potentially even encountering a constriction) and changes accordingly. For instance, at $t = 0$, there is no flow of cells 100 µm ahead of the front, but several hours later, once the cell sheet has invaded past that point, there clearly is. It is still possible that flow might be steady (or approximately steady) in different reference frames in this situation, however. For example, in a reference frame moving with the velocity of the cell front, the flow might not change over time (i.e. the flow 200 µm behind the front of the cell sheet might always be approximately the same, no matter how far the cell sheet has penetrated into the channel).

Inviscid vs. viscous vs. stokes flow

Both inertial and viscosity effects influence the dynamics of fluids. Flow can be categorized into different regimes according to which of the forces is dominant. Again, this behavior is captured by the Reynolds number.

When viscous forces are very strong compared to inertial forces ($Re \ll 1$), inertial forces can be neglected, leading to a regime known as Stokes flow (also referred to as creeping flow) [103]. Conversely, when inertial effects dominate over viscous ones ($Re \gg 1$), the flow can be modeled as inviscid by entirely neglecting the viscosity [93]. In both cases, neglecting some contributions serves to simplify the Navier-Stokes equation, to the point where it can sometimes be solved.

For inviscid flow, the Navier-Stokes equation (Eq. 2.5) simplifies to the Euler equations.

For an incompressible fluid, this is:

$$\rho \frac{Dv}{Dt} = -\nabla p + \rho g \tag{2.12}$$

For Stokes flow, the unsteady and convective terms in the Navier-Stokes equation are neglected, leading to the so-called Stokes equation [103]:

$$\nabla p = \eta \nabla^2 \mathbf{v} \tag{2.13}$$

Aside from potential time-dependent boundary conditions, the Stokes equation contains no more time dependence (which by default also makes it time reversible) [103]. Unfortunately, Stokes flows is always only an approximation, as all real flows have a finite Reynolds number. An acceptable rule of thumb for when the approximation is good appears to be $Re < 0.1$ [103].

Phenomenological observation of collectively migrating cell sheets regrettably indicates that they likely fall into the regime of viscous flows, where neither approximation is valid, and thus the full Navier-Stokes equation must be used, or it must be simplified in some other way.

2.3.3 Poiseuille flow through a pipe

As mentioned in section 2.3.1, there are, a handful of special cases for which the Navier-Stokes equation (Eq. 2.5) can be analytically solved. One of the most straightforward of these cases is a pipe with a circular cross-section, with an incompressible liquid driven through it due to a pressure difference between its two ends. In this case, some further simplifications of the Navier-Stokes equation for compressible fluids (Eq. 2.10) are possible [95]:

Translational invariance of the channel in x-direction (i.e. the direction the pipe is parallel to) and the fact that the gravitational force balances out with a hydrostatic pressure gradient in opposite direction lead to $(\mathbf{v} \cdot \nabla)\mathbf{v} = 0$ and consequently:

$$0 = -\nabla p + \eta \nabla^2 \left[v_x(y, z) \mathbf{e}_x \right] \tag{2.14}$$

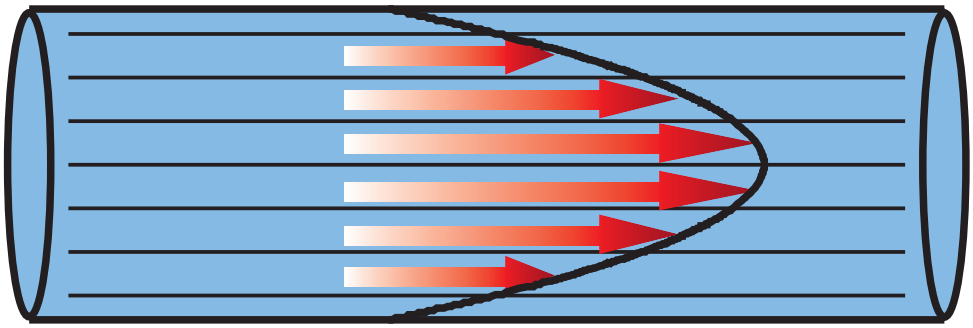

Figure 2.4: Flow of a Newtonian fluid through a pipe, showing the characteristic parabolic flow profile resulting from Hagen-Poiseuille's law. At the center of the tube the velocity is at its maximum, before dropping off all the way to zero at the pipe's edges.

Taking the condition for the boundary ∂C of a circular cross section C of radius a (Eq. 2.15) and the no-slip boundary condition (Eq. 2.16), the Navier-Stokes equation can be further reshaped and simplified.

$$\partial C : 1 - \frac{y^2 - z^2}{a^2} = 0 \tag{2.15}$$

$$v_x(y, z) = 0 \qquad \text{for} \quad (y, z) \in \partial C \tag{2.16}$$

The result is a second-order partial differential equation for $v_x(y, z)$ inside C (Eq. 2.17) and the corresponding solution (Eq. 2.18).

$$\left[\partial_y^2 + \partial_z^2\right] v_x(r) = -\frac{\nabla p}{\eta L} \tag{2.17}$$

$$v = -\frac{1}{4\eta}\frac{\Delta p}{\Delta x}(R^2 - r^2) \tag{2.18}$$

Thus, an incompressible fluid driven through a pipe by a pressure gradient shows a characteristic parabolic flow profile, where the velocity depends on the distance to the wall (see Fig. 2.4). For visualization, the fluid can be imagined as several circular layers (lamina) that each move with a velocity that only depends on their radial distance from the center. Due to the no-slip condition, the lamina touching the tube wall must be stationary, and viscosity slows down the proximate lamina as well. On the other hand, the velocity is maximal in the center of the channel, and viscosity drags along neighboring

lamina, speeding them up. Taken together, all the acting forces result in the parabolic shape.

Naturally, physical models for a pressure driven incompressible fluid need to expanded to describe collectively migrating cells, which include other contributions such as cell activity. Changes in the properties of the flowing material can drastically alter the flow profile. For instance, more turbulent flows show a profile that more strongly resembles a plug flow over most of the width [104]. As discussed, the Navier-Stokes equation is hard to solve analytically, however, so even finding a solution for something more closely resembling the dynamics of collectively migrating cells can be difficult. Phenomenologically, however, the problem can easily be accessed from the opposite direction, and the flow profile determined experimentally.

2.3.4 Fluid flow through a constriction

Expanding on the scenario of flow through a straight pipe, the diameter of the cross section need not be constant, such as in the case of fluid flow through a constriction. An incompressible Newtonian fluid in this situation (see Fig. 2.5) moves at a higher velocity in the part of the tube where the diameter is smaller, because the principle of conversation of mass dictates that the same amount of mass needs to be transported in the same time as in the areas with large diameter (where the same mass transport can be achieved with a slower velocity).

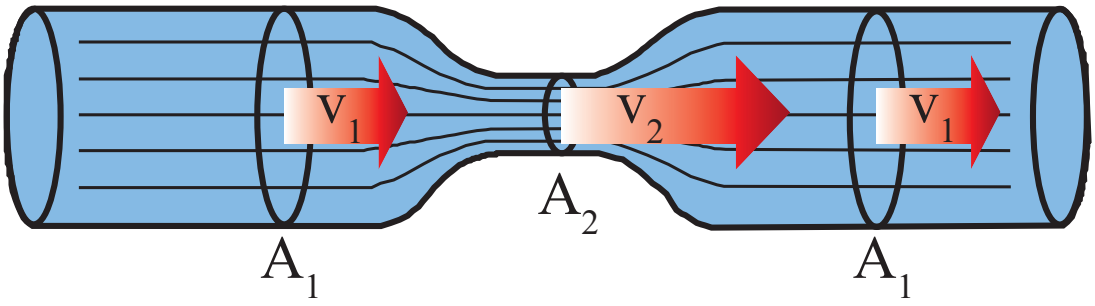

Figure 2.5: Flow of a Newtonian fluid through a constriction. Due to conservation of mass, the velocity of the fluid increases as it flows through the narrow part of the constriction, before dropping back to its original value once the original diameter is reached again.

In principle, in classical hydrodynamic situations this increase in velocity is accompa-

nied by a decrease in hydrostatic pressure, following Bernoulli's equation:

$$\frac{v^2}{2} + gz + \frac{p}{\rho} = \text{constant} \tag{2.19}$$

Here, the velocity of the fluid is given by v, g is the acceleration due to gravity, z is the elevation above a reference plane, p is the pressure at the chosen point and ρ is the density of the fluid. However, for the migrating cell sheets in this thesis, no equivalent parameter to the pressure was measured, and as such, the reduction in pressure is less interesting then the change in the flow field. The notion of the existence of a homeostatic pressure in tissue, however, highlights its potential importance in future work [105].

The intriguing question examined in this thesis is what the flow profile of a 2D cell sheet migrating through a constriction will look like. As mentioned above, the incompressible Newtonian fluid develops an increased velocity in the constriction, compared to both in front of it and behind it. This is a direct result of the mass continuity principle, however, which *ad initium* already does not hold true for migrating cell sheets, due to cell proliferation. On top of this, the cell sheet might be compressible, which would additionally break the incompressibility requirement. Given these differences, it is particularly intriguing to see how the cells will migrate when the constriction in the channel reduces the room they have available.

2.3.5 Diffusion theory

Diffusion is a term that can refer to two distinct processes. On the one hand, self-diffusion describes the random motion of individual particles in the absence of external gradients driving a mass flux. The most common case of self-diffusion is the diffusive movement of molecules propelled by thermal energy. On the other hand, collective diffusion indicates the movement of a large number of particles as a result of a particle density gradient. In contrast to self-diffusion, the interactions between the individual agents plays a critical role for collectively diffusing particles.

Even though both phenomena are distinct, they can be characterized by diffusion coefficients. The self-diffusion coefficient and the collective diffusion coefficient for a substance will have disparate values, however, unless the system in question includes no interactions between the individual particles (e.g. ideal gas). In a way, the discrepancy between self-

diffusion and collective diffusion is a measure for these interactions, and thus, measuring them both for any given system can be of interest.

Single particle diffusion: random walks

Self-diffusion constants are often determined by fitting the observed mean squared displacement (MSD) with random walk models. These are typically used to describe a variety of phenomena, such as the search paths of foraging animals [106], the folding of polymers [107], or the motion of isolated cells [108]. The term random walk defines motion in the form of successive steps, with both the step size and the direction of the step entirely random for each time point. There are several different instances of random walks, distinct from one another by whether or not they include such things as bias and correlation.

The most basic random walk model to describe mathematically is the unbiased and uncorrelated random walk [109]. In the context of these models, unbiased refers to the equal likelihood to move in all directions (as opposed to some directions being preferred), whereas uncorrelated indicates that each step is independent of all preceding steps. Unfortunately, this simple isotropic random walk model is often insufficient to describe biological scenarios. The most predominant expansions of the simple random walk model are the biased random walk, which includes a preferential direction for all steps, and the correlated or persistent random walk, in which each step has a higher probability of maintaining the same direction as the previous one than going in any other direction.

It is also possible to extend models by including waiting times between steps or incorporating barriers (implemented via reflecting or absorbing boundary conditions). Typically, when models allow for varying step sizes, only step size distributions with finite variances are considered. For sufficiently long times, the distribution of the location coordinate of a walker on any axis converges to a Gaussian distribution in these cases [109]. One example to the contrary is the Lévy flight, which has a heavy-tailed distribution of steps, meaning the occasional long step is included with the more frequent short steps. While Lévy flights have been used to successfully describe animal search patterns [110], their applicability is still controversial and unclear [111, 112].

In the context of this thesis, the self-diffusion of migrating cells is studied. The most prominent model to describe such cells is the persistent random walk [113, 114]. As noted above, the self-diffusion constant is related to the MSD, which is calculated by measuring the distance from the position at any starting point x_0 on the cell track to the position of

the cell Δt later, and then averaging over all possible starting points (Eq. 2.20). For the persistent random walk model, this relation is given by Fürth's formula (Eq. 2.21), with the MSD denoted as $\langle x^2 \rangle$, the diffusion coefficient denoted as D, and t and T_p indicating the time and the persistence time (the time scale on which the correlation in the steps' direction is preserved), respectively [113].

$$\langle x^2 \rangle = \langle (x(t + \Delta t) - x_0(t))^2 \rangle \tag{2.20}$$

$$\langle x^2 \rangle = 4D \cdot \left(t - T_p \cdot (1 - e^{-\frac{t}{T_p}}) \right) \tag{2.21}$$

For $t \gg T_p$, this formula can be simplified to Eq. 2.22. For short persistence times, this simplified equation also serves as a good approximation [114].

$$\langle x^2 \rangle = 4Dt \tag{2.22}$$

Collective diffusion: Fick's law

Collective diffusion refers to the diffusion of a large number of particles, typically with interactions between each other. In the presence of a spatial density gradient $\frac{\partial c}{\partial x}$, this particle diffusion with collective diffusion coefficient D will result in a macroscopic flux j as described by Fick's first law [115]:

$$j = -D \frac{\partial c}{\partial x} \tag{2.23}$$

More generally, the collective motion of a multitude of particles is described by the diffusion equation, which can be derived from the continuity equation:

$$\frac{\partial c}{\partial t} + \nabla \cdot \mathbf{j} = \sigma \tag{2.24}$$

Here, c is the density of particles per unit volume, t is the time, $\mathbf{j}$ is the particle flux, and σ represents the particle generation per unit volume per unit time ("sources" or "sinks"). Assuming there is no generation or destruction of particles ($\sigma = 0$) and the only source

of flux is diffusive flux (**j** taken from Eq. 2.23), the resulting diffusion equation is:

$$\frac{\partial c}{\partial t} = D\frac{\partial^2 c}{\partial x^2} \tag{2.25}$$

Expansion of this equation, to include other terms necessary to capture a system's features (e.g. reaction terms), is easily possible, as described in section 2.5.1. These equations then allow a good access point for determining the collective diffusion coefficient from experimental measurements of a system, such as, in this thesis, collectively migrating cell sheets.

2.4 Glass transitions in supercooled liquids and cell collectives

Cell sheets are known to flow like fluids at long scales, yet act more like a rigid solid on short scales, where motions of each cell are strongly confined by their neighbors [27, 70]. Intriguingly, such a solid-like character over short times, paired with collective flow over longer times is reminiscent of the behavior of supercooled liquids approaching a glass transition. Angelini et al. have suggested the notion that the collective motion of cells might undergo a similar transition, with density taking the role of temperature [38]. In particular, the idea is that an increase in cell density restricts the motion of each cell due to stronger crowding, forcing the cells to move in groups. Recent work has confirmed the role of this jamming or glass transition in cell migration [41, 46, 57]. To this end, this chapter gives a very brief introduction to the concept of the glass transition observed in supercooled fluids, and highlights the key characteristics of such fluids as they approach the transition that have also been found in cell collectives.

Glasses are materials that act mechanically like solids, but lack the periodicity of crystals [116]. They are most commonly produced by supercooling, i.e. cooling a viscous liquid fast enough to avoid crystallization. Specifically, the process works as follows [117]: As the liquid is cooled, viscosity increases and the constituent molecules move more and more slowly. This means that a longer time is necessary for the molecules to sample the available configuration space and the time for finding the optimal configuration for that temperature (i.e. the equilibrium) will increase. If the temperature is decreased at a con-

stant rate, eventually the time for finding this equilibrium will be longer than the time scale of cooling, and the configuration will begin to deviate from the optimum. Eventually, as the temperature continues to decrease, the molecules will move too slowly to sample any available configurations on the relevant time scales, essentially becoming "frozen". As no periodicity was reached, the resulting material is a glass. This changeover defines the glass transition temperature, though there are multiple options for the exact definition of its value [116].

While the field of supercooled liquids and the glass transition is very wide, and still has many unanswered questions, there are some phenomenological characteristics of supercooled fluids approaching the transition that are shared by cell collectives. Specifically, these are the appearance of dynamic heterogeneities, a transition from collective relaxation to highly constrained localized motion and the appearance of peaks in the density of states (DOS). Dynamic heterogeneities can be observed in the velocity fields of confluent epithelial monolayers. This means that the field is spatially heterogeneous, with variations in magnitude from region to region. Importantly, these different velocities are not randomly distributed, but rather organized in clusters, with faster cells (and, correspondingly, slower cells) frequently being grouped together. Likewise, the stress landscape throughout the monolayer shows the same dynamic clusters. These clusters of high velocity/stress are not structural, which means they do not relate to the cell density and they occur in a dynamic matter [38, 39]. As density increases, these dynamic heterogeneities increase in size, while at the same time the magnitude of observed velocities decreases, behavior known from supercooled fluids approaching a glass transition [38].

Collective cell sheets also show a transition density, below which cells move greater distances by directed migration than by stochastic motion. Above this density, motion is predominantly diffusive. Again, this transition from collective relaxation to confined, localized single cell motion is behavior reminiscent of a glass transition [38]. Intriguingly, the inverse cell diffusivity D_0, as a function of the cell density, is well-fitted by the Avramov-Milchev equation (Eq. 2.26), which describes stress relaxation in glass forming molecular fluids and glass forming colloidal fluids, as a function of temperature and density, respectively [118].

$$\frac{1}{D_0} = \frac{1}{D_{\max}} \exp\left[\epsilon \left(\frac{\sigma}{\sigma_g}\right)^{\alpha}\right] \tag{2.26}$$

Here, $D_{\max}$ is the diffusivity at zero density, ϵ is a dimensionless activation energy at

the glass transition density σ_g, and α is a fragility parameter. Fitting of experimental data by Angelini et al. resulted in values of $\alpha = 2.4$ and $\epsilon = 1.8$ [38]. This fragility parameter is about in the middle between "strong" glasses ($\alpha \approx 1$) and fragile glasses ($\alpha \approx 5 - 6$), indicating epithelial cell layers are best described as moderately fragile glass forming fluids. Meanwhile, the relative width of the activation energy spectrum is large compared to most molecular glasses, in which $\epsilon \approx 30$ [38, 118]. In summary, these findings indicate that collective migration within a confluent cell monolayer shows relaxation behavior very reminiscent to the non-Arrhenius relaxation of moderately fragile glass forming fluids.

The final characteristic behavior of supercooled fluids approaching a glass transition found in cell collectives is given by the appearance of peaks in the DOS. To analyze this, Angelini et al. studied the dynamic structure factor $S(q, \omega)$ of confluent cell motion, defined as the modulus squared of time and space Fourier transform of the image intensity. They fit their data by the frequently used damped harmonic oscillator model [38]:

$$\frac{S(q,\omega)}{S(q)} = I_0(q)\frac{\frac{1}{2}\Gamma_0(q)}{\omega^2 + \left(\frac{1}{2}\Gamma_0(q)\right)^2} + I(q)\frac{\Omega(q)\Gamma^2(q)}{\left[\omega^2 - \Omega^2(q)\right]^2 + \omega^2\Gamma^2(q)} \tag{2.27}$$

The first term of the sum is a Rayleigh peak, which quantifies the systems self-diffusivity. Its amplitude and its width are given by $I_0(q)$ and $\Gamma_0(q)$, respectively. The second term in the sum is a Brillouin peak, which measures the elastic response to density fluctuations. Its amplitude and width are given by $I(q)$ and $\Gamma(q)$ respectively. This fit can then be used to calculate the group velocity $c = d\Omega(q)/dq$, the reciprocal of which is $dq/d\omega$ and is necessary to calculate the DOS, which in 2D is given by Eq. 2.28 with a maximum wave vector $q_{\max}$.

$$n(\omega) = 2q_{\max}^{-2} q(dq/d\omega) \tag{2.28}$$

This DOS is found to have one peak at low densities, corresponding to cell body shape fluctuations, whereas at higher densities, a second peak corresponding to the cell division time appears [38].

Understanding the glass transition is already far from trivial for supercooled fluids, but for a system of cells there are several more features that will have to be taken into account, namely the fact that the system is active, and particles can generate forces internally, actively or passively change their shape, as well as proliferate. Similar to foams

which display a coarsening of bubbles over time [119], cell layers also age, increasing their density over time, which can lead to a change of local stresses and thereby adds another challenge to the issue.

In summary, hardly anything is known about active systems approaching a glass transition, though phenomenologically cell layers certainly display the features associated with such a transition. As a result, cells at low densities behave like a fluid, whereas cells at higher densities act as a glass, and structural relaxations take on the order of days [38].

2.5 Overview of cell migration models

A wide variety of theoretical frameworks is available for describing and reproducing collective cell behavior, a good overview of which is given in reference [4]: Reaction-diffusion models are the simplest approaches, taking only a term to describe collective diffusion and a term to describe cell proliferation and examining to what extent this (often analytically solvable) description is sufficient. More complex models that still aim at good conceptual understanding are continuum models. They can include far more detailed parameters to describe cell behavior (such as friction, viscosity, or diffusivities), but still work best at scales that are large compared to the individual agents (in this case cells). Less coarse-grained models attempt to achieve more detailed descriptions by modeling each cell as an individual particle and having them interact with each other. Of these particle-based models, the Vicsek model is probably the most well known. Finally, the most detailed models describe cells in an even more extended manner, not simply modeling each cell as an individual agent, but also including things like cell area, cell-cell adhesions, cell contractility and cell polarization explicitly. These quantities are key determinants of cell shape and motility, making their incorporation necessary if the goal is to study features on the scale of only a few cells. The two most prominent models from this category are the vertex model and the cellular Potts model.

This chapter gives a short introduction into each category of models, with special detail to models that were used in the course of this thesis.

2.5.1 Reaction-diffusion equations: Fisher-Kolmogorov

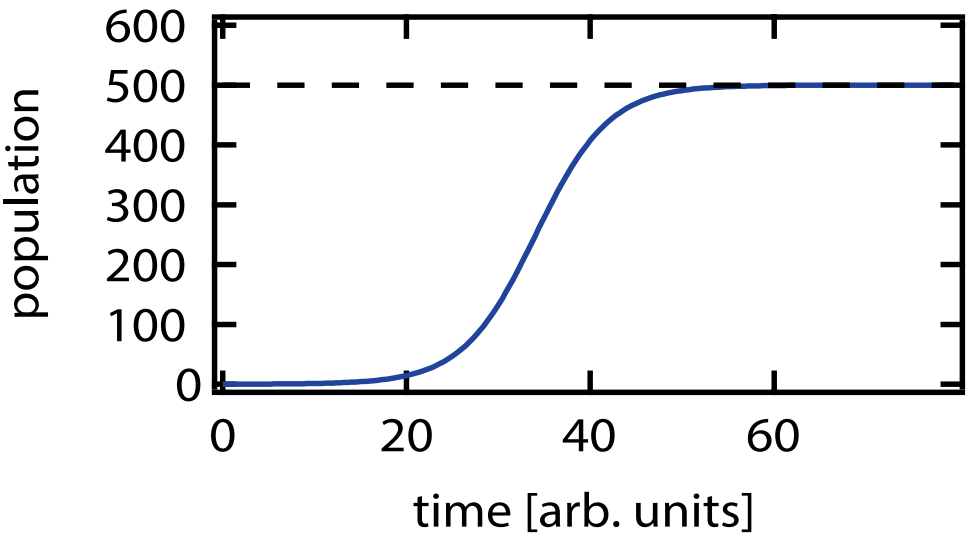

Figure 2.6: Theoretical population curve for ideal logistic growth. The population begins growing exponentially but slows down as it approaches the carrying capacity k=500, indicated by the dashed black line.

Random motion of individual particles and their interactions can result in macroscopic diffusion, described by Fick's law (see section 2.3.5). The most coarse-grained approach to modeling collective cell migration is to simply assume that the change of the cell density c over time t is described by the diffusion equation (Eq. 2.25). This is unlikely to be sufficient in most cases, however, as the cell density will change due to changes in cell number, following proliferation. Thus, the regular diffusion equation (Eq. 2.25) is expanded to include a term to account for this "reaction" of one cell turning into two cells. The result is a reaction-diffusion equation, generally of the form given in Eq. 2.29.

$$\frac{\partial c}{\partial t} = f + D\frac{\partial^2 c}{\partial x^2} \tag{2.29}$$

Here, f is a function of c, x and t that accounts for all reactions in the system [115]. While it is possible to choose many different reaction terms f, in the absence of any further knowledge of the system, the simplest approach is the best. In this case, the simplest model for cell proliferation is logistic growth, which assumes exponential growth at a rate λ until the system saturates when it approaches a maximum carrying capacity k as illustrated in Fig. 2.6.

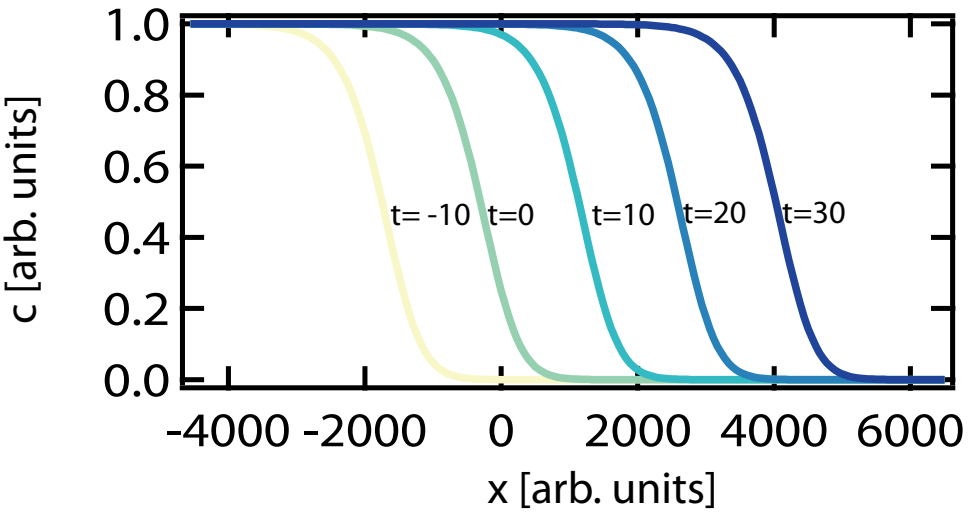

Figure 2.7: Traveling wave propagating in x-direction. As the time t increases (indicated by the color gradient from yellow to dark blue), the wave moves in positive x-direction. During this time, the density profile c remains in a constant shape. The wave moves with a constant velocity as can be seen by the equal distance between the wave fronts.

The result of inserting logistic growth into Eq. 2.29 is the Fisher-Kolmogorov equation (Eq. 2.30), the simplest nonlinear reaction-diffusion equation in one dimension.

$$\frac{\partial c}{\partial t} = \underbrace{\lambda c \cdot (1 - \frac{c}{k})}_{\text{reaction term}} + \underbrace{D\frac{\partial^2 c}{\partial x^2}}_{\text{diffusion term}} \tag{2.30}$$

As mentioned in the introduction of this system, one great advantage of simple descriptions via reaction-diffusion equations is that they can have analytical solutions. Specifically, the Fisher-Kolmogorov equation can be solved by traveling waves. These are waves that fulfill two distinct criteria: the shape of the propagating wave front is preserved over time, and the velocity of the wave front is constant [115], as illustrated in Fig. 2.7. Mathematically speaking, a solution of Eq. 2.30 is a traveling wave if it satisfies:

$$c(x,t) = c(x - vt) \tag{2.31}$$

Physically, such solutions can make sense for scenarios of expanding cell sheets, such as wound healing assays or invasion of channels. Such traveling wave solutions to the Fisher-Kolmogorov equation result in a well-defined relation (Eq. 2.32) between the collective

diffusion coefficient D and the front propagation speed v [115].

$$v = \sqrt{4D\lambda} \tag{2.32}$$

The growth rate λ is readily accessible through independent experimental measurements, and the front speed of an expanding cell sheet is also relatively straightforward to determine in a corresponding experiment. This makes this relation an intriguing possibility to validate whether the reaction-diffusion model properly describes the experimental system. Independently determining the third parameter, the collective diffusion coefficient D, however, is less straightforward and will complicate matters. In general, for purposes other than validating the model, a value can be obtained by fitting the Fisher-Kolmogorov equation's analytical solution (Eq. 2.33) to the experimentally determined density profiles [120]. In the process, this gives an additional check as to the applicability of Eq. 2.30 to the experimental system on hand.

$$f(x) = k \cdot \left[1 + \exp\left(-\frac{5}{6}\lambda t + \sqrt{\frac{\lambda}{6D}} \cdot x\right)\right]^{-2} \tag{2.33}$$

In publication P2, which is discussed in section 3.1 of this thesis, we studied collective cell migration of 2D epithelial sheets into microstructured channels [63]. The temporal and spatial evolution of the cell density profile is examined and modeled with the Fisher-Kolmogorov equation. At coarse-grained scales, these models reproduce observed phenomena surprisingly well given the simplicity of the approach.

2.5.2 The active isotropic-nematic mixture model

Continuous media approaches can be slightly more detailed than a description via a simple reaction-diffusion equation. While they cannot include biological details of cells and their interactions to the degree that more complex, cell based models can, mathematical analysis and thus conceptual understanding is typically simpler with continuous media approaches [4]. In these frameworks, the spatiotemporal dynamics of cell sheets are described using fields, while ignoring the individual cells that make up the studied matter. Typically, these models work well on length scales that are significantly larger than the scale of the agents that are being ignored, so they should be expected to be capable of giving accurate results down to a length scale of several cell lengths. Conceptually, the

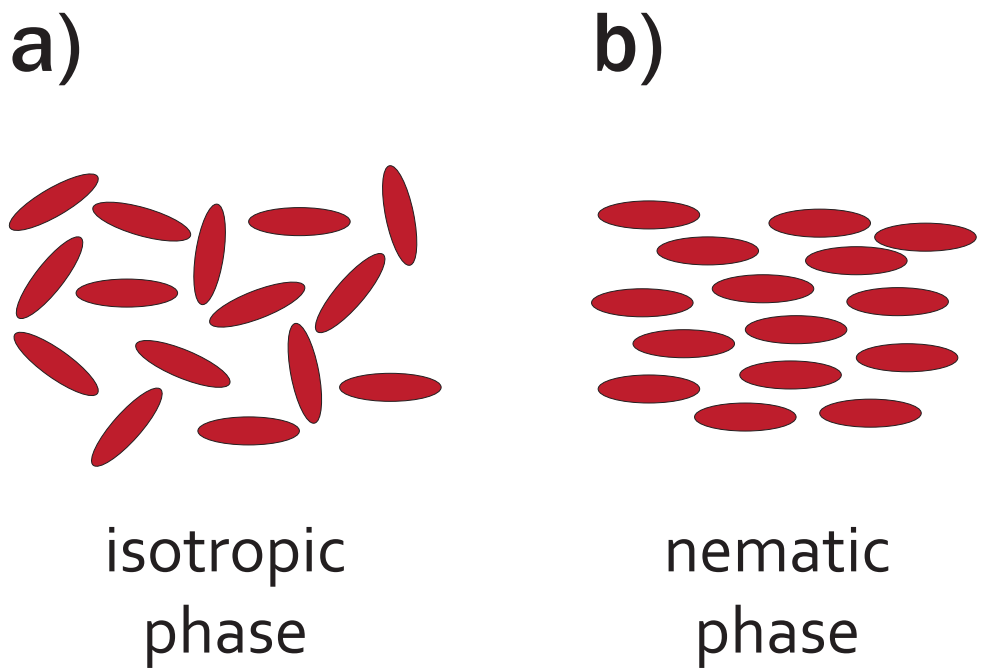

Figure 2.8: Illustration of orientation of liquid crystals in different mesophases. **a)** In the isotropic phase, the elongated liquid crystal molecules are randomly oriented. **b)** In the nematic phase, liquid crystals align so that they share long-range directional order, but the molecules share no positional order.

principle equations in continuum based models are partial differential equations derived from conservation laws (e.g. conservation of mass or momentum).

An example of this class of models, which has recently been used successfully for describing the relationship between topological defects and cell extrusion from an epithelium is a nematohydrodynamics simulation that accounts for the effects of both cell velocity and orientation [100]. It models cell sheets as an active mixture of a nematic phase and an isotropic phase (see Fig. 2.8). More specifically, the regions covered by the cell-sheet are modeled as nematic, and the "free area" the cell sheet can expand into is modeled as isotropic. The key parameters describing the system in this framework are the velocity and the nematic order. In brief, the model describes the evolution of the nematic order by the Beris-Edwards equation and the evolution of the velocity by the incompressible Navier-Stokes equation, with order influencing the evolution of velocity and vice versa. This chapter details the specifics of this model as they are outlined in reference [100]:

Order is one of the key parameters in this model, and the orientational order of cells is

given by the nematic order tensor:

$$\mathbf{Q} = \frac{3S(\mathbf{nn} - \mathbf{I}/3)}{2} \tag{2.34}$$

Here, $\mathbf{n}$ is the cell orientation, $\mathbf{I}$ is the identity matrix and S is the magnitude of the order. This equation accounts for the fact that unlike regular liquid crystals, cells are not symmetric and have a front end and a back end when they are polarized. The Beris-Edwards equation then gives the evolution of the nematic order [121]:

$$(\partial_t + u_k\partial_k)Q_{ij} - S_{ij} = \Gamma H_{ij} \tag{2.35}$$

Here, $(\partial_t + u_k\partial_k)$ is the total derivative, $\mathbf{u}$ is the velocity field and the co-rotation term accounting for the response of cell orientation to velocity gradients is denoted by S_{ij} and given by:

$$S_{ij} = (\lambda E_{ik}+\Omega_{ik})(Q_{kj}+\delta_{kj}/3)+(Q_{ik}+\delta_{ik}/3)(\lambda E_{kj}-\Omega_{kj})-2\lambda(Q_{ij}+\delta_{ij}/3)(Q_{kl}\partial_k u_l) \tag{2.36}$$

The velocity gradients, in form of extensional and rotational flows are characterized by the strain rate tensor E_{ij} (Eq. 2.37) and the vorticity tensor Ω_{ij} (Eq. 2.38), respectively.

$$E_{ij} = (\partial_i u_j + \partial_j u_i)/2 \tag{2.37}$$

$$\Omega_{ij} = (\partial_i u_j - \partial_j u_i)/2 \tag{2.38}$$

Finally, H_{ij} from Eq. 2.35 is a field describing the relaxation of orientational order towards the minimum of the free energy F (i.e. the equivalent of potential forces):

$$H_{ij} = \frac{\delta F}{\delta Q_{ij}} + \frac{\delta_{ij}}{3}\mathrm{Tr}\left(\frac{\delta F}{\delta Q_{kj}}\right) \tag{2.39}$$

The free energy f is calculated as the sum of the bulk free energy F_b and the free

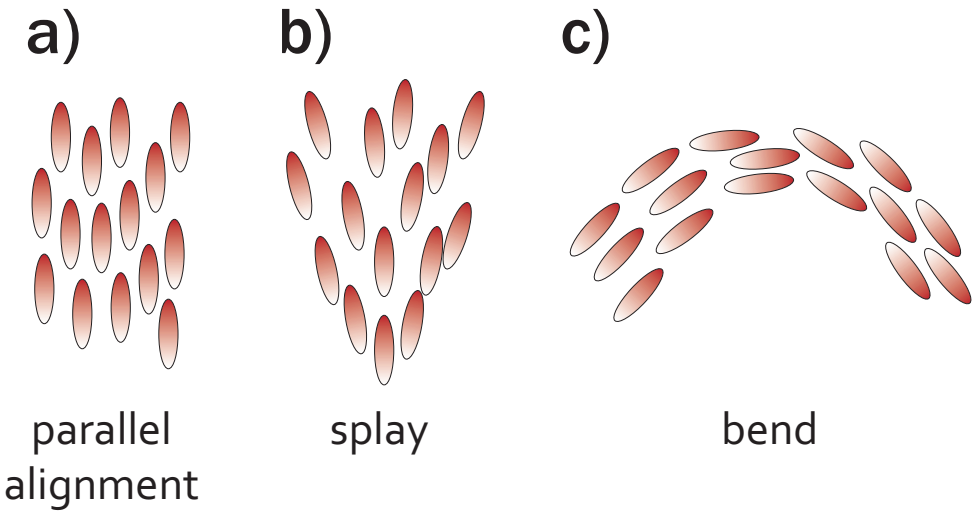

Figure 2.9: Orientations of liquid crystals in a nematic phase. **a)** Parallel alignment is energetically the most favorable. **b)** Splayed alignment, in which cells diverge. **c)** Bending alignment, in which cells groups of cells form an arc. Deviations from parallel alignment as seen in **b)** and **c)** cost energy.

energy corresponding to spatial inhomogeneities in the orientation field (i.e. deviations from parallel alignment):

$$F = F_b + F_{el} \tag{2.40}$$

The bulk free energy and the spatial inhomogeneity free energy are calculated according to Eq. 2.41 and 2.42, using the Landau-De Gennes expansion and the Oseen-Frank expansion with single elastic constant approximation, respectively:

$$F_b = \frac{A_Q(Q_{ij}Q_{ji})}{2} + \frac{B_Q(Q_{ij}Q_{jk}Q_{hi})}{3} + \frac{C_Q(Q_{ij}Q_{ji})^2}{4} \tag{2.41}$$

$$F_{el} = \frac{K(\partial_k Q_{ij})^2}{2} \tag{2.42}$$

A_Q, B_Q and C_Q are material constants in these equations, whereas K is the elastic constant. The elastic constant was set to equal values for both deviations from parallel alignment that are possible in 2D (splay and bend, as illustrated in Fig. 2.9).

Evolution of the nematic order is an important part of the model, but far from sufficient for the complete description of the system, which must also include equations for the

evolution of the velocity field. Under the assumption that the cell monolayer can be treated as an incompressible fluid (see chapter 2.3.2), the evolution of the velocity is given by the incompressible Navier-Stokes equation:

$$\rho \left(\partial_t + u_k \partial_k\right) u_i = \partial_j \sigma_{ij} \tag{2.43}$$

Stress gradients drive the rate of change of the velocity, and the total stress, σ is made up of several contributions: isotropic pressure $\sigma^{\text{isotropic}}$, viscous stress σ^{viscous}, nematic elastic stress σ^{el} and active stress σ^{active}:

$$\sigma_{ij}^{\text{isotropic}} = -P\delta_{ij} \tag{2.44}$$

$$\sigma_{ij}^{\text{viscous}} = 2\eta E_{ij} \tag{2.45}$$

$$\begin{aligned}\sigma_{ij}^{\text{el}} = 2\lambda(Q_{ij} + \delta_{ij}/3)(Q_{kl}H_{lk}) - \lambda H_{ik}(Q_{kj} + \delta_{kj}/3) - \lambda(Q_{ik} + \delta_{ik}/3)H_{kj} \\ -\partial_i Q_{kl}\left(\frac{\delta F}{\delta \partial_j Q_{ik}}\right) + Q_{ik}H_{kj} - H_{ik}Q_{kj}\end{aligned} \tag{2.46}$$

$$\sigma_{ij}^{\text{active}} = -\zeta Q_{ij} \tag{2.47}$$

Here, ζ is the activity coefficient, which determines the strength of activity of processes in the cell that generate local stresses, such as actomyosin polymerization and cell contractility. ζ can be set to positive or negative values, to create extensile or contractile stresses. In addition to the Navier-Stokes equation, the incompressibility assumption also gives:

$$\partial_i u_i = 0 \tag{2.48}$$

Finally, a field ϕ, coupled to the nematic order parameter, defines the state of the system. For $\phi = 0$ the system is isotropic, for $\phi \geq 1$ the system is nematic. In the context

of this model, any part of the system that is in the nematic state is considered to be part of the cell sheet, whereas the isotropic regimes represent the free area. Parameters are chosen so that transitions between isotropic and nematic are sharp. Cell division is implemented by local increases of ϕ randomly distributed throughout the cell sheet, occurring at a set division rate α.

These equations of motion (Eq. 2.35, 2.43 and 2.48) are then solved by a hybrid Lattice-Boltzman algorithm described in reference [122]. In section 3.3, this active nematic-isotropic mixture model was applied to the collective cell migration through channels with a constriction, and results from experiment and simulation compared.

2.5.3 Dissipative particle dynamics simulations

In the approaches presented so far, collective cell migration was described on a very coarse-grained level that ignored the individual agents in the system. In contrast, particle-based models represent each cell by a single particle with local interactions between neighbors that nonetheless give rise to correlated motion over long scales [4]. They are more complex than continuous media based approaches, but modeling the individual agents allows the inclusion of biological behavior of cells and their interactions. Best-known among these types of models is the Viscek model, originally established by Viscek et al. in 1995 [123], though by now many variations thereof and many similar models have been published.

In publication P3, which is discussed in section 3.2 of this thesis, the orientation of cell division in migrating epithelial sheets was studied and compared to the results from a dissipative particle dynamics simulation [65]. The full description of the model can be found in references [124] and [125]. This section gives a brief overview of the model as defined in those publications:

The idea behind this model is a minimalistic approach, modeling each cell as two particles i and j that repel each other with force $\mathbf{F}_{ij}^{G}$. Each cell's size is given by the distance between the two particles that form it. Due to the repulsive force between two particles of the same cell, each cell grows, until the distance between the two particles exceeds a size threshold R_c, at which point it deterministically divides. Division is implemented by the random placement of new particles a short distance r_c from the original cell (see Fig. 2.10). In contrast, apoptosis (respectively all forms of cell death in general) is implemented by randomly removing cells at a constant rate k_a.

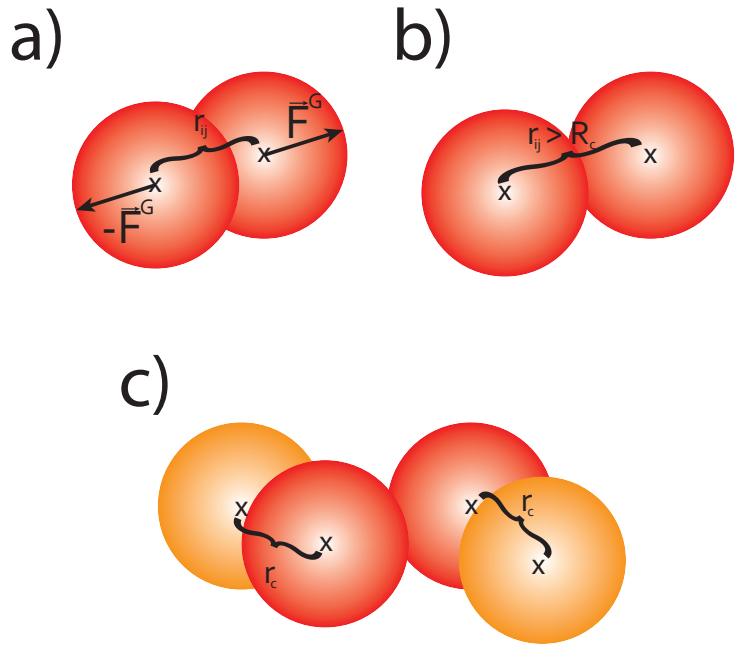

Figure 2.10: Illustration of the dissipative particle dynamics simulation. **a)** Cells are represented by two particles with a repulsive growth force acting between them. **b)** This growth force drives the two particles forming the cell farther apart until they reach a predefined critical distance R_c, at which point they divide. **c)** Cell division is implemented by insertion of a second particle (indicated in orange) a small distance r_c away from each original particle in a random direction.

The dissipative particle dynamics model assumes interactions between the cells only in the form of adhesion and volume exclusion. To this end, forces are defined between all particles i and j that do not belong to the same cell. The total force $\mathbf{F}_i$ acting on a particle i is given by:

$$\mathbf{F}_i = \mathbf{F}_{ic}^G + \sum_j \mathbf{F}_{ij}^{cc} + \mathbf{F}_{ij}^a \tag{2.49}$$

Here, $\mathbf{F}_{ij}^{cc}$ is a short range repulsive force, and $\mathbf{F}_{ij}^a$ is a constant attractive force if the particles i and j are within a certain range of each other. The sum over j is defined as running over all particles j except for the one particle that belongs to the same cell c as i.

The model must include some form of energy dissipation, which is achieved by using a dissipative particle dynamics (DPD) type thermostat, implemented according to reference [126]. Viscous dissipation between cells is implemented, while at the same time momentum

balance is preserved. The dissipative force in this case is given by Eq. 2.50.

$$\mathbf{F}_i^D = -\gamma\omega\left(r_{ij}\right)\left(\left(v_j - v_i\right)r_{ij}\right)\hat{r}_{ij} \tag{2.50}$$

Here, the vector between the particles i (located at $\mathbf{r}_i$) and j (located at $\mathbf{r}_j$) is defined by:

$$\mathbf{r}_{ij} = \mathbf{r}_i - \mathbf{r}_j \tag{2.51}$$

Direction and modulus of $\mathbf{r}_{ij}$ are given by $\hat{r}_{ij}$ and r_{ij}, respectively. A similar notation is used for the velocity $\mathbf{v}_i$, and ω is a weight function as defined in reference [126]. The dissipation constants are given by γ, which is chosen independently for particles of different cells (γ_t) and particles of the same cell (γ_c). The model also includes a background dissipation of γ_b, which represents the effect of an extracellular matrix. This DPD simulation is mainly designed for the modeling of epithelial sheets, however, where there is no bulk extracellular matrix and where dissipative forces are transferred mostly to neighboring cells and not the background. The striking advantage of the DPD approach versus Langevin simulations is that by choosing small values for γ_b, the model can accommodate the background dissipation not being dominant. Forces from the cytoskeleton are mimicked by addition of a random force, with noise amplitude $k_B T_n$.

The forces in Eq. 2.49 are defined in the following way:
The growth force F_{ij}^G driving the particles i and j (making up one cell) apart is proportional to the growth coefficient B according to:

$$\mathbf{F}_{ij}^G = \frac{B}{\left(r_{ji} + r_0\right)^2}\hat{r}_{ji} \tag{2.52}$$

The repuslive force between particles belonging to different cells to implement volume exclusion of cells is given by:

$$\mathbf{F}_{ij}^{CC} = \begin{cases} f_0\left(R_{pp}^5 / r_{ji}^{-5} - 1\right)\hat{r}_{ji} & \text{if} \quad r_{ji} \leq R_{pp} \\ 0 & \text{if} \quad r_{ji} > R_{pp} \end{cases} \tag{2.53}$$

Finally, the constant adhesion is given by:

$$\mathbf{F}_{ij}^{a} = \begin{cases} -f_1 \hat{r}_{ij} & \text{if} \quad r_{ji} \leq R_{pp} \\ 0 & \text{if} \quad r_{ji} > R_{pp} \end{cases} \tag{2.54}$$

While these interactions obviously are much simpler than all the interplay going on in actual tissue, this simple model is already successful at capturing some key behavior found in empirical systems, such as rounding up of unconfined tissue aggregates into spherical shape and the unmixing of combinations of tissue types with different adhesion properties.

The model can then be extended to account for the idea that motility forces in a migrating collective are coordinated by each individual cell's tendency to align its motility force with its velocity. Motility forces are implemented as follows: Cells can either be in a motile or a non-motile state. In the former, a cell actively exerts a force against the substrate in a random direction to propel itself forward in any direction. In the latter state, cells do not actively exert any force on the substrate. The rate k_{mot} with which cells switch from the non-motile into the motile state is constant, whereas the rate with which they switch back is a function of the velocity $\mathbf{v}$ and motility force $\mathbf{m}$. The simplest case for this is choosing two rates k_{non}^{-} and k_{non}^{+}, depending on whether $\mathbf{m}$ and $\mathbf{v}$ are parallel or anti-parallel. When the component of m along v is positive (i.e. the motility force points in the same direction as the velocity), the rate for switching back to the non-motile state is given by k_{non}^{+}, whereas it is k_{non}^{-} when the component of m along v is negative. To achieve the desired effect of cells having a tendency to align their motility force with their velocity, k_{non}^{+} is chosen to be smaller than k_{non}^{-}. In this way, cells where velocity and motility force are aligned stay in the motile state longer than those where this is not the case (and the others, once returned to the non-motile state have a chance of switching to motile again, with their motility force oriented in a random direction). This method of having cells align their motility force with their velocity is illustrated in Fig. 2.11.

Thus, the equation of motion for a particle in this DPD simulation can be stated as:

$$\frac{d\mathbf{p}}{dt} = \mathbf{m} + \mathbf{F}^{G} + \mathbf{F}^{int} + \mathbf{F}^{B} + \sum_{r \leq R_{pp}} \left(\mathbf{F}^{rep/ad} + \mathbf{F}^{df} + \eta \right) \tag{2.55}$$

Here, $\mathbf{p}$ is the particles momentum. $\mathbf{F}^{int}$, $\mathbf{F}^{B}$ and $\mathbf{F}^{df}$ are the explicit terms of the dissipative force (Eq. 2.50). $\mathbf{F}^{int}$ is the intracellular friction force between the two particles

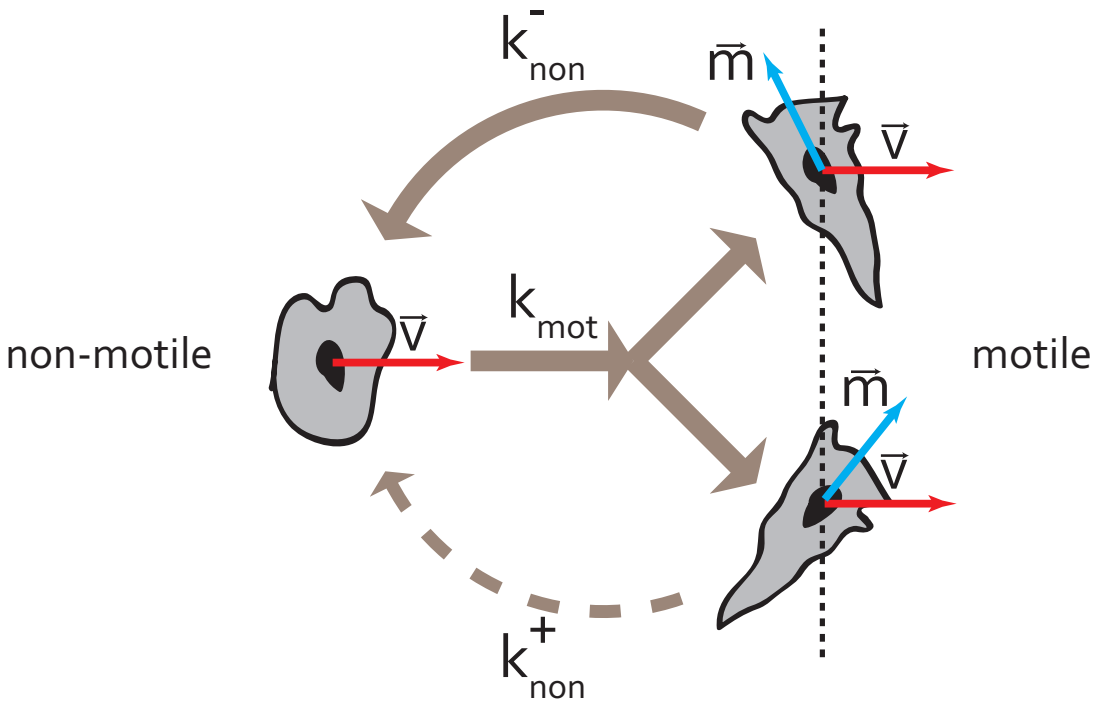

Figure 2.11: Illustration of the mechanism for aligning the motility force with velocity in the simulations. In the non-motile state, cells do not actively exert a motility force $\mathbf{m}$ on the substrate, in the motile state they do. Cells switch into the motile state with a constant rate k_{mot}, at which point the direction of the motility force is chosen at random. The transition back into the non-motile state, however, depends on the alignment of $\mathbf{m}$ and the velocity $\mathbf{v}$, specifically whether $\mathbf{m} \cdot \mathbf{v}$ is positive or negative. For $\mathbf{m} \cdot \mathbf{v} > 0$, the rate for switching is k^+, for $\mathbf{m} \cdot \mathbf{v} < 0$ it is k^-. Typically, these rates are chosen with $k^- > k^+$ so as to achieve alignment of motility force and velocity.

that make up the same cell (Eq. 2.56a), $\mathbf{F}^B$ is the friction force with the substrate (Eq. 2.56b) and $\mathbf{F}^{df}$ is the friction force between neighboring particles of different cells (Eq. 2.56c). Furthermore, $\mathbf{F}^{rep/ad}$ are the volume exclusion and adhesion terms (see Eq. 2.53 and 2.54) combined into one term (Eq. 2.57) and η is a momentum conserving noise force between particles.

$$\mathbf{F}^{int} = -\gamma_{int}\mathbf{v} \tag{2.56a}$$

$$\mathbf{F}^{B} = -\gamma_{B}\mathbf{v} \tag{2.56b}$$

$$\mathbf{F}^{df} = -\gamma_{df}\mathbf{v} \tag{2.56c}$$

$$\mathbf{F}^{rep/ad} = -\left(f_0\left(\frac{1}{r}-1\right)-f_1\right)\hat{r} \tag{2.57}$$

Using this refined model, several empirical phenomena observed in collectively migrating 2D epithelial sheets can be successfully reproduced, including the buildup of tensile stress throughout the tissue, and the density dependence of size and velocity of spontaneously occurring vortices.

2.5.4 The vertex model

Some phenomena in cell dynamics, for example cell segregation and developmental processes, are primarily controlled by interactions of cells with their neighbors rather than locomotion on a substrate [4]. To better capture these sorts of processes in models, it is desirable to explicitly include a description of cell shape and of the cell interface with a cell's neighbors. At an even less coarse-grained level than particle-based approaches, the vertex model belongs to the class of models that implement a detailed description of the cells and their interactions, including such things as cell-cell adhesion, cell substrate adhesion and cell contractility [4]. The 2D vertex model approximates each cell boundary by a straight segment, so that an epithelial sheet becomes a network of bordering polygons. Fig. 2.12 illustrates the good accuracy of such an approximation and clarifies the vertex model's nomenclature. The model adapts the theory of foams' assumption that in an equilibrium

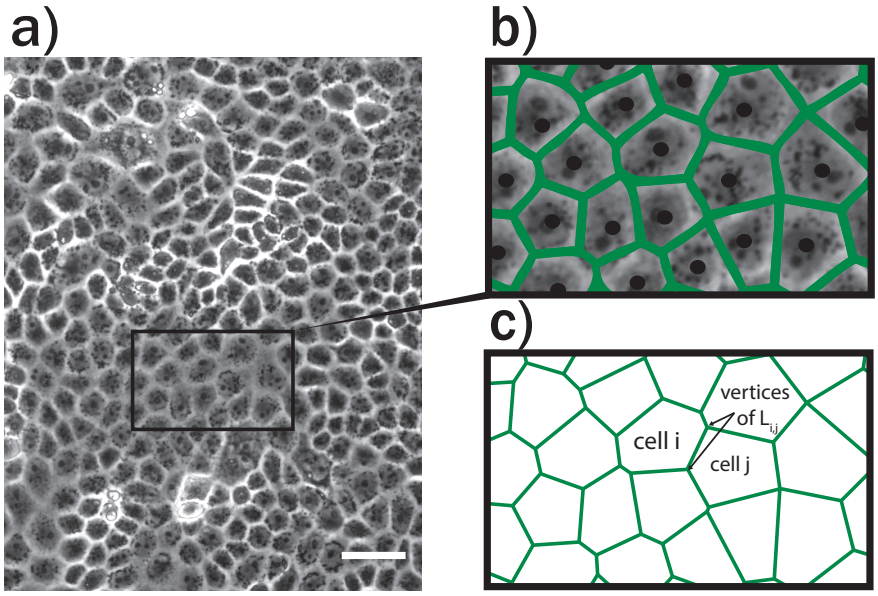

Figure 2.12: The shapes of an epithelical cell layer are close to polygons. **a)** Cells in an MDCK monolayer have very straight borders, reminiscent of polygons. Scale bar corresponds to 50 µm. **b)** A subsection of the same cell sheet with a polygonal network created by a Voronoi construction around the black dots marking the cells center points overlain in green. The Voronoi construction reproduces the orientation of the cell boundaries very well. **c)** Definition of the nomenclature for the vertex model. Figure adapted with permission from reference [64]. Copyright 2015 Elsevier B.V.

configuration the forces at each vertex have to vanish and thus cell/polygon motion is assumed to be driven by minimization of energy in the network. Several Hamiltonians have been used in this context as energy terms to minimize, though they are typically dependent on the same parameters, namely the cell areas A_i, the cell perimeter P_i and the length of the junction between two neighboring cells i and j, given by $L_{i,j}$. While the exact term incorporating each of these variables can be chosen in a number of ways based on the assumptions made, a popular choice was introduced by Farhadifar et al. [89]:

$$E(R_i) = \sum_{i \in \text{cells}} \frac{K_i}{2} \left(A_i - A_i^0\right)^2 + \sum_{j \in \nu(i)} \alpha_{i,j} L_{i,j} + \sum_i \frac{\kappa_i}{2} P_i^2 \tag{2.58}$$

In addition to the parameters mentioned above, this equation includes several constants: K_i is the elastic coefficient of the area, A_i^0 is the preferred area of the cell, $\alpha_{i,j}$ is the line tension per unit area and κ_i describes the cells contractility. As stated in reference [4],

this equation can also be rewritten as follows:

$$E(R_i) = \sum_i \left[\frac{\kappa_i}{2} \left(P_i - P_i^0 \right)^2 + \frac{K_i}{2} \left(A_i - A_i^0 \right)^2 \right] + \text{const.} \tag{2.59}$$

This sets a preferred cell perimeter P_i^0 according to:

$$P_i^0 = -\sum_{j \in \nu(i)} \frac{\alpha_{i,j}}{4\kappa_i} \tag{2.60}$$

This model is already able to capture polygon class distribution, variation of cell areas and packing geometry found in the *Drosophila* wing disc [89], as well as explain how increased tension along boundaries can preserve cell compartment boundaries even in the presence of remodeling through cell divisions.

The vertex model can be expanded to include cell motility [127]. To do so, an average location R_i, at which cell i adheres and pulls on the substrate, is introduced. The energy equation is then extended by:

$$E_{mot} = \frac{\kappa}{2} \sum_i ||\mathbf{R}_i - \mathbf{X}_i||^2 \tag{2.61}$$

Here, X_i is the "center of mass" of cell i, defined as the average coordinate of its vertices. The dynamics of the pulling location are assumed to be relaxational:

$$\sigma \frac{d\mathbf{R}_i}{dt} = \kappa \left(\mathbf{X}_i - \mathbf{R}_i \right) + \eta_i(t) \tag{2.62}$$

Here, η_i is a Langevin-type random force that represents motility and is defined by its second moment:

$$\langle \eta_i(t) \eta_j(0) \rangle = \kappa \delta(t) \delta_{ij} \tag{2.63}$$

As with the other energy terms in this model, motility could also be implemented with other approaches [4]. With these sorts of expansions, the vertex model becomes capable

of describing a wide range of collective phenomena. For instance, Puliafito et al. were able to reproduce all aspects of collective and single cell behavior observed in their epithelial contact inhibition experiments.

In the project detailed in section 3.4, we examine to what extent the vertex model can be used to calculate cell mechanics parameters from observations of epithelial arrangements without any force measurements.

2.5.5 The cellular Potts model

Similar to the vertex model the cellular Potts model is a prominent representative of the most detailed models, which explicitly take into account factors such as cell shape. The implementation of molecular processes on subcellular level is also possible. The cellular Potts model was adapted for the context of cell mechanics by Graner and Glazier [128, 129]. In this framework, each cell is represented by a domain of sites in a given Potts state σ. Each site i can be in a state $\sigma(i) = 1, ..., Q$ with each state representing one of $Q-1$ cells and the intercellular medium [4]. If each site is defined by the corresponding lattice vector $\mathbf{x}_j$, then the cell α is represented by the set of connected lattice sites $\{\mathbf{x}_k^{(\alpha)}\}$ (see Fig. 2.13a). Both cell motion and the deformation of the cell membrane are implemented as the annexation or rejection of individual boundary lattice sites (see Fig. 2.13b). In this context, annexation of a single lattice site corresponds to the formation of a cellular protrusion, whereas rejection of a lattice site corresponds to cellular retraction. Thus, cell migration is achieved as a consequence of subsequent annexations and rejections, analogous to how it is the consequence of subsequent cellular protrusions and retractions in biological systems. The occurrence of the annexations and rejections are stochastic, modeled with a Monte-Carlo scheme. Cell adhesion, cell polarity and cell adhesion are assumed to contribute via independent Hamiltonians to a goal function p that determines the scheme's update rules [130]:

$$p(E) = p_{\text{elastic}}(E) \cdot p_{\text{polarization}}(E) \cdot p_{\text{cell-adhesion}}(E) \tag{2.64}$$

E in this context is a placeholder for annexation events (E_a) and rejection events (E_r).

Cortical contractility of cells is implemented via two elastic parameters ("area stiffness" a and "perimeter stiffness" m), which penalize growing cells. The cell's elastic energy is

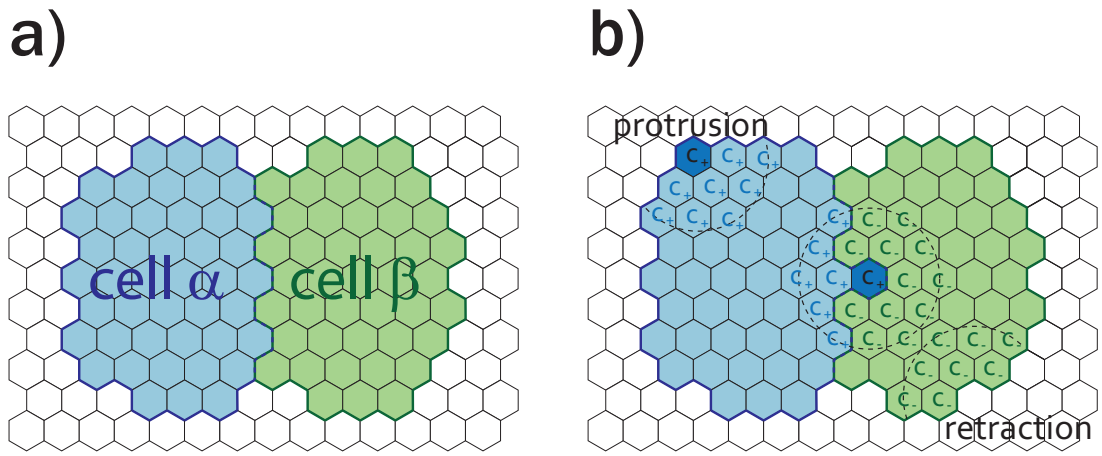

Figure 2.13: Illustration of the cellular Potts model. **a)** Hexagonal Potts lattice, with lattice sites in the states "cell α" (illustrated in blue), "cell β" (illustrated in green), or substrate (illustrated in white). **b)** Illustration of annexation and rejection of lattice sites. Cell α protrudes into the lattice site at its top left corner, as well as into one of cell β's lattice sites (annexed sites indicated in dark blue). Cell β retracts from the lattice site at its bottom right corner. At the end of each Monte-Carlo time step, lattice sites within the signaling radius (indicated by the dashed line circles) of these annexation/rejection events receive a chemical marker c_+/c_- that influences the cytoskeletal density $\rho(\mathbf{x})$. This polarization rule leads to a positive feedback loop that enables effective cell migration in the model.

given by:

$$H_{el}^{\alpha} = m_{\alpha} P^{(\alpha)2} + a_{\alpha} A^{(\alpha)2} \tag{2.65}$$

Here, $A^{(\alpha)}$ denotes the cells area, and $P^{(\alpha)}$ its perimeter. The total elastic energy difference resulting from event E is then given by:

$$\Delta H_{el}(E) = \sum_{\alpha} \Delta H_{el}^{\alpha}(E) \tag{2.66}$$

Using this, the elastic contribution to the goal function is defined as:

$$p_{\text{elastic}}(E) \equiv \exp\left[-\Delta H_{el}(E)\right] \tag{2.67}$$

The shrinkage of cells this would result in is counteracted by implementation of a scalar concentration field $\rho(\mathbf{x})$ which represents the filamentous cytoskeletal structure inherent to the cells. This field is defined over the whole body of each cell α, i.e. $\mathbf{x} \in \{\mathbf{x}_k^{(\alpha)}\}$ and

provides a force that pushes on the cell boundary.

The cellular Potts model described in reference [130] focuses on the mechanical aspects of cell migration. To this end, a feedback rule for mechanical signals in the form of cell polarization is essential. The implementation thereof is handled as follows: Each time any lattice site $\mathbf{x}_0^{(\alpha)}$ is annexed by cell α, all lattice sites $\mathbf{x} \in \{\mathbf{x}_k^{(\alpha)}\}$ within a defined "signaling radius" R receive a chemical marker c_+. Conversely, each time a lattice site is rejected, all lattice sites within R receive a chemical marker c_-. At the completion of each Monte-Carlo time step, the scalar field $\rho(\mathbf{x})$ representing cytoskeletal structures is updated according whether the marker c_+ is dominant at any given lattice position, as defined by Eq. 2.68.

$$\rho(\mathbf{x}, t + \Delta t) = \begin{cases} \rho(\mathbf{x}, t) + \tau \left[Q - \rho(\mathbf{x}, t) \right], & \text{predominantly } c_+ \\ \rho(\mathbf{x}, t) + \tau \left[q - \rho(\mathbf{x}, t) \right], & \text{else} \end{cases} \tag{2.68}$$

Here, Q and q denote the maximal and minimal levels of $\rho(\mathbf{x})$, so that if c_+ dominates $\rho(x)$ is increased, otherwise it is decreased. τ gives the rate at which the polarization field reacts to the chemical markers. This rule implies a positive feedback loop between cellular protrusions and cytoskeletal remodeling, and thus will favor successive cell protrusions and reactions and thereby enable effective cell migration.

In addition to the scalar field $\rho(\mathbf{x})$, which describes the cytoskeleton within the cells, the model includes a second scalar field $\rho_f(\mathbf{x})$ that measures the local density of anchoring points that cells can form focal adhesions with. This variable can be used either in a time-dependent manner to include changes to the substrate over time (such as because a cell has previously migrated over this surface and deposited ECM proteins, see section 2.1.1 for details), or to incorporate static micropatterns in an attempt to mimic a given experimental scenario (in which case its value can be kept constant throughout the simulation).

Taking the anchoring strength of focal adhesions to be given by the sum $\rho(\mathbf{x}) + \rho_f(\mathbf{x})$, the difference in polarization energy $\Delta H_p(E)$ is defined according to Eq. 2.69, which will

determine the polarization's contribution to the goal function.

$$\Delta H_p(E) \equiv \begin{cases} \rho(\mathbf{x}_l) - \rho(\mathbf{x}_k), & E \mathrel{\hat{=}} \text{annexation} \wedge \beta \geq 0 \\ \rho(\mathbf{x}_k) - \rho(\mathbf{x}_l), & E \mathrel{\hat{=}} \text{rejection} \wedge \beta \geq 0 \\ -[\rho(\mathbf{x}_k) + \rho_f(\mathbf{x}_l)], & E \mathrel{\hat{=}} \text{annexation} \wedge \beta < 0 \\ \rho(\mathbf{x}_k) + \rho_f(\mathbf{x}_l), & E \mathrel{\hat{=}} \text{rejection} \wedge \beta < 0 \end{cases} \tag{2.69}$$

Here, $\mathbf{x}_k$ is the source grid site for the annexation or rejection event and $\mathbf{x}_l$ is the target site. β defines whether the target site is part of an actual cell ($\beta \geq 0$), or part of the "empty" substrate ($\beta < 0$). The contribution of polarization to the goal function p is then defined as follows:

$$p_{\text{polarization}}(E) \equiv \exp\left[-\Delta H_p\left(E\right)\right] \tag{2.70}$$

Finally, to account for the effect of cell-cell adhesion, the adhesion matrices $A_{\alpha,\beta}$ and $B_{\alpha,\beta}$ are defined, which quantify the system's change in energy upon formation of a new bond between cells α and β and upon breaking of an existing bond between cells α and β by a third, intruding cell γ. These matrices are defined as having the following properties:

$$A_{\alpha,\beta} = A_{\beta,\alpha} \geq 0 \tag{2.71a}$$

$$B_{\alpha,\beta} = B_{\beta,\alpha} \geq 0 \tag{2.71b}$$

$$A_{\alpha,\alpha} = B_{\alpha,\alpha} = 0 \tag{2.71c}$$

$$A_{\alpha,\beta} = B_{\alpha,\beta} = 0 \text{ if } \alpha < 0 \vee \beta < 0 \tag{2.71d}$$

Making use of these adhesion matrices, the difference in the cell adhesion energy $\Delta H_a(E)$ can be defined separately for annexation and rejection events. For annexation of a grid site $\mathbf{x}_l$ by cell α, it is given by Eq. 2.72a, whereas for rejection of site $\mathbf{x}_k$ by

cell α, it is instead defined by Eq. 2.72b.

$$\Delta H_a(E) \equiv -\sum_{j \in N_l} \left[A_{\alpha,c(\mathbf{x}_j)} - \delta_{\alpha,c(\mathbf{x}_j)} A_{\alpha,\beta} \right] + \sum_{j \in N_l} B_{\beta,c(\mathbf{x}_j)} (1 - \delta_{\alpha,c(\mathbf{x}_j)}) \tag{2.72a}$$

$$\Delta H_a(E) \equiv -\sum_{j \in N_k} \left[A_{\beta,c(\mathbf{x}_j)} - \delta_{\beta,c(\mathbf{x}_j)} A_{\alpha,\beta} \right] + \sum_{j \in N_k} B_{\alpha,c(\mathbf{x}_j)} (1 - \delta_{\beta,c(\mathbf{x}_j)}) \tag{2.72b}$$

Here, $c(\mathbf{x}_j) \in \{\alpha, \beta, \cdots\}$ is the index of the cell the lattice site $\mathbf{x}_j$ is associated with, and N_j is the neighborhood of the lattice site $\mathbf{x}_j$, defined as:

$$N_j = \left\{ l \in \{1, \cdots, M\} \middle| \min ||\mathbf{x}_j - \mathbf{x}_l|| = 1 \right\} \tag{2.73}$$

Using the above definitions, the adhesion contribution to the Monte-Carlo goal function is defined as:

$$p_{\text{cell-adhesion}}(E) \equiv \exp\left[-\Delta H_a\left(E\right)\right] \tag{2.74}$$

This is the last contribution to the complete goal function (Eq. 2.64), but one final component is necessary for the model, which is handling the rupture of cell-cell contacts, which can occur as a result of a successful rejection event. To this end, the total energy differences for both cases $E = E_{\text{rupt}}$ and $E = E_{\text{retract}}$ (Eq. 2.75a and 2.75b) are examined and the energetically favorable event, rupture or regular retraction, is chosen.

$$\Delta H(E_{\text{retract}}) = \Delta H_{el}(E_{\text{retract}}) + \Delta H_p(E_{\text{retract}}) + \Delta H_a(E_{\text{retract}}) \tag{2.75a}$$

$$\Delta H(E_{\text{rupt}}) = \Delta H_{el}(E_{\text{rupt}}) + \Delta H_p(E_{\text{rupt}}) + \Delta H_a(E_{\text{rupt}}) \tag{2.75b}$$

The cellular Potts model was not directly used in the course of this thesis. It would, however, seem to be a suitable candidate for modeling collective cell migration through constricted channels, as described in section 3.3. We could show that in that context more coarse-grained models were insufficient to reproduce observed behavior. Consequently, a model that explicitly accounts for things such as cell shape is more promising for future work.

2.6 Machine learning for image processing

Image processing refers to the use of computer algorithms to analyze data that exists in the form of digital images. In particular, image processing is used for such tasks as pattern recognition, feature extraction or classification, using information such as pixel coordinates, intensities or gradients between neighboring pixels. Oftentimes this data analysis is either semi-automated (requiring some user input, such as setting intensity thresholds for each individual data set) or fully automated (requiring no user input). Traditionally, however, automated image processing in biosciences is performed with classical, non-adaptive algorithms. In essence, this means the computer is given rules in advance by which to make any decisions, such as a simple classification rule that divides an image into two subpopulations based on whether a pixel's intensity is greater than a value x or not. For many problems, such an analysis is sufficient, but in some cases, designing explicit rules that perform well can be infeasible. This can be the case if the quality of the data set fluctuates over time (e.g. due to fluctuating light sources, unstable flurophores, etc.), data sets that change over time (e.g. because cell divisions cause great modifications) or in cases where the human eye can recognize features, but it is not entirely clear which features allow this (and thus it is not clear how to capture the humans' ability in strict rules). When the design of explicit, static rules for the image processing algorithm becomes impractical or infeasible, machine learning offers a potential solution.

In machine learning, the rules for data processing are not defined by the user in advance, but rather the program learns from a series of examples [131]. Many applications of machine learning outside of biosciences have already found their way into our everyday lives. Some examples of this include spam filters for e-mails [132], automated recognition of speech [133] or handwriting [134], as well as evaluation of satellite images [135, 136].

2.6.1 Basic types of machine learning problems

Though a wide variety of problems can be addressed via machine learning, most of them fall into one of two groups [137]: classification or regression problems. In the case of regression, given an independent input variable X and a dependent output variable Y, the goal is to find a function $f(X)$ so that $\hat{y} = f(x)$ predicts the true value y of the output variable Y for input x of X as accurately as possible. Examples include algorithms for estimating a person's age from a photo or predicting a company's future stock price from

inputs such as performance measures and macroeconomic indicators [137].

In contrast, classification problems take an input X belonging to a finite set of classes $l = 1, 2..., k$ and attempt to determine the correct label $l = g(x)$ (with $l \in C$) indicating which class the input belongs to. Examples include the detection of human faces in a photograph, detecting all goals in the video of a soccer match, or classifying tissue images into healthy and diseased cells [137].

Other significant types of problems tackled by machine learning algorithms are hypothesis testing and confidence interval testing. These are less common, however, in particular when it comes to image processing applications.

2.6.2 General process

The process a machine learning algorithm uses to determine its dynamic decision rules varies between the studied problem and the algorithm used to tackle the issue. In most cases, however, the underlying structure of the process is the same. Taking classification problems as an example, the input data for machine learning comes in the form of values for individual attributes (such as "height", "weight" and "age") each associated with several objects (such as "person A", "person B", etc.) and the desired output is a label categorizing each object (such as "high risk" or "low risk" of falling ill with a specific disease). The input data is divided into a training sample, a validation sample and a test sample. The learner uses the training data to determine the model it will use to make its decisions or predictions. This model then predicts its response for the validation data set and compares its performance to the correct solution, potentially adjusting its model in order to improve its viability. Two things are typically accomplished during this step: the features relevant for the model are selected and the parameters are tuned, both while studying the model's performance on the validation data. This reduces the risk of overfitting to the training data set (i.e. coming up with rules so specific they work perfectly for the training data but not at all for any other data). Finally, the test data is used to evaluate the performance of the model in an unbiased way, which allows comparing and selecting between different algorithms.

2.6.3 Supervised and unsupervised learning

In principle, machine learning algorithms are categorized as either supervised or unsupervised learners, the distinction between the two being the form the test sample is presented in. Supervised learning algorithms receive labeled data as input, which means they are given both the data they are supposed to predict as well as the correct answer they are supposed to come up with [138]. These algorithms are frequently used for ranking and classification problems. For instance, spam filters for e-mails are trained by being given a collection of e-mails that have already been manually classified into which are spam and which are not. A more biological example would be a classification of an image of cells where different compartments are visible. Here, the training data would be images with labels which pixels belong to one organelle (e.g. the nucleus) and which to others (e.g. the actin cytoskeleton), which the algorithm would use to create a model that can then classify further images itself. In addition to ranking and classification problems, most regression algorithms use supervised learning methods [137]. The big disadvantage of supervised learning is this requirement of labeled training data, which can be hard to come by. For instance, in the cell image classification example, correctly labeling each pixel of the training data as belonging to the nucleus or actin cytoskeleton can quickly become tedious, in particular if large quantities of training data are necessary so that the algorithm performs well.

While there are many supervised algorithms for classification, a multitude of unsupervised approaches also exists for this class of problems. In contrast to their supervised counterparts, unsupervised learners receive no labeled training data. Instead of the algorithm trying to classify the objects into predetermined classes, it just groups them according to similarity. Depending on the specific case, the objects might be grouped into a defined amount of classes (e.g. when there is prior knowledge that there are exactly three classes the objects can be categorized into) or the algorithm might be asked to determine the most likely (according to a given criteria) number of classes itself. Unsupervised machine learning algorithms for classification are also frequently referred to as “clustering” algorithms.

2.6.4 Decision trees and random forests

In the context of this work, machine learning was of interest for classification of image data, specifically for identifying the junctions between cells in noisy fluorescence images. Thus, the problem at hand required the use of a machine learning algorithm for classification (as opposed to regression). Due to the noise in the image data, and the fact that the desired classes were known (namely "cell junction" and "not cell junction"), a supervised learning algorithm was chosen. From the multitude of possible algorithms available, in the context of this thesis only algorithms based on decision tree learning were implemented, though others, such as neural network approaches, should be possible as well.

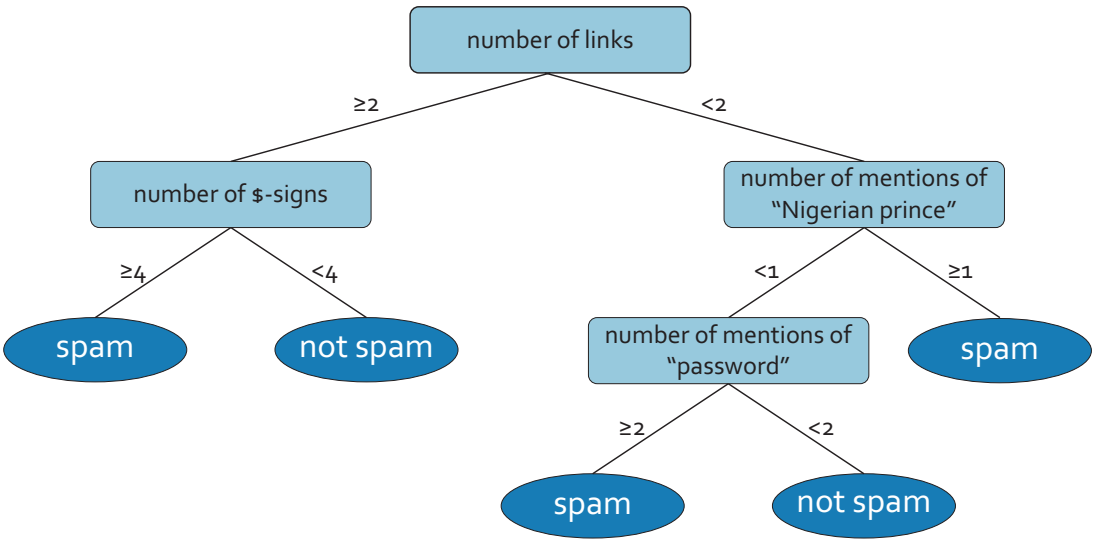

Figure 2.14: Simple, exemplary decision tree for categorizing e-mails into "spam" and "not spam", according to the amount of links, $-signs and mentions of "Nigerian prince" or "password" the mail contains.

Decision trees are essentially a hierarchical set of decision rules that are used to predict the output by taking the input and having it subsequently run through one path of decisions until its category is selected in a so-called terminal node (also referred to as leaves, in sticking with the tree nomenclature). For instance, Fig. 2.14 shows a simple decision tree for an e-mail spam filter. In this example, each e-mail starts at the first internal node (drawn at the top of the tree), where it is examined for the number of external web links it contains. If this amount is 2 or higher, the e-mail follows the left branch, if it is less than two it instead follows the right branch of the tree. Any e-mail that was sent along the left branch is then examined at the next internal node for the amount of $-signs that appear in its text. This is the final decision along this branch, and e-mails are categorized into "spam" or "not spam" based on whether they contain 4 or

more $-signs, or not. In contrast, most paths along the right branch of the first internal node (where the number of links was checked) are longer before they reach a terminal node, and the decision at the second internal node along this path can lead to instant classification at a terminal node or further differentiation according to another parameter at a third terminal node. More complex decision trees might also include decision rules for the same parameter more than once along a branch, splitting according to different values. In the example of Fig. 2.14, this could for instance see the terminal node along the ≥ 2 "number of mentions of password"-branch replaced by an internal node that makes a decision based on the number of links (that was already used at the first node), this time splitting according to ≥ 1 and < 1.

The example decision tree in Fig. 2.14 could be interpreted in the following manner: The most important factor determining whether an e-mail should be classified as spam is the number of links it includes, with e-mails containing more links more likely to be spam than those with few or none. Accordingly, the tree indicates that the number of times the words "Nigerian prince" are mentioned is only important in e-mails with few links. Intuitively, this likely does not hold true in reality (even e-mails with few links claiming to be from a Nigerian prince are likely spam), indicating that the presented tree is presumably an oversimplification. The fact that human intuition clashes with the rules of this particular tree highlights a crucial advantage decision tree algorithms have compared to some other approaches: They can be easily visualized and understood and the reasoning that leads them to their classification followed [139]. In contrast, algorithms such as neural networks offer little to no insight into which variables played strongly into the classification decision, acting more like a "black box" that transforms the input into the output in an unexplained way [140]. While this disadvantage makes decision trees a more favorable first choice for the problem at hand, the main goal machine learning is used for in this thesis is the pixelwise classification of an image, and an understanding of the causality that leads to this segmentation is not strictly necessary. Thus, neural networks might offer a feasible alternative approach to this problem in the future.

Classifying data along a given decision tree is no challenge, nor is it in fact actually machine learning, but rather just a simple application of predetermined decision rules to a given observation. In principle, there is nothing preventing the use of decision trees with rules designed by humans *a priori*. The difficulty in most cases, however, is the construction of the actual tree. Rather than coming up with the rules "manually", it is typically more convenient to let the computer find the entire decision tree (at which point the algorithm does become a machine learning application). The following description of

how this is typically achieved follows reference [139]:

The random variable for our observation (i.e. our input) shall be denoted by X, with the individual predictors denoted by X_i. In the above example of the spam filter, X would be {number of links, number of $-signs, number of mentions of "Nigerian prince", number of mentions of "password"} and the predictors $X_1, ...X_4$ would be "number of links", "number of $-signs", etc. A particular instantiation of X, denoted by x, would, for instance, be $\{3, 0, 5, 2\}$ in this example. To construct a decision tree, the space of all possible values the predictors $X_1, X_2, ..., X_p$ can take is divided into J regions $R_1, R_2, ..., R_J$ that do not overlap. These regions will later be used to make predictions, with every observation that falls into a region R_j being assigned the same response. Specifically, this response will be the most frequently appearing response value for observations from the training data set that fall into R_j. For instance, in a simple example with only two regions R_1 and R_2, if the majority of training observations that fall into R_1 are labeled as "spam", and the majority training observations that fall into R_2 are labeled as "not spam", then the resulting decision tree would classify all observations that fall into R_1 as "spam", and all that fall into R_2 as "not spam". The number of regions scales with the complexity of the used decision tree. Specifically, it is equal to the amount of terminal nodes in the tree. For instance, the example tree shown in Fig. 2.14 would have five regions, $R_1, R_2, ..., R_5$ (with e.g. R_1 being the region defined by "number of links"≥ 2 and "number of $-signs" ≥ 4, which corresponds to the very first terminal "spam"-node).

The main problem is how to divide the entire observation space into regions $R_1, R_2, ..., R_J$ so that these regions do a good job of classifying observations. A measure useful to this end is the *classification error rate* (see Eq. 2.76), which is the fraction of training observations in any given region whose label does not match the label predicted by this region (i.e. the most frequently occurring training label in this region).

$$E = 1 - \max_k(\hat{p}_{mk}) \tag{2.76}$$

Here, $\hat{p}_{mk}$ denotes the fraction of training observation in the m-th region labeled with k. In practice, two other measures are preferable to the classification error rate, however, as they are more sensitive for constructing a decision tree: The *Gini index* (see Eq. 2.77)

and the *cross-entropy* (see Eq. 2.78).

$$G = \sum_{k=1}^{K} \hat{p}_{mk}(1 - \hat{p}_{mk}) \tag{2.77}$$

$$D = -\sum_{k=1}^{K} \hat{p}_{mk} \log \hat{p}_{mk} \tag{2.78}$$

Both the Gini index and the cross-entropy measure the purity of a region/node, i.e. they give an indication whether the node contains mostly observations from a single class or not. If the node is relatively pure, then all of the $\hat{p}_{mk}$ will be close to zero or one and correspondingly the Gini index will take on small values. The same can be shown mathematically for the cross-entropy, but it is less straightforward to see than for the Gini index. Due to this, both can suitably be used to evaluate the splits in a decision tree. As it is infeasible from a computational standpoint to consider every possible division of the space into J boxes, a recursive binary splitting approach is used. This method works top-down, beginning at the top of the tree, where all observations still belong to one region, before successively dividing into the J desired regions. It also belongs to a type of approaches known as greedy algorithms, which means it makes each decision (in this case how to split the observation region) according to the currently optimal choice, without looking ahead at future choices (and choosing a split of the region that would lead to a better final result based on knowledge of future splits).

All predictors $X_1, ...X_p$ are considered, as well as all possible cutoff-points s for each predictor, splitting the initial region into two subregions given by $\{X|X_j < s\}$ (i.e. the part of the predictor space where the value of X_j is smaller than s) and $\{X|X_j \geq s\}$ (i.e. the part where X_j is larger than or equal to s). The split that leads to the highest node purity as indicated by the lowest value of the chosen measure (Gini index or cross-entropy) is chosen for the actual tree. This step of choosing the best predictor and cutoff is then repeated for each resulting branch of the tree, so that it minimizes the node-purity measure for each of the resulting regions. This process continues to repeat itself, with the regions divided into ever smaller subregions, until some predefined stop-criterion is reached. Such a criterion can be arbitrarily imposed on the algorithm in any way, such as by limiting the depth of the tree along each branch to a maximal number of nodes, though this would possibly be a poor choice that leads to some terminal nodes with much lower node-purity than others. A more useful stop-criterion might be limiting the amount

of training observations that may remain in each node.

While this greedy algorithm is unlikely to find the globally optimal solution, it typically produces decision trees that are good at correctly predicting the training data. Such trees frequently suffer from an issue of overfitting, however, which is to say the trees are too complex, splitting observations due to trivial differences that happen to be present in the training data but do not accurately capture the behavior of all data, in general. Overfitted trees tend to perform excellent (or, in the extreme case, perfectly) on the training data used to construct them, but perform poorly on the test set. The best way to circumvent this issue is by "pruning" the trees, i.e. initially growing a large decision tree and then reducing it to a simpler test tree. Which of the many possible subtrees the original tree is pruned to is determined by minimizing the cross-validation error (i.e. examining how the different subtrees perform on the test data set).

Despite the big advantage decision trees offer in terms of simplicity and interpretability, they lack the predictive accuracy of some other classification methods [139]. The reason for this lower accuracy compared to other classification algorithms is the high variance in decision trees, which in this context refers to the fact that if the training data were split into two halves and a decision tree constructed from each, the results would likely be very different. In comparison, an algorithm with low variance would likely return similar results when trained by each half of the training data.

Several different techniques are available for overcoming this weakness: bagging (also referred to as bootstrap aggregation), random forests and boosting. All of these methods greatly improve their predictive performance by combining many decision trees rather than using an individual one. The most straightforward approach in this case is bagging, which repeatedly takes large subsets of the training set and constructs a decision tree from each. The high variance in this method means that even when there is much overlap between the subsets of training data, the small differences that are present are enough to produce different decision trees. To keep variance between the trees high, unpruned trees are used for this method. While previously each observation x ran through one decision tree in order to be classified, it now runs through multiple (typically on the order of hundreds to thousands of trees), with each tree "voting" on the label that should be returned for this observation. Classification then follows according to the majority vote. In the above e-mail spam filter example, one e-mail running through 1000 different decision trees might return 750 votes for "spam" and 250 votes for "not spam" and thus be classified as spam. The use of multiple decision trees also allows statements to be

made about the certainty of the classification. For instance, an e-mail that is classified as "spam" by 900 out of 1000 trees is significantly more likely to be classified correctly than an e-mail that was only voted "spam" by 501 of 1000 trees.

It is worth noting that this improved prediction accuracy for the bagging approach comes at the cost of losing the decision tree's ease of interpretation. While a single decision tree clearly highlights which variables were important for classifying the data, this is no longer easily visible when the decision is the result of a majority vote between hundreds or thousands of trees.

Random forests, a simple example of which is shown in Fig. 2.15, are an approach that improves on bagged trees, specifically by decorrelating the multitude of used trees. A big issue for bagged trees is that if one of the predictors $X_1, ...X_p$ is a stronger predictor than most others, most of the trees grown even on different (overlapping) subsets of the training data will use the same predictor for the first split, which in turn leads to the trees being very correlated. For example, in the e-mail spam filter case, if the amount of links contained in an e-mail is a very strong predictor of whether or not an e-mail is spam, whereas the other predictors are only moderately strong, most of the constructed trees would initially split the data according to the number of links. This would result in many trees that do not differ too strongly from each other, and hence their predictions would strongly correlate. A greater reduction in variance by using many trees is achieved by the use of uncorrelated trees, however. Random forests manage to reduce correlation between the individual trees by only considering a randomly chosen subset of the predictors (typically on the order of $m = \sqrt{p}$) for each split, forbidding the algorithm from even examining the rest. In the spam filter example, this would mean that one tree might only have the option of splitting its data according to either "number of links" or "number of mentions of password" at the first node, while the next tree might also be allowed to use "number of mentions of password", but have "number of $-signs" as its second option. This second tree would not even consider the strong predictor "number of links" (for its first split) and thus would automatically look significantly different than the first one. Due to their greater predictive power over individual decision trees, the machine learning applications in this thesis were performed via random forests.

An alternative to bagging or random forests that also shows improved performance over individual trees is boosting. In brief, the major difference in this approach is that the multitude of used decision trees are not grown independently from one another, but rather they are constructed sequentially, each learning from the previous.

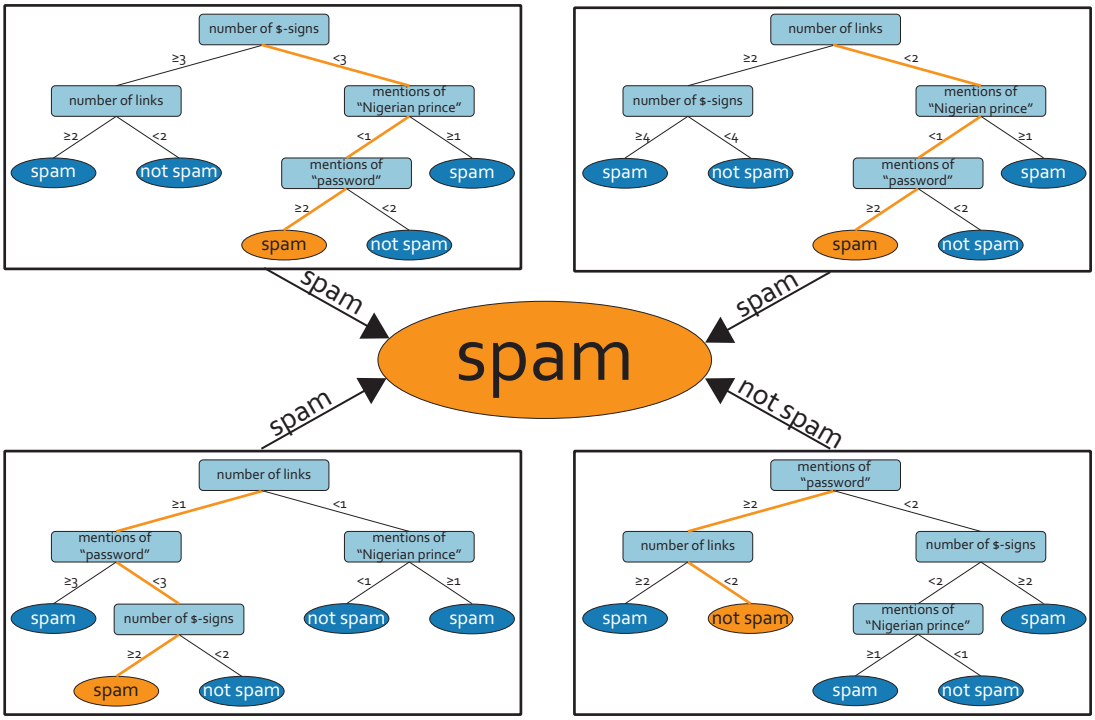

Figure 2.15: Simple, exemplary random forest for categorizing e-mails into "spam" and "not spam", consisting of four decision trees. For each tree, the path a sample e-mail with {number of links=1, number of $-signs=2, number of mentions of "password"=2, number of mentions of "Nigerian Prince"=0} takes on its way to being classified is highlighted in orange. The final classification node is likewise highlighted in orange. As the majority of the trees (three out of four) votes to do so, the random forest classifies the e-mail as spam.

Chapter

3

Cellular Hydrodynamics

Collective cell migration plays an important role in cancer progression, embryonic development and wound healing. Due to the relevance in these phenomena, many experiments have already been performed concerning collectively migrating cells and many models try to capture and describe observed behavior. On one end of the spectrum, cell-biological approaches attempt to account for the underlying molecular dynamics. This vast field includes such things as cytoskeleton dynamics, molecular motors generating forces, chemical signaling both between cells and as a result of external stimuli, as well as dynamic molecular activation and inhibition mechanisms (e.g. the interplay of RhoA and Rac1 and their role in the polarization of cells as part of the migration process). This classical bottom-up approach follows the logic that if all the individual components contributing to collective migration of connected cell groups are understood, the emergent behavior will necessarily follow.

While this sort of approach is necessary for a complete understanding of all molecular dynamics occurring in collective migration, it is also highly complex. On the other end of the spectrum, mechanistic, biophysical approaches eschew the objective of a faultless, exhaustive understanding of everything going on in the rich and complex observed phenomena. Instead, they focus on the multitude of intriguing features observed in collective cellular migration and attempt to determine mathematical rules that govern them. Frequently (but not exclusively), these approaches focus on phenomena where cells act like complex fluids, though the typical time scale found in flow behavior of cells is hours to days rather than the orders of magnitude faster time scales of more typical fluids. Further distinguishing them, cell sheets are always out-of-equilibrium systems, with each subunit capable of self-propulsion but in return consuming energy, and, critically, the ability to proliferate and thus change the number of players in the system. More generally, these out-of-equilibrium systems are studied in the field of active matter, where intriguing hydrodynamic properties such as swarming and turbulent swirling are known. For many phenomenological models, these behaviors, found in collectively migrating epithelial cells just the same as in other active matter systems, are the first point of contact. Instead of trying to understand the detailed underlying molecular occurrences, mechanistic approa-

ches aim to parametrize said activities in a very coarse-grained manner that is nonetheless sufficient to reproduce the observed phenomena.

Both approaches have their merits and their weaknesses, and in the end, it is likely that a combination of both approaches will lead to the best results. While computational limitations may make it infeasible to model and simulate the complete molecular processes going on within each cell for a large assembly, doing so for smaller groups of cells might be possible. The insights into molecular details gleaned from such systems can then in turn be implemented in a coarse-grained manner in the phenomenological models capable of describing large scale cellular behavior. For now, the gap between both approaches remains large enough that it has not been bridged, but every step on either side brings both ends of the spectrum closer together. To this end, this chapter focuses on the phenomenological analysis of cellular flow behavior. In particular, the focus is placed on collective migration in artificial confining geometries of microstructured environments.

Due to the similarities with fluids, these phenomenological descriptions can be thought of as a sort of cellular hydrodynamics. It is thus unsurprising that PIV (see section A.2.1), now established as a powerful tool for the analysis of collective cell migration, was originally used to visualize flows and currents in liquids. With such a method to extract the flow fields available, and with microstructured environments allowing us to dictate where cells can and cannot go, it is possible to study some of the typical phenomena of hydrodynamics that can be found in any physics textbook on the matter. Examples thereof include flow through a pipe, flow through a constriction or flow around an obstacle. The following four sections, detailing the results of publications P2 and P3, review publication P1, as well as two unpublished projects, discuss the results of typical hydrodynamic experiments performed on collectively migrating cells.

3.1 Flow and diffusion in channel-guided cell migration

One very standard experiment that every physics student is confronted with at the beginning of studying classical hydrodynamics is the flow of a liquid through a pipe. For a Newtonian fluid, such as water, the flow behavior through this cylindrical body is described by Hagen-Poiseuille's law (see section 2.3.3). Friction at the edge (no-slip condition) causes the water touching the edge to be stationary, while the water in the middle moves the fastest, leading to a parabolic flow profile throughout the channel. Sheets of epithelial cells are a distinctively non-Newtonian fluid, however, and as such, the flow profile across the channel for a collectively migrating epithelial sheet will deviate from an ideal parabola. The changes in this macroscopic behavior might allow insights into the underlying microscopic properties.

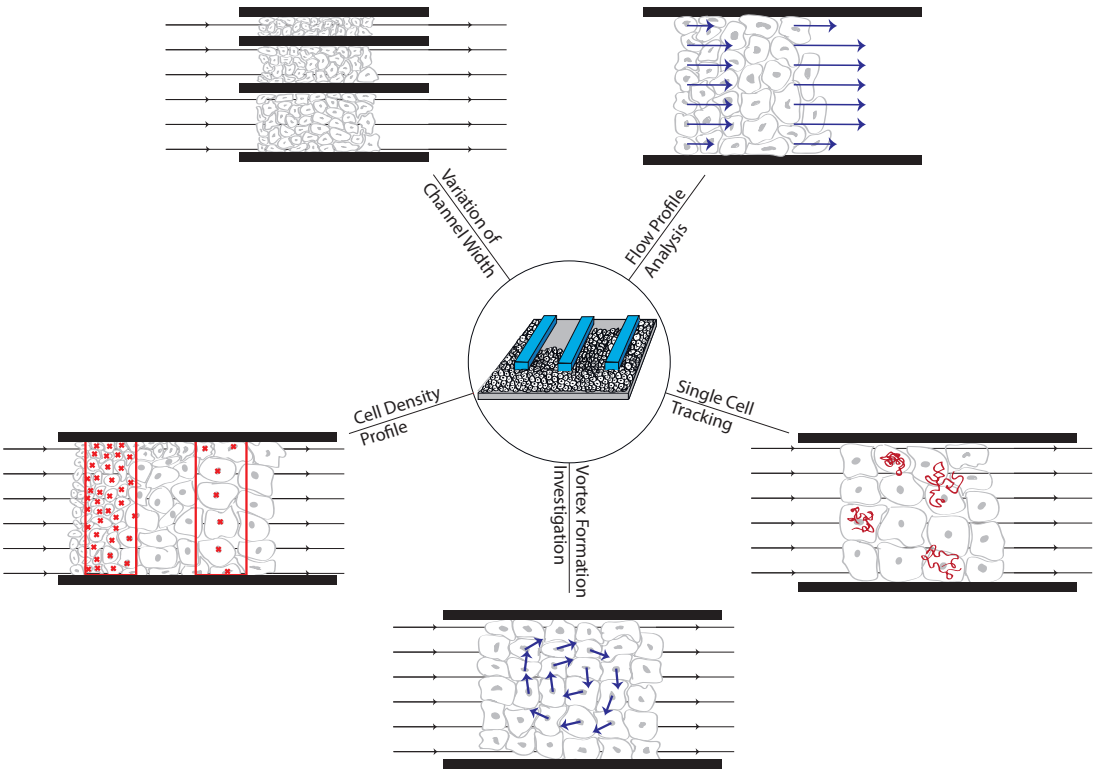

Figure 3.1: Overview of channel-guided cell migration study. Cells invade microstructured channels created from PEG-DMA polymer (center image). The influence of the confining geometry can be studied by variation of channel width. PIV analysis of brightfield microscopy data yields velocity fields describing the collective invasion of channels by cell sheets, which can be used to study the flow profile and the spontaneous formation of vortices (indicated in blue). Fluorescence images of nuclei allow for tracking of individual cells within the cell sheet and automated density determination (indicated in red).

In order to answer the question of the flow profile's shape, in publication P2 we confined a monolayer of MDCK cells to channels of $100-300$ µm width via the MIMIC method (see appendix A.1.1) [63]. This size corresponds to about 5 to 15 times the width of a single MDCK cell. In addition to the flow profile, several other features of the cell behavior (such as the evolution of the density profile and the formation of vortices) were investigated as well, as briefly highlighted in the overview of the study (see Fig. 3.1).

3.1.1 Cell front velocity and analysis of the flow field

The process of cell-sheet invasion into the channels is studied by time-lapse phase-contrast and fluorescence microscopy. In a first step, we analyzed the velocity of the invading cell front, as detected by an automated algorithm (see Fig. 3.2), and could determine that for our chosen range of channel widths there was no discernible difference in the speed (average velocity $v = 22 \pm 5\,\frac{\mu m}{h}$) (see Fig. 3.3). This leads us to conclude that the mode of migration is the same throughout all of our chosen channel widths. That this need not necessarily hold true can be seen in similar experiments performed by Vedula et al. [37], where a completely new, contraction-elongation type of migration appears for very low channel widths (corresponding to roughly the width of a single MDCK cell, approximately $\frac{1}{5}th$ of the narrowest channels used in our publication). Further analysis was no longer split according to channel size, as no effect on the invasion velocity was observed in the width range present in our experiments.

Taking all channels together, PIV analysis was performed to obtain the flow fields of the invading cell sheets (see Fig. 3.4). Immediately, strong spatial and temporal fluctuations become visible, overlaying a still clearly visible net flux towards the area not yet covered in cells. Successive time averaging as well as spatial coarse-graining revealed that on longer scales the directional flow becomes smooth (see Fig. 3.5).

Taking this flux purged of the fluctuations allows us to make statements about the general flow behavior that would otherwise be lost among the noise. In particular, this homogeneous flow field uncovers a decrease in flow velocity from the front of the sheet towards the back, potentially even in a linear manner (see Fig. 3.6). At the same time, the flow profile across the channel does indeed reveal distinctive differences from a parabolic Hagen-Poiseuille flow, as expected (see Fig. 3.7). Firstly, across almost the entirety of the channel, a flat plug-like flow is found, with all cells moving at the same speed. It is only at the very edge, close to the channel boundaries, that a steep decrease in velocity is

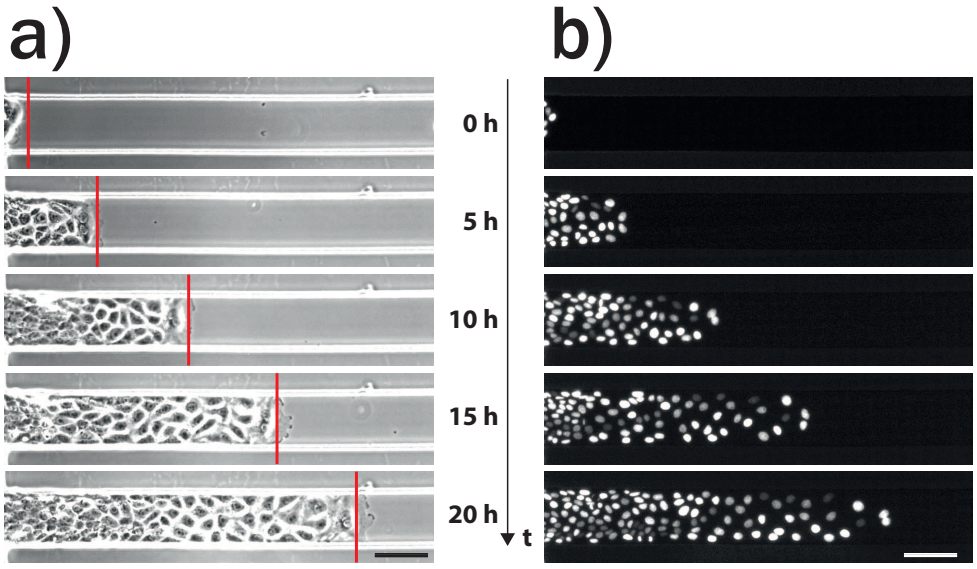

Figure 3.2: Time series showing invasion of channels by cell sheets. **a)** Brightfield images of a representative measurement, taken from selected time points at $t = 0$, 5, 10, 15 and 20 h. Good agreement of the actual cell front with the front detected by the automated algorithm (indicated by the red line) is confirmed. **b)** Fluorescence image of the cell nuclei corresponding to the brightfield images of a). The nuclei are later used for both cell separation during automated density measurements and cell tracking within the sheet. Scale bars correspond to 100 µm.

observed over the width of about two cell layers. The second biggest difference to Hagen-Poiseuille's law becomes visible in these outermost cell layers. Unlike for a perfect no-slip boundary condition, the velocity of these outermost cells is not zero and they still move at very roughly half of the speed of the center cells. Given the fact that the outermost cells in an epithelial layer are still discrete objects spanning a certain distance from the walls, and have strong adhesions to the cells further inside, it is not entirely surprising that these outermost cells do not stop entirely.

While they mask the general features of the flow behavior to a certain extent, the fluctuations in the original velocity fields also offer the opportunity to determine characteristic length and time scales of the system. To this end, the variance of the vertical flow component was plotted as a function of the coarse-graining length and the averaging time (see Fig. 3.8). Fitting exponential decay curves to this data yields $l_c = 80 \pm 10\,\mu\text{m}$ and $t_c = 1.1 \pm 0.1\,\text{h}$ as the distance/time by which point the variance has dropped to 1/e times its original value. This length scale is in good agreement with the value determined by other groups for the correlation length of coordinated cell migration in MDCK cells of comparable densities [38]. On the other hand, to our knowledge the equivalent correlation time scale for collective cellular migration had not been reported previous to our findings.

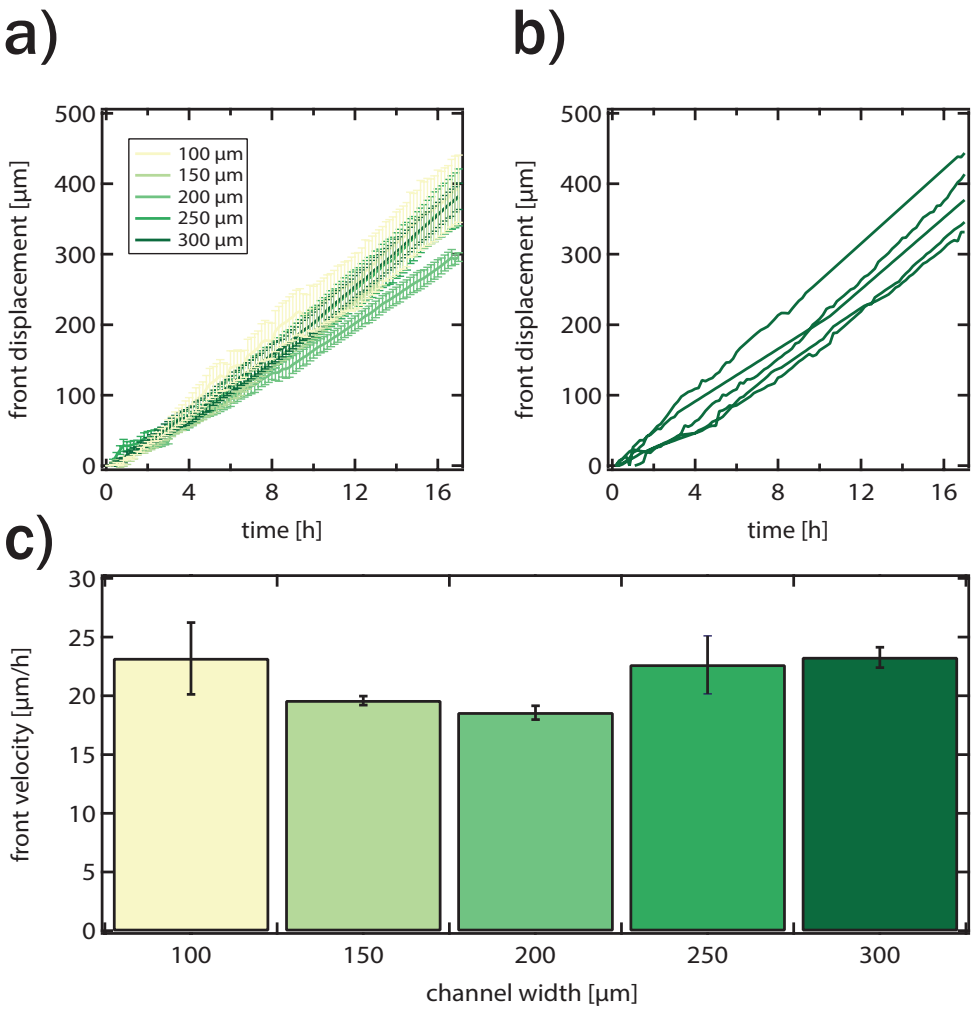

Figure 3.3: Average front displacement and velocities for invading cell sheets. a) The average front displacement shows no clear trend for different channel widths. b) For comparison, the scatter of the individual measurements for 300 µm wide channels is just as large as the difference between the averages of different widths. c) Average velocities of the cell front for different channel widths, calculated from the maximum average displacement for a particular width and the corresponding time needed to reach this distance. As already indicated by Fig. a), no dependence of the velocity on the channel width is visible. Fig. c) adapted with permission from reference [63]. Copyright 2014 Elsevier B.V.

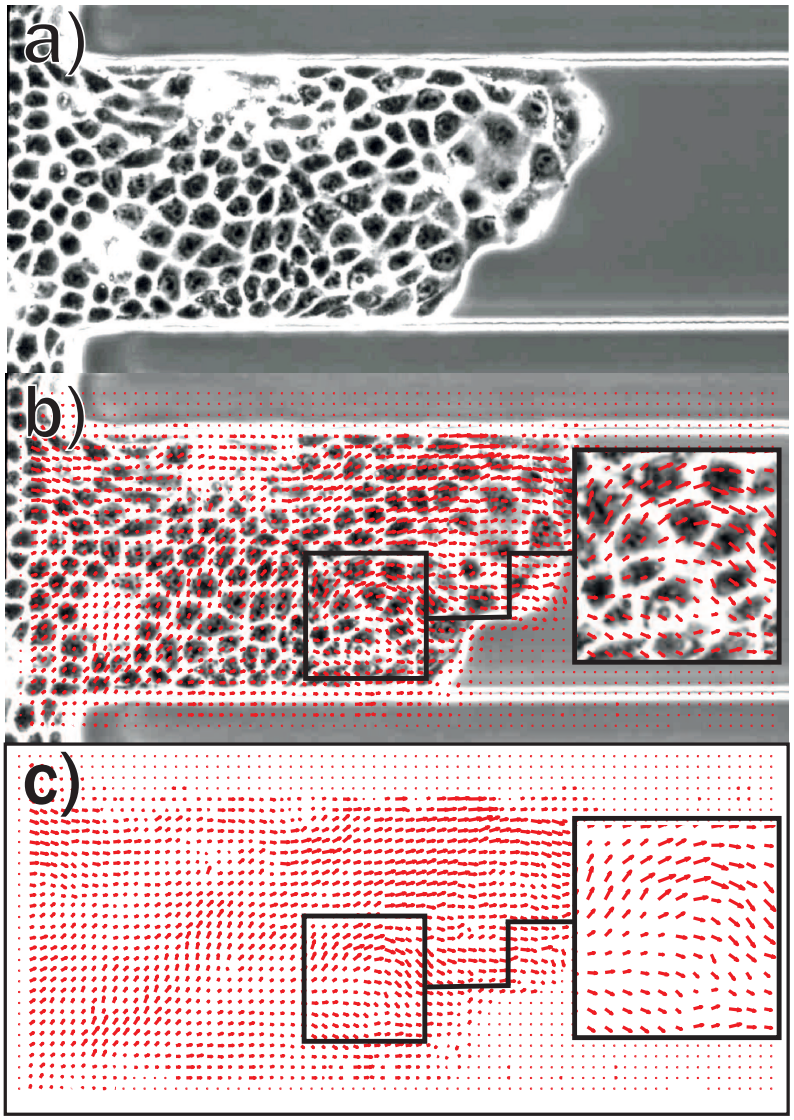

Figure 3.4: PIV analysis and resulting velocity fields. **a)** A representative brightfield image taken from the time-lapse movies that form the input for the PIV analysis. **b)** Pixel wise cross-correlation of subwindows in successive brightfield images yields a discrete velocity field quantifying the cells' motion. The overlay with the brightfield image shows that with the exception of the channel walls and slightly beyond the leading cells, the PIV analysis accurately finds motion only in areas covered by cells. **c)** For easier viewing and further use, the vector field is depicted without the underlying brightfield image.

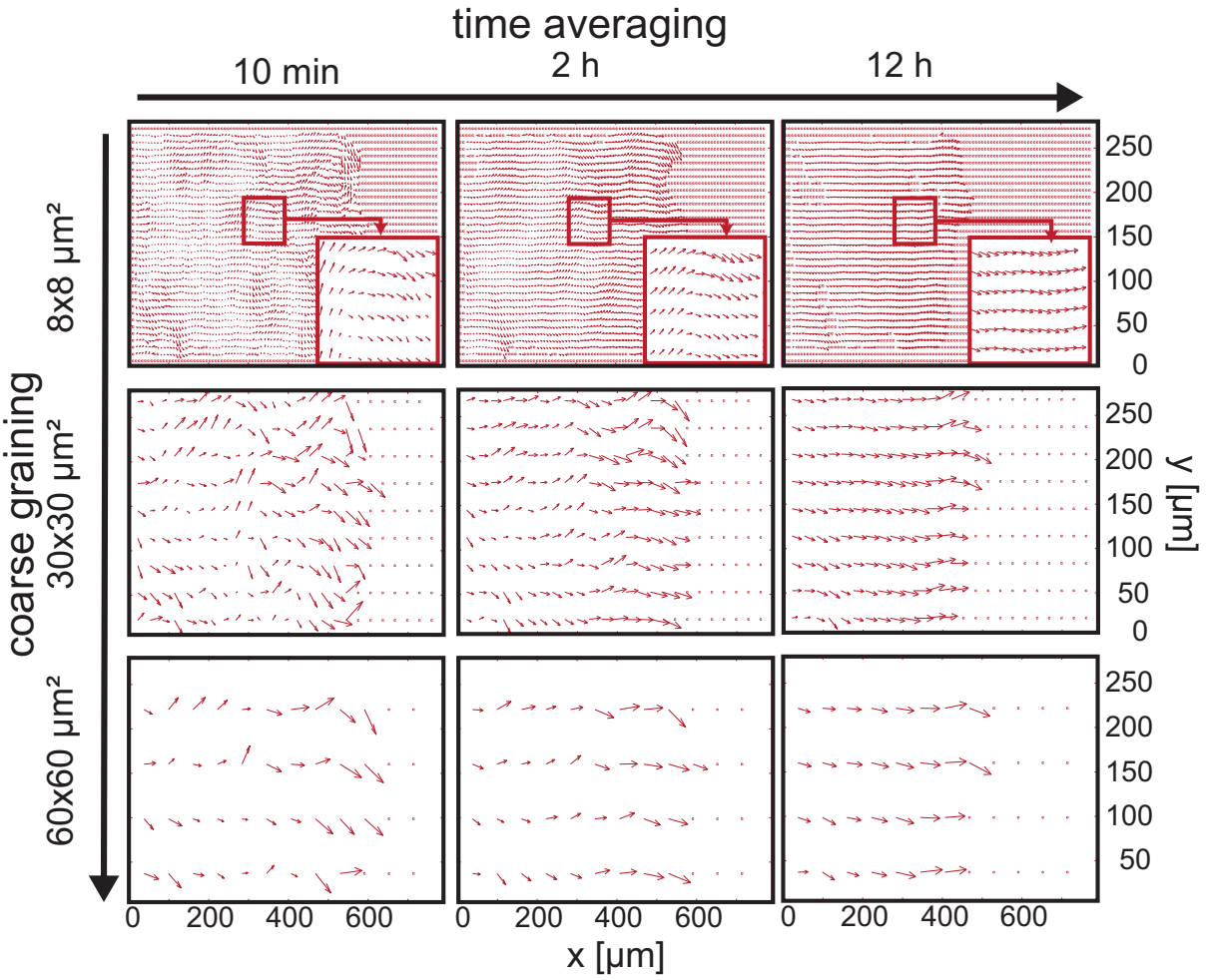

Figure 3.5: Smoothing of the velocity field by spatial and temporal averaging. The original vector field (top left) is coarse-grained over 4×4 neighboring vectors (middle row) and 8×8 neighboring vectors (bottom row), or averaged in time with all vector fields 1 or 6 hours before and after the current time point (center column and right column, respectively). Either of these averaging processes leads to visibly smoother vector fields, while the combination increases this effect even more. Clearly, despite temporal and spatial fluctuations, on long scales there is a smooth, directed flow parallel to the channel. Adapted with permission from reference [63]. Copyright 2014 Elsevier B.V.

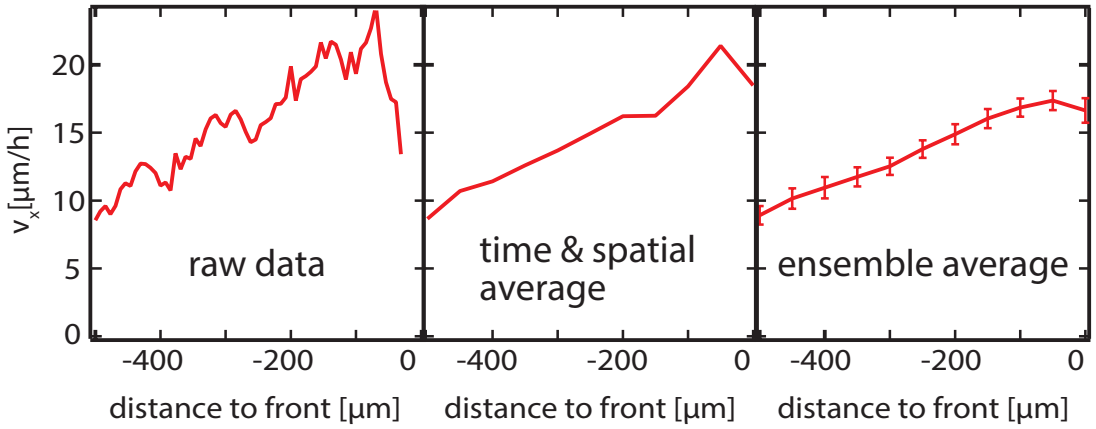

Figure 3.6: Profile of the velocity component v_x along the channel. Even in the raw data (unaveraged result of the PIV analysis of a single frame) a clear trend of increasing v_x towards the front of the cell sheet is visible. This tendency is highlighted more clearly when the individual frames are averaged over two hours and 50 µm in x-direction significantly reducing noisy behavior. The ensemble average over all measured channels shows that this trend holds up and becomes even more distinct when examining the entirety of the data. In this case, the increase appears to be linear with the exception of a dip in the velocity at the leading edge. Error bars indicate the standard error.

Notably, the time of one hour is significantly shorter than the cell doubling time (in this case approx. 25 h), introducing an entirely new time scale into the system. It is unclear where this new time stems from biologically speaking, though one potential candidate would be the time scale on which cells repolarize internally. Maiuri et al. measured the lifetime of stably polarized states in mouse bone-marrow-derived dentritic cells to be on the order of 10 min [141], while still unpublished work in our lab measured the repolarization time in MDA-MD 231 cells to be roughly on the order of 100 min (determined from the turn-around times of such cells oscillating on short stripes). While both are obviously very different cell lines from epithelial MDCK cells, the observed times are on the same order as the correlation time of $t_c = 1.1 \pm 0.1$ h, supporting the hypothesis that repolarization relates to this underlying time scale.

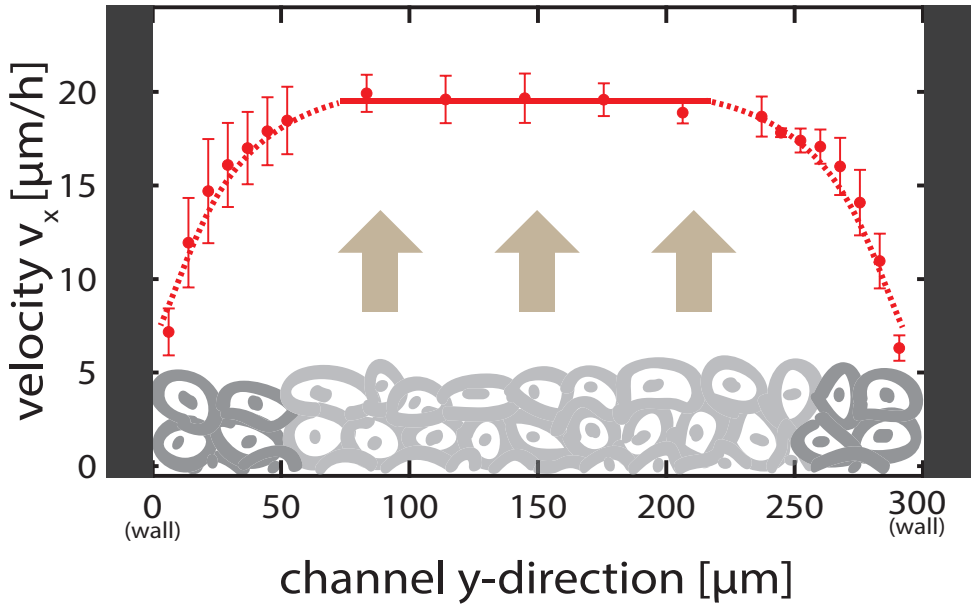

Figure 3.7: Average profile of the velocity component v_x (parallel to the channel) in y-direction (perpendicular to the channel). Over most of the width of the channel, the velocity is constant and a plug-flow like behavior is found. Only at the very edge of the channels, over about a width of two cells, is a drop in velocity discernible. Strikingly, the velocity does not drop to zero, however, as it would for perfect no-slip boundary conditions. In order to receive a profile where the short-term fluctuations are smoothed out, the points in the middle of the channel (everything connected by the solid line fit) are calculated by first averaging the individual velocity profiles in time (2 h) and space (15 µm × 15 µm) before averaging over all measured 300 µm channels. Since this would leave only very few points to characterize the drop in velocity, however, for the points at the edge of the channel the coarse-graining step is eschewed. This way, more points remain along the y-axis (at the cost of correspondingly higher error bars). Error bars indicate the standard error.

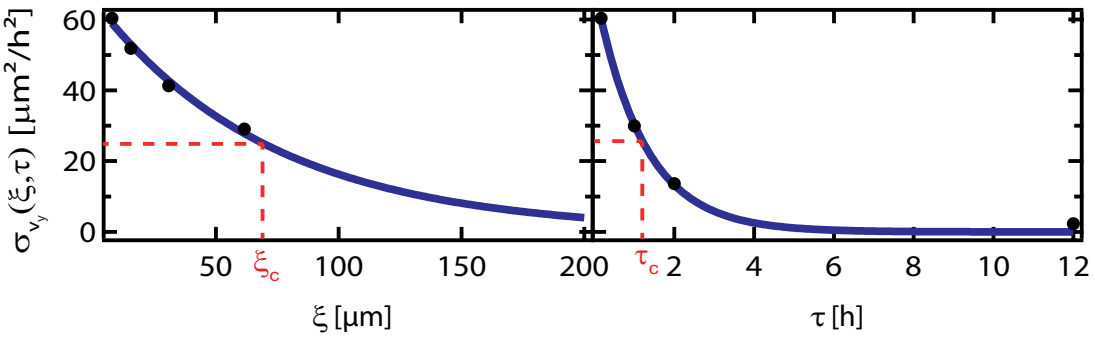

Figure 3.8: Variance of the v_y component of a velocity field in dependence on degree of averaging for representative channels. The variance of v_y is calculated after averaging over different temporal and spatial lengths and plotted against these values. Exponential decays can be fitted to calculate the correlation time $\tau_{cor} = 1.2\,\mathrm{h}$ and length $\xi_{cor} = 70\,\mu\mathrm{m}$ over which averaging has to be performed to decrease the variance of the field in y-direction to 1/e.

3.1.2 Cell density and diffusive flux

In addition to the flow field extracted via PIV analysis, further information about the observed collective cell migration in these experiments can be gleaned from the distribution of the cell number density throughout the channel. Extracted via automated counting of fluorescent nuclei, the density profile along the channel quickly reveals higher cell number densities at the back of the channels, towards the reservoir, and lower densities toward the tip of the migrating cell sheet. Hence, the average flow in these cell sheets (from the back towards the tip) is oriented along a density gradient. It is thus an intriguing possibility that the cell flux might follow a linear Onsager relation equivalent to Fick's first law of diffusion. To investigate this notion, the flux $J = v \cdot c$ was determined from the measured cell density c and flow velocity v. Again, the immediate values fluctuated strongly, and time averaging was necessary to allow studying of the general flux behavior. A linear Onsager relation would imply that the cell density flux J is directly proportional to (with the collective diffusion constant D_c as proportionality constant) a density gradient dc/dx, with a possible offset J_0 for an underlying density independent contribution to the flow, according to Eq. 3.1.

$$J = -D_c \cdot \frac{dc}{dx} + J_0 \tag{3.1}$$

As illustrated in Fig. 3.9, even for the time averaged data, a linear correlation between cell flux and density gradient is not immediately apparent. A more detailed analysis, splitting the data points according to total density, however, shows a clearer picture. Step by step exclusion of data, starting with the lowest absolute density and incrementally increasing the cutoff density below which the data points are discarded reveals a sigmoidal dependence of the Pearson product-moment correlation coefficient r on said threshold. This indicates that for higher absolute densities in the analyzed section of the invading cell sheet - r is found to be larger than 0.5 here - the cell density flux does indeed depend linearly on the density gradient in accordance with Eq. 3.1. On the other hand, for lower absolute densities, where r drops to roughly 0.2, the Onsager relation does not hold true at all, even though the high density data points are included in this calculation as well. Interestingly, the density for which a sigmoidal fit to the correlation coefficient values reaches half ($c = 2.2 \times 10^{-3} \frac{1}{\mu m^2}$) of its maximum height, corresponds well to the critical density (roughly $c = 2 \times 10^{-3} \frac{1}{\mu m^2}$) reported by Doxzen et al. for the onset of collective behavior in their systems [142] and Rosen et al., who observed that wound healing did not

occur until their monolayer had reached this density [143]. It is possible that the ability to properly follow a density gradient is also a form of behavior that requires collectivity in cell migration, and thus requires the same density threshold to be surpassed as in these earlier works. A linear fit of flux to density gradient for the data points above the critical density yields a collective diffusion coefficient of $D_c = 1500 \pm 500 \, \frac{\mu m^2}{h}$. It is clear, however, that this linear fit does not go through 0, but instead intersects the flux axis at a positive value $J_0 = (24 \pm 3) \times 10^{-3} \, \frac{1}{\mu m \, h}$. Taking into account the average cell density of $c = 0.0026 \, \frac{cells}{\mu m^2}$ in the area the flux was determined from, this J_0 corresponds to a velocity of $9 \pm 2 \, \frac{\mu m}{h}$. As discussed above, this is the velocity of an underlying, spatially uniform and density independent drift. Thus, at the macroscopic level, there are two contributions to channel-guided cell migration. Specifically, there is firstly a density gradient dependent, diffusion mediated transport and secondly, the density independent drift. In regular matter, such a drift typically only occurs as a result of an externally applied field. In contrast, for our system of collectively migrating cells, this drift might well correspond to polarization and the resulting active self-propulsion of the individual cells. Symmetry-breaking by the walls of the channel might even induce a state of collective polarization in the direction of the channel. Independent of the cause of this underlying drift, it is worth taking note of the fact that both the constant drift and the density gradient dependent flux (including proliferation) are of the same magnitude. Together they need to approximately add up to the determined velocity of the cell front of $22 \, \frac{\mu m}{h}$. Thus, both effects contribute roughly equally to generate the entirety of the collective migration.

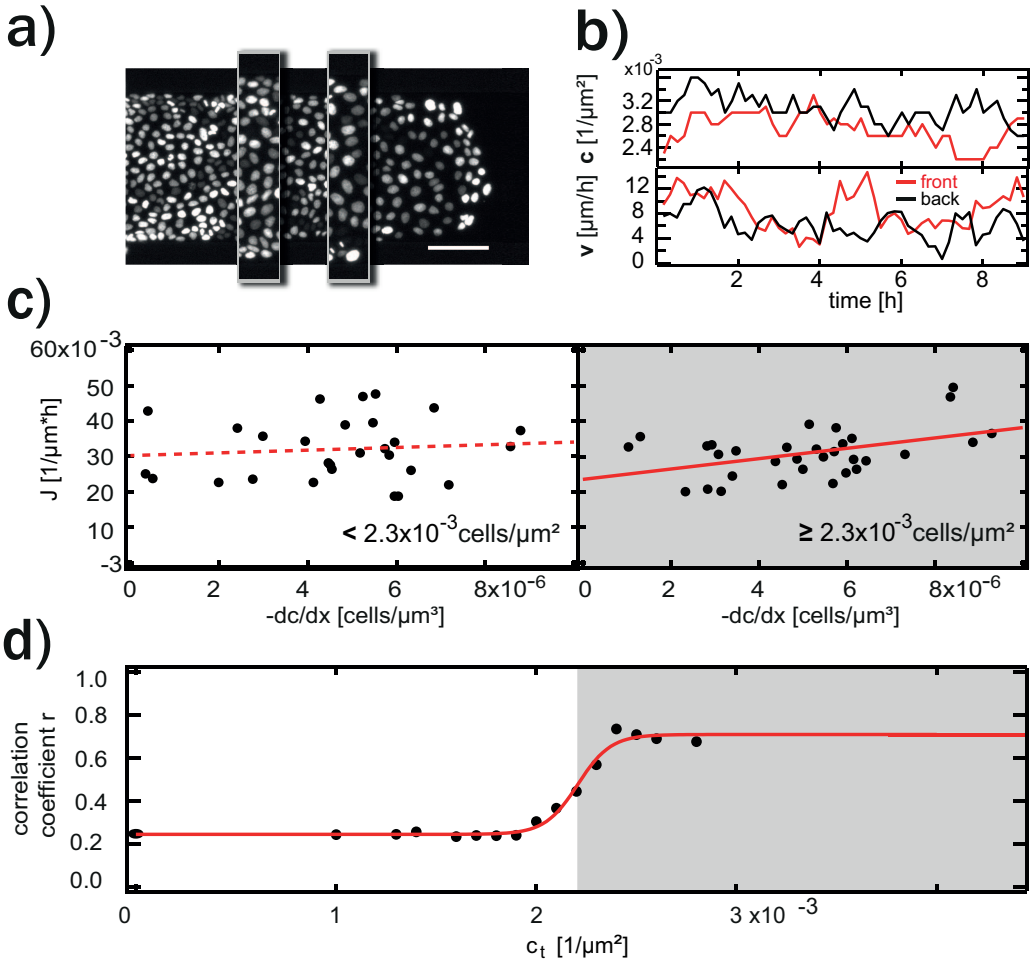

Figure 3.9: Cell density flux in a migrating monolayer. The cell flux and corresponding density gradient are calculated for three pairs of 50 µm wide observation windows, with each pair being 150 µm apart. All the examined bins together span an area 100 µm to 400 µm from the front of the cell sheet. **a)** Fluorescence image of the nuclei used for density determination, with one pair of the bins used for calculation shown as an example (200 µm and 350 µm away from cell front). **b)** Time evolution of cell density and velocity for one representative measurement and one bin combination, showing strong fluctuations. **c)** Splitting all data points according to the absolute density they were measured at shows very weak correlation for low overall densities, whereas the correlation is stronger when the values recorded at $c \geq 2.3 \times 10^{-3} \frac{1}{\mu m^2}$ are examined. In this case, a linear fit of the Onsager relation yields a collective diffusion coefficient of $D_c = 1500 \pm 500 \frac{\mu m^2}{h}$. **d)** In order to choose the cutoff-density used in c), the correlation coefficient r between the cell flux and the density gradient is calculated. Initially ($c_t = 0$ in the plot), all value pairs are included, then all values below the incrementally increasing cutoff density c_t are removed. The relation between correlation coefficient and average included density is well-fitted by a sigmoidal curve, and the point of half height chosen as the cutoff density. Fig. a) and b) reprinted with permission from reference [63]. Fig. c) and d) adapted with permission from reference [63]. Copyright 2014 Elsevier B.V.

3.1.3 Reaction-diffusion model

The above description via a linear Onsager relation and an underlying, spatially uniform drift does not explicitly take into account the effect of cell proliferation on the observed collective motion. With a measured cell doubling time of $25.2 \pm 4.2\,\mathrm{h}$ very much of the same order as the experimental observation time, however, it is unlikely that cell divisions do not contribute in any way. To gain access to the contribution of cell divisions more easily, it is helpful to analyze the spatially uniform drift and the diffusion-mediated effects separately. This is possible because mass balance dictates the cell density profile $c(x,t)$ does not depend on the actual flux J, but rather on its gradient ∇J. Thus, the spatially uniform component of J does not contribute at all, and the diffusion-mediated component can be studied decoupled from it. The cell density profile hence should only depend on unordered motion and proliferation. With no further information available how the individual components contribute in a system, the most reasonable approach to modeling is to use the most generic model and not make any assumptions. In this case, the most universal model to incorporate both cell proliferation (reaction) and diffusive-like motion (diffusion) is a reaction-diffusion equation. Specifically, inserting logistic growth for the cell proliferation results in the Fisher-Kolmogorov Eq. 3.2.

$$\frac{\partial c}{\partial t} = \underbrace{D_c \nabla^2 c}_{\text{diffusion term}} + \underbrace{\lambda c \left(1 - \frac{c}{K}\right)}_{\text{reaction term}} \tag{3.2}$$

Here D_c designates the collective diffusion coefficient, λ is the growth rate and K is the maximum carrying capacity supported by the cell monolayer. For simplicity, this equation is given in the reference frame moving with the underlying drift velocity of $9\,\frac{\mu\mathrm{m}}{\mathrm{h}}$.
The analytical solution to the Fisher-Kolmogorov equation (Eq. 3.3) results in traveling waves with a constant front speed given by Eq. 3.4.

$$u(x,t) = k\left[1 + exp\left(-\frac{5}{6}\lambda \cdot t + \sqrt{\frac{\lambda}{6D}} \cdot x\right)\right]^{-2} \tag{3.3}$$

$$s = \sqrt{4 D_c \lambda} \tag{3.4}$$

Again, it is worth noting that this is the front speed in the moving reference frame and

the underlying drift velocity of $9\,\frac{\mu m}{h}$ will need to be added back on top of it to obtain the actual front velocity in the observer's resting frame of reference. Experimentally, the evolution of the density profiles does indeed show a traveling wave-like behavior (see Fig. 3.10), though the stationary, shallow shape of the density profile is not reached immediately but instead develops from an initially steep profile. We thus analyzed the late stage density profiles of various channels (in order to sensibly average the density profiles were transformed in such a way that the coordinate origin is at the current position of the cell front) and found that the resulting averaged density profile is well-described by fitting the theoretical profile resulting from Eq. 3.2. The main shortcoming of the theoretical curve is that it fails to predict the sharp drop at the front of the cell sheet. Here, the Fisher-Kolmogorov equation predicts an asymptotical behavior, whereas the experimental data, consisting of discrete cells by its nature has a discrete end where the density drops to zero. In addition, it is not ideal that all the measured cell densities only fall on the front part of the fitted curve, with none of them reaching close to the resulting carrying capacity. Presumably the traveling wave penetrates beyond the channel entrance and into the bulk cell monolayer and densities in this unobserved area would reach closer to the carrying capacity.

Nonetheless, the carrying capacity of $K = 0.0100 \pm 0.0003\,\frac{\text{cells}}{\mu m^2}$ resulting from fitting the theoretical curve is in good agreement with values given in literature [127, 143] and the collective diffusion coefficient of $D_c = 1150 \pm 120\,\frac{\mu m^2}{h}$ agrees well with the value of $1500 \pm 500\,\frac{\mu m^2}{h}$ determined from fitting the linear Onsager relation (Eq. 3.1) to the cell flux in the previous section. The third parameter, the growth rate, was fixed at $\lambda = 0.0283 \pm 0.0005\,\frac{1}{h}$, as determined from independent measurements of exponentially increasing cell number in a confluent monolayer confined to the same channels used for this experiment. It is noteworthy that with one of the parameters fixed in this way, the obtained values for the other two fit parameters are not arbitrary. Significant changes to either D_c or K cause the respectively other parameter of the pair to take values inconsistent with expectations and, additionally, lead to strong deviations between the shape of the theoretical curve and the experimental data points.

As expected, the theoretical speed of the cell front predicted by Eq. 3.4 is in good agreement with the empirically observed velocity. Inserting the obtained values for D_c and K results in a theoretical $s_{th} = 11\,\frac{\mu m}{h}$, which, as noted above, is the velocity in the moving reference frame. Adding the previously determined drift velocity of $v = 9\,\frac{\mu m}{h}$, we obtain $s_{tot} = 20\,\frac{\mu m}{h}$, well within the range of error of the experimental value $s_{exp} = 22 \pm 5\,\frac{\mu m}{h}$. Confirmation that the solution of the Fisher-Kolmogorov equation only works as long as

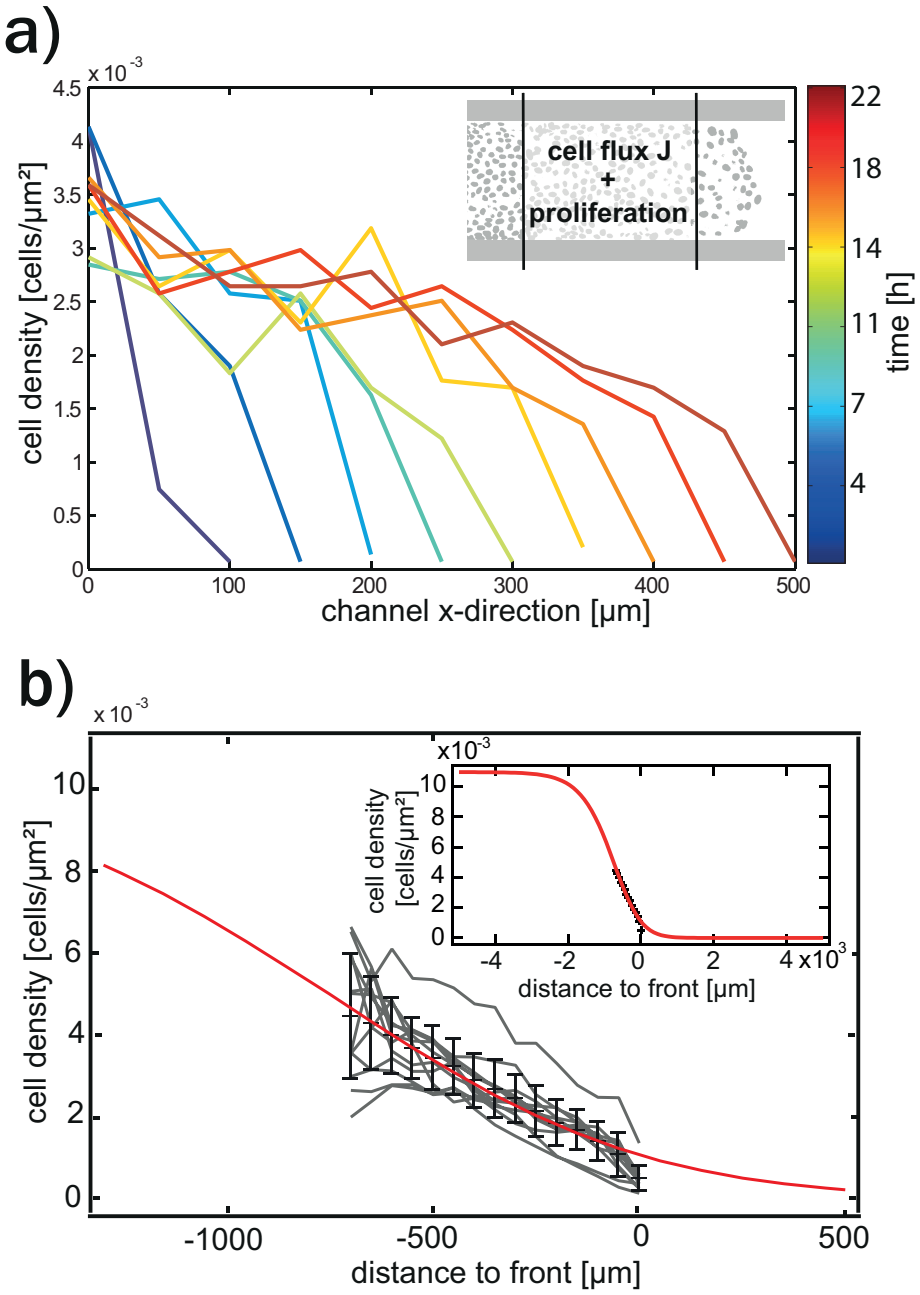

Figure 3.10: Traveling wave analysis of the cell density profile **a)** Time evolution of the cell density profile. Once the migrating cell sheet has invaded the channels to a certain extent, the density profile takes a relatively stationary shape that is translated along the channel at a constant velocity. **b)** End-point density distributions of all measurements that penetrate at least 750 µm into the channel (*gray curves*) and the average density profile (*black crosses*). With the exception of the leading edge of the cell sheet, the fit of the analytical solution of the Fisher-Kolmogorov equation matches the experimental values well, with the resulting values of $D_c = 1140 \pm 120 \, \frac{\mu m^2}{h}$ and $K = 0.0110 \pm 0.0003 \, \frac{cells}{\mu m^2}$ in good agreement with the collective diffusion coefficient determined from the linear Onsager relation and maximum cell density values found in literature, respectively. The expanded view in the inset highlights that the experimental values only cover a small fraction of the density profile the fit implies. Reprinted with permission from reference [63]. Copyright 2014 Elsevier B.V.

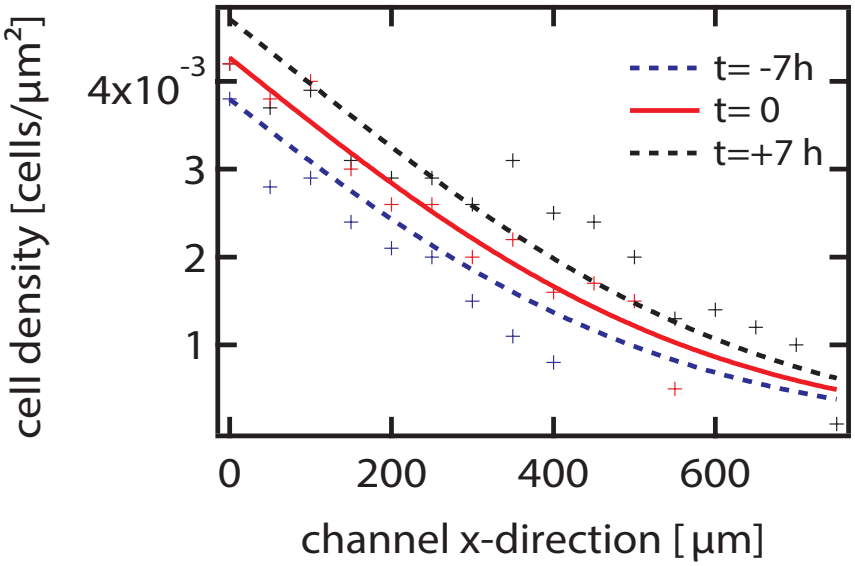

Figure 3.11: Fit of the traveling wave for several time points. A fit (*solid red line*) of the time-dependent solution to the Fisher-Kolmogorov equation to the density profile of a single time point (*red crosses*). The quality of agreement between data and fit is good, in particular when taking into account the higher scattering due to lack of any averaging. With the resulting parameters fixed, the fit is performed twice more but with the time shifted by 7h in both directions (*dashed lines*). While the shape of both of these curves looks to be in relatively good agreement with the trend of the empirical values (*blue and black crosses*), they show an insufficient x-shift compared to the first curve to align properly with these values.

the moving frame of reference is taken into account is given by the result of trying to fit the density profile for multiple time points (see Fig. 3.11). Good agreement can be found by fitting Eq. 3.3 to the middle time points, but using the same fit parameters for earlier and later time points results in an x-offset between the fits and the empirical data points, even though the shape of the fit would seem to follow the data points' trend. As the fitted parameters for D and c result in a lower front speed s (namely the speed in the moving reference frame) the theoretical curves are displaced less along the x-axis than the measured data points. Beyond confirming that there really must be a spatially uniform drift, our resulting values of $s_{th} = 11\,\frac{\mu m}{h}$ for the diffusion component and $v = 9\,\frac{\mu m}{h}$ for the drift prove that both the density gradient-driven diffusive migration and the spatially uniform, density independent drift contribute about equally to the overall migration speed.

3.1.4 Analysis of vorticity in the flow field

The occurrence of spontaneously forming vortices is a well-documented aspect of cell migration [27, 37, 60] and can also be observed in our experiments. While cell density has been shown to play a role on the size of emerging vortices [27], the effect of an underlying

preferential migration direction as it is present in our channels had to our knowledge not been studied yet prior to our publication. In order to properly scrutinize the influence of directional migration and separate it from other potential influence factors such as the confinement in the channel, we created a comparable control system (for details see appendix A.1.1) in which cells are seeded in the same channels evenly from the top. Rather than migrating in one general direction, the cells fill the entire channel in this case and are effectively at rest, which here refers to the absence of large scale displacements of individual cells. Instead, movement is limited to short range motion of cells or groups of cells in a wafting manner. Frequently, areas of cells contract, temporarily increasing the local cell number density while decreasing it in surrounding areas, before relaxing again. In addition, the expected short scale collective rotational motion (spontaneous vortex formation) is also frequent.

In order to investigate the vortex formation in a quantitative manner, both in the resting case and the case with a preferential migration direction, we calculated the vorticity Ω from the PIV vector fields. To this end, a coarse-graining distance was chosen so that in the resulting flow field each vector corresponds to roughly the area of one cell. The curl is then calculated from the perpendicular components of the relative velocities v of the neighboring lattice sites according to Eq. 3.5 by using the unit vector in z-direction $\mathbf{e}_z$.

$$\Omega_i = \mathbf{e}_z \cdot (\mathbf{curl} \cdot \mathbf{v})_i \tag{3.5}$$

As it is harder to distinguish areas of rotation from those without activity while the sign of the vorticity is preserved (see Fig. 3.12), the squared value Ω^2 is considered for all further investigations. Immediately, the data for the resting, confluent cell sheets confirms the effect of cell density on vorticity. Both heatmaps and a direct plot of vorticity value distribution against density show that with increasing cell density, vorticity decreases significantly (see Fig. 3.13). This also holds true for the channels with invading cell sheets. In the manner examined in the previous section, a density gradient develops in the cell sheet in these cases, with high densities towards the bulk of the cell monolayer, and low densities towards the cell front. As the heatmaps clearly show, the strength of vorticity is highest towards the front of the cell sheet, where densities are lowest.

Despite the same qualitative behavior in relation to density, quantitatively things are quite different in both cases. When comparing areas of the invading cell sheets to channels of the same average density in the resting case, the frequency of vortex formation is

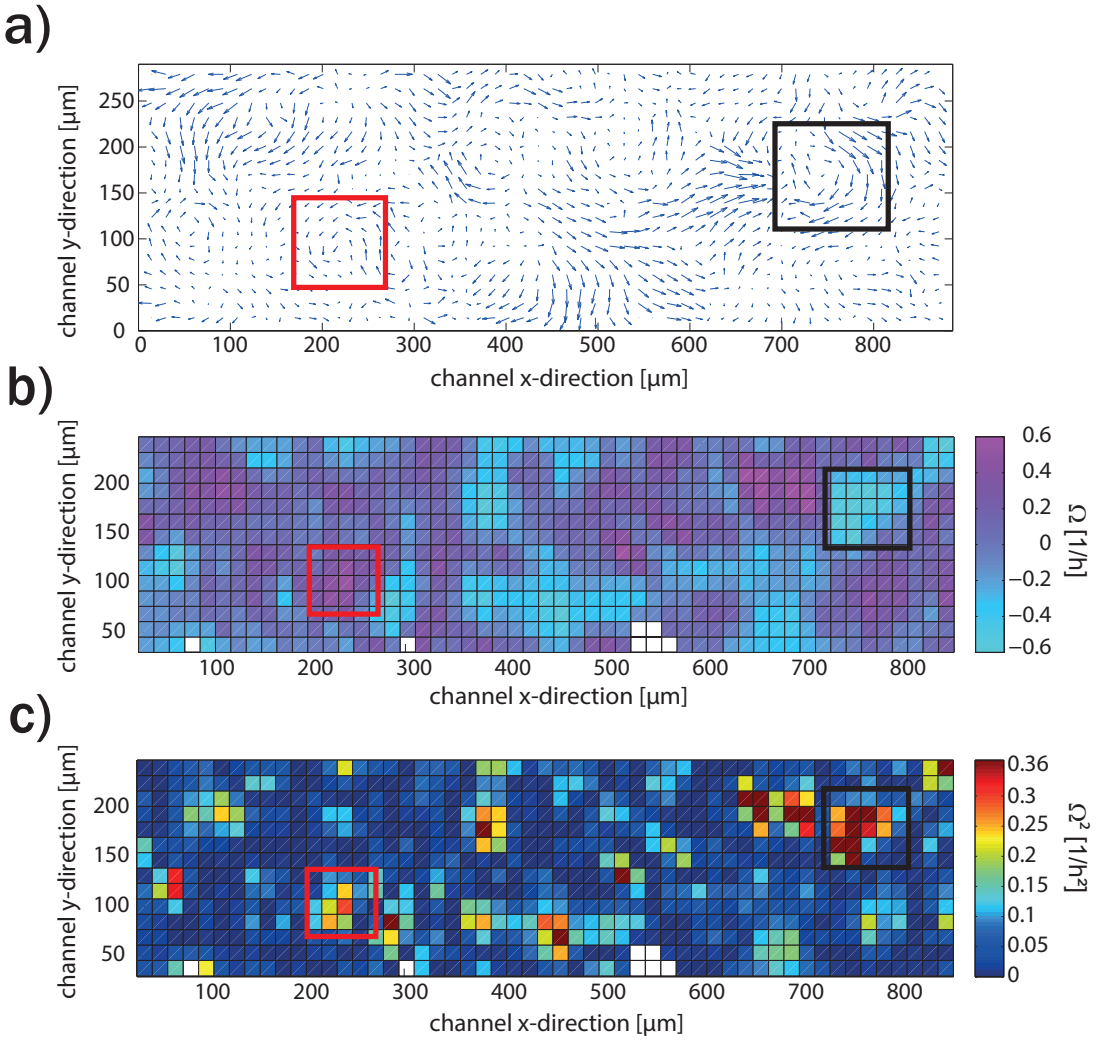

Figure 3.12: Vortex formation in confined cell sheets. **a)** Underlying PIV field used for vorticity calculation, visibly showing several vortices. One clockwise (*black square*) and one counter-clockwise vortex (*red square*) highlighted for ease of viewing. **b)** Heatmap of calculated vorticity with sign taken into account. Positive values (counter-clockwise rotation) are indicated in *purple*, negative values (clockwise rotation) are indicated in *blue*. While upon close examination the vortices highlighted in a) can be found again, it is hard to distinguish areas with strong rotational activity from calmer areas at a glance. **c)** Heatmap of squared vorticity values calculated from the same underlying PIV field of Fig. a). It becomes much more intuitive to distinguish areas of high activity (*dark red*) from areas of low activity (*dark blue*), though in return the information on directionality is lost. White squares indicate areas where no vorticity values could be calculated.

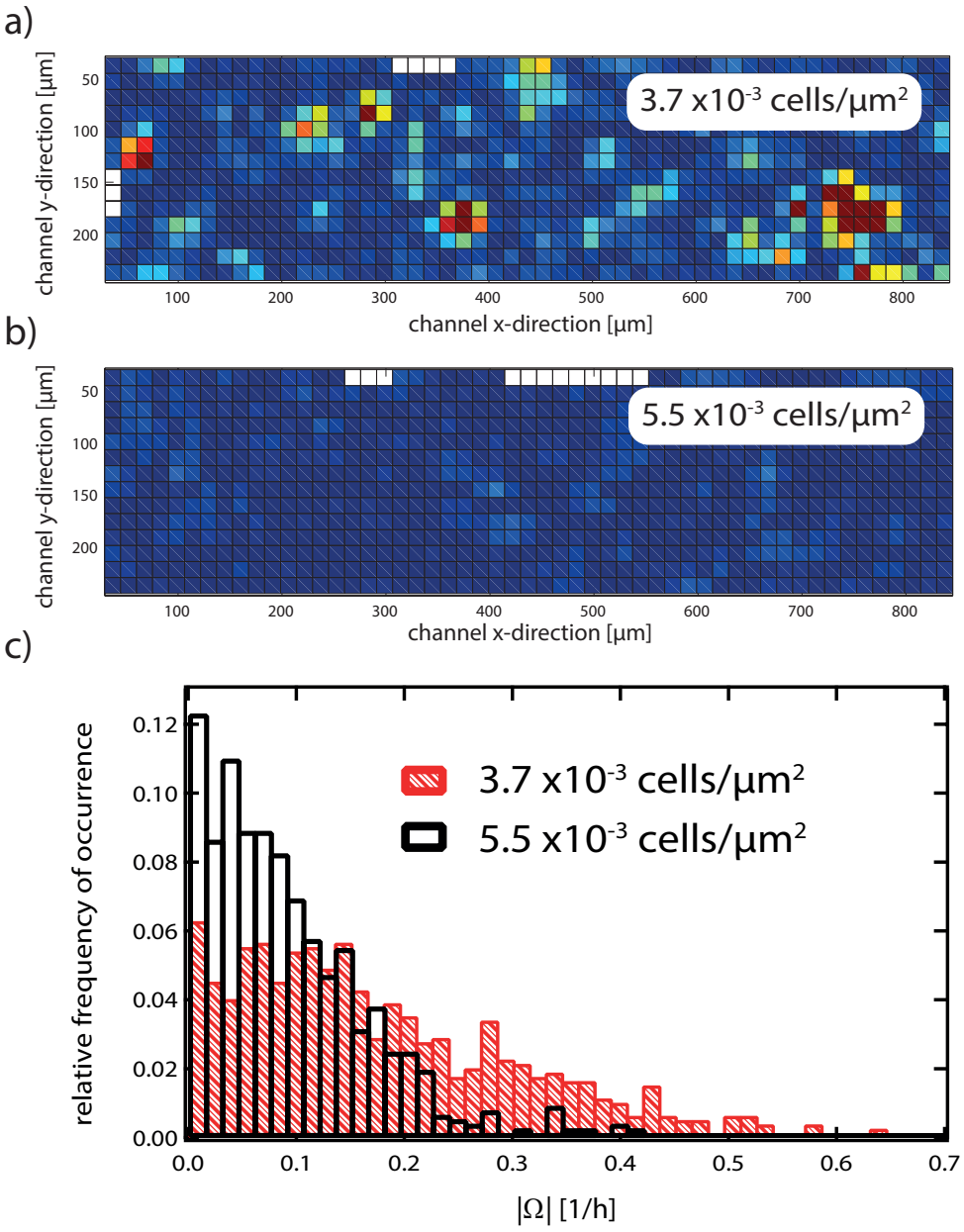

Figure 3.13: Effect of density on vorticity in confluent cell layers without preferential migration direction. **a)** Representative heatmap from a confluent channel for an early time point of low cell density. As above, area of high activity are shown in *dark red*, whereas areas of low activity are *dark blue*. **b)** Representative heatmap for late time point with high density from the same measurement. Rotational activity has decreased significantly for the higher density. **c)** Histograms of $|\Omega|$-value occurrence across all grid squares in both cases. Quantifying the above visual result, a broad distribution of vorticity values is found at low densities, while at high densities the distribution becomes narrow, with predominantly low values and high values becoming rare. Heatmaps in a) and b) reprinted with permission from reference [63]. Copyright 2014 Elsevier B.V.

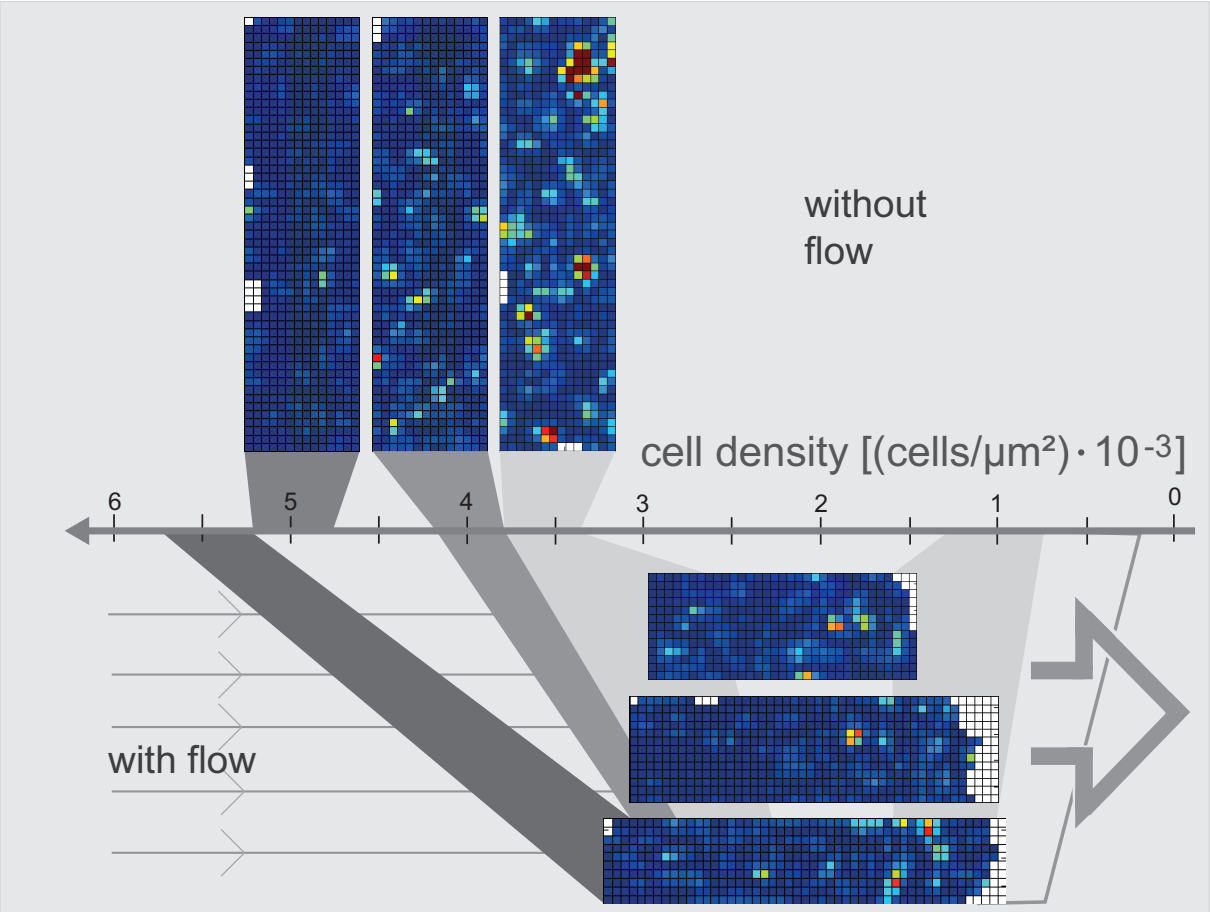

Figure 3.14: Heatmaps depicting the influence of density and flow on vorticity. In the resting case, cell sheets have a relatively well-defined density, while in the flowing case large density gradients appear throughout one sheet. The gray shaded areas indicate the mapping of heatmaps to the density axis. Heatmaps for the cell sheets without flow are rotated by 90° compared to their typical orientation to indicate they are uniformly assigned to the indicated density region. Heatmaps for the directionally migrating cell sheets are depicted in their usual orientation and their density is indicated separately for the front of the sheet and the back. The flowing cell sheets show the same density dependence found in confluent sheets: Vortices appear predominantly close to the leading edge, where the density is lowest. Comparing regions of similar density (e.g. $3.5 \cdot 10^{-3}$ μm^2) shows that vorticity is reduced in the presence of directed migration. Adapted with permission from reference [63]. Copyright 2014 Elsevier B.V.

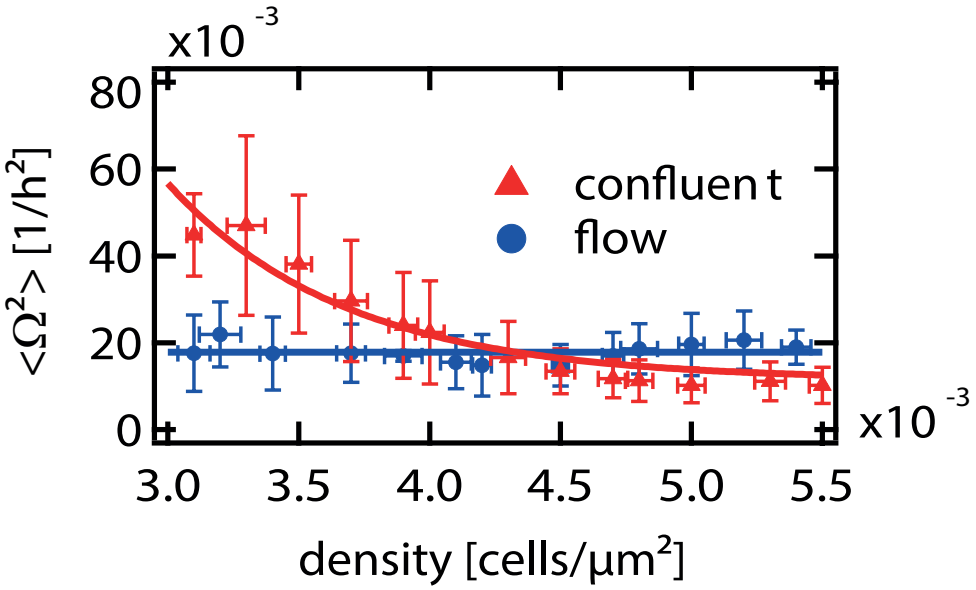

Figure 3.15: Quantification of the influence of flow on vorticity. At equal densities, vorticity is much lower under flow (blue circles) compared to the resting case (red triangles), indicating that there is less rotational migration in this scenario. Fits to guide the eye (solid lines) show that while without flow there is a decrease in Ω^2, the value seems to hold relatively constant for cells invading the channel. Adapted with permission from reference [63]. Copyright 2014 Elsevier B.V.

consistently higher in the resting cases. This difference can be most clearly seen for the abundance of vortex formation observed for the channel without preferential migration direction at a density of 3.5×10^{-3} cells/µm^2, which vanishes entirely in flowing cell sheets of equivalent density (see Fig. 3.14). Fig. 3.15 shows this relation in a quantitative manner across all measured cell sheet densities.

Naturally, with spontaneously occurring rotations, the question of directionality arises. For collectively rotating cells, the question of a preferential direction, perhaps resulting from an underlying chirality of e.g. the actin cytoskeleton, has been posed before [144]. Within the accuracy of our measurement, however, we found left-handed and right-handed vortices to be equally present, both for our resting and for our invading cell sheets (see Fig. 3.16). The size of our observed vortices, as estimated from the heatmaps, appears to be up to six cell diameters, which is in good agreement with values from literature [37].

Due to the strong confinement of the individual cells, particularly in the confluent channels, it is worth taking note of the average lifetime of the observed vortices, as well as the average path lengths the cells actually travel in these rotations. The standardized auto-correlation of the time evolution of the vorticity was calculated on each grid point

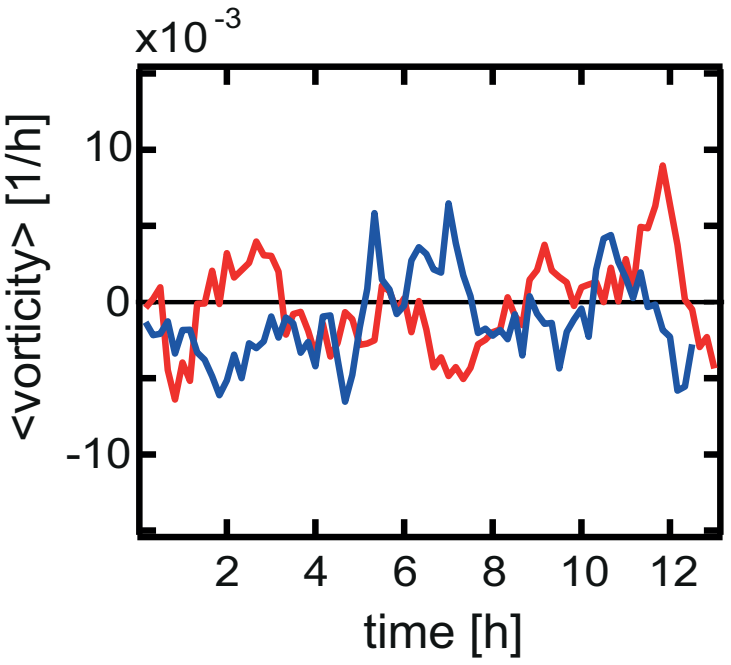

Figure 3.16: Directionality of vorticity. Within the accuracy of the measurement, there is no preference for clockwise (negative vorticity values) or counterclockwise (positive vorticity values) vortices to form both for the confluent resting case (*red curve*) and for cell sheets under flow (*blue curve*). Reprinted with permission from reference [63]. Copyright 2014 Elsevier B.V.

according to Eq. 3.6.

$$G(\tau) = \frac{\langle \Omega^2(t) \cdot \Omega^2(t+\tau) \rangle}{\langle \Omega^4 \rangle} \tag{3.6}$$

This auto-correlation, a measure for the self-similarity of the vorticity values on each grid point, gives an indication about the decay times of the observed vortices. In order to quantify this lifetime, an exponential decay was fitted to the average of all individual auto-correlation curves (see Fig. 3.17). The relaxation time over which $G(\tau)$ drops to 1/e times the value of $G(0) - G(\tau \to \infty)$ was thus determined to be $t_R = 15 \pm 1\,\mathrm{min}$. These short lifetimes are close to the resolution limit with which images were acquired (one every 10 minutes), so for a closer examination of the dynamics of individual vortices a higher time resolution of image acquisition would be advantageous. In any case, however, this short lifetime must also correspond to a short actual distance covered by the collectively rotating cells. In order to get a feeling for this path length, the vorticity values for a hypothetical set of eight cells rotating around a center cell were calculated for incrementally increasing rotation angles (see appendix A.2.6). By comparing the squared vorticity values for this optimal, synchronized and uninhibited rotation to the measured squared vorticity values

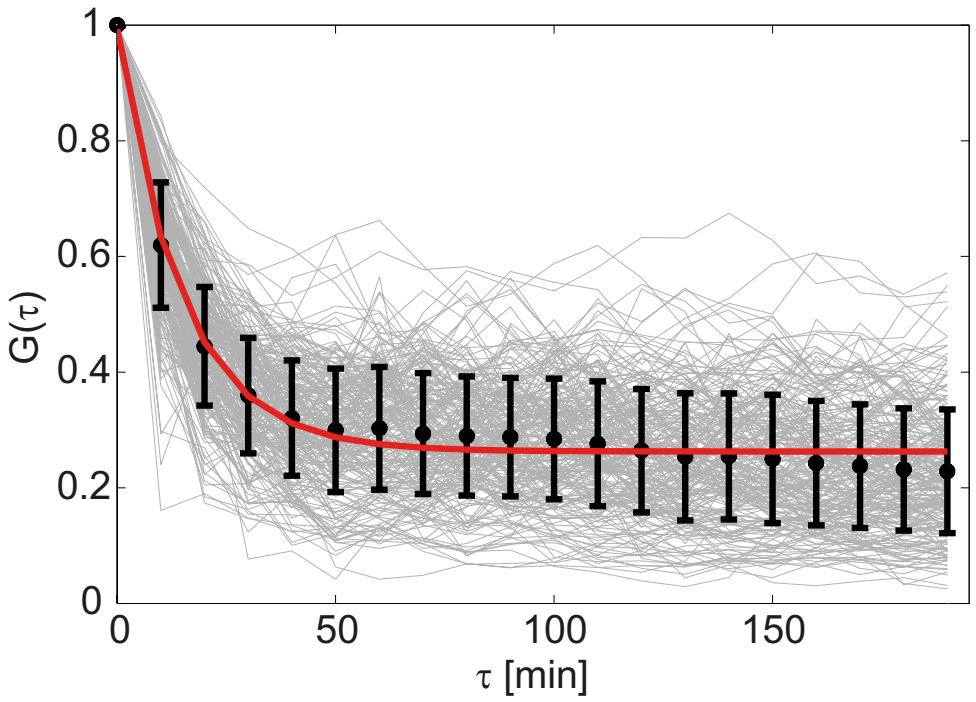

Figure 3.17: Decay time of vortices in confluent cell layers. The normalized correlation function of Ω^2 is calculated on individual grid points of the vorticity map (gray curves). While the individual curves show large fluctuations, the average curve appears to be very smooth (black circles). The decay is quantified temporally by fitting of an exponential decay (red line) to the mean values and retrieving the time $\tau_{\mathrm{decay}} = 15\,\mathrm{min}$ necessary for the original amplitude to drop to 1/e. Reprinted with permission from supporting information of reference [63]. Copyright 2014 Elsevier B.V.

in the heatmaps, the effective path length of collective rotation could be estimated to be within the range of 9°(*dark red squares* in the heatmaps). As for the correlation time of collective motion calculated from the decay of the variance of the PIV field, the time scale observed here is much shorter than the cell doubling time. On the other hand, with 15 min this vortex lifetime is on the same order of magnitude as the 1.1 h correlation time for collective migration (albeit a factor 4.4 times smaller). Given this, the idea that perhaps the same underlying physical process plays a role in both collective rotation and collective directed migration suggests itself.

3.1.5 Single cell motility

It is well known that the migration of individual cells can be described by some manner of random walk, with both persistent random walk models and bimodal models (alternating states of directional migration and reorientation) enjoying success [145–148]. The situati-

on is more complicated and less well studied when it comes to the motion of individual cells within a connected monolayer. Thus, we investigated whether in this scenario cells still undergo effectively random motions. In addition, we asked the question of whether in the case of channels with a preferential collective migration direction, the individual cells' motion can be recovered from a superimposition of diffusive motion and directional cell migration. The latter tracks were centered by subtracting an average drift velocity from the individual cell traces, chosen in such a manner that the average displacement from their starting point in x-direction was zero (see appendix A.2.8). The justification for this is straightforward. The previous findings suggest that the collective motion of the cell sheet is well-described by the traveling wave solutions of the Fisher-Kolmogorov equation with underlying drift. As these traveling waves move at a constant velocity, there has to be a constant velocity that can be subtracted to remove this collective migration component and transform the cell tracks into a coordinate system where only their individual motion remains. A simple visual inspection of representative tracks from both classes (see Fig. 3.18) shows that at a glance, the discrepancies between cells within one class are larger than the discrepancies between both classes. This is a first clue that the nature of the motion of the individual cells might indeed be a superposition of directed migration and the diffusive behavior they show in confinement, however, a closer, quantitative examination is necessary.

One quantity typically studied to gain insight into the diffusivity of single particle tracks is the MSD. Thus, we calculated the two-dimensional MSD of cells both in the resting and in the flowing (centered) scenario. For robustness, the MSD is averaged over all tracked cells belonging to the same class. Despite the similarity of the single cell tracks of both cases, the MSD instantly reveals striking differences (see Fig. 3.19). While in the short time scale and length-scale regime the slopes of both classes are very similar, as soon as displacements beyond one cell area are examined, only the flowing cells show a slope close to 1 (the value expected for perfectly diffusive motion) in the log-log plot. On the same time scales, the cells from the resting tissue show clear subdiffusive behavior and even over a time of ten hours do not significantly translocate farther than one cell length. This indicates that in a regular confluent monolayer, the bonds between individual cells are strong enough that rearrangements, such as two cells switching position, rarely transpire. In contrast, when all cells are already in motion due to a present collective migration in a preferential direction, tissue remodeling is significantly easier. Thus, in this case the individual cells are not as tied to their local position in the cell sheet and can perform what is effectively a random walk over a distance amounting to several cell lengths. By fitting a persistent random walk (Fürth's formula, Eq. 3.7) model to the MSD data, a

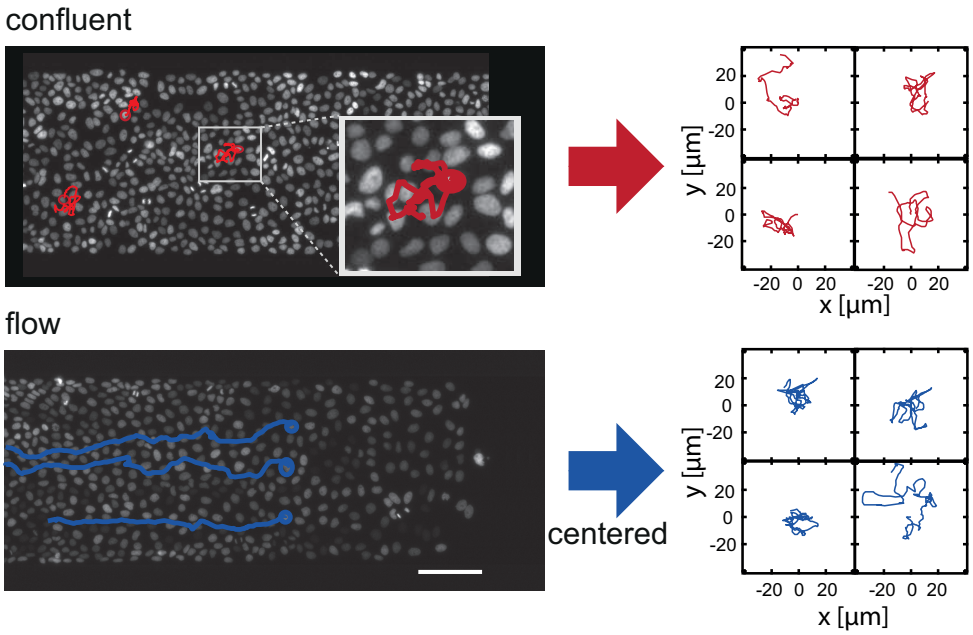

Figure 3.18: Tracks of the motion of individual cells within the sheet with and without flow. Representative tracks obtained by following cell nuclei are depicted on the right hand side, with cells from the flowing sheets centered in x-direction by subtraction of one constant velocity from all time points. Tracks from both classes of cells look qualitatively similar, with variations between cells of the same class appearing equally large. Adapted with permission from reference [63]. Copyright 2014 Elsevier B.V.

self-diffusion coefficient of $D_{\text{flow}} = 25.3 \pm 0.1 \, \frac{\mu\text{m}^2}{\text{h}}$ is obtained.

$$\langle x^2 \rangle = 4D \cdot \left(t - T_p \cdot \left(1 - e^{-\frac{t}{T_p}} \right) \right) \tag{3.7}$$

The obtained persistence time is on the order of 0, however, and a straight random walk fit results in the same diffusion coefficient, indicating that the contribution of persistence to the random walk does not account for a significant part of the cells' motion. The diffusion coefficient is nearly twice as high as the coefficient received for the confluent case, $D_{\text{confluent}} = 13.7 \pm 0.1 \, \frac{\mu\text{m}^2}{\text{h}}$, indicating that cells move around much more in this case. However, this value needs to be taken with considerable care, as it is obtained by fitting a persistent random walk model to data that is clearly subdiffusive in nature. The resulting fit thus does a poor job of capturing the qualitative features seen in the MSD values for the confluent data. In contrast, D_{flow} is the result of a fit that captures the qualitative behavior of the data it is supposed to model. The obtained value is of particular noteworthiness for two reasons. Firstly, it is two order of magnitudes smaller than the collective diffusion coefficient $D_c = 1150 \pm 120 \, \frac{\mu\text{m}^2}{\text{h}}$. It is not to be expected that the resulting values for single cell diffusion and collective diffusion would be similar, as this

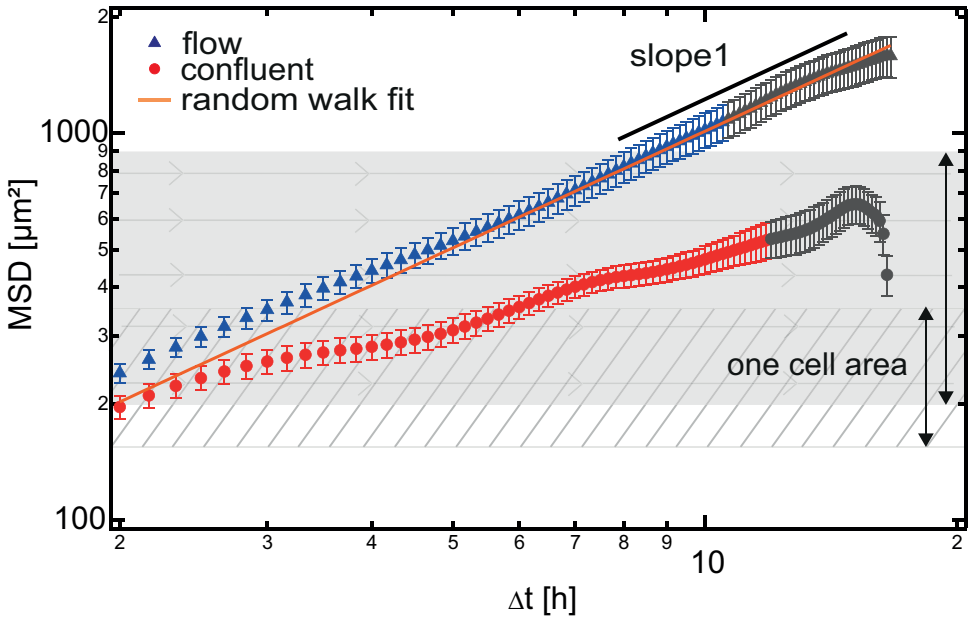

Figure 3.19: MSD of cells under flow (centered) and in confluent layers. Whereas the cells in sheets migrating in a preferential direction show diffusive behavior even on long time scales (slope 1 *black line* drawn for comparison), the cells in the resting layers behave in a strikingly subdiffusive way except at very short time scales. This becomes increasingly apparent for areas above the approximate area of one cell (indicated by the *hatched area* for the resting cells and the *shaded box* for the directionally migrating cells). A random walk fit (orange line) agrees well with the values measured for flow (there are some deviations at the very short time scales, but due to the nature of the log plot this is comparatively small fraction of the time looks exaggerated). The grayed out areas of the MSD curves indicate the points where the standard deviation of the individual measurements has reached 90% (with flow) and 70% (without flow) of the depicted mean values. In particular due to cell divisions, few cells can be tracked over sufficiently long time scales that they can contribute to these sections of the curves, rendering the obtained MSD values increasingly less reliable for high times. Error bars indicate standard errors. Adapted with permission from reference [63].

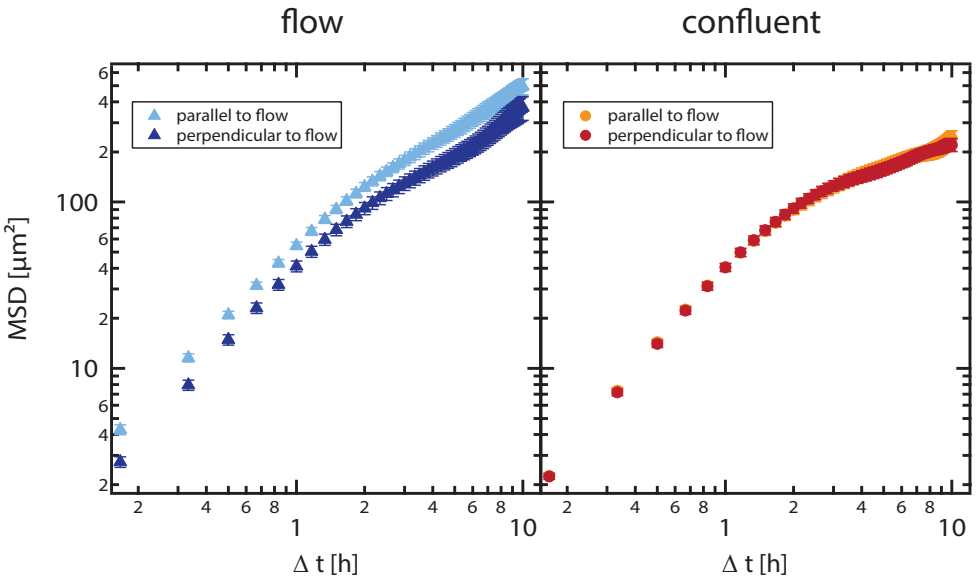

Figure 3.20: MSD analysis split in x- and y-direction, parallel and perpendicular to flow, respectively. In the case with a preferential migration direction (*blue triangles*), the MSD parallel to this direction appears to be higher than perpendicular to it. In contrast, for the resting cells (*red circles*), there appears to be no such effect. Error bars indicate standard errors.

would only be the case if there were no interactions between the cells. The significantly higher collective diffusion coefficient confirms the cooperative behavior present in the system. Secondly, the found value of $25\,\frac{\mu m^2}{h}$ agrees well with the value Angelini et al. obtained from studying the dynamic structure factor of a confluent MDCK monolayer at zero density ($D_{max} = 30 \pm 4\,\frac{\mu m^2}{h}$) [38]. While the density of the migrating monolayer is not zero in reality, the difference in diffusive behavior between the confluent and the flowing case observed in our experiments hints at the cells in the flowing sheet being less confined by their neighbors. Thus, this presence of the global migration might act as an effective reduction in the density the cells "feel" from their neighbors, letting the diffusivity approach the theoretical value for no density.

An interesting question arises as to the similarity of the MSDs in both cases (confluent and flowing) for short time scales (roughly the first 2.5 h). Given that in the long term the differences in motion are as pronounced as they are, the fact that the slope is nearly identical for short times indicates that this MSD does not describe actual cell locomotion. Instead, it is likely that at these short time scales the MSD captures features such as fluctuations of the nuclei position within the cell, or cell shape fluctuations that result in minor fluctuations of the nucleus position, the latter of which happens on time scales comparable to 1 h [38].

In addition to just examining the two dimensional MSD, it is also possible to separate it into its contributions coming from motion in x-direction (parallel to the channel walls) and y-direction (perpendicular to the channel walls). For cells in flowing cell sheets, the parallel component seems to contribute 1.4 times more strongly than the perpendicular component, whereas no significant difference is observed in the resting cells. It is, however, impossible to rule out that this is an artifact resulting from the centering routine performed on the cell tracks from the directionally migrating sheet. If the effect is real, it would imply that cells can glide past each other more easily parallel to the direction of motion, as opposed to perpendicular to it, which makes for an interesting notion.

3.1.6 Discussion

In summary, studying the flow of cells confined to channels from a hydrodynamic perspective leads to intriguing results. In contrast to the classical parabolic flow profile found according to Hagen-Poissueille's law for a Newtonian liquid in a pipe, migrating cell sheets develop a very flat, plug-flow like profile. The cells move at roughly the same speed independent of their distance to the wall up until roughly the two cell layers immediately proximate to the boundary. Unlike for a laminarly flowing fluid, however, the discrete-sized cells cannot be divided into infinitely thin lamina flowing at different speeds and exerting a shear force on one another. Unless the cells are torn apart, it is impossible for one part of the cell to move at a different speed than another part of the cell for a prolonged period of time. While for short time periods this would be possible by deformation of the cell, eventually the cells' elasticity would no longer be sufficient. Thus, for sustained collective flow through a channel, even if the channel walls were to represent perfect no-slip boundary conditions, the outermost cell layer would still be left with a nonzero velocity, which we indeed find in our experiments. Here, the speed of the cells proximal to the wall drops to roughly half the speed of the cells in the center of the channel.

A deeper investigation taking into account the cells' area density throughout the channel reveals that the shape of the density profile eventually reaches a steady state and is then only moved along the channel at a constant velocity in traveling wave like manner. The shape of the density profile is well-described by the solution of the Fisher-Kolmogorov equation, the simplest reaction-diffusion equation containing diffusive balancing out of a density gradient and cell proliferation by logistic growth. While it recovers the shape, the Fisher-Kolmogorov equation is insufficient to reproduce the profile's time evolution. In order to successfully capture the dynamics, an underlying density-independent drift of a

constant velocity needs to be added on top of the mechanism that balances out the density gradient in the system. Intriguingly, we find both contributions to be on the same order of magnitude. The underlying mechanism that leads to this macroscopic drift remains unclear. It seems plausible, however, that it could be the same mechanism responsible for the spontaneous occurrence of collective rotation observed in disc-like systems [60, 142], where due to the circular geometry there are no front or back edges, and hence no density gradients. Here, the most likely candidate leading to the rotation is polarization of the cells along the symmetry breaking boundary conditions. The outermost cells do not have an equal probability of polarizing in all directions and thus are more likely to polarize along the boundary. This polarization is then passed on to neighboring cells up to one correlation length, as indicated by the fact that for very large discs, Doxzen et al. observe a breakdown of collective rotation [142]. Transferring this idea to our channel system, symmetry is broken by the boundary walls, thus cells immediately adjacent to them have an increased probability to polarize parallel to the direction of migration. Possibly, the fact that there is already a preferential migration direction present due to balancing out the density gradient further biases the preferential polarization direction to align towards the cell front and away from the bulk. This polarization is then again passed on to neighboring cells as far as one correlation length. In our case, with a measured correlation length on the order of 100 µm, and polarization stemming from two opposing walls, this would imply that this polarization mechanism works well up to channel widths of 200 µm, close to the greatest width of 300 µm used in our experiments. For significantly larger channel widths, up to the limit case of unconfined cell sheets such as in wound healing assays, the contribution of a biased polarization might vanish. This could explain why in such cases, people have found the Fisher-Kolmogorov equation to be an adequate description [149–151] within the accuracy of their measurements. On the other hand, it cannot be ruled out that the confinement by neighboring cells on the side is sufficient to reduce likelihood of polarization in that direction. In this case, polarization would not necessarily be induced by the walls but rather by the fact that cells at the leading edge would have a higher probability of polarizing towards the open area, where they are not confined. Again, this polarization could then couple across multiple cell layers into the sheet. Correspondingly, cells in an expanding monolayer would then be expected to move just as fast as those confined by walls.

Interestingly, the global, long-range flow also seems to alter the short scale noise in our system. Both the MSD of individual cells and the vorticity are good measures of short scale fluctuations in the system. Our study showed that the MSD of single cells within the monolayer is increased under flow, indicating nearly diffusive behavior, as

opposed to the resting monolayers, where cells appear caged by their neighbors and show subdiffusive motion. The remodeling already going on in the tissue when it migrates collectively into one direction seems to facilitate the movement of individuals within this assembly, allowing them to switch places or squeeze by each other. It is worth noting that an increase of the MSD is not a phenomenon unique to migrating cells, but in fact is well known from systems, such as colloidal glasses, that show shear melting [152]. Given other similarities of cell monolayers to glass-like behavior, such as the appearance of dynamic heterogeneities that grow in size as the density increases and other observations evocative of a glass transition [38], it is perhaps not entirely surprising that these initially very different seeming types of systems would have this in common. Very recently, Chepizhko et al. found evidence for unjamming of a monolayer from a glassy state to a fluid state in response to a wound [46], which confirms our findings of cells being more capable of moving around in this situation.

At the same time as the MSD of individual cells increases, the second indicator of short scale fluctuations in our system, the frequency of vortex formation, decreases under flow. It seems unlikely that the simple presence of a preferential migration direction could suppress these bursts of collective rotation. The MSD analysis, however, showed that while cells are relatively caged in the resting case, they are more free to move around in the flowing case. As such, the interpretation that the bursts of collective behavior can also break out of their cages suggests itself. In the resting case, the bursts would be confined to short range rotational movement, as this does not actually require any directional translocation of the cells. Under flow, however, these bursts could instead orient themselves along the density gradient and even it out. It is thus likely not the motion of single cells that causes the long range diffusion, but rather bursts of correlated short scale active migration of parts of the cell sheet. A confirmation of this theory is to some extent given by examining the obtained correlation length $l_c = 80\,\mu\text{m}$ and correlation time $t_c = 1.1\,\text{h}$ of coordinated migration. Interpreted as diffusing quasi-particles, these random bursts of coordinated motion would yield a diffusion coefficient of $D_{\text{burst}} = l^2/4t_c = 1500\,\frac{\mu\text{m}^2}{\text{h}}$, in good agreement with the measured collective diffusion coefficient of $D_c = 1200\,\frac{\mu\text{m}^2}{\text{h}}$. The presence of such active bursts in collective cell migration has recently been observed by Chepizhko et al. for a variety of cell lines, though intriguingly, they find a distribution of length of these clusters of coordinated activity that covers several orders of magnitude (10^0 to 10^3) [1]. Hence, bursts of collective activity truly exist in collective cell migration, as they do in many externally driven glassy systems [153], lending credibility to the notion that they are responsible for the balancing out of the density gradient with the observed collective diffusion coefficient. With the bursts of collective activity displaying a wide range of

length scales, it is possible that D_c is actually an effective diffusion coefficient resulting from surges on different length scales.

Our results thus indicate that collective cell migration shows bursts of motion of cell mass that, depending on the confinement of the cells, either is more rotational or more directed in nature. Strikingly, Vedula et al. also find the disappearance of vorticity and the emergence of a new contraction-elongation type of movement when they confine the cells even farther on strips with a width of roughly one cell diameter, giving a further hint at the fact that the boundary conditions can change the behavior and directionality of the coordinated movement of collectively migrating epithelial cell sheets [37].

The rich phenomena that already emerge from a simple experiment of confinement in channels lend credibility to the notion that the tools available for microstructuring of surfaces are ideal for creating experimental conditions reminiscent of classical hydrodynamic investigations. In addition, these initial successes also arouse interest in the phenomena cells might exhibit when placed into other, more complicated geometries known from classical fluid experiments, vindicating the notion of cellular hydrodynamics as a legitimate phenomenological approach to studying collective cell migration.

3.2 Alignment of cell division axis in directed epithelial cell migration

In the previous section, cell migration in channels was described using an analytically solvable continuum model. We found that three components contribute to the collective migration of cells: a diffusion-like part that attempts to balance out density gradients together with the second contribution, the proliferation of cells, and finally a constant, underlying drift (possibly directed migration due to alignment of cell polarization). Cell divisions clearly play an important role in the overall behavior, considering the balancing out of the density gradient had to be described by the Fisher-Kolmogorov equation, which includes a reaction term for cell proliferation in addition to "pure" diffusion. In this section, which deals with the contents of publication P3, we examine cell division events in migrating epithelial sheets [65]. In particular, as tensile stresses apply to cells in collective cell migration and these affect cell shape and polarity, the orientation of cell divisions is predicted to correlate with the cellular flow pattern. The orientation of the cell division axis plays a vital role, both in maintaining tissue functionality over time and in embryogenesis. For instance, oriented cell division has been shown to be capable of controlling shape changes during tissue developments, such as the development of the imaginal disks of the fruit fly *Drosophila melanogaster* [154]. An understanding of cell division orientation is therefore essential.

Thus, using the experimental setup from the previous section, we investigated the degree of the orientation of the cell division axis in directed channel invasion and compare it to the degree of orientation in the "resting" case where there is no preferential migration direction. We compare the experimental results to simulations performed with a previously published [105, 124, 125], particle-based model (for details see section 2.5.3). Fig 3.21 shows an overview over the experimental setup and the simulation.

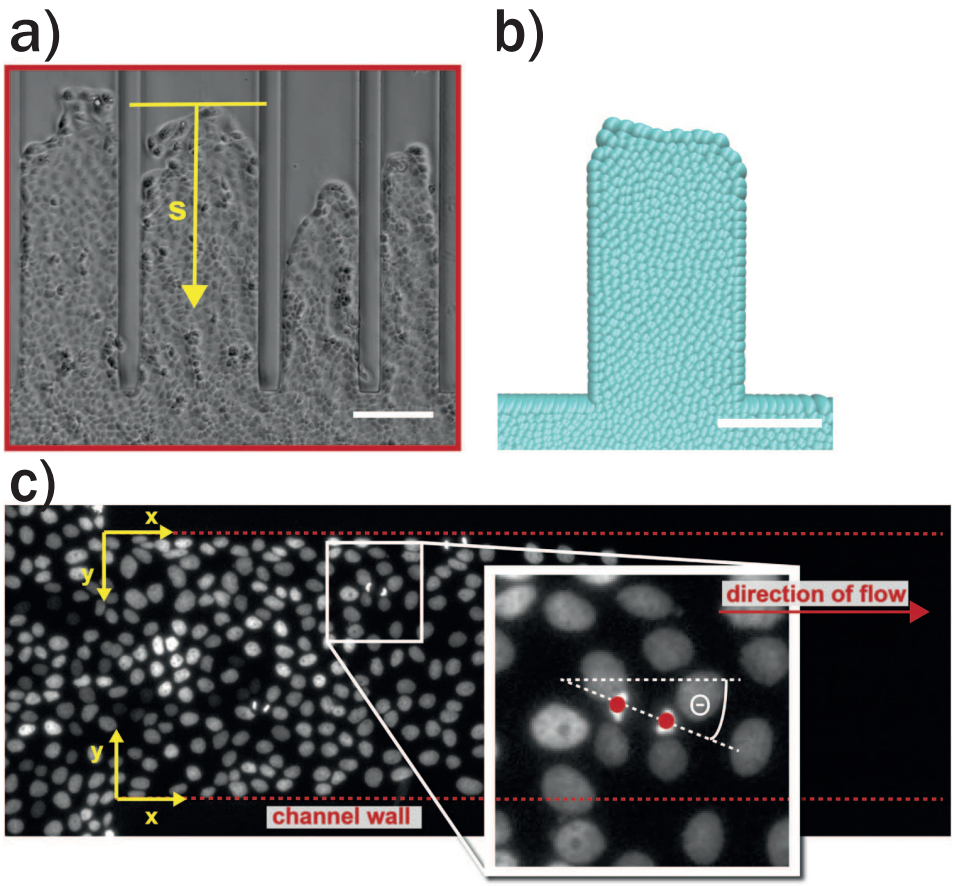

Figure 3.21: Collective migration into channels in experiment and simulation. **a)** As in publication P2, MDCK cells are confined to PEG-DMA channels of different widths [63]. The coordinate s measures the distance to the front. **b)** Computer simulation of expansion into microchannels using a particle-based approach. **c)** Fluorescence image of labeled nuclei used for detection of division events with the drawn vectors illustrating the used coordinate system. The x-coordinate runs parallel to the channel walls from the entrance to the front, while y denotes the distance to the wall. The cell division axis **d** is defined as the vector connecting the nuclei of two daughter cells in the first frame after the division. The orientation of this axis compared to the x-direction of the channel is denoted by the angle θ. Scale bars correspond to 200 µm. Reprinted from reference [65] within the framework of Creative Commons Attribution 3.0 license.

3.2.1 Flow and density profiles in the model

In order to confirm the chosen model's applicability to our experimental system, in a first step the simulated data is compared to the experimental data concerning several key phenomenological features observed in chapter 3.1 (see Fig. 3.22). In particular, we find a constant, channel-width independent invasion velocity, in good agreement with the experiment. For the velocity profiles, simulation yields a perfect plug-flow across the channel, which matches experimental data except for the behavior at the boundary. In addition, the velocity profile along the channel shows the same behavior of speed increasing towards the cell front that was found in the experiment. Likewise, the yielded density profile matches the experimental one. Given the good agreement between both the shapes of the density profile and the constant invasion velocity in experiment and theory, they are used as units of measure to rescale the simulation to physical units.

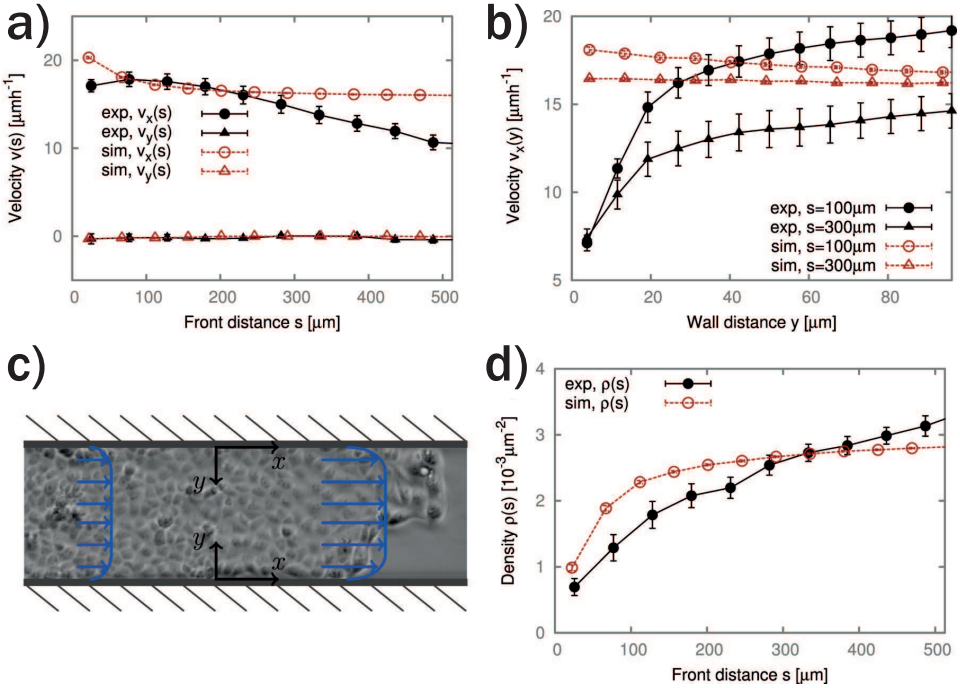

Figure 3.22: Flow profiles and density distribution in experiment and simulation. **a)** Velocity v_x resulting from PIV analysis as a function of the distance to the front. The values from the simulation of the particle-based model show the same general trend. **b)** Velocity as a function of the distance to the wall y for different distances to the front s. The experimental data shows the decrease previously discussed in chapter 3.1 with decreasing distance to the wall. The simulated data on the other hand shows a perfect plug flow. **c)** Illustration of the velocity profile at various distances to the front. **d)** Profile of the cell density ρ. The simulated data agrees well with the shape of the experimental profile already discussed in chapter 3.1. All plots result from averages over ten measurements. Reprinted from reference [65] within the framework of Creative Commons Attribution 3.0 license.

All in all, good agreement is found between the data from simulation and experiment on a phenomenological level. This is a good indication that the chosen model is in principle applicable. The discrepancies in the flow profile at the boundaries, however, suggests that the model works best for the bulk of the cell sheet and it is worth paying particular attention to the behavior at boundaries in the following analysis.

3.2.2 Orientation of the cell division axis with respect to global flow

With the model deemed principally in agreement with the experiment, it is feasible to also use it to study cell divisions. The first question we ask is to what extent the orientation of the division axes of all cell divisions are affected by a global flow. To this end, the axes of all individual cell divisions in the experimental data are determined manually from the position of the two daughter cells in the first frame after their appearance. Their orientation is described by the angle θ between the axis and the x-direction of the channel (see Fig. 3.21c) or by a unit vector $\mathbf{d}$. As the cell division axis is mirror symmetric, the orientation is characterized well by the nematic order tensor $\mathbf{Q}_{ij}$ (see Eq. 3.8), more typically known from liquid crystals.

$$Q_{ij} = 2d_i d_j - \delta_{ij} \tag{3.8}$$

Here, i and j represent the spatial directions. In particular, we can describe the order of one orientation ($\mathbf{a}$) relative to another ($\mathbf{b}$) by a simpler, scalar quantity:

$$S_b^a = 2(\mathbf{a} \cdot \mathbf{b})^2 - 1 \tag{3.9}$$

We want to study the order of the division axes with respect to the global flow. Considering that in publication P2 we found that the average flow in the experimental system is oriented parallel to the channel [63], we can simply take the x-axis of the channel to represent the orientation of the global flow. Thus, we examine the order of the cell division axes with respect to this channel axis:

$$S_x^d = e_x \mathbf{Q} e_x = 2\langle cos^2\theta \rangle - 1 \tag{3.10}$$

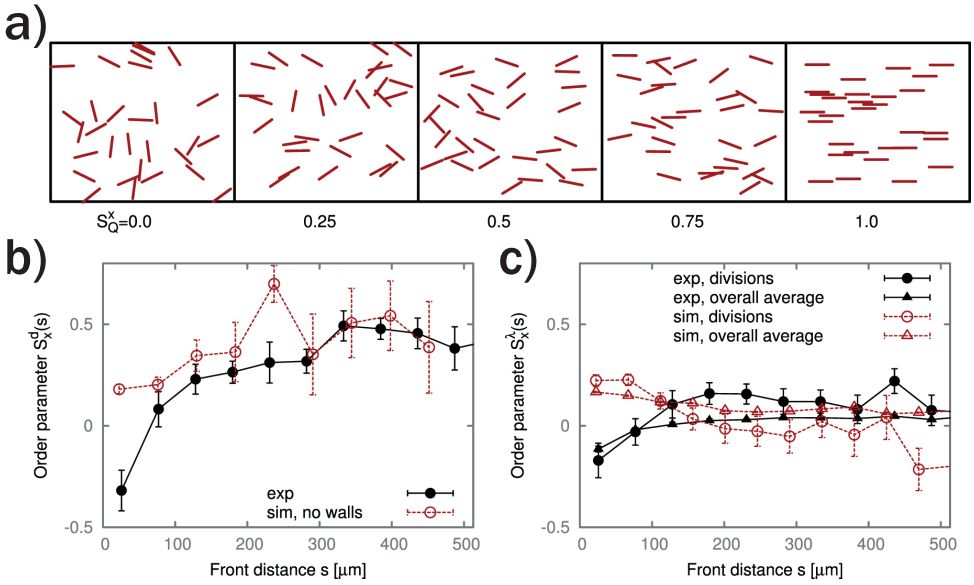

Figure 3.23: Order of the division axis in cell sheets invading channels with preferential migration direction. **a)** Examples of order parameter for illustrative purposes. S^d_x indicates no order (isotropic), while S^d_x signifies absolute alignment of the cell division axis with the x-axis. **b)** Order parameter S^d_x, indicating orientation of the cell division axis with respect to the x-axis, as a function of the distance to the front s. For the simulation values, cells closer than 42 µm to the wall were excluded. The simulation quantitatively reproduces the experimental data, though it deviates close to the cell front. **c)** Order parameter S^λ_x, capturing the orientation of the eigenvector of the greatest eigenvalue of the velocity gradient tensor with respect to the x-axis, as a function of the distance to the front s. The order is examined both for all positions and only for sites of cell division. No correlation is found for the overall average, but there is a weak correlation at the division sites. Again, the simulation agrees well with the experimental behavior in the bulk, but differs near the front. All plots result from averages over ten experiments. Reprinted from reference [65] within the framework of Creative Commons Attribution 3.0 license.

While $S_x^d = 0$ describes isotropy, $S_x^d = 1$ represents perfect alignment of the two chosen axes (see Fig 3.23a for illustration of what degree of order different values represent). Over most of the cell sheet, we find significant alignment (order in the range of $S_x^d = 0.2$ to 0.5) of the cell division axes with the x-axis in the experimental data (see Fig 3.23b). Upon drawing closer to the leading edge, however, the order parameter begins to drop, even reaching negative values, which represent an alignment of the orientation axis perpendicular to the channel. Movies of the experiments confirm this behavior. The correlation length in fingers of MDCK cells has been determined to be 200 µm [28], so we expect cells further than these 200 µm behind the front to be unaffected by border instabilities. Everything falling beyond this cutoff is thus defined as the "bulk" of the cell sheet. This definition, made independently of any of our own measurements, accurately excludes the range of distances to the cell front where we find the order parameter S_x^d to drop below 0.2, with divisions in the bulk showing good alignment with the x-axis.

The simulation shows the same qualitative behavior, though deviations are found at the boundaries (both at the channel walls and the leading edge). Given that the model was already incapable of correctly reproducing the flow profile at the boundaries, this is not unexpected. Excluding the division of particles closer to the wall than 42 µm from the evaluation of the simulation data even yields quantitative agreement of the dimensionless order parameter (see Fig 3.23b).

In order to confirm that this alignment is really caused by the presence of a global flow and not an artifact of the channel walls influencing the orientation of cell divisions, we used the data from the experiments where cells were seeded uniformly throughout the channels and have no preferential migration direction (for details see chapter 3.1). Simulations were performed to mimic these conditions. As the values for the order parameter S_x^d demonstrate (see Fig. 3.24), both experiment and simulation show no order in the bulk of the sheet. The experimental data, however, reveals nearly perfect alignment with the PEG-DMA walls close to these boundaries, while the simulated data remains isotropic. The decay of alignment with increasing distance to the wall for the empirical data is well described by:

$$S_x^d = exp\left(-\frac{y - y_0}{\xi}\right) + S_0 \tag{3.11}$$

The resulting fit yields a minimal distance to the wall of $y_0 = 6.2 \pm 0.7\,\mu m$, a nearly isotropic average order $S_0 = -0.04 \pm 0.02$ and a decay length of $\xi = 6.7 \pm 1.3\,\mu m$ for

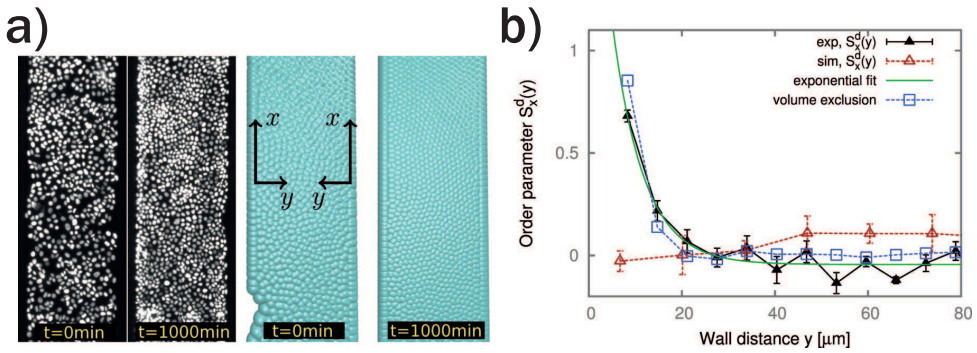

Figure 3.24: Order of the cell division axis in sheets without preferential migration direction. **a)** Cell division and velocities are tracked for confluent monolayers that do not migrate collectively in a preferred direction. The two pictures show an early and a late time point of experiment and simulation, respectively. The density starts at $2.6 \times 10^{-3}\,\frac{1}{\mu m^2}$ for t=0 min and reaches $4.4 \times 10^{-3}\,\frac{1}{\mu m^2}$ at $t = 1000$ min for both cases. **b)** Order parameter S_x^d capturing the degree of alignment between the division axis and the x-axis for the confluent cell sheet, in dependence on the distance to the wall. The simulation data shows isotropic behavior (S_x^d around 0) over the entire width, whereas the experimental data only follows this behavior in the bulk, but shows parallel alignment close to the walls ($S_x^d = 1$ would indicate perfect parallel alignment, $S_x^d = -1$ perfect perpendicular alignment to the wall). A simple volume exclusion simulation reproduces the shape of the experimental data. The plot is the result of averaging over the whole channel length and seven experiments. Reprinted from reference [65] within the framework of Creative Commons Attribution 3.0 license.

the order, which corresponds to one cell layer or less. The straightforward assumption that cell divisions are entirely random under constraint is supported by the success of a simple volume exclusion model in reproducing the experimentally observed behavior. When center of mass positions and division angles are drawn from uniform distributions, with all events where the line connecting the two daughter cells (distance set to a fixed value of 16 µm) intersects the wall discarded, the resulting order agrees well with the experimental data. It thus stands to reason that the observed alignment with the channel wall is simply a result of a decreased range of possible orientations for the division axis when the dividing cell is too close to the wall. As shown in the supplement of publication P3, such an alignment is also seen in the presence of a global flow, though it is less pronounced [65]. Taking the observations from the resting monolayers into account, we deduce that the strong alignment seen in invading cell sheets is indeed caused by the global orientation of the flow, and not by the presence of the boundaries.

While a value of 0.5 for the order parameter already indicates good alignment of the division axes with the global flow, it is not high enough that it rules out other contributing factors that could play a role in aligning the axis of a cell division in the sheet. We thus investigate the question of whether stresses in the monolayer could be responsible for orienting cell divisions. While no direct stress measurements were performed in the expe-

riments, it is known in principle that a tensile stress is built up in collectively migrating cell sheets [39, 70, 82]. In addition, in fluids (including most complex fluids) the stress tensor is directly proportional to the strain rate tensor, which can be calculated from the derivatives of the velocities according to Eq. 3.12.

$$E_{ij} = \frac{1}{2}\left(\frac{dv_i}{dx_j} + \frac{dv_j}{dx_i}\right) \tag{3.12}$$

It describes the deformation rates in all directions at each point. We designate the direction of the largest extensile (or least contractile) flow as the "main axis". This direction is given by the eigenvector λ associated with the larger eigenvalue λ_1. We also define the difference between λ_1 and λ_2 (the smaller eigenvalue) as the dipole strength $p = \lambda_1 - \lambda_2$, in analogy to a force dipol. It is indicative of the asymmetry of the flow gradient. On the other hand, the sum of the eigenvalues gives the divergence of the flow. Examining the orientation of the main axis with respect to the x-axis, we find isotropic order (see Fig. 3.23c for values of the order parameter S_x^λ). At the points of division, a weak correlation between the two axes appears. In the bulk of the cell sheet, the simulations agree with the experiment, showing no correlation between λ and the x-axis, though the trend of higher correlation for the points of division is not confirmed. Close to the front, however, the results of experiment and simulation diverge. While in the experiment λ follows the trend of the cell division axes and aligns perpendicular to the channel walls ($S_x^\lambda < 0$), the simulation actually shows increased order compared to the x-axis.

3.2.3 Orientation of the cell division axis with respect to local flow

The previous section clearly showed the presence of alignment of the cell division axes with the orientation of global flow, however, cells have no known mechanism for sensing long-range parameters. Thus, something other than the global flow field should arguably be responsible for the division axes' orientation. In this section, a possible underlying cause is investigated by analyzing the correlation between the division axes and various local variables.

Examination of the relationship between local velocity vectors and the orientation of cell divisions rules out assumptions of flow aligning the division axis. Most strikingly, the degree of alignment of division axes with the x-axis and v_x show opposite behaviors for increasing distance to the front of the cell sheet (the velocity decreases, whereas the order

increases). In a quantified manner, the order between the local velocity vector and the division axes is on average 0.16 ± 0.014 with directed migration present, and 0.06 ± 0.014 without (errors indicate standard deviation of mean). These values, smaller than the correlations found with the global flow, are interpreted as results of both local velocity and cell divisions on average being oriented with the x-axis, so sharing a common cause rather than actually depending on each other.

Local flow being ruled out does not, however, preclude the possibility of local flow gradients orienting the cell division axes. This idea is supported by the fact that it has been shown in literature that mechanical stresses orient cell divisions [155] and this is actually a necessity for explaining fluidization of tissue due to cellular divisions [105]. In order to investigate the relationship between orientation of the division axes and local flow gradients, the average order of divisions with the direction of the flow gradients is calculated:

$$S_\lambda^d = 2\langle cos\Phi \rangle - 1 \tag{3.13}$$

Here, Φ defines the angle between the division axis and the eigenvector corresponding to the strain rate tensor's largest eigenvalue (see inset in Fig. 3.25b). The resulting average value of $S_\lambda^d = 0.29 \pm 0.02$ shows a clear correlation in cell sheets with a preferential migration direction. Reinforcing this notion of correlation between cell division axes and local flow gradient, we find that the degree of alignment scales linearly with the asymmetry of the flow gradient (see Fig. 3.25), as quantified by the dipolar strength (i.e. the difference between the strain rate tensor's largest and smallest eigenvalue). While in the absence of a preferential migration direction for the cell sheet the alignment between flow gradient and division axis is smaller ($S_\lambda^d = 0.15 \pm 0.02$), the found alignment is twice as large as with the local flow velocity both for the resting and the migrating case. This result is in good agreement with the simulations, which show an even more pronounced alignment of division axes with the local flow gradient, independent of global flow.

Detailed analysis of the local velocity field shows a discrepancy in the divergence at the site of divisions. While in experiments these events are overall contractile ($\langle div(v) \rangle = -0.10\,\frac{1}{\mathrm{h}}$ with a preferential migration direction, $\langle div(v) \rangle = -0.11\,\frac{1}{\mathrm{h}}$ without), in simulations they are extensile ($\langle div(v) \rangle = 0.06\,\frac{1}{\mathrm{h}}$ with preferential migration direction, $\langle div(v) \rangle = 0.04\,\frac{1}{\mathrm{h}}$ without). Both for experiments and simulations, however, the fluctuations are large ($\sigma = 0.34\,\frac{1}{\mathrm{h}}$ and $\sigma = 0.27\,\frac{1}{\mathrm{h}}$, respectively). It is worth noting that the overall flow field in

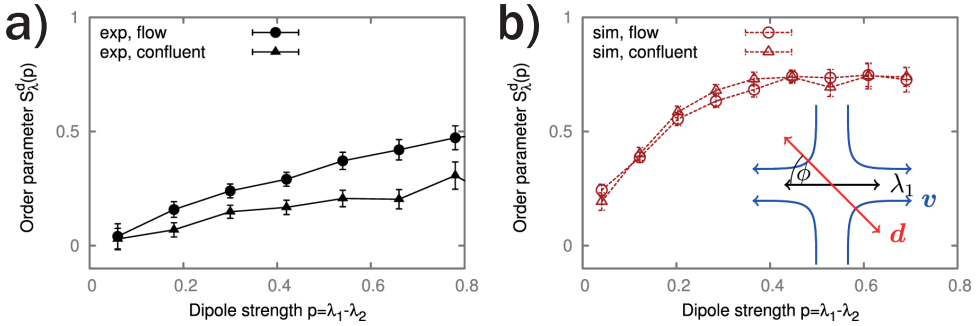

Figure 3.25: Alignment of cell divisions with local flow gradients in experiment and simulation, in dependence on the dipolar strength $p = \lambda_1 - \lambda_2$, a measure for the asymmetry of the local flow gradient. **a)** A clear correlation between divisions and the strain rate tensor is found in invading sheets in the experiment. A less pronounced correlation is also present for the confluently plated cells. A seemingly linear dependence of the alignment on the dipolar strength is observed. **b)** In the simulations, the alignment with the local flow gradient is even stronger, independently of the presence or absence of a global flow. The inset shows a sketch of a division axis and a velocity field, along with its corresponding eigenvector. The plots are averages consisting of ten and seven experiments, for the flowing and the confluent case, respectively. Reprinted from reference [65] within the framework of Creative Commons Attribution 3.0 license.

the bulk in experiments showed positive divergence in the presence of a global flow (see Fig. 3.22), and divergence close to zero for the confluently plated cells. Furthermore, while an excluded area larger than the cell size for calculation of the derivative avoids taking into account directed motion within the dividing cell, it is still possible that the fact that cells round up at the moment of division biases the results. A more detailed study of the flow gradients along the cells' trajectory prior to the division would allow investigation of the growth and orientation phase

In contrast to the divergence, the dipole moment is positive both for experiment and simulation data. We found $\langle \partial_\parallel v_\parallel - \partial_\perp v_\perp \rangle = 0.16\,\frac{1}{\mathrm{h}}$, $\sigma = 0.36\,\frac{1}{\mathrm{h}}$ in the experiments with a preferential migration direction, and, in good, even quantitative agreement, $\langle \partial_\parallel v_\parallel - \partial_\perp v_\perp \rangle = 0.15\,\frac{1}{\mathrm{h}}$, $\sigma = 0.33\,\frac{1}{\mathrm{h}}$ in the corresponding simulations. Without the preferential migration direction, agreement between experiment and simulation is only qualitative ($\langle \partial_\parallel v_\parallel - \partial_\perp v_\perp \rangle = 0.07\,\frac{1}{\mathrm{h}}$, $\sigma = 0.38\,\frac{1}{\mathrm{h}}$) and $\langle \partial_\parallel v_\parallel - \partial_\perp v_\perp \rangle = 0.16\,\frac{1}{\mathrm{h}}$, $\sigma = 0.24\,\frac{1}{\mathrm{h}}$, respectively).

3.2.4 Discussion

In conclusion, the results of this section show the effect of an underlying global migration direction on the orientation of the cell division axes in collective invasion of MDCK cells into PEG-DMA channels. The correlation of flow fields and cell division events yielded

quantitative insight into the motion of cell sheets. Strong alignment is present between the orientation of the division axes and the underlying migration direction. To confirm the global flow as the cause, a control experiment was performed with the same cells seeded uniformly into PEG-DMA microchannels. In this quasi-resting scenario, the cell division axis is oriented randomly, ruling out boundary effects of the walls and confirming the hypothesis of a preferential migration direction as the major cause of orientation.

With cells unable to sense global quantities such as underlying flow, the relationship between the division axes' orientation and local quantities was investigated. The best correlation exists between the axes' orientation and local flow gradients. Specifically, the average order between the division axes' orientation and the strain rate tensor's main axis is twice that between division axes and the local flow direction. This agrees well with the hypothesis that stresses in the migrating cell sheet are proportional to the velocity gradient, and these stresses subsequently orient the cell divisions.

Most of the experimental results agreed well with simulations based on a previously published particle model [105, 124, 125]. In this model, cells are represented by two particles that repel each other in order to grow. This results in the intrinsic, oriented feedback between growth and mechanics necessary to study rheology of three-dimensional tissues, the model's original purpose. Without any further modifications, this model was sufficient to reproduce viscoelastic properties of tissue spheroids [105] and describe their growth [156, 157]. Even with the model later on extended by a simple motility algorithm in order to understand certain phenomena of growing motile tissues (such as fingering instabilities at the front of the cell sheet), it was never meant to study divisional orientation. Thus, the agreement between the experiment and the computer simulations in many phenomena is particularly noteworthy. Specifically, the simulations showed the same characteristic cell number density profile, similar velocity profiles both along and across the channels, and strong correlations between the main axis of the strain rate tensor and the orientation of the division axes. Despite this good agreement, discrepancies between experiment and simulations were found near boundaries (both at the leading edge of the cell sheet and the channel walls). It is clear that the model would need to be extended in order to achieve a better agreement here. For instance, it might be necessary to describe cells by more than two particles in order to capture their deformability and complex interior structure, both of which could play an important role for the dynamics close to interfaces. Of course, such a change would complicate the model and likely increase the necessary computational resources.

On the experimental side, the current setup can easily be adapted to other adherent cell lines (e.g. MCF10A) in order to investigate the universality of the discovered results. More intriguingly, there is no reason that the orientation mechanism for the cell division axes should not work in three dimensions. Confirming this with the help of motility experiments extended into three dimensions, an adaption not without significant challenges, would be highly intriguing. Such an investigation would be aided by the fact that the particle-based simulations are already inherently three-dimensional and would require little adjustment.

How the cell division axis is oriented in migrating tissues continues to be of interest due to the role it could play in wound healing and development. Our experiments showed that expanding tissue will orient individual cell divisions in the direction of growth, thus reducing principal stress. While it makes sense for them to do so, it would be of particular interest to see if these results hold up in *in vivo* experiments, both in 2D and 3D, or if cell divisions show a different behavior in these cases.

3.3 Collective cell migration through a constricted channel

In the previous two chapters of this thesis, collective migration of cells in a straight channel was studied in detail. In particular, the motion of the cell sheet was related to that of a fluid. Despite the success of this approach, cell monolayers at high densities display glass-like dynamics (for more details see section 2.4), with increasing cell density leading to lower velocities but also increased regions of cooperative movement [38]. This raises the question, how it is possible that cell collectives can be both fluid-like and solid? Recently, one attempted explanation has risen to prominence, in which the answer to this dilemma is given by jamming of the monolayer [41]: The notion here is that the dynamics of the monolayer are constrained by several physical factors that also dominate the behavior of other condensed systems, such as foams or groups of colloidal particles. These factors include, among others, volume exclusion, size, deformability, mutual crowding and adhesion. Thus, depending on these factors, a monolayer might find itself at different points on a phase diagram in different situations, being more solid-like when density and thus crowding is higher, and more fluid-like when the opposite is the case.

Relating this notion back to biology, it would make sense for a monolayer to be in a jammed state naturally, when it functions primarily as a barrier, but then unjam when necessary, such as in order to collectively migrate for wound healing [41, 46, 82]. Conversely, this jamming phenomenon also seems to play a crucial role in the other direction, in the case of cancer invasion. For quite some time, collective invasion phenotypes have been known to occur in at least some types of cancers, such as melanoma and rhabdomyosarcoma [76, 158]. Recent results, however, suggest the collective migration mode of mesenchymal cells in confined environments likely occurs as a consequence of being jammed [22]. This further highlights how important the microenvironment really is to cell migration, which is in agreement with other recent findings [18, 159]. In particular, it is noteworthy that collective cell migration *in vivo* does often occur in confinement [36], and that frequently this confinement is sufficient to induce jamming. Specifically, in 3D environments this is the case when cells follow the path of least resistance through present tracks, which are either the result of proteolytic activity of a leader cell [160, 161] or simply preexisting *in vivo* [162, 163].

Live-cell imaging *in vivo* can be problematic, however, between high intensities causing

damage to the living systems and two-photon processes not necessarily penetrating far enough into the tissue to see everything of interest. In addition, the environment the cells migrate in under such circumstances cannot really be characterized well, which makes understanding the observed behavior complicated. Thus, artificial systems mimicking confinement are good alternatives, and particularly for 2D migration, a lot of work has been performed in that direction. The simplest approach to confining collective cell migration is straight stripes, as already discussed in chapter 3.1. On such geometries, Vedula et al. found the emergence of an entirely new contraction-elongation type of migration when the cells were confined to particularly narrow channels [37]. Though a density gradient develops over the length of the channel in such systems [63], they are not particularly ideal for studying the notion of jamming. More promising towards this goal are geometries from the work of Yang et al. [164], where the cells migrate on converging and diverging stripes. Though their goal in these experiments was to study the effect of leader cells in cell migration, their geometries still force cells to encounter regions where they gradually have less room available and the monolayer could thus potentially be jammed (converging stripes) or where there is gradually more area available and cells might become less jammed (diverging stripes). These experiments result in velocity profiles with maximum velocity at the front of the cell sheet and a decrease further back independent of the geometry. They do find higher (lower) velocities in general for the converging (diverging) stripes compared to the straight reference, explaining this with the change in leader cell density. This behavior has in principle been reproduced with a particle-based model with Viscek-type orientational interactions by Tarle et al. [165]. It is of particular note, however, that even though the model is specifically constructed with a curvature-dependent motility feedback that allows the formation of leader cells [166], these are not the driving reason behind the velocity difference for straight, converging and diverging channels. Instead, Tarle et al. find that the different velocities in all three scenarios are mainly driven by the Bernoulli effect (see chapter 2.3.4), as a consequence of mass conservation.

This raises an interesting question, however, from a more physical perspective: To what extent can an active cellular flow be expected to follow a classical liquid theory that obeys Bernoulli's principle, when over long time periods proliferation breaks mass conservation and remodeling of cells into 3D can mimic compressibility? In particular, if the notion of jamming in high density regimes is correct, the behavior of collectively migrating cells can be expected to deviate strongly from that of a Newtonian liquid if the confinement induces areas of high densities.

To this extent, this chapter deals with the collective migration of epithelial cell sheets

through a channel that includes a constriction, mimicking another experiment from classical hydrodynamics. In these experiments, MCF10A cell sheets migrate into an initially straight channel, eventually encounter a constriction to pass through, before reemerging into the original channel width. The central question posed is how the flow profile for this system deviates from what would be expected from a Newtonian fluid. This would simply be a constant flux as a result of mass conservation, and thus a higher flow velocity in the constriction compared to both before and after it.

In contrast, several factors are likely to contribute to the velocity profile of cell layers in this system: First of all, our results in the straight channels and the findings of other groups in various scenarios, show that migrating cell sheets exhibit a gradient in velocity, with maximal velocity at the front, which decreases further back [18, 63, 164]. Thus the monolayer is already expected to display a gradient in velocity simply in the straight part of the channel before the constriction. Secondly, the presence of a constriction can be expected to cause the cells to become backed up, as more cells arrive than can continue progressing through the constriction, which would lead to a build-up of density at its entrance. Following previous results [38], this increased density would lead to a decrease in velocity. Thirdly, such a build up in density would break the previously present density gradient. The balancing out of this gradient by bursts of collective cell migration was found to be one of the main contributions to the forward motion of the migrating cell sheets (see chapter 3.1), so this gradient vanishing, or potentially even being temporarily reversed in parts of the monolayer could have significant consequences on the overall motion. Due to the intriguing behavior each of these effects on its own could have, observing the result of their interplay on the velocity profile is particularly interesting.

In an attempt to understand the mechanisms underlying the observed behavior, experimental results are compared to an active isotropic-nematic mixture model. This type of continuous media based approach typically work well on scales significantly above that of the individual constituent agents that are not explicitly accounted for. As even the smallest constriction used in this thesis was chosen so as to still allow several cells to pass through it in parallel, this, coarse-grained model should ideally be capable of reproducing the experimental results and provide some insight into them.

In summary, this chapter investigates the collective migration of an epithelial cell sheet through a constricted channel, comparing experiment and theory. Particular interest is placed on how the jamming prior to the constriction influences the velocity profile, and how this resulting profile for a cellular flow without mass conservation deviates from that

of a Newtonian fluid governed by the Bernoulli effect and mass conservation.

3.3.1 Evolution of the cell front

In order to investigate the effect of a constriction on collective cell migration, human mammary epithelial cells (MCF10A) are confined to 300 µm wide channels with various constriction geometries via micromolding in capillaries (see section A.1.1). All channels are created in such a way that cell sheets have a distance of 600 µm to cross in a straight channel, before the environment begins confining. Length and diameter of this constricted area, as well as abruptness of how quickly the channel constricts to its minimal width were varied in an attempt to answer different questions about the resulting velocity profile. In principle, constriction widths ranging from 100 µm (i.e. 1/3 of the initial channel width) to 300 µm (i.e. no constriction at all, for reference) were used. The length of constrictions, defined as the segment where the channel is at minimal width without the transition areas before and afterward, was varied from 50 µm to 700 µm. The transition area in which the channel shrinks from its maximal width to the minimal constriction width (and after the constriction, expands again to the initial width) was set to either 300 µm or 500 µm.

The process of cells invading into the channels as a connected monolayer is studied by time-lapse phase-contrast microscopy (see Fig. 3.26). Compared to the MDCK cells used in chapter 3.1, the MCF10A cells migrate slightly less collectively in this experimental setup, with occasionally an individual cell (or a small group of cells) detaching from the cell collective at the front and migrating individually.

As this makes an automated detection of the cell front analogous to chapter 3.1 problematic, the evolution of the cell front over time is only evaluated exemplarily, by manual tracking. Fig. 3.27 shows the evolution of the front position for measurements of one particular constriction geometry and a straight, unconfined channel as reference. Again, quite some variance can be seen between individual measurements. In principle, however, cell sheets seem to progress linearly through the channels both with constriction and without constriction (when ignoring the occasional sharp drops in the position of the cell front which correspond to detachments at the front of the sheet). There is no clear effect of the constriction, in the sense that the evolution of the front position shows no difference in slope before, during or after passing through the constriction. Likewise, when comparing the evolution of the front position for the constricted and the unconstricted channel, the differences between individual measurements for each case are as large as the differences

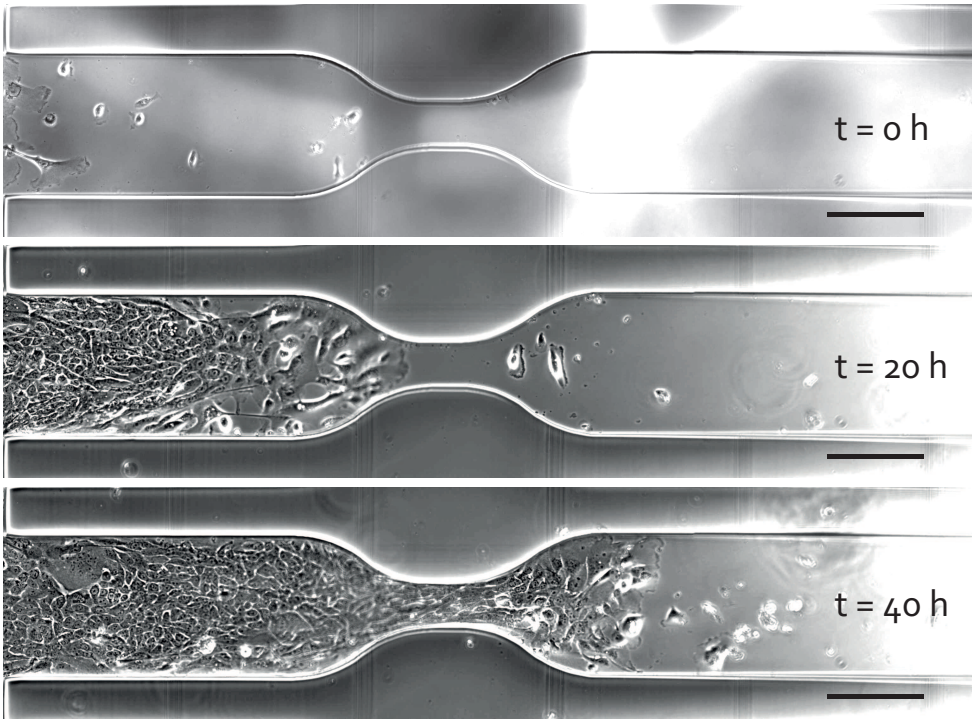

Figure 3.26: Time series of MCF10A cells collectively migrating through a constriction in a channel. Cells enter the channel and migrate as a sheet towards the constriction, which they have to squeeze through to progress. Once they reach the other side, the cells expand once more. Halos in illumination at early time point result from condensation on sample lid during temperature equilibration at the beginning of an experiment. Scale bar corresponds to 200 µm.

between both measurements and there is no systematic trend. Thus, it can be concluded that the front of the cell sheet moves through the constriction relatively uninfluenced, neither speeding up nor slowing down.

This makes it even more intriguing to analyze the entire velocity profile over the whole channel, however. A Newtonian fluid flowing through a constriction speeds up in the narrow part so that a constant flux can be achieved. If the cell sheet does not do so, as the data indicates, there are two options: Either cells have to be tightly compressed as they flow through the constriction so that the cell flux density remains constant throughout the channel, which seems unlikely, or the flux of cells arriving at the entrance of the constriction is higher than the flux of cells being transported away. In this case, cells necessarily need to back up prior to the constriction, causing an increase in density and potentially entering a jamming regime.

In addition to the position of the front, the evolution of the shape of the front is also interesting, but even harder to analyze systematically. Fig. 3.28 shows one representative

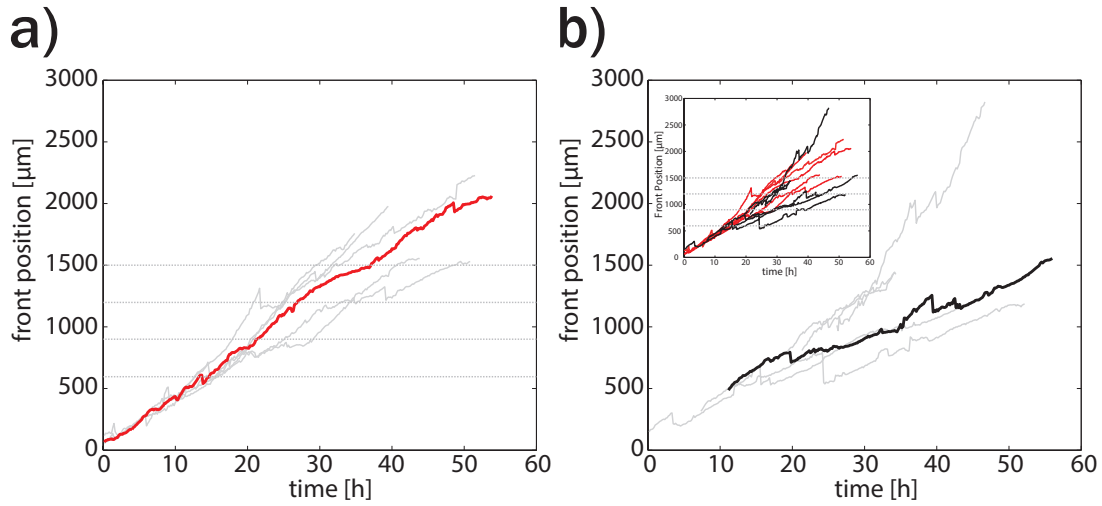

Figure 3.27: Evolution of the position of the cell front over time. **a)** Position of the cell front over time for different channels with the same constriction. Each individual channel is depicted as a gray curve, one of which is highlighted in red for ease of viewing. The horizontal lines indicate the position of the constriction (from bottom to top: position where channel begins constricting, position where channel reaches minimal width, position where channel begins expanding, position where channel reaches maximum width). No systematic effect of the constriction upon the velocity of the front is observed. The curves display characteristic buckling where the position of the front rapidly drops to a lower value when an individual cell or a small group of cells tear off from the front of the sheet. **b)** For comparison, the evolution of the cell front position for unconstricted channels of the same width as depicted in a) is shown. All curves from both graphs are overlayed in the inset (red with constriction, black without), again highlighting that there is no clear effect of a constriction being present.

individual measurement of migration through constricted channel (corresponding to the geometry also depicted in Fig. 3.27a). The contour of the cell front was traced manually every four hours. As is common in collective cell migration, the leading edge is rough when the front is in the 300 µm wide sections (prior to or after the constriction). While passing through the 100 µm narrow constriction, the cell front is much smoother, as there is much less room for it to actually become rough. In the initial period after passing through the constriction, the cells seem to spread along the channel boundary (i.e. the cell sheet covers the entire channel width). This would be in agreement with the results seen by Tarle et al., who briefly qualitatively examined the emergence of a cell monolayer from a constriction and find highly anisotropic invasion into a wide region mostly perpendicular to the previous migration direction, guided by curvature induced leader cells [165]. This would not necessarily need to be the case in the experiments presented here, as the curvature at the exit of their constriction is much higher than the smoother exit here. It is of note, however, that as the migration of the cell sheet further into the region of maximal width is examined, the monolayers in the experiments of this thesis frequently do not keep in contact with the boundaries, but rather progressed in a narrower finger that does not span the entire width of the channel.

While the evolution of the front shape shown in Fig. 3.28 is representative of the generally observed development, studying its behavior in more detail would require a more systematic evaluation. As this is a whole additional question, this analysis was not performed as part of this thesis. Though this might well be of interest in future work, the example presented here is only intended to give a general impression of how a cell sheet migrates through the constricted channel and does not claim to be a complete description.

3.3.2 Influx at channel entrance

Prior to a detailed analysis of the flow field for cell sheets migrating through channels with constrictions, it makes sense to briefly examine the boundary conditions in an attempt to understand the source of the cell sheet's migration. What the driving component behind the monolayer's expansion is, plays a major role in understanding what is actually happening when it encounters a constriction, and it is also essential when attempting to create a model that does not only reproduce the experimental results, but correctly emulates the underlying process. Specifically, the question for invasion of a channel by a cell sheet is whether the sheet (in the experiments discussed in this thesis) expands primarily due to an influx of cells at the channel entrance, or due to proliferation of cells already inside

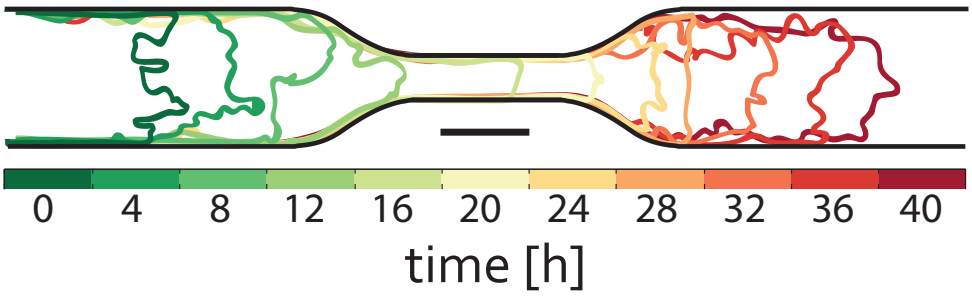

Figure 3.28: Evolution of the shape of the front of a cell sheet invading a constricted channel. The cell sheet's contour was traced manually every four hours, and is depicted with a color scale going from dark green to dark red. Before the constriction, the cell front is rough, whereas within the narrow constriction it is smoother by necessity. After leaving the choked part of the channel, the cell front roughens once more. Initially, the cells seem to spread along the boundaries, but eventually, the sheet moves forward in a narrower finger that does not cover the entire width of the channel. Scale bar corresponds to 200 µm

the channel, or due to some combination of both. Naturally, in the beginning, when no cells are yet inside of the channel, the dominant mechanism has to be an influx from the outside reservoir, but it is possible a transition occurs once enough cells have entered that the contribution from proliferation becomes dominant. One big reason why this difference is relevant is that a constant influx from the channel entrance presumably has the same effect throughout the cell sheet, whereas proliferation occurring throughout the channel at a similar rate would affect different areas of the sheet in different ways. Specifically, cells far from the front would have few cell divisions behind them that would push them forwards, whereas cells close to the front would be pushed by the sum of all cell divisions in the full length of the sheet behind them. This would be a possible explanation for why higher velocities were observed in chapter 3.1 the closer one got to the front of the sheet.

With only the phase-contrast images of the invading cell sheets available, it is much harder to answer this question than it might be with, for instance, a fluorescence image of the nuclei. This would allow easy cell number counting for proliferation measurement, as well as tracking of individual cells within the layer and thus easy counting of how many cells actually enter the channel, as we did in the supporting information of publication P2 to show the cell influx depended linearly on the channel width [63]. While the experiments in that publication are not identical to the experiments in this chapter (the cell line is different, the invasion into channels was studied over a shorter distance, and the channels had no constriction), they offer a first reference point. For the MDCK cells in those experiments, for 300 µm wide channels, the cell influx at the channel entrance was determined to be roughly $J_{\text{Influx}} = 12\,\frac{1}{\text{h}}$, while the cell growth rate was measured at $\lambda = 0.0283\,\frac{1}{\text{h}}$.

With this growth rate, assuming exponential growth according to $N(t) = N_0 \exp(\lambda t)$, $N_0 = 418$ cells need to be already present in the channel in order for proliferation to produce 12 new cells in one hour (and thus match the influx at the channel entrance). Due to the density gradient that forms in expanding monolayers, it is hard to estimate an exact density, but for a rough approximation, $c = 0.003 \frac{\text{cells}}{\mu\text{m}^2}$ is assumed from Fig. 3.10. If the cell sheet uniformly assumed this density while invading 300 µm wide channels, an MDCK monolayer would need to penetrate 464 µm into them for this many cells to be present in the channel. This distance is less than the 600 µm before the channels in this chapter even begin to constrict. Thus, within the framework of this very rough approximation, before the cell sheet enters the constriction, influx at the channel entrance and proliferation are contributing new cells at an equal rate. The cell influx at the channel remains roughly constant, however, while the contribution from proliferation continues to increase as more and more cells fill the channel.

The presence of the constriction changes things, however, both for the influx and for cell proliferation. If the previous notion that cells back up at the entrance to the constriction is correct, the density here will increase. Thus there will initially be more cells and proliferation will contribute even more strongly than it otherwise would for the same depth of invasion into the channels, unless the density increases so much that cells in the backed up region become affected by contact inhibition of proliferation. In that case the proliferation contribution would be lower than the total number of cells in the channel would suggest.

Likewise, there are some clues as to changes in the influx behavior at the nozzle entrance as well, as highlighted exemplarily in Fig. 3.29. The figure shows kymographs at the channel entrance (one in the center of the channel and one closer to each of the channel walls) that extend the first 100 µm into the channel (for the data set also shown in Fig. 3.28). In contrast to the situation when using cells with fluorescently labeled nuclei, a quantitative evaluation of the cell influx is not possible from these kymographs, however, the features can still give some qualitative information about the influx behavior: The part of the images corresponding to early time points are dominated by lines tilted diagonally from top left to lower right (at a relatively shallow angle), which corresponds to dark or light features in the image moving along the kymograph lines in positive x-direction (i.e. into the channel) over time. The parts of the image corresponding to later time points, however, are lines that curve back and forth, which indicates that the noticeable features are not moving into the channel consistently, but rather back and forth along the lines over which the kymograph was taken. This indicates that while early in the measurement,

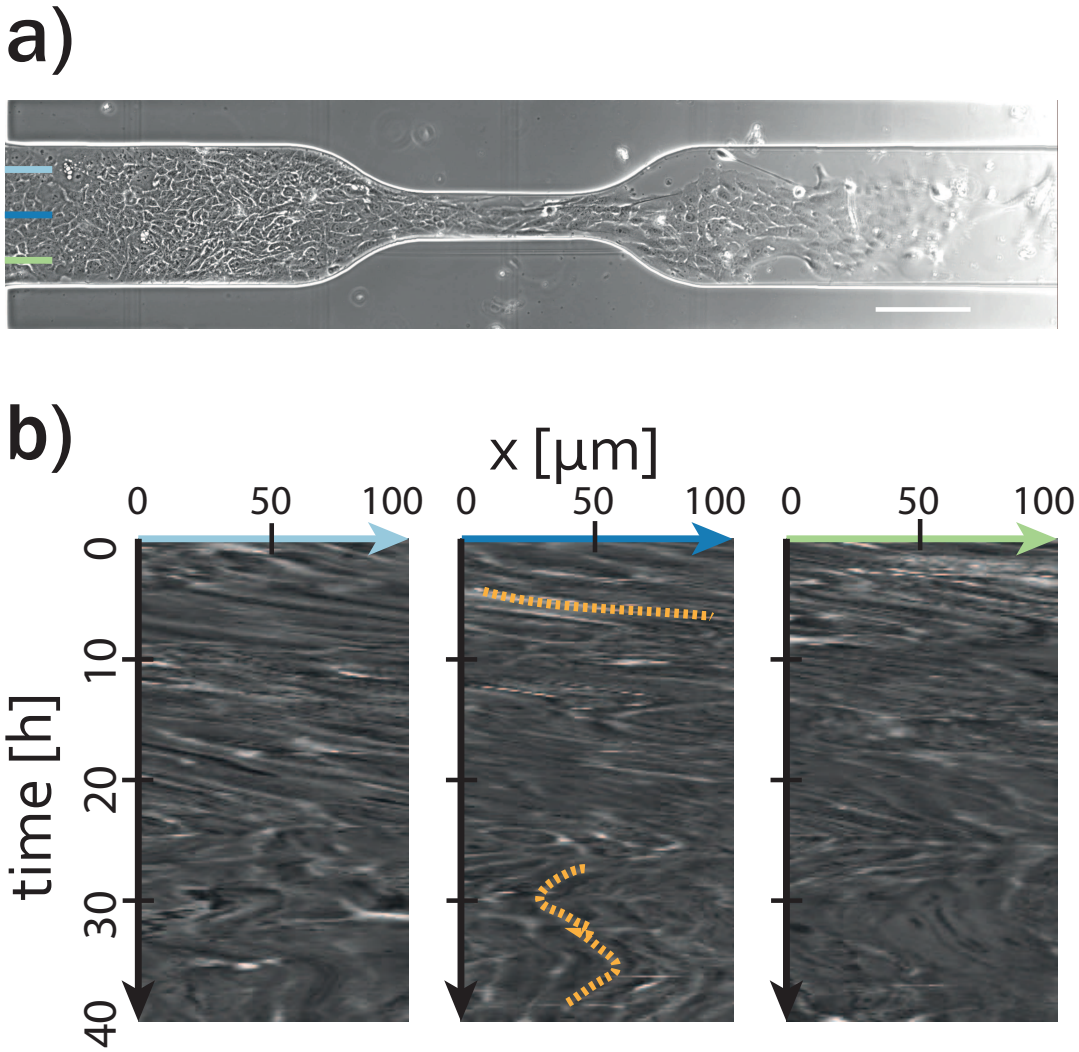

Figure 3.29: Influx of cells into the channel. **a)** Phase-contrast image of a late time point from the data set shown in Fig. 3.28. The influx is examined along one pixel wide lines of 100 µm length, at the channel entrance. Their exact position is marked by the light blue, dark blue and green line (drawn wider than one pixel for visibility purposes). **b)** Kymographs along the three lines shown in a). At early time points, the behavior both in the middle and at the edge is dominated by sloped lines from top left to bottom right, as indicated by the top orange line traced along one of these prominent features. This corresponds to dark or light regions associated with cells and their boundaries moving along the lines shown in a), and thus cells flowing into the channel. At late time points, starting around 25 h this behavior changes, and the dominant features in the kymograph become lines that curve back and forth, as highlighted by the second orange curve. This time roughly corresponds to the cell front emerging from the constriction for this particular data set, as seen in Fig. 3.28.

when the cell sheet is still moving in the part of the channel prior to the constriction, influx into the channel is occurring as expected. Later on, however, which at least for this particular measured channel corresponds roughly to the point where the cell sheet has emerged from the constriction, there is no real positive net flux into the channel, or it is at least reduced compared to early on. A possible interpretation is that the influx into the channel stops once cells have backed up outside of the entrance to the constriction to a sufficient degree (potentially once they have backed up enough that the density gradient between the channel entrance and the entrance to the constriction has balanced out).

All in all, a deeper investigation of influx and proliferation in this specific experimental system is likely necessary for future work. The above rough approximation of how far the cells likely would have to migrate into the channel before proliferation starts outperforming the influx, and the fact that the kymographs suggest the influx slows down as time progresses and the cell sheet penetrates farther into the channel, however, suggest that proliferation is the dominant component driving migration into the channel by the time the cell sheet emerges from the constriction. Likely, it is already the more dominant part when the cell sheet enters the narrowing part of the channel .

3.3.3 Flow field analysis

In order to answer the central question as to the effect of the constriction on the velocity profile, a more detailed analysis of the cell sheet's flow field is necessary. To this extent, PIV is performed between successive frames of the time-lapse sequence as detailed in appendix A.2.1. One example of a resulting velocity field can be seen in Fig. 3.30. Though the majority of velocity vectors are roughly pointing in positive x-direction, as is to be expected, on short scales there can also be more complex behavior, as highlighted in the magnified regions.

Given the large area spanned by the data and the resolution of the PIV analysis, it is hard to make out any detail just examining the velocity field, unless specific regions are magnified. This is convenient for a closer study of certain subsections of the field, but not practical for a general overview. To this end, Fig. 3.31 shows heatmaps depicting the magnitudes of the x-component of the velocity and the absolute velocity. Intriguingly, domains form where v_x takes negative values. After the constriction, this is perhaps less surprising, as the cell sheet does not fill the entire width, and thus there is space available where the groups of cells at the edges can "curve back". In front of the constriction,

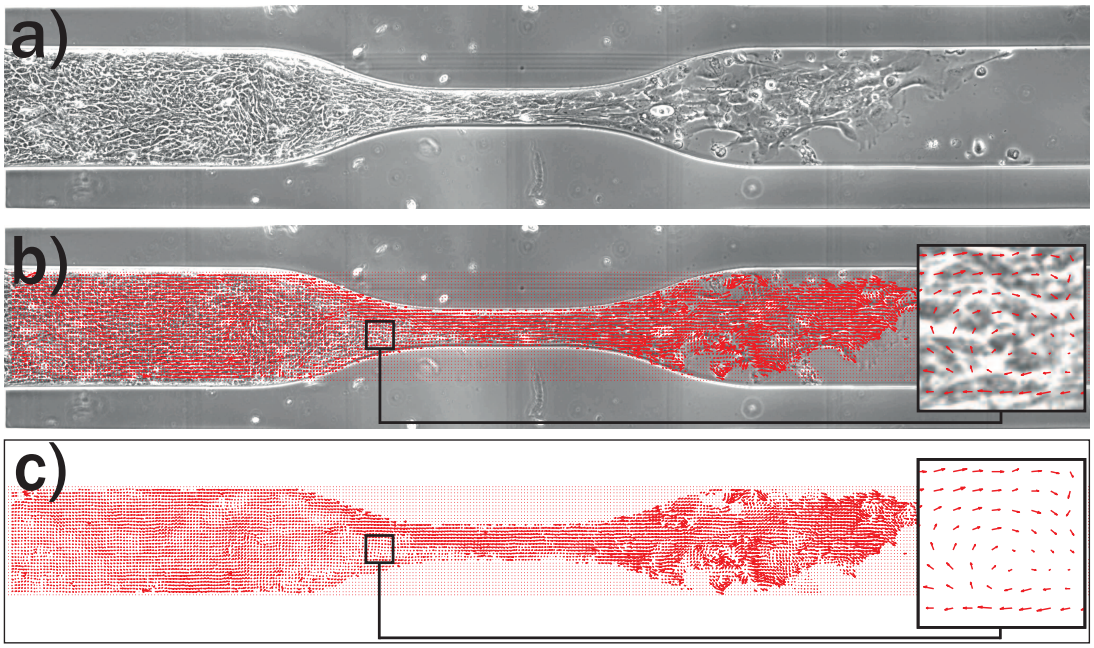

Figure 3.30: PIV analysis and resulting velocity fields. **a)** A representative phase-contrast image taken as input for the PIV analysis. **b)** The same image with the velocity field resulting from the pixel wise cross-correlation of successive images performed by the PIV analysis overlaid on top. **c)** For ease of viewing, the vector field is shown without the underlying phase-contrast image.

however, a large domain has developed in the depicted example along the bottom edge of the narrowing segment, where cells run back towards the channel entrance. This is just a snapshot of a single moment, and this behavior is not expected to be stable. In fact, in addition to the inherent asymmetry of cells moving in the opposite direction along the top narrowing wall, cells farther back along the bottom wall are moving forward. If the cells towards the back are moving forward, and the cells farther forward are moving backwards, this would lead to an accumulation and thus a higher cell density somewhere in between. Since part of the expansion of the monolayer in this experiment is due to balancing out of density gradients, eventually this density gradient along the bottom wall would become large enough to reverse the flow towards the forwards direction again. Purely speculatively, it is possible that at that point the flow along the constriction entrance at the top part of the channel would reverse, causing a build up of a stronger density gradient there, while the one at the bottom is balanced out.

The other thing that immediately becomes apparent, especially when examining the heatmap of the absolute values of velocities, is that the cell sheet moves faster in and after the constriction than prior to it. This already shows a first difference to how a Newtonian fluid following mass conservation would behave. While an increase in velocity within the

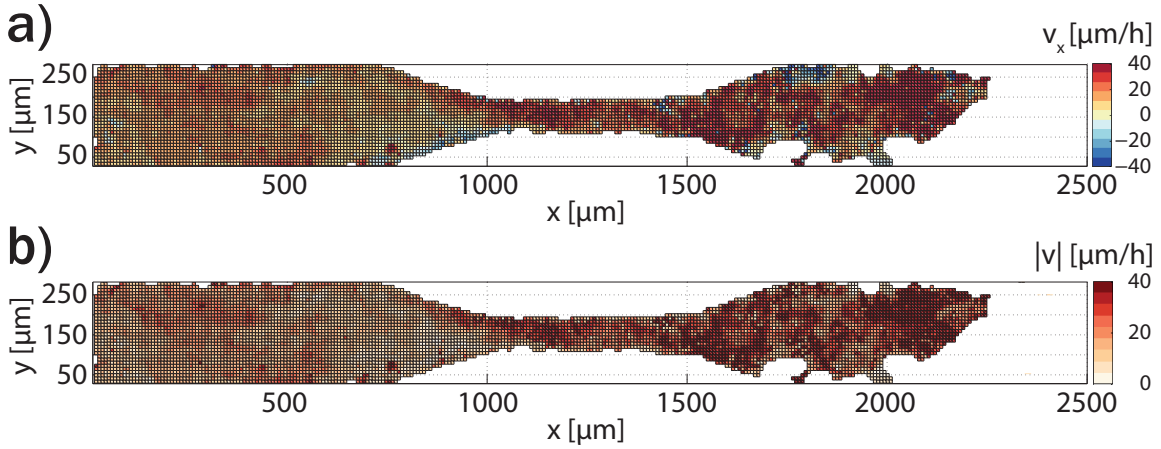

Figure 3.31: Heatmap corresponding to the PIV field shown in Fig. 3.30. **a)** Heatmap indicating the magnitude of the x-component of the velocity (i.e. parallel to the channel). Intriguingly, some small domains of backflow (blue regions) seem to form. **b)** Heatmap indicating the absolute magnitude of the velocity. Immediately, it becomes apparent that the velocities before the constriction are lower than inside, but not than after it.

constriction is consistent, Bernoulli's principle dictates a decrease in the velocity once the fluid returns to the original width, which does not appear to be the case here. This will become even more apparent later in a more precise quantification of the flow profile and will be discussed in more detail at that point. It is intriguing to see, however, that there does appear to be a jamming effect due to an increase of cell density prior to the constriction, leading to a decreased velocity in that region.

As learned in the previous work on straight channels (see chapter 3.1), the velocity profiles can be smoothed via time averaging and coarse-graining, removing short scale noise and making general trends of the flow behavior more readily apparent. At the same time, this noise can be used to quantify the characteristic time and length scales of the system by examining how it changes during this smoothing process. Fig. 3.32 shows the effect on the velocity field of averaging over two different time scales, whereas Fig. 3.33 respectively shows this for coarse-graining on two different scales. In both cases, the variance of the velocity component perpendicular to the channel (representing the short scale fluctuations in the system) is plotted against the respective averaging parameter in analogy to chapter 3.1. Here, however, the variance is examined not over the whole channel but separated into three regions: prior to, in and after the constriction. Strikingly, the variance is highest after the constriction and lowest prior to the constriction. The fact that the lowest variance is found before the constriction might simply be a result of the velocities being lower there in general. In contrast, high velocities were found both inside and after the constriction, but the variance of the perpendicular velocity component is

much higher in the latter of the two regimes. It follows that the cells flowing through the narrow constriction are more limited in their movement perpendicular to the channel, as they are jammed in by the many neighbors who are all moving through the thin passage simultaneously. In contrast, after the constriction, the cell sheet does not even fill the entire width of the channel. Thus cells are much less confined, allowing ample opportunity for movements perpendicular to the general direction of motion.

Independent of the examined region, the variance decreases both for temporal and spatial averaging. To extract the characteristic time and length scales, exponential decays are fitted to each curve and the degree of averaging required for the variance to drop to $1/e$ of its original value determined. For the time averaging, the resulting correlation times range from $\tau_{\text{corr}} = 2.23\,\text{h}$ before the constriction, over $\tau_{\text{corr}} = 1.50\,\text{h}$ in the constriction to $\tau_{\text{corr}} = 0.86\,\text{h}$ after the constriction. This would be in agreement with the cells at higher densities being jammed and correlations increasing as a consequence. For the spatial averaging, resulting correlation lengths range from $\xi_{\text{corr}} = 58\,\mu\text{m}$ before the constriction, over $\xi_{\text{corr}} = 72\,\mu\text{m}$ in the constriction to $\xi_{\text{corr}} = 144\,\mu\text{m}$ after the constriction. This would be exactly contrary to expectations of the higher density increasing correlation lengths, however, these values must also be treated much more carefully than the correlation times. It is relatively straightforward to average over long periods of time and thus achieve a significant reduction of the variance, but in contrast, it is not really feasible to average over length scales much above 60 µm simply due to the diameter of the constriction only being 100 µm. Coarse-graining over that distance still leaves the variance comparatively high, however, and thus the fit of the exponential decay is based on points only on that part of the curve, which makes it much less robust, especially when trying to compare three fits with each other. In an attempt to ensure more equality between the three scenarios, the exponential decays can be forced to go to zero, rather than allowing them a minimal y-offset that might result in a slightly better fit. Doing this for the spatial variance, resulting correlation lengths suddenly only range from $\xi_{\text{corr}} = 82\,\mu\text{m}$ before the constriction, over $\xi_{\text{corr}} = 99\,\mu\text{m}$ in the constriction to $\xi_{\text{corr}} = 110\,\mu\text{m}$ after the constriction, which is hardly any difference at all. In contrast, doing the same for the time averaged curves maintains the trend of a clear difference, with the resulting correlation times ranging from $\tau_{\text{corr}} = 3.47\,\text{h}$ before the constriction, over $\tau_{\text{corr}} = 3.13\,\text{h}$ in the constriction to $\tau_{\text{corr}} = 1.06\,\text{h}$ after the constriction. Given that a loss of spatial resolution in the narrow segments of the channel is impractical, and that coarse-graining only has a very limited effect on smoothing out the flow field, compared to averaging over time, which even performed over very reasonable time scales leads to a significant reduction in the variance of the perpendicular velocity component, it makes sense to refrain from coarse-graining the velocity field prior to further

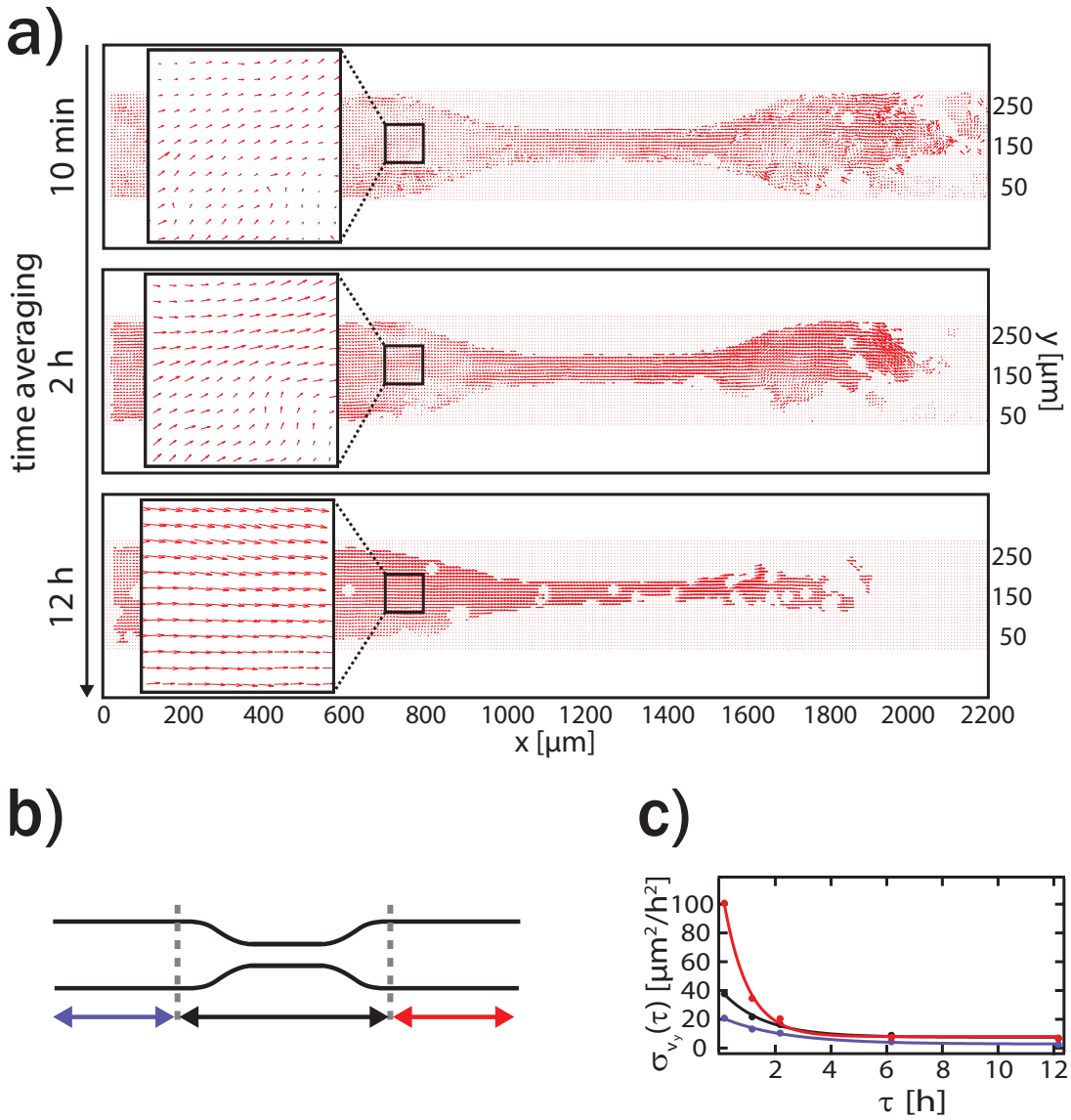

Figure 3.32: Smoothing of velocity field through time averaging. **a)** Velocity fields from PIV analysis, calculated from two subsequent image frames (top), or by averaging over a period of 2 h (middle) or 12 h (bottom). Holes in the velocity field are the results of missing vectors during the averaging step (for details, see appendix A.2.2). The magnified region shows how the noise in the y-component of the velocity is reduced by increased averaging, to the point where the resulting field is very homogeneous. **b)** For quantification of the smoothing, the channel is divided into three regions, as indicated by the blue (before the constriction), the black (inside the constriction) and the red (after the constriction) arrows. **c)** The smoothing is quantified by calculating the variance in the y-component of the velocity field, averaged over the entirety of each subregion defined in b). It is immediately apparent that the variance is much higher after the constriction, where the cell sheet does not necessarily fill out the entire width of the channel and the cell density is much lower than before the constriction, both of which likely leads to less confinement for the cells. Additionally, in all three of the subregions, the variance decreases the more the velocity field was averaged in time prior to determining the variance. Fitting an exponential decay (solid lines) to each of the three curves, a velocity correlation time can be calculated in each case. The resulting values range from $\tau_{\mathrm{corr}} = 2.23\,\mathrm{h}$ before the constriction, over $\tau_{\mathrm{corr}} = 1.50\,\mathrm{h}$ in the constriction to $\tau_{\mathrm{corr}} = 0.86\,\mathrm{h}$ after the constriction. This would be in agreement with both density and confinement increasing correlations.

analysis. Instead, velocity fields will be averaged over 2 h to achieve relatively smooth fields without losing too much information.

3.3.4 The detailed velocity profile

As discussed above, gaining a true understanding of the effect of the constriction on the collectively migrating cell sheet requires a detailed analysis of the velocity profile that develops. For the purpose of comparison to a Newtonian liquid obeying mass conservation, the relevant part of the flow field is that along the channel (as opposed to across the channel). To this end, all velocity profiles in this section are taken by averaging the velocity (either the x-component or the absolute magnitude) from the PIV analysis over the entire channel width for each grid point along the channel. Due to the results from the previous section, PIV flow fields are averaged over two hours prior to this average over the channel width, to smooth out the short scale fluctuations. Finally, the velocity profiles are ensemble-averaged over multiple invaded channels in order to uncover the general behavior inherent to the process. For the purpose of averaging multiple measurements, time points are taken at which each of the sheets had invaded to the same point in the channel (e.g. 250 µm past the constriction).

In order to understand the effect of a constriction on the flow profile of a collectively migrating cell sheet, it is first necessary to understand the effect confinement of different widths has. To this end, Fig. 3.34 shows the flow profile of the velocity component parallel to the channel and the absolute magnitude of velocity for unconstricted channels of different widths when the cell sheets had migrated 1500 µm into them. In agreement with the work on MDCK cells in chapter 3.1 (though on a three times longer length scale), an increase in velocity towards the front of the cell sheet is observed. This behavior is present independently of the width (over the width range studied here). Similarly, like for the MDCK cells, at the very front of the cell sheet the velocity decreases slightly. The fact that this decrease is more pronounced in the x-component of the velocity than in the absolute magnitude shows that part of the reason is that at the monolayer's leading edge it does not fill the entire width of the channel and thus more of the cells' velocity can be diverted perpendicular to the channel than farther back. This does not explain the entire velocity decrease, however. In addition, it seems like the velocity decrease spans a longer distance from the front of the sheet than in previous results, which could be either a consequence of the different cell line used, or the significantly longer distance the cell sheets were allowed to invade into the channels.

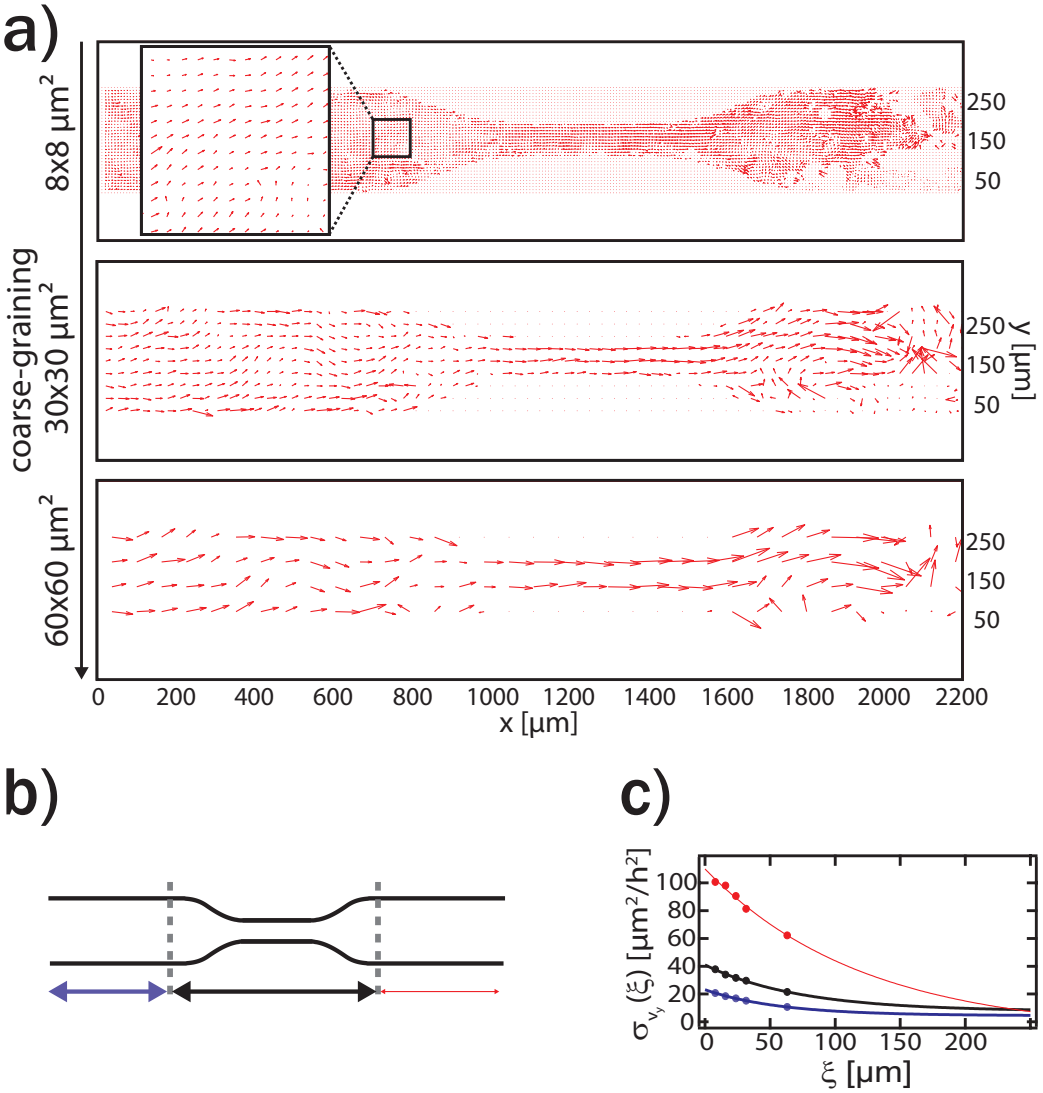

Figure 3.33: Smoothing of velocity field through coarse-graining. **a)** Velocity fields from PIV analysis, calculated from two subsequent image frames at a resolution of $8 \times 8\,\mu m$ (top), or by subsequently larger coarse-graining. **b)** For quantification of the smoothing, the channel is divided into three regions analogous to Fig. 3.32, as indicated by the blue (before the constriction), the black (inside the constriction) and the red (after the constriction) arrows. **c)** The smoothing is quantified by calculating the variance in the y-component of the velocity field, averaged over the entirety of each subregion defined in b). As in Fig. 3.32, the variance is highest for the area after the constriction and decreases with increasing averaging, though the effect is less pronounced. Fitting an exponential decay (solid lines) to each of the three curves, a velocity correlation length can be calculated in each case. The resulting values range from $\xi_{corr} = 58\,\mu m$ before the constriction, over $\xi_{corr} = 72\,\mu m$ in the constriction to $\xi_{corr} = 144\,\mu m$ after the constriction.

For all of the observed widths except for the most narrow channels (100 µm), there seems to be no effect of the size of the confinement, as the velocity profiles are very similar and for the most part overlap within their margins of error. For the 100 µm wide channels, however, a clear difference appears and the velocity seems to be lower over most of the channel length. Interestingly, this difference appears to be less pronounced in v_x than in $|v|$. The velocity profile is also different qualitatively. For an unclear reason, in the narrowest channels, the profile increases stepwise, with intermittent plateaus, somewhat reminiscent of the velocity profiles found by Vedula et al. when they observe a contraction-elongation mode of migration (albeit on even narrower stripes) [37]. It is possible that the mode of migration in these channels changes (or begins to change) compared to the wider channels and the threshold for this change is just at a wider width for MCF10A cells. Of particular note is that over about the first 300 µm, the velocity profiles, especially for x-component of the velocity, do not deviate too strongly from that of wider channels. In addition, the velocity reached by the cell sheet in the narrow channels still reaches up to the same values as the velocity in the wider channels, as these seem to eventually reach a plateau prior to the decay right at the leading edge. Taking all of this into account, the constrictions used in this thesis were limited to a minimal width of 100 µm and, where possible, to a maximal length of 300 µm. Going forward, only velocity profiles for v_x are examined, as this is also where there seems to be less of an effect of just the width of the channel. All of this should ideally prevent the introduction of new modes of migration into the system and allow studying the effect of a constriction on collective cell migration more cleanly. Of course, in the context of cells invading collectively through narrow, pre-existing passages in the body, examining even smaller constrictions where different modes of migration are relevant would also be of interest in potential future work.

With the effect of the size of confinement examined for a straight channel, the next step is to introduce a constriction and study how this changes the velocity profile. Fig. 3.35 compares the profile for the unconstricted channel with those of channels with various constriction diameters ranging all the way down to 100 µm, at the time point when the cell sheets have penetrated 250 µm into the area of maximal width after the constriction (or the equivalent distance for the unconstricted reference). While no clear, systematic difference can be seen between the curves for various constriction diameters, all of them show a clear difference to the profile without constriction. Specifically, the velocity in the straight channel increases from the channel entrance up until it reaches a plateau around $30\,\frac{\mu m}{h}$, whereas the velocity profiles for all of the constricted channels exhibit a plateau immediately from the entrance of the channel until roughly halfway into segment where the channel narrows prior to the constriction. It is only at that point that they begin

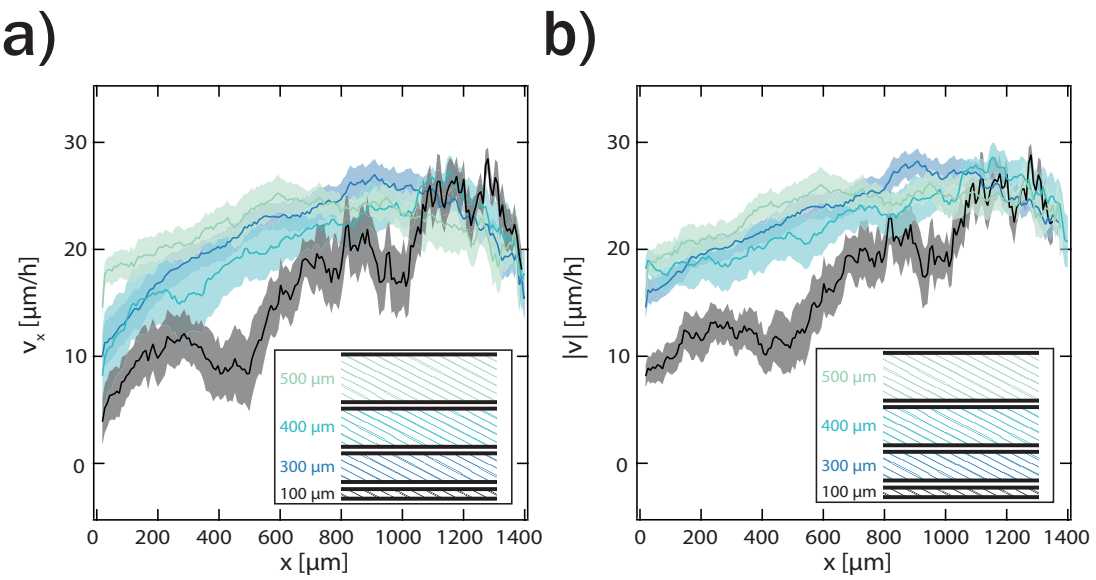

Figure 3.34: Velocity profile of collectively migrating cells in straight channels in dependence on channel diameter. **a)** x-component of the velocity (i.e. parallel to the channel) for different positions along the channel (averaged across the width of the channel at that position) for cell sheets that had penetrated 1500 µm into the channels (averaged over a period of 2 h centered around the time when said depth was reached). As previously found, the velocity increases towards the front of the cell sheet. For 300 µm, 400 µm and 500 µm there appears to be no clear effect of the channel width, as there is no systematic trend in the data. For the 100 µm wide channels, there seems to be a noticeable decrease in velocity. The inset shows the color code for the different channel widths. **b)** Same data as in a), except the absolute value of the velocity is examined rather than the x-component. Though the values change, the quantitative behavior is relatively similar to the behavior of the x-component, as most of the cell motion is oriented parallel to the channel. There still seems to be no pronounced effect of the width in the wider regime, and only the 100 µm wide channels show a noticeably lower speed. Shaded regions indicate standard error of the mean.

increasing, at roughly the same incline, which seems to be steeper than the incline of the gradient for the unconstricted channel. Eventually, the velocity profiles level off at roughly the same level as the straight channel profile levels off. The absolute plateau values in most cases do appear to be slightly below the plateau for the straight reference, but given the small difference and the margin of error, it is hard to determine whether this is a real effect or mainly the result of day to day variations between the collectively migrating cells.

The effect the introduction of a constriction has on the early part of the velocity profile is particularly interesting. The appearance of a plateau in velocity indicates that cells are indeed being jammed, either by increased density or by the confinement simply preventing them from flowing away through the constriction as fast as they are reaching the area in front of it. The part of the cell sheet in the constriction, however, is clearly unjammed, as this is the area where the velocity begins increasing. Of particular note is the fact that the diameter of the constriction seems to have no clear effect on the slope of this increase, or the point of onset of this increase, which confirms the idea that cells within them are moving in an unjammed state, and are not noticeably more or less jammed for different diameters. In future work, a more detailed analysis, including the actual cell densities in the various constrictions and in the region prior to them could help give further insights into this jamming and the correlations between density and cell velocities.

Without a fluorescent nucleus label to measure the cell densities, further insight into the effect the constriction has on the velocity profile can still be gained by examining the evolution of the velocity profile before it reaches the state shown in Fig. 3.35. One relevant question, for instance, is how much of an immediate effect encountering the constriction in the channel has on the velocity profile compared to the buildup in density (and consequent jamming) that is expected to occur over time as more cells arrive at the entrance to the narrow part than can continue moving on. To investigate this, the velocity profile for the channel with the strongest constriction is examined at four points: once the leading edge of the cell sheet has reached the segment where the channel begins to narrow, once it has reached the minimal width, once it has passed through the constriction and arrived in the segment where the channel begins to widen again, and finally at 250 µm past the point where the confinement has returned to maximal width (see Fig. 3.36).

This final point corresponds to the invasion depth at which the velocity profiles are shown in Fig. 3.35, where the plateau prior to the nozzle entrance had already fully developed. At earlier time points, however, this is not yet the case. Cell sheets migrating

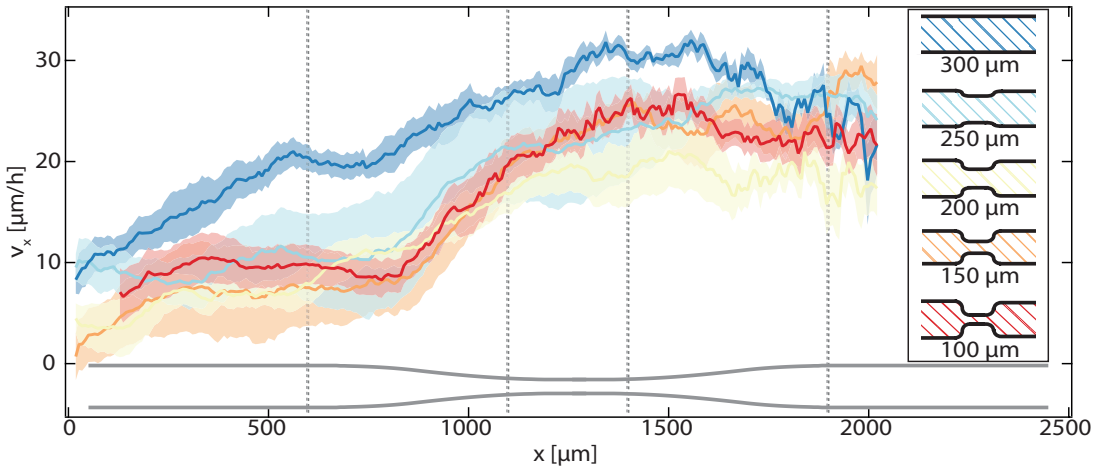

Figure 3.35: Profile of the x-component of the velocity (i.e. parallel to the channel) along the channel in dependence on constriction diameter. The ensemble average of two hour time averages around the moment when the cell sheets have penetrated 250 µm past the point of maximal width is shown from no constriction (*dark blue*) to a constriction 1/3 of the full channel width (*dark red*) as indicated by the color scheme in the inset. The dashed gray lines indicate (from left to right) the point where the channel begins constricting, the point where minimal width is reached, the point where the channel begins widening again, and the point where the channel has once more reached full width. This is reiterated in the gray schematic of the channel which highlights the channel segment corresponding to each region of the velocity profile. While the reference profile with no constriction (*dark blue*) shows an increase in velocity towards the cell front until a plateau (or possibly even a slight decrease) is reached, all channels with a constriction show a plateau at the beginning of the channel and do not show a pronounced increase until about midway through the narrowing channel segment. The total velocity they reach before going into another plateau is no lower than for the unconstrained channel within the margin of error. Shaded regions indicate standard errors of the mean.

in the straight part of the channel, before it begins to narrow, show the expected increase in velocity towards the cell front. Even after cells have migrated through the entire 500 µm of the channel's narrowing segment and the leading edge has reached the minimal width of the constriction, the velocity profile still shows the same qualitative behavior: v_x increases towards the front until a plateau value is reached. Things appear to begin to change as the front of the sheet progresses farther through the constriction, and, presumably, the density before the constriction entrance begins to increase as cells accumulate. The velocity profile still displays high values in the region prior to the constriction, but seems to have already formed a plateau to a certain degree, which is not yet quite as smooth as those observed for deeper invasion depths. About halfway through the narrowing segment, the increase in velocity begins, reaching up roughly to the maximal values also achieved at earlier time points. Finally, as already discussed, by the time the leading edge of the cell sheet has reached 250 µm past the return to maximal width, the plateau in front of the constriction has fully formed and the velocities there have significantly dropped. Thus, this effect is not instantaneous, as it would be if it were simply a result of cells being slowed down by not being able to migrate through the constriction at the same velocity.

For reference, these profiles are compared to the velocity profiles in the straight channels at depths equivalent to these last two points. For the first case, when the leading edge has reached the point where the channel is getting wider again, the magnitudes of velocities in the early part of the channel are similar, though the straight channel shows the typical increase in velocity towards the leading edge, as opposed to the plateau for the constricted case. In the latter case, where the constricted channel now shows a strikingly different behavior than for the earlier points, the velocity profile for the straight channel has barely changed in the back part of the channel, though the increase eventually reaches a plateau. All in all, these observations support the hypothesis that it is a buildup in density prior to the nozzle that leads to the striking change in the velocity profile upon introduction of a constriction into the channel, likely via a mechanism of a certain degree of jamming.

To further investigate the notion of to what degree the cells in the actual constriction are jammed, the velocity profiles for channels with constrictions of different lengths are compared (see Fig. 3.37). Interestingly, the length of the nozzle plays no role in determining the location of the switch from plateau in the velocity profile to the sloped portion. This holds true both when comparing the flow profile of the channel with the 100 µm wide constriction used up until now to an identical set of channels with a longer constriction, and also for a second set of geometries that is identical to each other aside from varying length of the constriction but differs from the previously studied geometry in length of

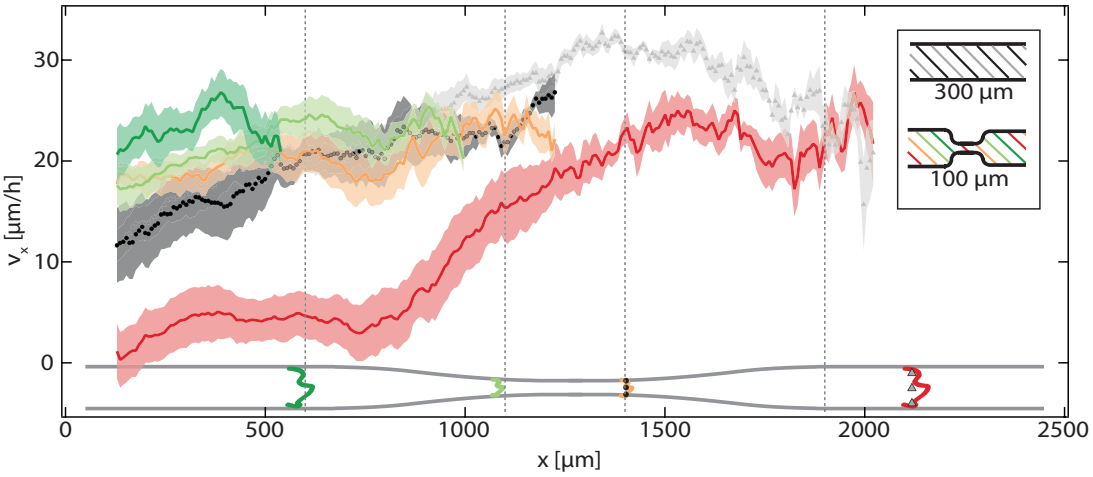

Figure 3.36: Evolution of flow through a constricted channel over time. The profile of the x-component of the velocity (i.e. parallel to the channel) along the channel for the narrowest constriction from Fig. 3.35 is depicted at different points of invasion into the channel: *dark green* as the cell sheet enters the narrowing part of the channel, *light green* as it has reached minimal width, *orange* as the segment where the channel widens is reached and *dark red* for 250 µm past the point of maximal width (as indicated in the schematic channel representation below the profiles). The plateau in the velocity prior to the constriction seen for this geometry in Fig. 3.35 does not develop until the cell sheet has already reached the area of the channel where it has returned to its maximal width, as opposed to it quickly developing once the constriction is encountered (all curves after *dark green*). For reference, the velocity profiles corresponding to a distance of equal penetration into a straight, unconstricted channel are shown as well for the two farther invasion depths (*black circles* correspond to *orange* curve, *gray triangles* correspond to *dark red* curve). The deviation between the two profiles when the cells in the constricted case have migrated through the tightest part of the channel is within the margin of error, and only becomes clearly visible for the last velocity profile. Velocity profiles for the same geometry were retrieved from the same set of measurements at time points corresponding to the various invasion depths, with the exception of the earliest velocity profile for the constricted case (*dark green*), which was determined from a separate set of measurements as statistics are too poor to observe both very shallow and very deep penetration depths from a consistent set. The dark red curve corresponds to the dark red curve in Fig. 3.35, except that channels were excluded from which no data was measured for the earlier invasion depths. Velocity profiles are slightly shorter than the current invasion depth due to the time averaging step. Shaded regions indicate standard error of the mean.

the narrowing/widening region (i.e. the steepness at which the channel is reduced to its constricted width).

As channels with these shorter transition regions are easier to achieve good statistics for due to the way the microstructuring process works, five different lengths of the constriction were examined in this instance. The length of the constriction was varied from 50 µm to 700 µm, with the resulting velocity profiles showing almost no difference in the location of the onset of the slope (see Fig. 3.37b). Any differences observed do not follow a systematic trend according to the length of constriction. Likewise, there is no real difference in the height of the plateau at the channel entrance, and at least for this second set of geometries, the initial slope when the velocity does begin increasing seems to be very similar within the margin of error. In summary, these results indicate that the cells in front of the constriction do not become more jammed even if the constriction is longer, and further support the hypothesis that the sheet moves through the constriction in a relatively unjammed manner.

As the results so far indicate that the plateau always reaches to about the halfway point of the segment where the channel is narrowing, it is worth directly comparing the velocity profile for geometries that are identical except in the length of this transition area. To this end, Fig. 3.38 shows the velocity profile for constricted channels with two different degrees of steepness for the narrowing (and widening) channel region. Immediately, it becomes apparent that the difference between the position of onset of the velocity increase is much more pronounced than it was for different lengths of constriction, so it either is influenced by the steepness of the transition area or its location simply depends on the location of the point where the constriction reaches its minimal width. To fully clarify the cause, further experiments would be necessary, that keep the position where the constriction reaches minimal width constant while varying the steepness of the transition area in front of it (which would consequently then begin at varying points) and examining whether or not the onset points fall together or are spatially separated.

Perhaps even more striking than the difference in onset points for the velocity increase in the curves in Fig. 3.38 is the behavior prior to that onset. Here the velocity profile corresponding to the geometry with the steeper transition region shows a clear pronounced dip in the velocity, rather than a simple plateau (which upon closer examination can actually be seen in all of the curves in Fig. 3.37b to a certain extent). This is intriguing behavior, as this region, immediately prior to the entrance into the constriction is where one would expect to get the highest cell density and thus the strongest jamming. In

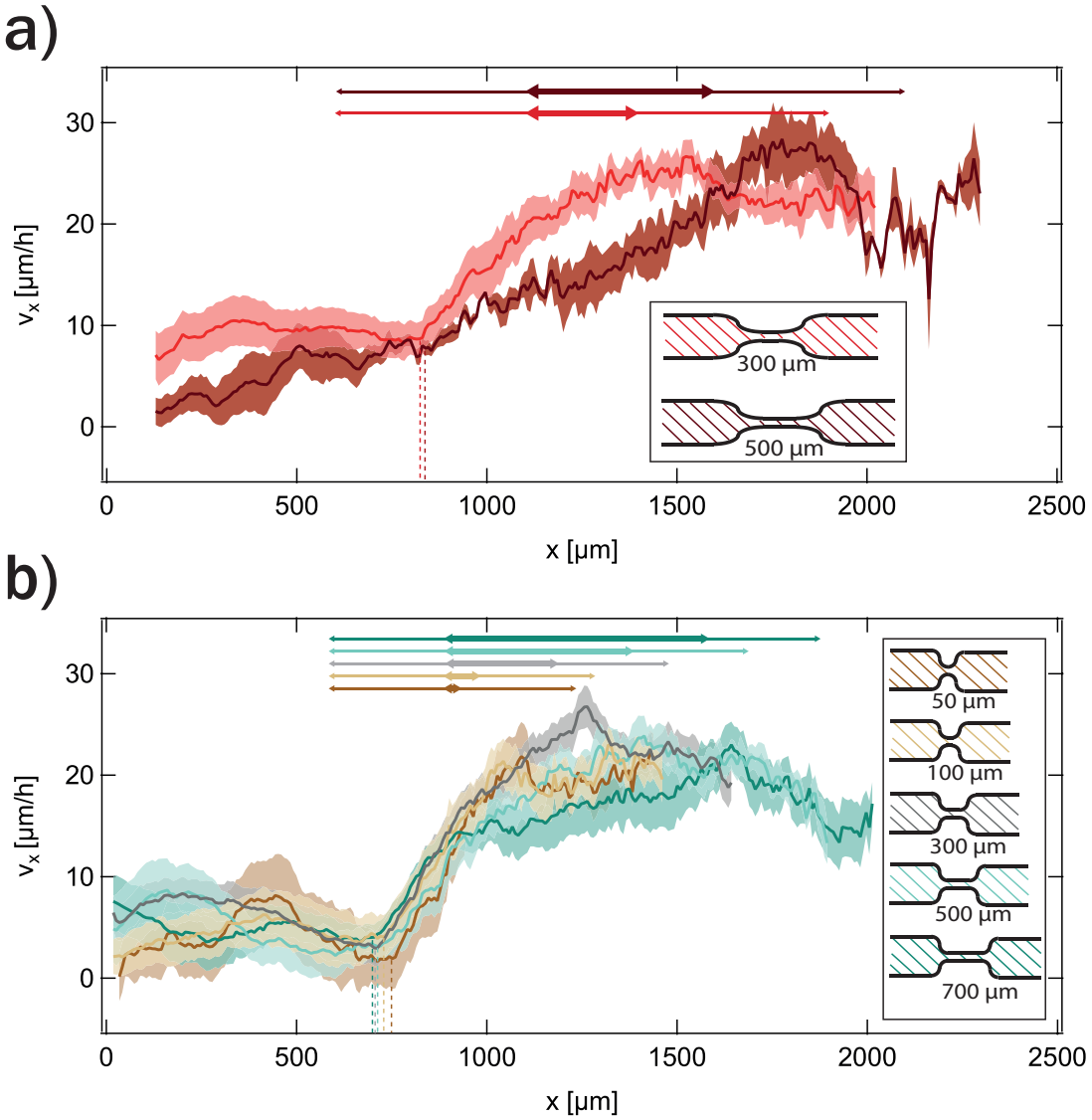

Figure 3.37: Profile of the x-component of the velocity (i.e. parallel to the channel) along the channel for different constriction lengths. **a)** Profile for the same constriction geometry as shown in Fig. 3.36 (*lighter red*) compared to identical geometry with the segment of minimal width extended from 300 µm to 500 µm (*darker red*). Both profiles are ensemble averages of measurements time averaged over 2 h around the point where the cell sheet has reached 250 µm into the area where the channel returns to maximal width. Arrows at the top of the figure indicate the position of the constriction (thick arrow denotes segment of minimal width, thin arrow includes area where channel becomes thinner). The dashed lines indicate where the plateau ends and the increase in velocity occurs. In both cases this onset occurs at roughly the same position in the channel, indicating that the longer constriction does not lead to more of a backup at its entrance. The difference in the steepness of this incline is likely a result of low statistics for the longer constriction length. **b)** Profiles for a separate set of geometries from those shown in a). Again the channels only vary among each other in the length of their constriction, though compared to the geometries in a) the segments where the channel becomes narrower or widens are reduced from 500 µm to 300 µm. Higher statistics and more different constriction lengths were achieved for these geometries. As in a), position of the constrictions are indicated by the arrows, and the approximate end of the plateau is indicated by the dashed lines. Again, no real effect of the constriction length on the beginning of the incline can be seen, confirming that longer constrictions do not lead to more backing up in front of them. The slope of the velocity profile during this initial incline seems to be very similar for the various geometries within the margin of error. Shaded areas indicate standard errors of the mean.

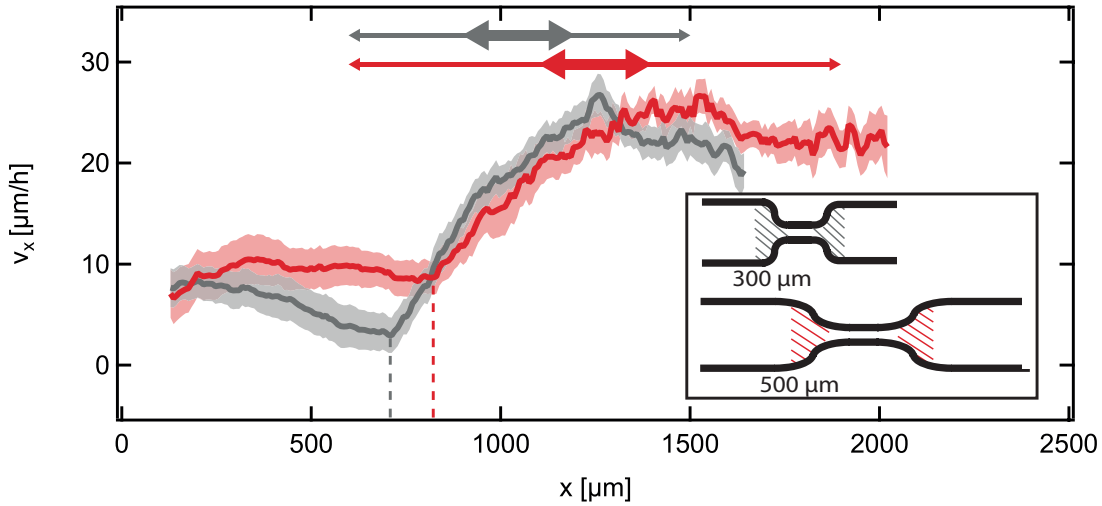

Figure 3.38: Profile of the x-component of the velocity (i.e. parallel to the channel) along the channel for different steepness of the narrowing (and widening) segments. Two velocity profiles (ensemble averages of 2 h time averages around the point the sheet has reached 250 µm into the area of maximal width) for channel geometries that are identical except in the steepness of the transition area from maximal to minimal width. The *dark red* curve corresponds to the dark red curve in Fig. 3.37a (length of the transition area: 500 µm) , the *dark gray* curve to the dark gray curve in Fig. 3.37b (length of the transition area: 300 µm), as shown schematically in the inset (difference exaggerated for clarity). Arrows at the top of the figure indicate the position of the constriction (thick arrow denotes segment of minimal width, thin arrow includes area where channel becomes thinner). The dashed lines indicate where the plateau ends and the increase in velocity begins. The difference in this onset is more pronounced than any difference for width of the constriction, indicating the greater steepness either causes more of a backup of cells prior to the constriction, or the backup depends only on where the area of minimal width begins. Within the margin of error, both inclines seem to show the same slope, however, the velocity profile for the geometry with the steeper transition to minimal width seems to show a more pronounced dip in velocity prior to the incline. Shaded areas indicate standard errors of the mean.

particular, it would be unsurprising to find a stronger or quicker buildup of a high density here for the channels with the steeper geometry, which then likely results in even stronger local jamming in precisely this spot. Again, this is something that could be studied in even more detail in future work, both by use of a fluorescent nucleus marker to actually evaluate the local cell density and correlate it with the velocity, and by further variation of the transition steepness.

3.3.5 Comparison with cell migration models

Further insights into the whole process of collective migration through a constricted channel can be gained by attempting to model the process. Seeing which features underlying the cell behavior are necessary to reproduce the emergent phenomena in a model can lead

to an understanding of how these phenomena arise in the experiment.

To this end, experimental data for collective epithelial cell migration through constricted channels is compared to an active isotropic-nematic mixture model that was recently successfully used to relate cell extrusions in an epithelium to underlying topological defects [100]. The implementation of the model was performed by Felix M. Kempf in the group of Prof. Erwin Frey (LMU München).

In brief, this model is a continuous medium approach that describes the spatiotemporal dynamics of cell sheets via fields and corresponding time-evolution equations derived from conservation laws (e.g. mass or momentum conservation), ignoring the individual agents making up the monolayer. In particular, the cell sheet is modeled as nematic phase and the "free region" it invades into is modeled as isotropic phase. The evolution of the nematic order is modeled by the Beris-Edwards equation and the evolution of the velocity is modeled by the incompressible Navier-Stokes equation, with order influencing the evolution of velocity and vice versa. A more detailed description of the model can be found in section 2.5.2 or in reference [100].

The two key observables in both experiment and simulation are the velocity field and the orientation field, so the initial step for comparison between the two is an examination of qualitative behavior in both cases. To this end, Fig. 3.39 shows the distribution of magnitudes of velocity over the constricted channel in a representative measurement for both theory and experiment. The experimental data is averaged over 2 h to smooth out short scale fluctuations in the velocity field, but this averaging does not change anything about the field's qualitative behavior.

Immediately, striking differences are apparent between simulation and experiment. In the model, the highest velocity magnitudes occur in the region prior to the constriction, whereas velocity is low within it. In contrast, as described previously, the experimental data shows exactly opposite behavior, with velocities in front of the constriction entrance low, but increasing within the constriction and assuming the highest values close to the cell sheet's leading edge.

Disagreement is even more pronounced when examining the direction of the velocity (see Fig. 3.40). Here, the simulation shows large flows perpendicular to the channel, in particular in the region ahead of the constriction. The experimental data instead shows a pronounced migration parallel to the channel, with perpendicular velocities only occurring on small scales and not in a coordinated manner. While in the data from the model

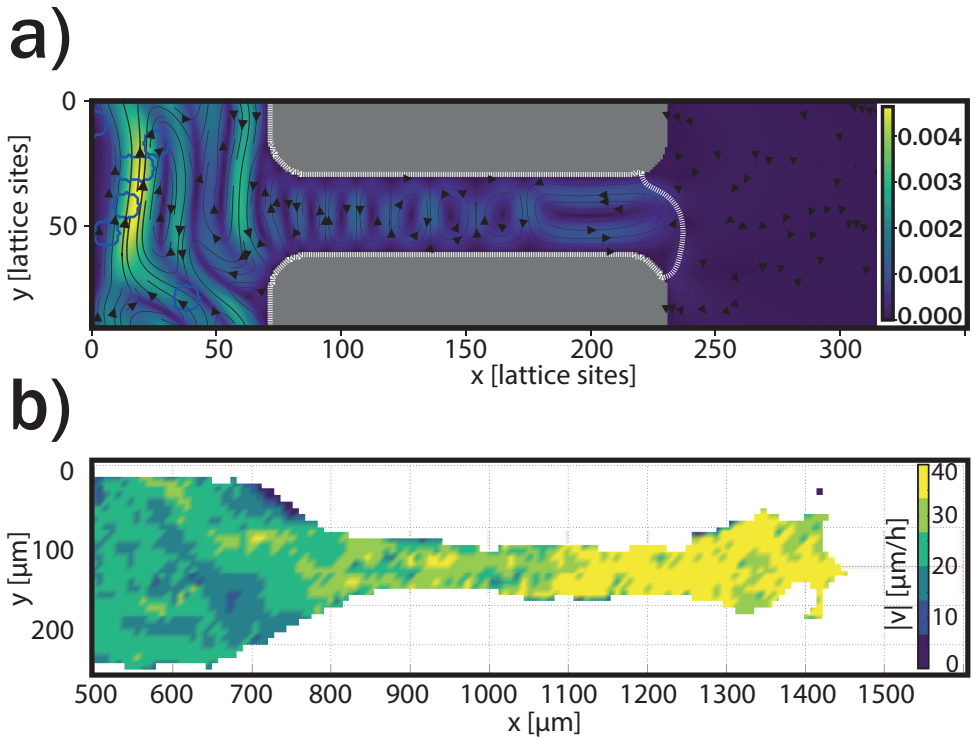

Figure 3.39: Comparison of the magnitude of velocity in experiment and theory. **a)** Velocity field resulting from the active isotropic-nematic mixture model, with color-coded velocity magnitudes. The white dashed line illustrates the current border between nematic phase and isotropic phase. Velocities are highest in the region before the constriction. **b)** Heatmap of velocity field from experiment. Velocities are lowest prior to the constriction and increase towards the front of the cell sheet. Simulation image courtesy of F.M. Kempf, AG Erwin Frey, LMU München. Experimental data is averaged over 2 h to smooth out short scale noise. Colormap for the experimental data adjusted to be comparable to theory.

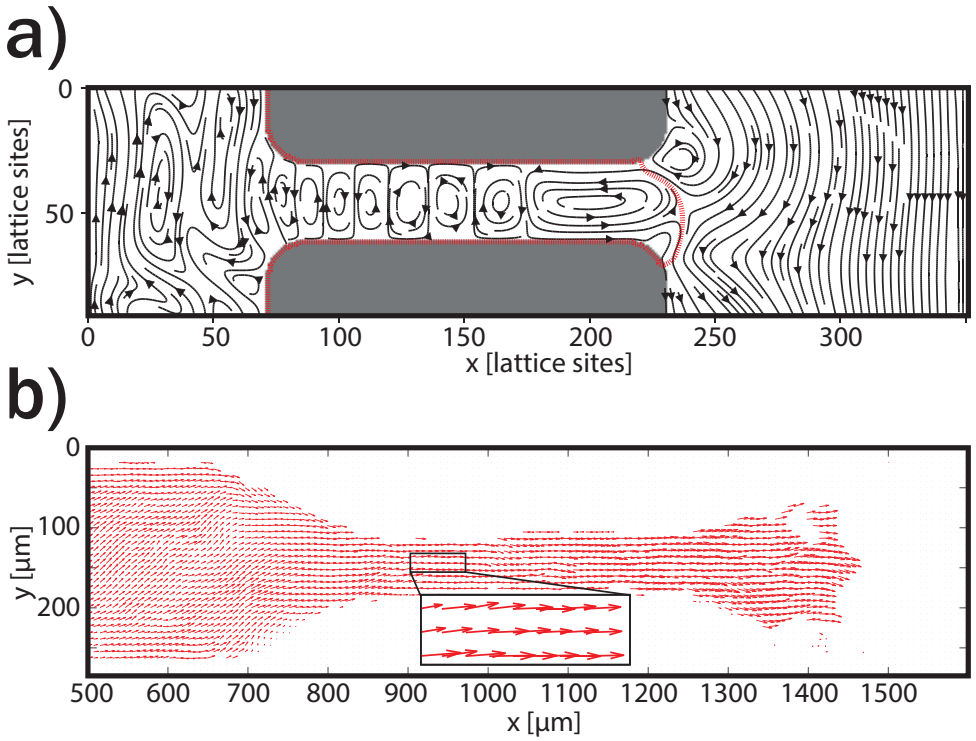

Figure 3.40: Comparison of orientation of velocity in experiment and theory. **a)** Velocity field orientation from the active isotropic-nematic mixture model. The red dashed line illustrates the current border between nematic phase and isotropic phase. Flows perpendicular to the channel dominate in the region prior to the constriction, and formation of vortices within the constriction is a hallmark of the model behavior. **b)** Velocity field from the experimental data. The general orientation of the flow tends to be parallel to the channel in most regions, and particularly so in the constricted area, as seen in the magnified area. Vortices seem to form very rarely, if ever, in the constriction. Simulation image adapted from Fig. 3.39a, courtesy of F.M. Kempf, AG Erwin Frey, LMU München. Experimental data is averaged over 2 h to smooth out short scale noise.

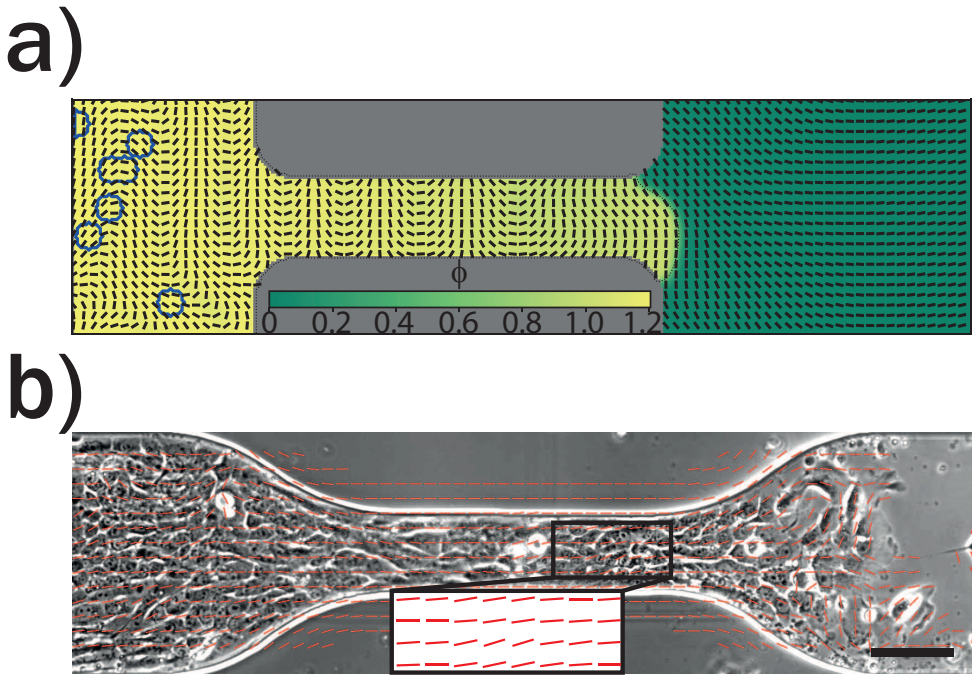

Figure 3.41: Comparison of orientation field in experiment and theory. **a)** Orientation field in the active isotropic-nematic mixture model. Orientation varies throughout the channel, but in general there are significant domains where orientation is perpendicular to the channel, in particular at the front of the cell sheet/the front of the nematic phase. The color scale represents the ϕ-field, which defines whether the system is in the nematic phase ($\phi \geq 1$) or the isotropic phase ($\phi = 0$). **b)** Orientation in the experiment. There is much less variation in orientation, and orientation parallel to the channel dominates. In particular, in the constricted region of the channel, cells are almost exclusively oriented parallel, as highlighted in the magnified region. Scale bar corresponds to 100 µm. Simulation image courtesy of F.M. Kempf, AG Erwin Frey, LMU München.

the perpendicular movement is so pronounced that it forms visible domains, in the experiment the perpendicular contributions are mostly removed when some spatial averaging is performed (as was discussed in Fig. 3.33).

In addition, the behavior within the constriction shows very clear differences between simulation and experiment. The nematic phase in the model forms very prominent and defined vortices within the constriction, while for the experiment the velocities become even more strongly aligned parallel to the channel. This striking vortex formation within the constriction is a robust feature in the model that occurred over a wide range of parameter regimes that the simulations were run for.

Similar issues come to light when examining the orientation fields (see Fig. 3.41). For the purpose of comparison with the theory, the orientation field for the experimental data was retrieved from the phase-contrast time-lapse microscopy images via an intensity

gradient-based orientation estimator (for details see appendix A.2.7). This method works relatively well, though interpretation of the results makes the most sense in the constricted region of the channel. Here, cells tend to be more elongated and thus it is easier to really define an orientation. In contrast, in the region prior to the nozzle, where cells are more symmetrically shaped and thus do not even necessarily have a real orientation, the resulting values for the orientation must be taken with a grain of salt. Still, even in these regions, the algorithm seems to perform decently well.

The simulated data shows varying domains of orientation both parallel and perpendicular to the channel, and in particular a significant area at the edge of the nematic phase where all orientation is perpendicular to the channel. In contrast, in the experimental data, parallel orientation is the much more dominant feature, with perpendicular orientations being very rare, though parts of the orientation field prior to the nozzle do show some contribution in that direction. Within the constriction, however, such orientation is nonexistent and all cells are aligned parallel to the channel walls (as well as frequently elongated along that direction to a certain extent). There is some agreement between simulation and experiment directly behind the leading edge of the cell sheet, where the migrating cell sheet also shows perpendicular order, though over a much shorter region than this is the case in the simulated nematic.

All in all, over a wide regime of parameters used for the simulation, qualitatively striking differences remained between theory and experiment, that could not be overcome. Thus, it must be concluded that the model is not a good fit for describing cell migration, at least in this scenario. It is possible that the model might still succeed and be useful for describing cell migration in other geometric arrangements, but for migration of an epithelial layer through a channel with a constriction, other models are likely more suitable. One possible big reason why no agreement could be reached between the active isotropic-nematic mixture model and experimental data even on a qualitative level is compressibility. A key assumption for the model is that the evolution of the velocity is given by the incompressible Navier-Stokes equation. In principle, the divergence of the velocity field for MCF10A cells has been shown to be close to zero on average by Saw et al. [100], which is a sufficient condition for the flow field to be incompressible. Geometrical boundary conditions, however, likely play a role. In this scenario of collective cell migration through a constriction, experimental data revealed evidence to support the hypothesis that the cells are being jammed in the region ahead of the constriction. For such a situation, where outside confinement leads to a large buildup in density, it is possible that this incompressibility requirement is no longer sufficiently true. The consequence would then

be qualitatively very different behavior between model and experiment.

For future work, attempting to model epithelial cell migration through a constricted channel with a model that takes into account individual cells, and can thus account for such things as regions of denser packing, makes sense. To this end, the cellular Potts model (for details see section 2.5.5) is a promising candidate. While computationally more expensive than a continuous medium approach, it offers the necessary level of detail to study whether the observed changes in the velocity profile as result of migration through a constriction are emergent properties of an active and proliferating particle system. If jamming is really the key mechanism driving this behavior, it should be a physically relatively universal phenomenon. Thus it should be reproducible by a more detailed model that accounts for compressibility.

3.3.6 Discussion

In summary, epithelial cells migrating collectively through a constricted channel reveal intriguing behavior that changes over the time course of the experiment. Early on, when the cell layer migrates in the straight part of the channel, prior to encountering a constriction, the velocity profile takes the shape, already observed in previous experiments for straight channels and circular wound closure, which is an increase of velocity towards the leading edge. Upon encountering the constriction, this leading edge appears to continue migrating relatively undeterred, and the flow profile throughout the sheet also does not show any significant change initially.

As the cell sheet progresses through the constriction, the continued imbalance between the number of cells that arrive at the narrow part of the channel and the lower number of cells that can actually continue moving forward leads to a buildup of density in the segment where the channel narrows. This is accompanied by the formation of a plateau in the velocity profile, which eventually shifts down towards lower values. While further investigation is necessary in future work, this behavior is consistent with a density dependent jamming mechanism, in particular since the effect is not immediate when the leading edge encounters the narrow confinement, but rather develops over time. Further proof of this notion is given by the fact that the influx at the channel seems to decrease over time, though this could only be analyzed in a very approximate manner.

The low velocity plateau spanning the area prior to the choke point appears indepen-

dently of the diameter of the constriction over the entire examined range down to 1/3 of the original channel width, but did not appear when cells were allowed to invade into a straight channel over the same distance. No clear difference in the flow profile was visible for the different constriction diameters, though the data comes with relatively large error margins. One potential reason for the large deviations observed for individual measurements of the same geometry is that the initial density the cell sheet arriving at the constriction is only controllable to a certain extent within the experimental framework. Thus, in some cases, cells might already arrive at the constriction at a slightly higher density than in others. Correspondingly, by the time the leading edge has migrated through the constriction, the density and corresponding jamming in the region prior to the constriction would also be slightly higher than in cases where the initial density upon arrival at the narrow segment was lower.

Interestingly, the plateau of velocity before the constriction seems to span the same distance independently of the length of the narrow segment, and the increase in speed always seems to begin roughly halfway through the narrowing region. This is consistent with the notions that cells are jammed prior to this entrance, but not jammed in the actual constriction, where the sheet seems to behave as if unconfined.

A noticeable effect on the velocity profile does occur, however, when the steepness of the transition area, where the channel becomes narrower, is changed. For steeper changeovers, the velocity profile seems to develop a dip prior to the constriction, with velocity actually dropping off to a minimal value before the increase in region of minimal width begins. It is conceivable that a steeper transition area leads to a quicker or more pronounced buildup of density localized to that area and less spread through the channel up until that point as might be the case for a "gentler" transition.

Comparing experimental data with simulation results from a continuous medium model where the migrating cell sheet is represented by an active isotropic-nematic mixture, deviations are found for both of the most important observables, velocity and nematic orientation. In the simulation, velocities are highest in the region prior to the constriction. Flows perpendicular to the channel are frequent throughout the entire nematic phase, which corresponds to the cell layer, and the occurrence of vortices within the constricted area is a key feature, which is robust to changes in the model parameters over a large examined regime. In contrast, in the experiment, the velocities are highest towards the leading edge, and higher throughout the entire constriction compared to the area before the narrow segment. Velocities are generally aligned predominantly parallel to the channel,

and perpendicular flows are rare and less pronounced. In particular, vortices never seem to form within the constricted area. Instead, velocities in this region are even more strongly aligned parallel to each other, and perpendicular components are suppressed even more strongly than in the wider regions.

Likewise, the orientation field shows discrepancies between experiment and simulation, with the experiment predominantly showing orientation of the cells parallel to the channel, while the model also features large domains of perpendicular nematic orientation. Again, this discrepancy is most noticeable within the constriction, where cells in the experiment tend to be aligned parallel to the channel almost exclusively, whereas this is not the case in the simulation. Best agreement for the orientation between experiment and simulation is found close to the leading edge, where both scenarios favor perpendicular alignment, though even here this region extends much farther back into the cell sheet in the model.

As a consequence, in future work a different choice of model makes sense. As the most likely reason for the incompatibility between experiment and theory is the fact that the continuous media model was based on the assumption of an incompressible flow, a theoretical approach that takes into account individual cells is conceivably more promising for capturing the experimental phenomena. The cellular Potts model is a strong candidate in this case, as it not only accounts for individual agents, it also includes details like cell shape, which has recently been shown to play a role in jamming transitions of cell collectives [57]. Modeling the experiment in a way that can account for this, it should hopefully be possible to elucidate the role of jamming in the observed changes of the velocity profile, and study to what extent this phenomena is simply a generic, emergent property from actively migrating, self-replicating cells.

On the experimental side, the introduction of a fluorescent nucleus label would be very advantageous. With its help, it would be possible to determine the local cell number density throughout the channel. This would allow a closer study of the correlation between cell density and velocity, and thus help shine a light onto the role and strength of the jamming that seems to occur at the constriction entrance. Without an actual density measurement, it is only possible to say that the constriction does lead to cells backing up and thus density increasing before its entrance. To what extent this is the case, and whether this density buildup is very local or propagates through the whole wide channel segment in front of the constriction, however, is hard to even speculate.

To this end, a stable cell line with a fluorescent nucleus would be the best possible solution. First attempts at the creation of such a cell line (MCF10A transfected with

mCherry expressing histone 2B (H2B)) were performed in the course of this thesis, but proved troublesome in the short term. Still, in the long term producing this stable cell line should be possible. Alternative approaches to determining the density are a transient messenger RNA (mRNA) transfection, or fixing the cells and staining the nuclei with a fluorescent probe such as DRAQ5. The latter would at least allow for a static examination of the density at different invasion depths. Live cell imaging with 25 nM Hoechst 33342 dye (Invitrogen) is not possible, as the autofluorescence of the PEG-DMA channel walls in the UV range proved to be too high.

In addition to measurements of density, a fluorescent nucleus label would also allow easy tracking of individual cells within the monolayer, which could help quantify how the influx at the channel entrance changes as the leading edge of the sheet moves through different regimes. Furthermore, following single cell movement might be beneficial to a further investigation of the backflow that can occur at the entrance to the narrow channel segment, where parts of the channel move against the general direction of motion.

Aside from an investigation of density and single cell behavior, the velocity profile in the experiment can still be studied in further detail. Previous work has, for instance, shown the emergence of vortices in channel-guided cell migration. Decomposing the experimental flow fields into rotational and diverging components might be of interest to study how the constriction affects this behavior. Many factors come into play where this is concerned, from the increased density prior to the constriction (which would typically be associated with larger, but slower vortices), over the gradient in general velocity, to the narrower confinement within the constriction that appears to be restrictive to perpendicular movements. On top of all of that, it is possible that the curvature of the narrowing channel segments leads to some alignment of the velocities following this bend, which in turn could be favorable starting conditions for the formation of full scale vortices.

This more detailed decomposition of the velocity field also makes sense in terms of comparison to future modeling results. Once the model is in principle qualitative agreement with the experiment, an examination of specific features of the flow fields, such as where vortices predominantly occur, is necessary for fine-tuning the simulation, and hence gaining a deeper understanding of the components relevant for the emergence of the experimentally observed behavior.

In terms of comparison to a Potts model, the use of inhibitor drugs or small interfering ribonucleic acid (siRNA) to change some of the underlying cell parameters, and seeing whether the model can predict qualitative changes to the emergent collective behavior, will

be of interest. For instance, blebbistatin, which inhibits myosin II-mediated contractility, has been used in the past to inhibit actomyosin activity and thus the activity of the constituent cells in the monolayer [100]. The effect of this reduced activity on the collective behavior and whether the model captures this would be an intriguing question. Another potential avenue is the application of Mitomycin C, a cell cycle antagonist that can be used to separate the effects of proliferation and migration, especially as it appears to have no effect on the migration of MCF10A cells [167]. In this way, the influx at the channel entrance could be cleanly separated from movement as a result of cell proliferation. At the same time, tuning the division rate in a cellular Potts model is straightforward. An intriguing question suggests itself, as to whether the jamming behavior at the constriction entrance changes qualitatively when cells no longer contribute to a density buildup by proliferating.

The work in this thesis has shown the experimental geometry of cells migrating through a channel with a constriction to be of great interest from a hydrodynamics perspective, as the phenomenon of jamming might be responsible for the transition from fluid like behavior of epithelial sheets to more glassy behavior. In a long term view, from a biological perspective it would be intriguing to use such a constricted channel geometry with a cell line that normally does not migrate collectively and see whether the jamming within a sufficient constriction can lead to the emergence of collective migration in this case, as the jamming theory would predict [41].

3.4 Hydrodynamics of minimal collective cellular units

The previous chapters examined the hydrodynamics of large-scale assemblies consisting of many cells. Emphasis was placed on the fact that collectively migrating cells were on the one hand shown to behave like a fluid in many ways, but on the other hand also show behavior typically associated with glassy materials, such as dynamic heterogeneities and caging [38, 168, 169]. In order for this behavior to be possible, cells within the epithelium need to be able to rearrange. These rearrangements are governed by the interplay of mechanical forces within the cell layer [59, 170–172] and their significance, in particular when it comes to morphogenesis, has been highlighted in recent years [83, 170, 173]. For better understanding, a glassy material is one that spends most of its time near a mechanically stable minimal potential energy, where the potential energy of the material is specified by all the degrees of freedom, such as particle position [58]. Rearrangements are thus accompanied by an energy barrier that needs to be overcome, yet unlike inactive glassy materials, cells in confluent layers regularly do surpass these and rearrange [174], to the point of the whole material acting like a fluid under some circumstances, such as lower density.

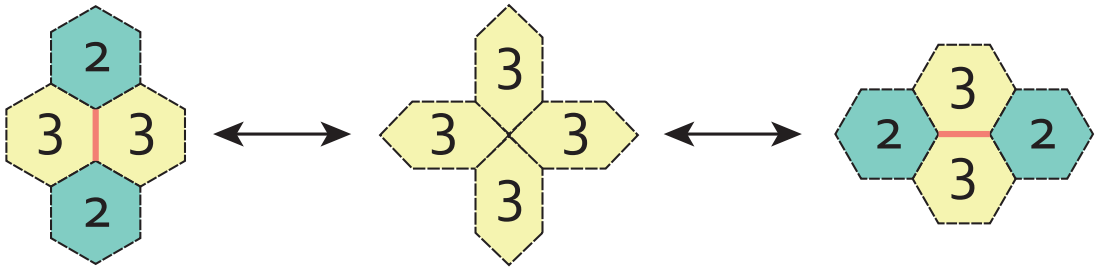

Figure 3.42: Schematic of a T1 transition. This transition occurs at the interface of four cells. Such cells break symmetry in their arrangement (left), with two cells sharing interfaces with two cells (green cells) and two cells sharing interfaces with three cells (yellow cells). In a T1 transition, the two three-neighbored cells lose their shared boundary (indicated in red), and after passing through a perfectly symmetrical configuration where all cells share one common vertex (middle), a new boundary is formed between the two remaining cells (right). This configuration is energetically equivalent to the initial arrangement, though each cell now has a different number of neighbors it shares boundaries with. Despite energetic equivalency, an energy barrier must still be overcome to perform a T1 transition. This figure is identical to Fig. 2.1 in section 2.1.2, but repeated here to clarify the T1 process.

Upon examination, topological rearrangements within a confluent cell layer turn out to only be possible via cell division, cell extrusion or so-called T1 transitions [58]. This type of transition (shown schematically in Fig. 3.42) can take place when four cells within the tissue are arranged in such a way that they form two threefold vertices, so that two

of the cells share a border with all three other cells, whereas the remaining two cells only share a border with two of the others, having no direct contact with each other. In the T1 transition, the two threefold vertices move closer together until they join in a single fourfold vertex where all four cells meet, before two new threefold vertices appear in such a manner that the two cells that previously were not in contact remain neighbors, while the other two cells no longer share a common border (for more details, see chapter 2.1.2). Theoretical work can show that such fourfold vertices must always be unstable unless tensions are allowed to depend on edge orientation [175]. In recent years, studies have shown T1 transitions are common during remodeling of epithelial layers [174] and that their occurrence contributes significantly to arising shear, for instance in the case of large scale deformations occurring during the formation of the *Drosophila* wing blade [59]. In the framework of describing cells with glassy dynamics and a jamming transition, however, these rearrangements play a crucial role in all processes that involve collective migration, such as wound healing and cancer invasion [57, 58]. In addition to density dependent transitions, theoretical work on the vertex model has used these transitions to show a shape parameter dependent transition that relates only to single cell properties and helps explain how different tissues of the same density can show distinct relaxation times, while at the same time being potentially relevant to the occurrence of EMT during cancer tumorigenesis [176].

The mechanical properties of cell sheets are highly relevant, due to their relation to forces and shear within them. Direct measurements of these properties *in-vivo* are challenging, however, given the complexity of the systems at hand, which typically consist of hundreds to thousands of cells. One common approach to accessing at least some of the parameters is laser ablation of the tissue, followed by observation of the subsequent relaxation processes in the epithelium, which can give information about cortical tension [177]. Given the invasive nature of this method, a way of studying the undisturbed tissue mechanics in a time-resolved way would be preferable.

In this chapter, a novel oligocellular *in-vitro* array is presented, where groups of up to four cells share a micropattern, offering an intermediate stage between experiments performed on whole cell sheets (e.g. wound healing assays) and single cell measurements, both of which are quite common nowadays [23, 37, 63, 178]. With the micropatterns' defined boundaries, and with the controlled, low number of cells, this assay allows studying phenomena that are too intricate to analyze at the scale of whole tissues, but that are emergent properties of multiple cells and thus do not appear when observing single cells. In particular, four cells together on one adhesive island present the minimal system necessary

for the occurrence of a T1 transition. In recent theoretical work, Bi et al. showed that even in a full-scale tissue, most of the change in energy caused in the system by such a T1 transition is localized to the four involved cells [58], so in principle our model system without the surrounding tissue should be sufficient to study these rearrangements. The basis for the energy calculation in their publication is the vertex model, which abstracts cell-cell contacts as straight lines and calculates the mechanical energy of the cells from its perimeter and its area and has shown great success at predicting cell arrangements according to minimal energy shapes [89, 179–181].

Using the vertex model on our small groups of cells, we ask the question to what extent mechanical parameters can be calculated simply from the arrangement of cells, assuming they organize according to minimal energy patterns. As Segerer et al. recently showed, however, oligocellular epithelial groups confined to micropatterns do not arrange in one static configuration, instead displaying collective rotational states [60]. To this extent, we study how varying the geometry from a large square shared by all cells to a more complex cloverleaf shape, with four smaller adhesion islands connected by a cross, can stifle the emergence of these rotational states for groups of four cells. We find that on these patterns, cells preferentially arrange in the same geometrical pattern typically found for quartets of cells on large square adhesion sites (two threefold vertices connected by a junction), but with each individual cell tending to sit on one of the four adhesion islands rather than all of them moving collectively. Taking the length of the junction connecting the two threefold vertices as an example, we find that pinning the cells down in such a manner also reduces the temporal fluctuations of parameters characterizing the cell arrangement, suggesting that in this case the cells might not fluctuate as much from an equilibrium configuration as for the less confined case. Thus, they are the more attractive targets for application of the vertex model for calculation of mechanical parameters from the observed oligocellular arrangements.

Additionally, we use our assay to probe the dynamics of multicellular systems. It is known that energy barriers exist between different configurations of cells, which must be overcome in order for cells to rearrange [58]. As cells use these reorganizations to generate stresses within the tissue during development [59], they must therefore regularly overcome these barriers. As such, the height of the energy barrier and its dependence on the concrete cell arrangement is of great interest. We investigate the statistics of T1 transitions in our minimal model system of four cells, an arrangement that has previously been examined theoretically [176]. This is only made possible by the introduction of the cloverleaf geometry, which inhibits the onset of collective rotation states that otherwise

form in such systems due to internal polarization. This leads to transiently stable cell arrangements that are sufficient to allow first observations of T1 transitions. By increasing (decreasing) the distance between the four adhesion islands of the cloverleaf pattern, we can artificially stretch (compress) the four connected cells apart, mimicking a change of cortical tension. Our results show that the average junction length between the two threefold vertices that have to degenerate into one fourfold vertex for the T1 transition to occur scales with the size of the four cell system. Though the data comes with large error bars, the results from the experiments suggest that T1 transitions occur more frequently for smaller systems, where the mean junction length is smaller, in agreement with the expectation that the energy barrier that needs to be overcome would be reduced in these cases.

3.4.1 Cell arrangement and description via the vertex model

In order to study the mechanics and energy barriers of systems of few cells, arrays of adhesive patterns are created via microcontactprinting (see appendix A.1.2). Initially, this pattern consists of a simple square with a side length of 57 µm. MDCK cells were seeded in such a way that as many of the squares in the array are occupied by one cell or few cells as possible. After a few hours for the cells to adhere, the sample is rinsed with phosphate buffered saline (PBS) to remove cells not on the adhesive patterns. The sample is then left to rest for 24 to 48 h, giving the cells that have spread on the pattern time to divide. The resulting array then has squares occupied by arrangements of various cell numbers. Fig. 3.43 shows the appearance of systems consisting of one to four cells, though more cells can also occur. The work in this thesis focused on systems of two and four cells, though in principle other cell numbers could also be of interest. In particular, systems of three or five cells might give access to further mechanical insights into the cells, though for five cells a closer examination of whether they have sufficient space on the pattern and do not shove each other off would be necessary. In contrast, as seen in Fig. 3.43, a single MDCK cell does not typically spread across the whole area of the large adhesive square, which renders it unsuitable for studying mechanical properties as the cell will never relax.

In the following, the geometry of how systems of two and four cells pack into square adhesive patterns is examined and analyzed in terms of a vertex model (see section 2.5.4). In particular, the question whether the cells arrange into stable packing states that are described by energetically minimal configurations of the vertex model is investigated. To this extent, the cell-cell boundary lines are approximated as shown in Fig. 3.44. Given the

boundary conditions of the adhesive micropatterns, the total area available to the cells is fixed. For two cells, experimental data suggests the pair divides the area evenly between them, and thus for these cases $A_i = A_{total}/2$ is assumed to hold true in order to simplify the model. With this condition, Eq. 2.58 simplifies to Eq. 3.14 as the contribution of area elasticity vanishes.

$$E = \sum_{i \in cells}^{N} \left(\kappa P_i^2 - \alpha \sum_{j \in \nu(i)} L_{i,j} \right) \tag{3.14}$$

Here, κ represents the cell cortex contractility, α the cell-cell adhesion parameter, P_i the perimeter of cell i and $L_{i,j}$ the cell-cell contact line between cell i and one of its neighbors $j \in \nu(i)$. More specifically, for two cells the total energy of the system can explicitly be written as:

$$E = 8\kappa l^2 + \frac{8\kappa l^2}{\cos(\vartheta)} + \frac{2\kappa l^2}{\cos^2(\vartheta)} - \frac{2\alpha l}{\cos(\vartheta)} \tag{3.15}$$

Here, the geometric parameters are defined as in Fig. 3.44: l is the side length of the adhesive square and ϑ is the angle between the cell junction and the pattern border. Due to symmetry of the problem, only $\vartheta \in [0, 45°]$ designates energetically distinct packing states, and thus the angle is defined over this region. Eq. 3.15 has also made use of replacing the junction length L as follows:

$$L = \frac{l}{\cos(\vartheta)} \tag{3.16}$$

As can be seen, the energy of a two cell system on a square of a given size (l fixed) depends only on the angle between the cell-cell junction and the pattern boundary. The energetically optimal configuration (assuming one exists) thus corresponds to a specific angle of this junction. Specifically, setting the derivative of Eq. 3.15 to zero, the condition for minimization of the energy is found to be:

$$\cos(\vartheta) = \left(\frac{\alpha}{2\kappa l} - 2 \right)^{-1} \tag{3.17}$$

As shown in Fig 3.45, systems of two cells do not remain in any stable position over

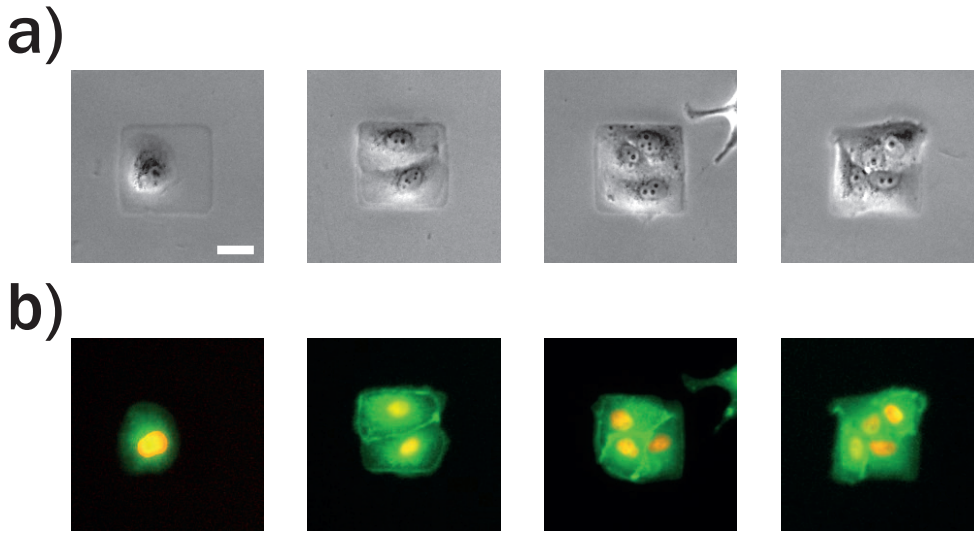

Figure 3.43: Arrangement of cells on large square micropatterns. **a)** Brightfield images of one, two, three and four cells on a micropattern. The single cell is too small to fill out the entire pattern, whereas two to four cells easily fill out the entire square, even pushing slightly into the passivated area around it. The occurrence of the various cell numbers on each adhesion site is stochastic to a certain extent. **b)** Overlay of corresponding fluorescent images of the cells from a). Actin, labeled by lifeact-eGFP is indicated in green, the nucleus, labelled by H2B expressing mCherry, is indicated in red. The actin label highlights the boundaries between individual cells, whereas the nucleus label can be used as a surrogate for the position of each cell. Scale bar corresponds to 25 µm.

time, instead, in agreement with the results of Segerer et al. [60], they rotate on the pattern due to internal polarization. Fig 3.45b shows the evolution of the junction angle for several representative pairs of cells (the cell-cell junction was tracked manually from the lifeact-enhanced green fluorescent protein (eGFP) fluorescence images). Even over a period of 20 h, none of the two cell systems reaches a stable configuration. Still, compared to circular patterns, the square adhesion geometry breaks the symmetry, leading to a fluctuating cell-cell junction length (and correspondingly cell perimeter) with fluctuating angles. Thus, an energetically preferential arrangement as given by Eq. 3.17 might still play a role (such as the cells spending more time there than in energetically less favorable configurations). Indeed, as shown in Fig 3.45c, the distribution of all angle configurations observed for 127 pairs of cells is far from uniform, with small angles occurring much more frequently than larger angles (observed angles were grouped into 14 bins of 3.21° to create the histogram). Systems of two cells on similar geometries have already been studied by Tseng et al. [182]. For systems where the underlying ECM pattern was a square frame, they found the same behavior of cells moving in most image frames, and the most frequently occurring angles of the nucleus-nucleus axis were those parallel to the borders of the square.

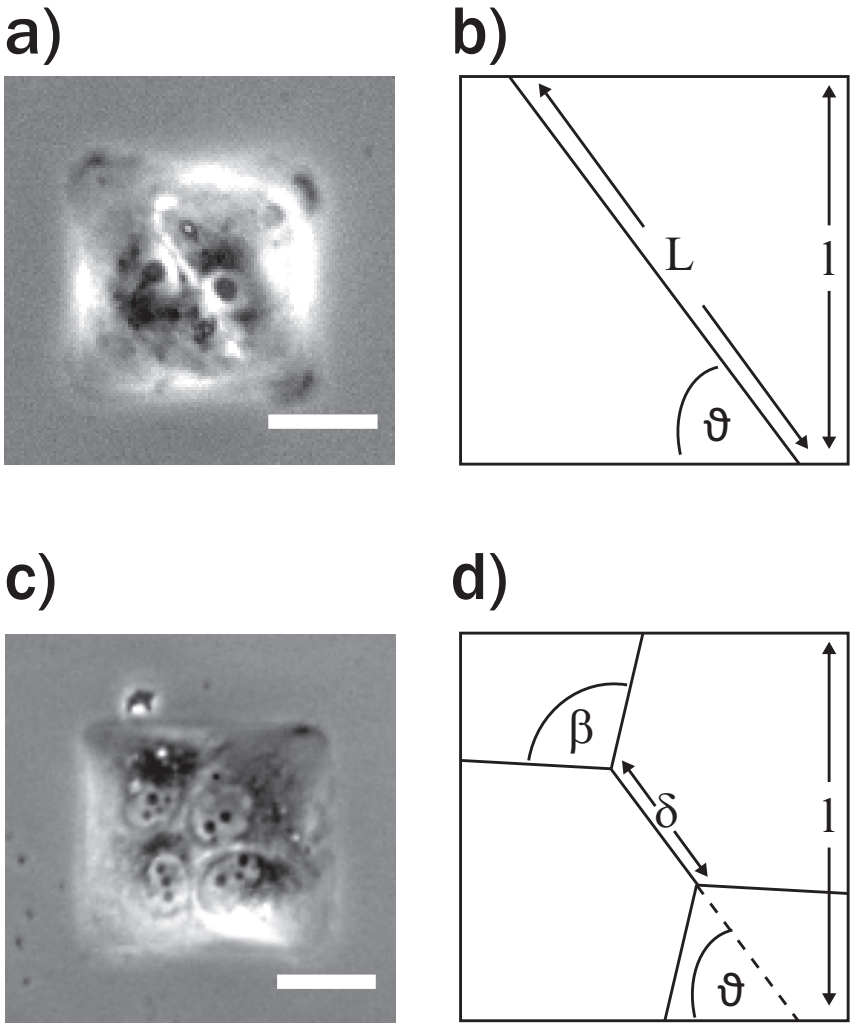

Figure 3.44: Geometrical arrangement of cells on pattern and their representation with cell-cell junctions abstracted as straight lines. **a)** A typical pair of cells sitting on a large square pattern. **b)** If the cell-cell junction is assumed to be a straight line, the organization of the two cells can be described by the side length l of the square pattern, the length of the junction L and the angle ϑ between junction and the pattern boundary. Two of these parameters are sufficient to fully characterize the arrangement. **c)** A typical arrangement of four cells on a large square pattern. **d)** More parameters are necessary to characterize the arrangement of four cells on the pattern. In addition to the length of the junction δ shared by the two cells that have three neighbors, the angle β, which defines the angle the cell-cell junction lines meet at in the threefold vertices, is required for the full characterization. The arrangement is assumed to be symmetrical in the sense that the angle β is identical for both threefold vertices and that both these vertices are the same distance from the corner of the pattern. Scale bars correspond to 25 µm.

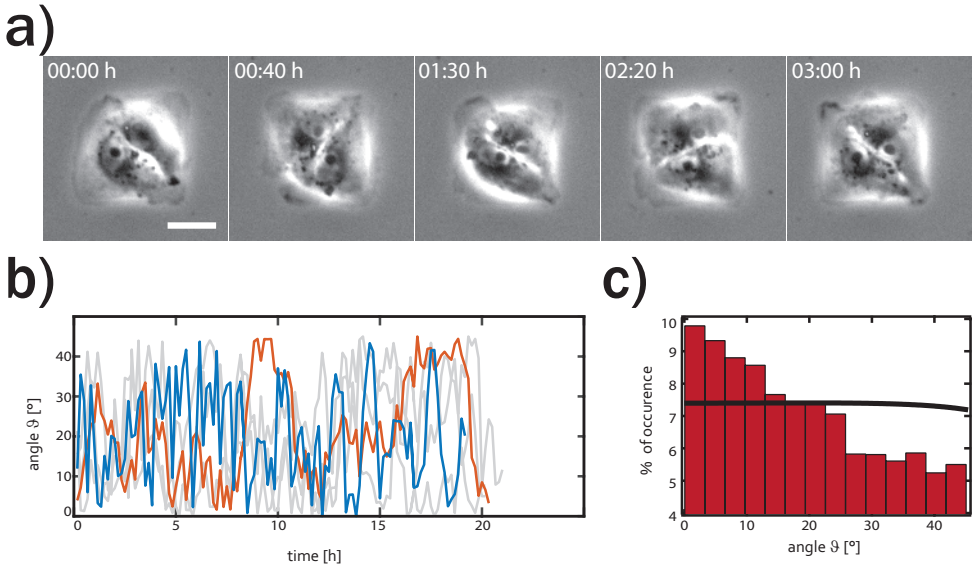

Figure 3.45: Rotation of two-cell system. **a)** Phase-contrast time-lapse images of a pair of cells over time. As can be seen by the junction between the two cells (light), the system rotates over time. **b)** Time development of the angle ϑ (defined according to Fig. 3.44) of the junctions shown for five exemplary traces (one highlighted in red, one in blue for ease of viewing). **c)** Frequency of occurrence of the junction angle ϑ during each observed time point for 127 systems of two cells. Small angles dominate, whereas large angles are infrequent. Each bin encompasses 3.21°. The solid black line indicates a fit of the distribution of angles with the vertex model, showing very poor agreement. Scale bar corresponds to 50 µm.

Contrary to the first indication in our data given by the presence of a maximum in the angle distribution, its shape is poorly fitted by the vertex model assumed above (solid black line in Fig. 3.45c).

This fit is performed by assuming the packing states for various angles are distributed according to a statistical weight, in analogy to a Boltzmann distribution, with an effective inverse temperature τ:

$$p(\vartheta) = \frac{e^{-\tau E(\vartheta)}}{\int d\vartheta e^{-\tau E(\vartheta)}} \tag{3.18}$$

The fit is performed assuming the minimum in the energy is found at the most frequently encountered angle (which in this case is the bin centered around the angle 1.6°). Inputting this angle into Eq. 3.17 results in $\alpha/l\kappa = 6.0008$, which leaves only τ as a free fit parameter. The fit shown in Fig. 3.45c) results in $\tau = 0.23\kappa^{-1}l^{-2}$, but the fitted curve does not capture any of the features seen in the angle distribution. Other values of τ do not significantly alter the qualitative shape of the curve. Likewise, taking the energy minimum to be at

the average observed angle $\langle \vartheta \rangle = 19.89°$ rather than the most frequently observed angle does not lead to a fit that captures the shape of the distribution any better.

Consequently, either the underlying vertex model is insufficient and needs to be expanded to include other contributions (though for instance even the inclusion of a cellular anisotropy term does not appear to significantly change the qualitative shape of the energy landscape for pairs of cells [183]), or minimization of energy from cell arrangement is not the driving force underlying the observed behavior.

3.4.2 Stabilization of cell arrangements through choice of the underlying geometry

As the previous section clearly shows, application of the vertex model to a system of two cells is not particularly promising, as the rotation behavior seems to outweigh the desire to minimize the energy of the system by choice of the geometry. Thus, the goal of this chapter is to improve on the simple square adhesion geometry, creating a pattern where cells still organize in the same general way as they originally did, but where collective rotation is inhibited. As the energy in the two-cell system was entirely defined by the angle of the cell-cell junction, which would be fixed by any geometry that inhibits rotation, the focus is placed on systems of four cells. To this end, a cloverleaf geometry is chosen, which consists of four individual adhesive islands, one for each cell. These islands are connected by narrow bridges, that allow the cells to spread and come into contact in the middle. The full length of the diagonal of the cloverleaf pattern from the outer edge of one adhesive island to the opposite one is 85 µm, very slightly above the 81 µm diagonal of the square (which has a side length of 57 µm). The same geometry was also tested without the connecting bridges, leaving just four individual islands, but this was found to result in the cells not forming any cell-cell adhesions in a large percentage of cases and cells just sitting on their individual, small islands.

As can be seen in Fig. 3.46, groups of four cells on the cloverleaf patterns do form cell-cell junctions, spreading some of their area over the passivated regions. Frequently, these cells will arrange with one cell sitting predominantly on each island, as desired (see Fig. 3.46b), though some cells might need to migrate some distance to reach this position (see the red and purple tracks in Fig. 3.46d). Compared to the square geometries, where the cell collective spends most of the time rotating, on the cloverleaf patterns states that are at least transiently stable can sometimes be observed (see Fig.3.46b-d).

The analyzed groups ($N = 25$) of four cells that ever reached this arrangement on patterns during observation were found to be in a stable configuration in $58.3 \pm 0.3\,\%$ of the observed time frames (determined by manual observation), with the lifetime of such a state lasting anywhere from around 1 h to roughly 8 h. While a more stable occupation of these transient configurations would be preferable and might be achieved in future work by changing the patterning process to something with improved passivation of the non-adherent areas (thus more strongly confining each cell to its individual island), the process is robust enough to hint at some initial results.

Firstly, in terms of energy examination with the vertex model, during these transiently stable configurations, the angle ϑ between the junction connecting the two threefold vertices and the boundary of a hypothetical square pattern overlaid over the cloverleaf, can be assumed to be constant at $\vartheta = 45°$, as it can be seen not to deviate from this strongly in the experiment. This already simplifies the geometrical arrangement significantly and eliminates the parameter ϑ from the ansatz for the energy of the system. Unlike in the two cell system, however, groups of four cells do not appear to necessarily distribute the area available to them evenly, with some cells appearing to be significantly larger than others. Thus, at the very least, the energy term needs to be expanded again to include the term for area elasticity:

$$E = \sum_{i \in cells}^{4} \left(\kappa P_i^2 - \alpha \sum_{j \in \nu(i)} L_{i,j} + \frac{K_i}{2} \left(A_i - A_0 \right) \right) \tag{3.19}$$

On top of this, inclusion of a term explicitly accounting for the energy of free spanning arcs over none-adhesive areas, as suggested by Albert et al. [184] makes sense given that large parts of the area in the observed cell arrangements are actually not on top of the adhesive pattern. Such a term would take the shape:

$$E_{\text{arc}} = \sum_{\text{arc i}} \frac{k}{2L_{0,i}} \left(\xi_i - \xi_{0,i} \right)^2 \tag{3.20}$$

Here, k is the elastic rigidity, which controls the degree to which the arc regions contribute to the energy, and ξ_i and $\xi_{0,i}$ are the length of each edge and the rest length of each edge, respectively.

Even without inclusion of the energy contribution of these arcs, however, the energy

term for four cells is already significantly more complicated than for two cells:

$$E = \kappa\left(2P_1 + 2P_2\right) + K\left(A_1^2 + A_2^2 + 2A_0^2 - 2A_0\left(A_1 + A_2\right)\right) - 2\alpha\left(4L_{1,2} + \delta\right) \tag{3.21}$$

Here, $P_1 = P_3$ denotes the perimeter of the two cells not in direct contact with each other, and $P_2 = P_4$ denotes the perimeter of the other two cells. Likewise, $A_1 = A_3$ and $A_2 = A_4$ give the areas of these cells, and $L_{1,2} = L_{1,4} = L_{2,3} = L_{3,4}$ describes the junctions between all cell pairs other than the one junction connecting the two threefold vertices, which is given by δ as defined above. This equation assumes the case that the system is symmetrical as shown in Fig. 3.44.

The terms for the perimeters are given by Eq. 3.22 and 3.23 (assuming $\beta > 90°$):

$$P_1 = P_3 = \left(l - \frac{\delta}{2}\right) \cdot \left[1 + 2\tan\left(\frac{|\beta - 90°|}{2} + \frac{\sqrt{2}}{\cos(\beta/2) + \sin(\beta/2)}\right)\right] \tag{3.22}$$

$$P_2 = P_4 = \delta + \left(l - \frac{\delta}{2}\right) \cdot \left[1 - 2\tan\left(\frac{|\beta - 90°|}{2}\right) + \frac{\sqrt{2}}{\cos(\beta/2) + \sin(\beta/2)}\right] \tag{3.23}$$

The terms for the areas are given by Eq. 3.24 and 3.25:

$$A_1 = A_3 = \left(\frac{l - \delta/\sqrt{2}}{2}\right)^2 \cdot \left[1 + 3 \cdot \tan\left(\frac{|\beta - 90°|}{2}\right) + \left(\tan\left(\frac{|\beta - 90°|}{2}\right)\right)^2\right] \tag{3.24}$$

$$A_2 = A_4 = \frac{l^2 - 2A_1}{2} \tag{3.25}$$

And finally, the junction lengths are given by:

$$L_{1,2} = L_{1,4} = L_{2,3} = L_{3,4} = \frac{\sqrt{2}l - \delta}{2\left[\cos\left(\beta/2\right) + \sin\left(\beta/2\right)\right]} \tag{3.26}$$

Despite the complexity of the terms, the energy of the four cell system using this approach depends only on two parameters that describe their geometric arrangement (see Fig. 3.44d for definition of the parameters): the length of the junction connecting the two threefold vertices δ and the "opening" angle β, which describes the angle under which the cell-cell junctions meet in each threefold vertex.

For the sake of confirming that the cloverleaf geometry contributes to pinning the cells down into an energetically stable configuration, the junction length δ was tracked manually for both cells on this geometry and the original square pattern. Fig. 3.46e) shows the evolution of this parameter for five systems in both cases. The cells on the cloverleaf geometry show reduced fluctuations of their junction length over time, as can be seen by the fact that these traces show narrower confinement along the δ-axis than the cells on the squares. This is also quantified in the inset to this figure, which shows the mean value $\langle\delta\rangle$ of each time trace, along with their variance in the form or error bars. Though there is fluctuation between the individual four cell systems, in general the groups on the simple square pattern show a higher variance.

This confirms that even though the stable states observed on the cloverleafs are only transient, this already helps reduce the fluctuations in one of the key parameters that determines the energy of the system. This could be interpreted as meaning that with collective rotation suppressed (to a certain degree), the system spends more time close to its energetic minimum, which would make the vertex model more applicable than it was for the system of two cells discussed above.

For the purpose of this test, the parameter δ was determined by manual tracking of the two threefold vertices from the lifeact-eGFP images. This work is tedious, however, especially when hoping to achieve larger statistics, and, on top of that, is error prone, in particular when the junction assumes small lengths. A proper examination of the energy, however, requires an accurate measurement of not only δ but also β, for a large number of time points of a large number of systems (to ensure their mean values are captured properly despite the fluctuations that are still present in the "stabilized" systems).

To this end, part of this thesis was devoted to developing an automated algorithm for extraction of said parameters from the lifeact-eGFP images.

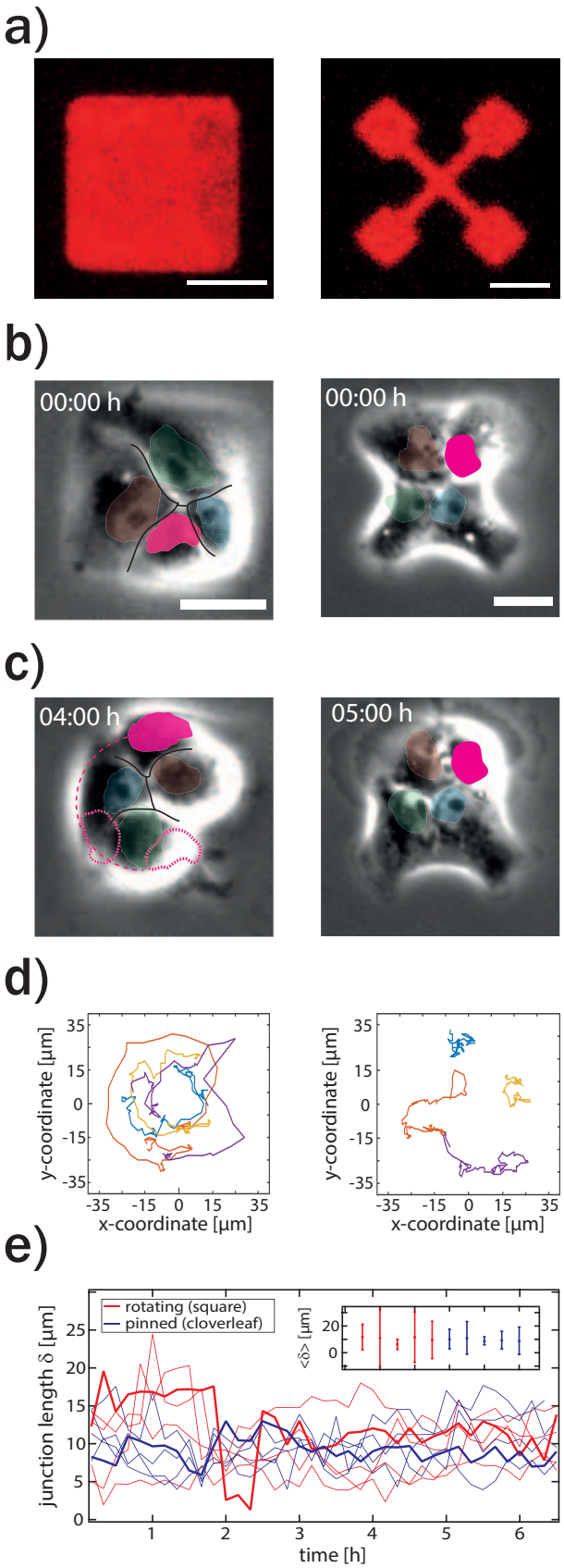

Figure 3.46: Pinning of cells by choice of adhesion geometry. **a)** Fluorescence image of the two different adhesion geometries for systems of four cells. **b)** Phase-contrast images of initial configuration of four cells on the square (left) and the cloverleaf (right). Time point for the cloverleaf chosen so the four cells have reached a configuration where each cell predominantly sits on one of the adhesive islands and arbitrarily for the square. Contact lines between the cells on the square traced in black. The nuclei, as extracted from the corresponding fluorescence image, are overlaid in color. **c)** Configurations of the cell arrangement at time points four or five hours later. The cells on the square pattern have rotated, as indicated by the dashed pink line roughly highlighting the pink cells trajectory and the contact lines between the cells. On the cloverleaf pattern, the cells have not moved much. **d)** Exemplary cell tracks of a four cell system on a square (left) and a cloverleaf (right). The cells on the square rotate, whereas the cells on the cloverleaf only move from their initial positions (see the red and the purple trace) until they reach a stable arrangement as the one shown in b) and c), at which point the only fluctuate around that position. **e)** Junction length for five sets of four cell systems on squares (red) and cloverleafs (blue) over time, with one of each highlighted for easier viewing. The junction length seems to fluctuate more for the rotating cells on the square, whereas those pinned on the cloverleaf show less scattering in their time courses. The inset shows the time averaged junction length for each track (dot), along with their variance (bar), confirming that the length of the junction fluctuates more on the square. Scale bars correspond to 25 µm.

3.4.3 Towards a machine learning algorithm for automated cell-cell junction readout

Actin is present throughout the entire cell bodies, though the lifeact-eGFP fluorescence images show a preferred accumulation along the cell-cell junctions (see e.g. Fig. 3.43). While most of the time this stronger fluorescence signal is sufficient for the human eye to be able to determine the contact lines between the cells and the vertices where they meet, the signal is too noisy (and too variable between groups of cells) for a classical image processing algorithm to consistently achieve good results. As described in chapter 2.6, when traditional algorithms with fixed rules are insufficient, machine learning algorithms can offer a powerful alternative.

In the course of this work, two machine learning approaches were compared, one based on custom code written in Matlab (The MathWorks Inc., Natick, Massachusetts, United States) and one based on the freely available software Ilastik [185]. *A priori*, the completely developed Ilastik software has the advantage of a more convenient interface and a better performance when it comes to calculation times. On the other hand, a self-written program can be perfectly tailored to the presented problem. It can thus be programmed to account for any desired feature, whereas a preexisting program allows only the choice between predefined features.

Details for both approaches can be found in appendix A.2.11, but in short, the key difference between the two programs is that the Ilastik software uses a large number of features describing intensity, edge and texture (on several length scales) of the input images for its prediction, while in contrast the less efficient custom algorithm uses less of these parameters but includes information about the x- and y-coordinate of each pixel, as well as how far it is from a Voronoi construction created from the nuclei positions. In essence, the custom algorithm makes use of the *a priori* knowledge of the expected position of the cell-junctions, namely that they are approximately described by the Voronoi construction and should not deviate too strongly from it [186] and that they are located more towards the centers of the cell and farther from the corner. The expectation is thus that the Ilastik software will be more sensitive in cell-cell junction detection, but also more likely to falsely identify points not on the cell-cell junctions (in particular signal stemming from an actin cortex forming along the cells perimeter) than the custom algorithm.

The results from both algorithms agree with this, as seen in Fig. 3.47. The custom algorithm has a low error rate of pixels falsely identified as belonging to cell-cell junctions,

especially towards the edge of the image. It does, however, also fail to identify significant portions of the junctions. In contrast, the Ilastik algorithm is more sensitive to correctly identifying the junctions, but as expected, it also picks up a lot of noise, in particular along the cell boundaries.

These impressions are quantified in Fig. 3.48 which shows the junction identification rate and the misclassification rate for both algorithms for the 25 images belonging to the test data set. The junction identification rate is defined as the ratio of pixels correctly identified as belonging to the cell-cell junctions N_{correct} over the total number of pixels manually determined to belong to the junction N_{junction}:

$$r_{\text{junc}} = \frac{N_{\text{correct}}}{N_{\text{junction}}} \tag{3.27}$$

Meanwhile, the misclassification rate is defined as the ratio as points incorrectly labeled as belonging to the cell-cell junctions N_{wrong} over the total number of pixels belonging to the junction N_{junction}:

$$r_{\text{missclass}} = \frac{N_{\text{wrong}}}{N_{\text{junction}}} \tag{3.28}$$

As already seen by visual inspection, the custom algorithm has a much lower junction identification rate of $r_{\text{junc}} = 8.5 \pm 5.8\,\%$ (error here and for following rates indicates the standard deviation) than the Ilastik algorithm's rate of $r_{\text{junc}} = 90.0 \pm 5.1\,\%$. On the flip side, however, the missclassification rate of the Ilastik prediction is also significantly higher, with $r_{\text{missclass}} = 439 \pm 196\,\%$ compared to the custom algorithm's $r_{\text{missclass}} = 7.2 \pm 5.0\,\%$.

These error rates show that the algorithms qualitatively behave as expected: The custom algorithm is less sensitive but more robust to noise, whereas the Ilastik algorithm is more prone to misidentifying other features in the image as part of the cell-cell junction, but much less likely to miss parts of the actual junction. Quantitatively, however, both algorithms perform poorly, with the custom algorithm detecting less than 10 % of the junction and the Ilastik algorithm misidentifying four times as many points as are actually present in the real junctions. As could be seen in Fig. 3.47, however, much of the misclassification occurs along the cell perimeter. Assuming the cell-cell junctions are only of interest for the energetic description via the vertex model, however, these areas are not necessarily relevant. If the cell-cell junction lines are approximated by straight lines, then

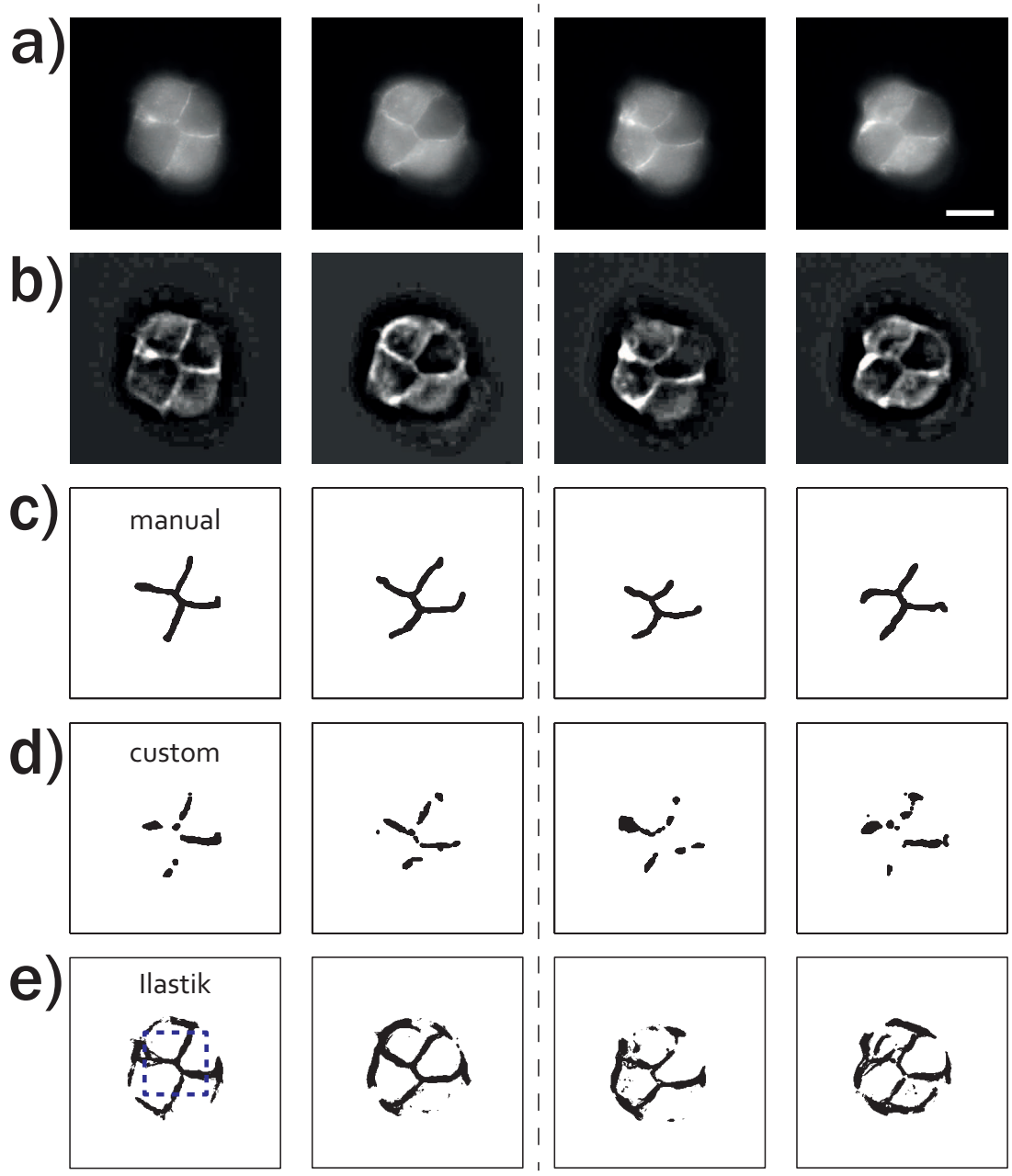

Figure 3.47: Machine learning algorithm results for automated cell-cell junction recognition. For the images shown, the algorithms were trained on 25 % of the available data. The first two columns show images that belonged to the training data set, the second two column show the results for images that were not part of the training data. **a)** Lifeact-eGFP fluorescence images used as input for the image analysis. **b)** The same images after preprocessing with a Gaussian blur and a bandpass filter. **c)** Reference cell-cell junction lines for training and validation, obtained by manual image segmentation. **d)** Results for the custom recognition algorithm. **e)** Results obtained with the preexisting Ilastik software. The dashed blue square highlights the area considered when examining the algorithms performance only around the center.

the angle under which they meet in the vertices is the important parameter that fully defines the junctions all the way out to the perimeter. It is of course worth noting that the approximation of this angle might be more precise if taking the full junctions into account, but if the actual junctions are close to straight lines to begin with the deviations are minor.

To this end, an examination of how the Ilastik algorithm performed just in the central part of the image makes sense. If the misclassification rate there is low, the algorithm might still be useable and only require exclusion of the outer part of the image. Thus, the third curves in Fig. 3.48 show r_{junc} and r_{misclass} for the Ilastik prediction when only taking into account the center of the image (specifically a square with the side lengths reduced to 30 % of the full image, centered around the middle of the image as highlighted in Fig. 3.47). The result is a drop in the misclassification rate by more than a factor of 2 to $r_{\mathrm{missclass}} = 176.0 \pm 99.2\,\%$. At the same time, the rate of correct junction identification is barely affected at $r_{\mathrm{junc}} = 89.3 \pm 6.2\,\%$. This confirms that a majority of the misclassifications occur along the cell periphery. Consequently, this approach seems to be more promising than the custom algorithm for future work, though even the reduced misclassification rate is still very high. A best case scenario would thus combine the multitude of intensity, texture and edge features used by the Ilastik algorithm with the additional parameters implemented in the custom algorithm (x- and y-coordinates, distance to the approximation via Voronoi construction) that help suppress misidentification along the periphery. Alternatively, pre- or postprocessing to reduce the images or the prediction results to their central part would also be a feasible approach. Unfortunately, the junction identification rate is also not quite high enough to expect the cell-cell interfaces to be extracted robustly. Fig. 3.48a shows that for some of the images in the test set, where the signal-to-noise ratio was particularly poor, the rate fell below 80 %. In cases where the observed distances in the image become particularly small (e.g. the junction connecting the two threefold vertices can drop below 5 µm as seen earlier in Fig. 3.46), this rate will be insufficient. It remains to be seen, however, what rate is really necessary to extract all the important parameters. For the time being though, the algorithms are incapable of producing the necessary robustness that is required for measuring the parameters δ and β, and thus an examination of the energetic behavior of the four cell systems via the vertex model was not possible. Further improvements of the algorithms or even the noisy underlying image data would change this, however.

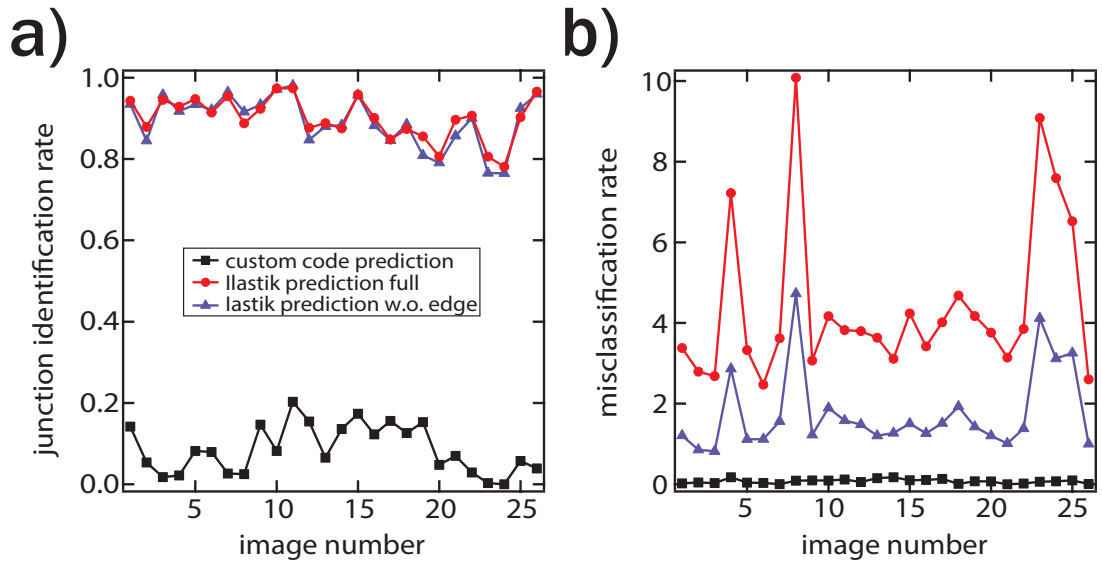

Figure 3.48: Quantification of classification rates for the various algorithms. **a)** Rate at which pixels labeled as belonging to the junction are correctly identified. The custom algorithm has a low accuracy and misses many of the pixels belonging to the junction, while the Ilastik algorithm performs well most of the time. Despite this, there are instances where the accuracy drops below 80 %, typically when the signal-to-noise ratio in the images is particularly poor. **b)** Rate at which pixels labeled as not belonging to the junction are falsely identified as such by the algorithms. The custom algorithm has a very high accuracy and has hardly any false positives, whereas the Ilastik algorithms labels many pixels as belonging to the junction even though they do not. This performance is significantly improved (roughly by a factor of 2) when the edge is excluded, but even so the rate is still high.

3.4.4 T1 transitions in minimal four cell systems

While an investigation into the packing states of the four cell systems in terms of the energy levels in a vertex model requires complete knowledge of length and orientation of the cell-cell junctions which was not yet possible, these groups also allow probing T1 transitions. The necessary information for this is simply the change of the orientation of the junction connecting the threefold vertices, which could also be extracted from a successful automated image analysis. Lacking this, however, it is still possible to observe the occurrence of T1 transitions manually. Fig. 3.49 schematically shows a T1 transition for a minimal system on the cloverleaf pattern, as well as the lifeact-eGFP fluorescence images showing the time evolution of one T1 transition observed in the experiment. This confirms that the fundamental grouping of four cells is sufficient for these critical cell rearrangements to arise. It also indicates that the effective noise in the system is sufficient to overcome the energy barrier associated with shrinkage of the distance between the two threefold vertices [58], as the system is symmetrical in itself and isolated from any surrounding cells or other sources of external forces that could actively drive the transition. No stable fourfold vertices are observed, in contrast to some recent findings of tissues where they are stable over relatively long periods of time [187–189]. This is, however, in agreement with theoretical findings that these vertices are always unstable unless the edge tensions depend on edge orientation, which in this symmetrical arrangement should not be the case [175].

To further probe this energy barrier, the size of the adhesive pattern is reduced. The theoretical work by Bi et al. examined the energy of a four cell system within a monolayer as it undergoes a T1 transition [58]. The system's energy increases as the junction length decreases until it reaches a maximum when the two threefold vertices fuse into a fourfold vertex. Fig. 3.50 shows a rough hypothetical schematic for the energy of two different groups of four cell systems, one on larger and one on smaller patterns. The energy minimum $E_{0,s}$ for the smaller pattern lies higher up on the slope than the minimum for $E_{0,l}$, assuming the average length of the junction shrinks with shrinking pattern size and the length of this junction dominates the energy term. As the energy barrier ΔE the cells need to overcome to run through a T1 transition is given by the difference between the minimal and the maximal energy $E_{\delta=0}$, the cells need to overcome a smaller barrier ΔE_s on the small cloverleafs than the barrier ΔE_l the cells on the large cloverleafs need to surmount.

Bi et al. suggest the rate of transition between the two metastable, energetically minimal

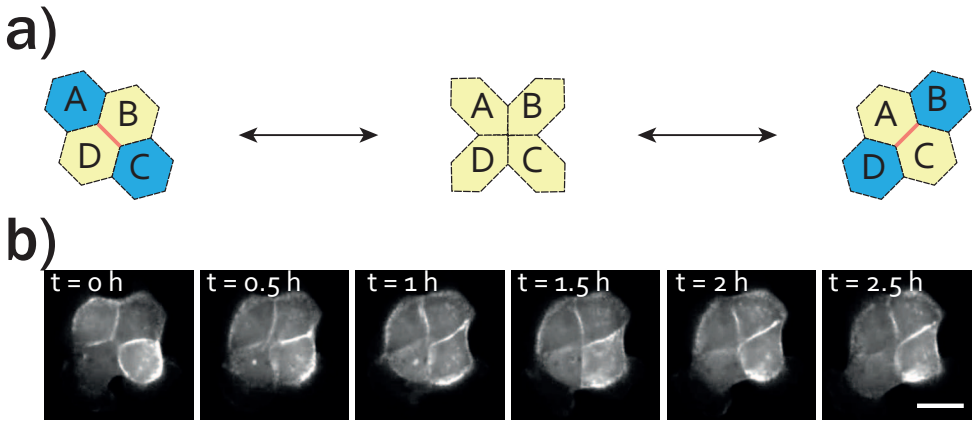

Figure 3.49: T1 transitions in minimal four cell system. **a)** Schematic drawing of a T1 transition in a system of four cells (labeled A, B, C and D). Each cell remains in the same position, but their configuration changes. Initially, two of the cells (indicated in blue) only have two directly neighboring cells, whereas the other two (indicated in yellow) have three direct neighbors. The two threefold vertices move together until they fuse into one fourfold vertex in an intermediate state, where all four cells have three neighbors. Finally, the fourfold vertex degenerates into two threefold vertices, with the two initially separated cells remaining in contact and the other two cells now separated. **b)** Experimental occurrence of a T1 transition in a four cell system on a cloverleaf pattern. An observation period of 2.5 h is shown, during which the neighbor configuration switches as described in a). Scale bar corresponds to 25 µm.

states is described in analogy to an Arrhenius process [58, 176]:

$$R = \omega_0 e^{-\Delta E/\epsilon} \tag{3.29}$$

Classically, ΔE in this equation describes the energy barrier between the two states, $\epsilon = k_b T$ is the scale of fluctuations of the energy, whereas ω_0 denotes the frequency at which the system attempts to escape its metastable state. In cell collectives, ω_0 and ϵ are related to the frequency of cell protrusion formation and active fluctuations of the cell shape. Taking only ΔE to be a collective property, and assuming ω_0 and ϵ are single cell properties, Eq. 3.29 predicts that the T1 transition rate between groups of four cells of the same type on cloverleaf patterns scales (in some undetermined matter) with the energy barrier. As detailed above, if cells are confined to smaller cloverleaf patterns, their energy barrier ΔE_s is smaller than for larger cloverleafs, and correspondingly the T1 transition rate should be higher.

Despite the fact that the junction length fluctuates significantly over time even for cells in transiently stable arrangements (see Fig. 3.51), this behavior is confirmed by the initial results shown in Fig. 3.52. As expected, cells confined to smaller cloverleaf patterns show a

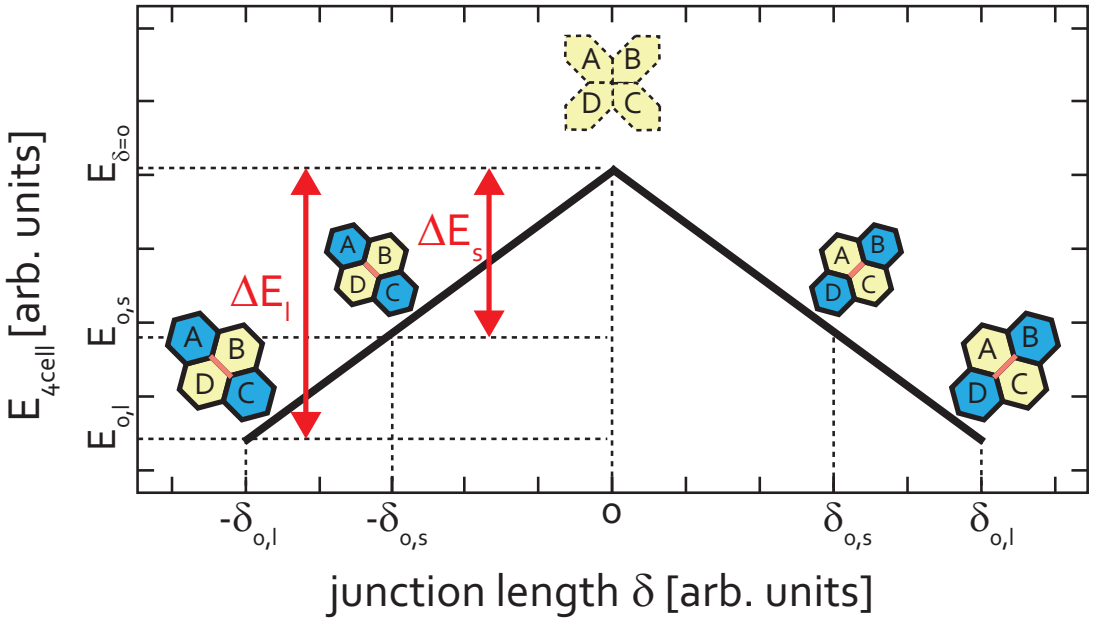

Figure 3.50: Schematic of hypothetical energy landscape for the total energy of two different four cell systems undergoing T1 transition. The simplified curve for the energy is chosen so that it conforms to the general trend of increasing energy with decreasing junction length determined theoretically by Bi et al. [58], though any further features such as curvature are approximated by a linear trend, because the increase of E with decreasing δ is the feature of relevance for discussion here. The larger four cell system's energetic minimum (which is assumed to correspond to a single junction length $\delta_{0,l}$) lies at $E_{0,l}$. As the length of the junction δ shrinks in the process of undergoing T1 transition, the energy of the system increases, until it reaches its maximum $E_{\delta=0}$ when the two threefold vertices have fused into a fourfold vertex. The energy barrier for this system's transition is given by $\Delta E_l = E_{\delta=0} - E_{0,l}$. In contrast, the energetic minimum for a system confined to a smaller cloverleaf $E_{0,s}$ is assumed to be higher than $E_{0,l}$, because its mean junction length is already smaller (see Fig. 3.52). Consequently, the corresponding energy barrier ΔE_s for a T1 transition to occur is also smaller than ΔE_l.

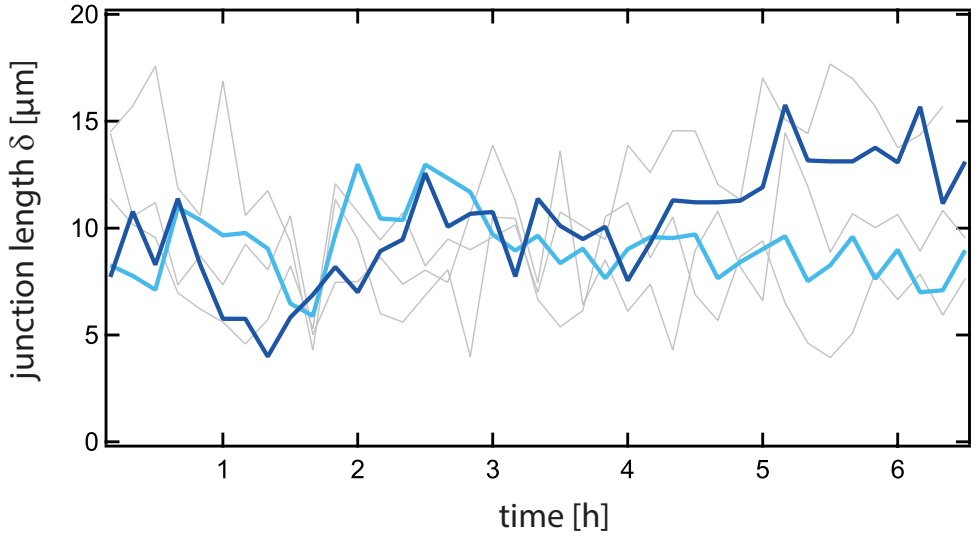

Figure 3.51: Fluctuation of junction length δ in a four cell system. The junction length was measured by manual tracking of the positions of the threefold vertices. Traces of the time evolution of the junction length are shown for five systems of four cells, with two curves highlighted in blue for ease of viewing. Even in transiently stable states, the length of the junction fluctuates significantly.

decreased mean junction length δ between the two threefold vertices. This is accompanied by the inverse trend in the frequency of occurrence of T1 transitions, which appears to be higher on the smaller patterns. The determined values come with high error bars, however, as the manual observation of T1 transitions is not perfect. In particular, the signal-to-noise ratio in the lifeact-eGFP fluorescence images is insufficient to clearly pick up T1 transitions of the type where the new cell-cell junction that forms after reaching a fourfold vertex is between the same pair of cells that was already sharing a junction before assuming the fourfold vertex arrangement. T1 transitions where the junction forms between the other pair are easier to identify, as they are characterized by a flip in the orientation of said junction, but Etournay et al. showed that there are even regimes where the dominant form of T1 transitions occurring both loses and gains connections oriented along the same axis [59].

Naively, in the symmetric setup of the cloverleaf pattern with no outside cells or other external forces, one would assume the probability of forming a junction between either of the two possible cell pairs is equal when starting from the unstable arrangement with a single fourfold vertex. This is reflected in the symmetry in the schematic energy landscape sketched in Fig. 3.50, though it is worth noting that this was only roughly true for the explicit Hamiltonian used by Bi et al. [176]. They also found a dependence of this energy on the local topology when theoretically examining these transitions in a tissue where the

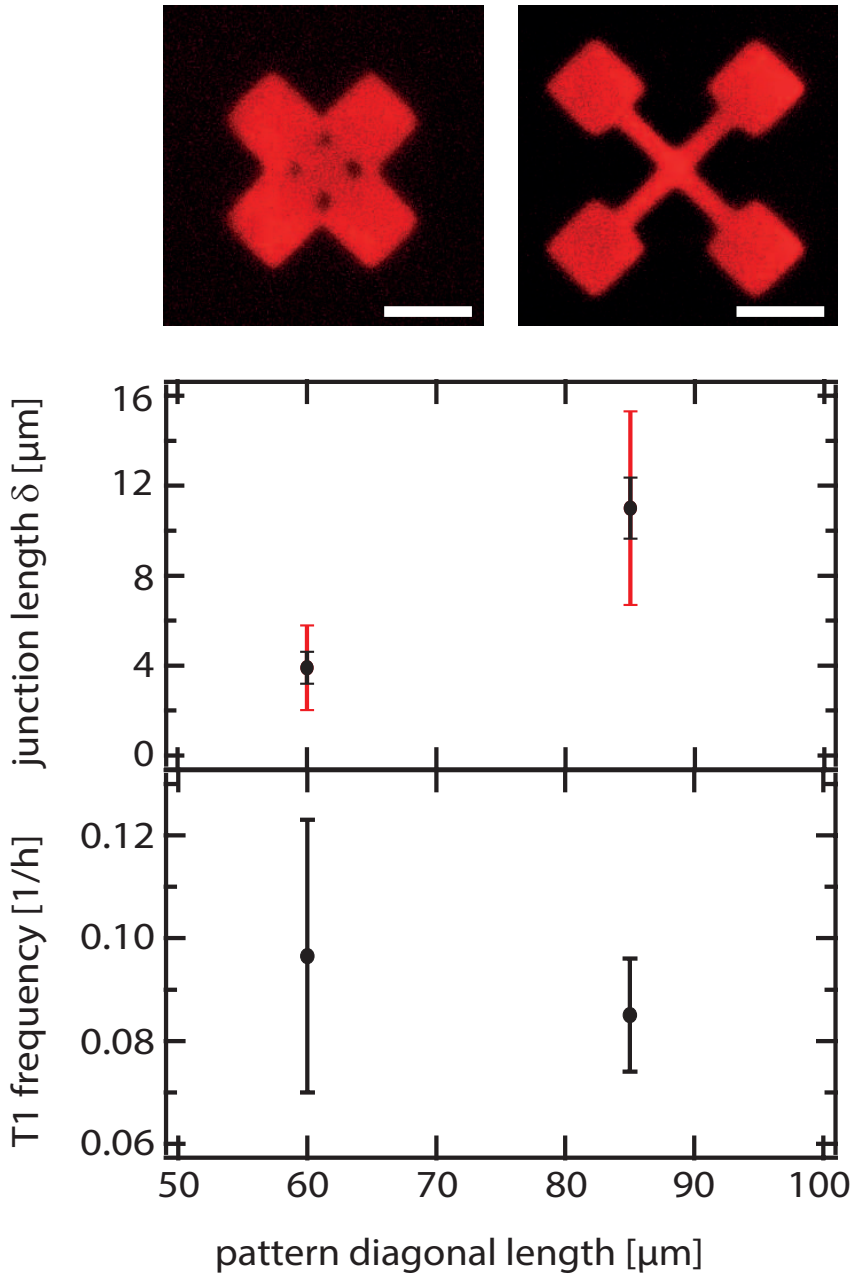

Figure 3.52: Artificial stretching/compressing of cell arrangement. Cells are placed on cloverleaf structures of different diagonal length (scale bars corresponds to 25 µm). The mean junction length δ and the frequency of T1 occurrence for groups of four cells are shown in dependence of the size of the underlying pattern. For the junction length, the standard deviation (red error bar) is shown in addition to the standard error of the mean (black error bar), to highlight the large fluctuations. Error bar for T1 Frequency is calculated by Gaussian error propagation of the estimated uncertainty in amount of T1 transitions observed and estimated uncertainty in the time spent in the stable configuration.

four participating cells had neighbors [58]. In this case the energy landscape is no longer symmetrical and thus there is likely a preferential direction for the new junction to be formed. The presence of neighbors might be of particular relevance, as it can affect the

shape of the cells involved in the T1 transition, which can in turn influence the height of the energy barrier for the T1 transition, with a critical transition when the energy barrier vanishes and the tissue becomes fluid [57].

3.4.5 Discussion

In conclusion, the study of minimal units necessary for the emergence of collective phenomena in cell behavior is an intriguing field. Groups of two or four cells placed on large square adhesive islands organize into typical geometrical arrangements. In agreement with previous results, however, the cells do not remain stably pinned in any configuration, but rather display collective rotation behavior. Still, the characteristic organizations that can be observed at least transiently suggest energy minimization plays a critical role in the small collectives' behavior. Capable of capturing cell-cell interactions as well as cell shapes, the vertex model is an intuitive choice to interpret observed phenomena. In addition, by observing packing on the large squares, it might be possible to extract mechanical parameters simply by optical measurements.

In the simplest case, the energy of a system of two rotating cells on a square depends only on the current angle between their cell-cell junction and the pattern wall. The observed distribution of angles for all time points of all observed cell pairs shows a maximum around 0°, which decays relatively steadily as the angle increases. Assuming cell pairs spend the most time in the energetically optimal arrangement, the minimal energy must correspond to the peak in the observed angle distribution. Using this assumption, a ratio $\alpha/l\kappa = 6.0008$ can be calculated from the minimal energy condition of the vertex model (Eq. 3.17) for the MDCK cells used in the experiment, defining a scaling between the cell-cell adhesion parameter α and the cell cortex contractility κ (scaled by the side length of the square pattern l). Unfortunately, however, fitting the distribution of observed angles in analogy to a Boltzmann distribution results in very poor agreement.

Due to this discrepancy between the model and the experimental observations on rotating cells, the adhesive geometry was optimized for systems of four cells, by replacing the large square pattern with a more complicated cloverleaf. On these geometries, each of the four cells is more or less pinned to its own adhesion island, but the collective still forms cell-cell junctions on the adhesive bridges connecting them. Observed packing is very reminiscent of a common arrangement of four cell systems observed on large square patterns, with two threefold vertices, separated by a cell-cell junction between the two cells

in the system that have three direct neighbors. While confinement was not yet perfect, these systems were shown to suppress collective rotation to an extent, leading to transiently stable arrangements. These stable states were observed to last between one hour and eight hours, and the cell collectives were deemed to be in these stable arrangements for about 58 % of the time they were observed.

These transiently stable states should be conducive for applying a vertex model and extracting mechanical parameters from the optical measurements, as it seems likely that these stabilized systems that can fluctuate less will spend more time near their energetic minimum. For instance, the energy of the four cell system in the vertex model depends on the length δ of the junction connecting the two threefold vertices. This work showed that while the length of this junction fluctuates even for the stable arrangements, the fluctuations in junction length for cells on the cloverleaf pattern appear to be reduced compared to cells on the simple square patterns.

An exact analysis with the vertex model would require an automated algorithm for extraction of this junction length as well as other parameters such as the angle β under which the cell-cell junctions meet in the three-fold vertices, in order to achieve the necessary statistics to extract meaningful parameters from the fluctuating systems. Unfortunately, the image quality of the lifeact-eGFP fluorescence time-lapse movies used in this work proved to be insufficient for traditional image analysis algorithms. To this end, in this work, automated image processing via machine learning algorithms was attempted. Though the results via these decision tree methods were significantly improved compared to standard methods, in the scope of this thesis it was not possible to overcome the underlying problem of poor image quality entirely.

Unlike the exact analysis of energetic states, examining the occurrence of T1 transitions in these four cell systems does not necessarily require and automated readout of the cell-cell junction lines (though it would also benefit from it). Manual observation was sufficient to hint at a dependence of the T1 transition rate on the average length of the junction δ, which agrees with theoretical predictions of the energy landscape and its dependence on said length. The results must be taken with care, however, as the difference in rates observed for systems of four cells with smaller and larger mean junction lengths (achieved via variation of the size of the underlying adhesive cloverleaf pattern) lies well within the range of the rather large error.

One reason these rates cannot be determined more precisely is the same as for the failure of the automated image analysis: the underlying image quality is insufficient, particularly

when the junction length δ takes on small values. In future work, this problem could be circumvented by switching to a cell line with a different fluorescent label. For a good signal of the cell-cell junctions in comparison to their background, E-cadherin is a suitable target, as well as the cell membrane, markers for which have successfully been used for such image segmentation problems in the past, for instance in the *Drosophila* pupal wing [190].

In the process, improving the confinement of the four cells to their individual places would also be beneficial, either by fine tuning the cloverleaf patterns further, or by switching patterning techniques altogether from microcontact printing to gold patterns, with the passivation by PLL-PEG replaced by something even more cell repellent, such as Pluronic (F127). Improving this confinement would not only increase the frequency at which four cells appear on a pattern together, it would likely also increase both the percentage of time those four cell systems spend in their "stable" configurations, and the length of these stable states. Currently, while these states last long enough that T1 transitions were observed in the experiments, they are actually too short for a proper study. Transitions were observed with a rate slightly below $f = 0.1\,\frac{1}{\mathrm{h}}$ for the smaller cloverleaf pattern, which corresponds to a mean time $t = 10\,\mathrm{h}$ between transitions, on the order of the longest stable periods observed in the experiment. Frequently, the quasi-stable states in the experiment lasted less long. To make matters worse, on the large cloverleaf patterns the observed mean time between transitions was even longer, at $t = 12\,\mathrm{h}$. In order to properly study these transitions and the energy barriers governing them, the periods spent in stable configurations need to be increased to be larger than the mean transition time.

In addition to improving the confinement, inhibition of cell division could prove beneficial in achieving this goal. Frequently, experimentally observed systems of four cells had very short lifetimes, as one of the cells on the pattern divided, greatly reducing the usable statistics. Additionally, it is likely that preparations for division, during which cells drastically change their shape, already introduce perturbations into the system, and these perturbations might be one factor contributing to driving the system out of its quasi-stable states. Preventing cell division thus could increase the stability of these systems. In the past, Mitomycin C has been used successfully to inhibit proliferation in various systems [100, 191, 192].

In particular, if cell proliferation were inhibited, but in general for an increase in the currently poor statistics, having four cells on as many patterns as possible is necessary. To this end, the use of still novel single cell printer technology might be conceivable, if it

can be adjusted to print four cells next to each other rather than a single cell, and if a sufficient throughput of cell seeding can be achieved.

Taken together, there is still much room for improvement on this project in future work, though the initial results are intriguing enough to be worth the effort.

Chapter

4

Conclusion and Outlook

In this thesis, collective cell migration was studied in confined geometries. Microstructuring methods were used to restrict cells to geometries akin to those found in classical fluid dynamics experiments, and on long time scales, migration of cell collectives is very reminiscent of fluid flows. Thus, the phenomenological description of this behavior can be considered cellular hydrodynamics. The work in this thesis constitutes an expansion of previous studies on collective cell migration. These have examined collective motion of unconfined cell monolayers (e.g. in the Weitz group [27, 38]), as well as spreading of large cell sheets into model wounds (e.g. in the Ladoux and Silberzan groups [17, 28]). Radial spreading of large circular colonies (e.g. in the Losert group [29]), but also of smaller patches (e.g. in past work of the Rädler group [32]), has been analyzed as well. Most closely related to the work of this thesis, the Ladoux group has studied the emergence of a new mode of collective migration when cells were confined to sufficiently narrow stripes [37].

Using a similar straight confinement, in section 3.1 we explored the flow and diffusion of an epithelial sheet expanding into artificial microchannels. It is well-known that a Newtonian fluid in similar circumstances displays the parabolic flow profile associated with Hagen-Poiseuille's law, but this behavior depends on the underlying microscopic properties. For instance, the inclusion of turbulence rather than strictly laminar flow would lead to changes in the resulting velocity profile. Vice versa, with the help of modeling, it is possible to relate observed velocity profiles back to the underlying microscopic behavior. This is of particular interest when the underlying microscopic mechanisms are not as clear as they are in externally driven Newtonian fluids. The flow profiles of active fluids in pipe flow are less well studied, however, than those of their Newtonian counterparts, and equivalent experiments examining the detailed velocity profile of collectively migrating cells did not previously exist.

Our study showed that a collectively migrating epithelial sheet adapts a very flat, plug-flow like profile. The cell number density along the channel displayed a gradient, with densities increasing from the leading edge to the back of the cell sheet. The Fisher-Kolmogorov reaction-diffusion equation successfully captures the form of the density profile, including

its propagation in form of a traveling wave. These results are in agreement with previous successful descriptions of collective migration of unconfined epithelial sheets via said equation [149, 150]. In order to reproduce the speed of the cell sheet's leading edge, however, a density independent constant drift velocity with unclear underlying mechanism needed to be introduced. It seems plausible that this drift is related to cell polarization and is the same mechanism that is responsible for collective migration in systems without density gradients, such as circular systems that show the spontaneous onset of collective rotation [60, 142]. Specifically, a break in symmetry at some point in the system leading to a preferred polarization direction, in association with coupling of this polarization over multiple rows of cells, is a good candidate for such a mechanism.

Our study showed that the MSD of single cells within the monolayer is increased when it migrates collectively in one direction. This would be consistent with the notion of a monolayer in its confluent state approaching a jamming transition, whereas the appearance of a free edge leads to an unjamming of the whole system. In contrast to the MSD, the frequency of vortex formation also decreases under flow. These bursts of collective migration are likely not being suppressed by the presence of a preferential migration direction, but instead might be oriented along the density gradients, evening them out. Thus, it is not the motion of single cells, but rather collective bursts of correlated short scale active migration that cause the long range diffusive behavior. This interpretation is also in agreement with more recently published results that likewise show evidence of clusters of coordinated activity in collective cell migration [1].

Given the likely role of preferential polarization due to symmetry breaking on the resulting collective migration, future experimental work visualizing the polarization dynamics would be of interest. Fluorescent labeling of the early markers of polarization, such as Rac1 or RhoA, might allow insights into the coupling of polarization, both between cells and to the boundaries, and help elucidate its exact contribution. Experiments directly comparing the collective migration in narrow channels to unconfined scenarios, such as wound healing, might help shed light on the question of where the relevant symmetry breaking in the system occurs. Polarization might be preferentially oriented by the presence of the channel walls, but it is also possible that the confinement of neighboring cells suffices to reduce the likelihood of polarization in that direction.

As a significant contribution to the migration of the cell sheet in our channels stems from proliferation, in section 3.2, we studied the effect of an underlying global migration direction on the orientation of the cells' division axes. Flow fields and cell division events

were correlated to gain insight into the motion of expanding monolayers, revealing strong alignment between the orientation of the division axes and the underlying migration direction.

As cells have no known mechanism for sensing global quantities such as the underlying flow, the relationship between division axes and local quantities was investigated. We found the strongest correlation between the orientation of the cells' division axes and local flow gradients. Specifically, the average order between the axes' orientation and the strain rate tensor's main axis was twice as high as the order between division axes and the local flow direction. This agrees well with the hypothesis that stresses in the migrating cell sheet are proportional to the velocity gradient, and that these stresses subsequently orient the cell divisions. It would also make sense for an expanding tissue to orient individual cell divisions in the direction of expansion, in order to minimize the principle stress.

Many of the phenomena observed in this context could be reproduced with a previously published particle-based model. This model had in the past successfully recreated the viscoelastic properties of tissue spheroids and their growth as well as the fingering instabilities at the front of a motile tissue [105, 124, 125, 156, 157]. The model's success at capturing the division orientation despite never having been intended for this purpose is of particular noteworthiness. Despite good agreement in general, the simulations failed to capture experimental behavior close to the boundaries. In future work, it might be necessary to describe the cells by more than the two particles that are currently being used to describe them. This would help better capture the cells deformability and complex interior structure, which might play crucial roles close to the boundary. On the experimental side, future work might test other cell lines in the same experimental setup in order to probe universality of the observed behavior. In addition, seeing whether the orientation mechanism holds up in 3D would certainly be of great interest, as many collective cell migration phenomena *in vivo*, in particular cancer invasion, occur in 3D.

In addition to the fluid-like behavior observed in straight channels, cell monolayers can also show a more solid-like, glassy behavior under certain circumstances, such as high densities. Thus, in section 3.3 we examined epithelial cell sheets migrating through channels that contained a constriction, which is expected to lead to a buildup of cell density and potentially jamming. For a Newtonian fluid under the same conditions, the resulting velocity profile is determined by Bernoulli's principle and mass conservation, with increased velocities in the bottleneck. This allows maintaining a constant flux all throughout the channel for these incompressible fluids. Migrating cell sheets are quite different, however,

potentially being compressible and with proliferation breaking mass conservation. Again, the resulting large scale flow profile should contribute to an insight into the underlying microscopic mechanisms. Our results show that a plateau of low velocity forms prior to the constriction, but from there on, through the constriction and reaching into the wider area behind the channel, the velocity increases relatively linearly until eventually another plateau is reached. This plateau in velocity prior to the constriction indeed seems to be the result of the cell layer approaching a jamming transition and becoming more solid-like as the cell density increases in this region. This result would agree with previous work by Angelini et al. studying cell monolayers approaching a glass transition with increasing density, that found increased regions of correlated motions but reduced velocities [38].

Our experimentally observed flow profile changes noticeably when the steepness of the transition area from wide channel to narrow constriction is adjusted. For steeper changeovers, the velocity profile seems to develop a dip prior to the constriction, with velocity actually dropping off to a minimal value in front of the constriction. Starting from this decrease, the velocity then increases roughly linearly in the constricted area, as previously. Conceivably, the steeper transition area leads to a quicker or more pronounced buildup of density localized to the width transition area, whereas for smoother transitions the higher density might spread out more over the wide part of the channel. In future work, it might be interesting to observe the development of this velocity dip over time. It is possible that as more time passes, the localized high density in the transition region can spread out more and thus the local minimum would vanish or become less pronounced.

Results from the experiment were compared with simulations from an active isotropic-nematic mixture model, but strong qualitative differences were found for both the velocity field and the orientation field. Based on these results, this continuous media approach is deemed unsuitable for describing the collective migration of cell sheets through a constricted channel. Potential compressibility of the cell sheet and the approaching of a jamming transition in the region prior to the bottleneck are likely reasons for this failure. Thus, in future work, modeling this process with a more detailed theoretical framework will be necessary. The cellular Potts model is a strong candidate due to the fact that it not only models the individual cells, but also accounts for details such as their shape. The shape of cells has recently been shown to play a role in jamming transitions of cell collectives [57], so a model capable of accounting for these should be more successful than a simple self-propelled particle-based approach. Successful modeling of collective cell migration through a constricted channel will be a key component in linking the observed macroscopic flow profiles to underlying microscopic mechanisms.

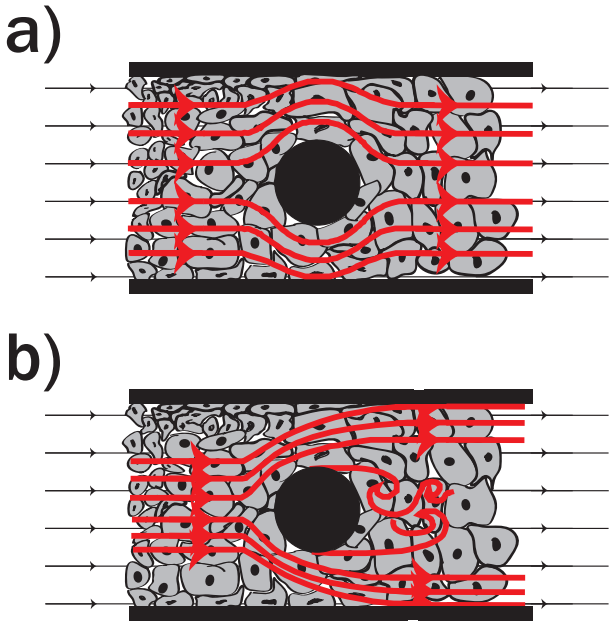

Figure 4.1: Possible experimental setup for future cellular hydrodynamics studies. In traditional fluid dynamics, the flow around an obstacle can be either laminar or turbulent, depending on conditions. It is possible various regimes might be accessible for collective cell migration. The flowlines for hypothetical collective cell migration under **a)** laminar conditions and **b)** turbulent conditions are shown.

Experimental work continuing this project should focus on direct measurements of the cell density through introduction of a fluorescent nucleus label. Determining the local cell number density would allow a much closer investigation of the relation between velocity and density, and thus could clarify the role and strength of jamming that seems to occur at the constriction entrance.

Further work could also focus on a closer investigation of the backflow that was found to sometimes occur at the entrance to the channel constriction, and its dependance on the steepness of the transition area. To this end, both single cell tracking via fluorescent nuclei and a more detailed local examination of the velocity profile in these regions might prove fruitful. In addition to examining this backflow, the velocity field in general could still be studied in more detail, for instance by examining how the constriction influences the formation of vortices.

Going a step further, other experiments inspired by classical fluid dynamics are imaginable to expand the "playing field" of cellular hydrodynamics. For instance, the collective migration of cells around an obstacle might prove interesting, as even in classical fluid dynamics, the flow field after the obstacle can be laminar or turbulent, depending on the Reynolds number (see Fig. 4.1). It is unclear how cells would react in this situation, and

whether or not both laminar and more turbulent behavior would be possible, depending on such things as geometry, velocity, strength of adhesion and density. Again, with the help of modeling, gaining some insight into the microscopic processes governing collective cell migration from the observed macroscopic flow behavior in this situation should be possible.

Finally, in section 3.4, microscopic rearrangements underlying macroscopic motion were studied directly by examining minimal systems of four cells. This is the minimal number of cells necessary for the occurrence of a T1 transition, and in this work, cloverleaf geometries were successfully used to create transiently stable configurations. These suppressed polarization induced collective rotation, which would perturb a regular appearance of T1 transitions. Our results showed an increased frequency of T1 transitions for smaller average lengths of the cell-cell junction which disappears during this transition. These results must be taken with a grain of salt, due to lying well within the range of the rather large error. They would, however, be in agreement with recent theoretical descriptions of T1 transitions in the framework of an energy landscape, where the system energy depends on the length of the contracting junction and is maximal at the transition point where it vanishes [58, 176].

The reason for the high error in the transition rate measurement are twofold. One large issue is the insufficient image quality associated with the lifeact-eGFP label used to visualized cell-cell junctions. This leads to the possibility of missing some T1 transitions or counting false positives. Due to this, in future work switching to a cell line with a different fluorescene label could prove fruitful. Both E-cadherin and the cell membrane are suitable targets. The other issue is, that although the cloverleaf patterns suppress collective rotation to a certain degree, they still only lead to transiently stable systems. The observed mean time between T1 transitions is on the order of the lifetime of these quasi-stable cell arrangements. For a cleaner study of the transition frequency, these lifetimes would need to be increased, which requires an improved confinement. To this end, a further fine tuning of the cloverleaf pattern might provide some improvement. Even more promising would be switching patterning techniques to something with stronger cell-repellent properties in the passivated area. Aside from improving confinement, suppression of cell proliferation could also help increase the lifetime of quasi-stable states, as the occurrence of a cell division immediately ends the observation period for any given system of four cells. In general, an increase in measurement throughput of these systems would also be very beneficial. Currently, the bottleneck is the frequency at which exactly four cells appear on the micropatterns. In the future, the use of still novel single-cell printer technology might

be conceivable as a method for increasing these occurrences, if it can be adjusted to print four cells adjacently.

All in all, the results of this thesis contribute to expanding our current understanding of the complex migration process of cell collectives. Such studies of the macroscopic phenomenology, along with similar approaches in the community, can allow insights into underlying microscopic mechanisms governing collective migration when combined with theoretical modeling. Given the important role this migration plays not only in the development of life, but also in diseases as prevalent and fatal as cancer, a better understanding of the entire mechanism is essential. The life sciences are becoming increasingly interdisciplinary, with researchers from various fields making significant contributions. Recent developments regarding how jamming or unjamming plays a role in cancer invasion prove that physics contributes to this group of diseases in a significant manner. Thus, if humanity wishes to continue making progress in its long-lived "war on cancer" [193–195], the contributions of physicists will be just as integral to research and treatment as insights coming from biology, chemistry or medicine.

Appendix A

Methods and Experimental Protocols

A.1 Microstructuring

A.1.1 Micromolding in capillaries for 3D structures

In order to perform experiments reminiscent of those from classical hydrodynamics with collectively migrating cells, it is necessary to create microstructured channels. These structures must be created on cell compatible surfaces and cells need to be seeded selectively only outside of them, so that they can then collectively invade.

To this end, poly(ethyleneglycol) dimethacrylate (PEG-DMA) channel walls are created on treated polymer surfaces ("ibiTreat" surface, Ibidi, Martinsried, Germany) via the micromolding in capillaries (MIMIC) method [196–199]. In this way, cells can be studied on a substrate that is established in cell-culture and extensively tested concerning biocompatibility, while at the same time they can be restricted to the desired geometries. The process for the production of samples, as it was used in publication P2 and P3 (see chapters 3.1 and 3.2), is shown in detail in Fig. A.1.

A poly-dimethylsiloxan (PDMS) mold is created from a silicon master wafer produced by laser direct imaging photolithography under cleanroom conditions. It is trimmed down to the appropriate size (ensuring to leave a slight edge on one side so the channels do not penetrate to the end of the PDMS). After treatment with argon plasma to render the structures hydrophilic, the PDMS is placed on the dish face down. Before the hydrophilic treatment wears off, a large drop of 2 % (v/v) solution of the photoinitiator 2-hydrody-2-methylpropiophenone in PEG-DMA (Mn=550, both Sigma-Aldrich Chemie GmbH, Munich, Germany), is placed in front of the PDMS, where capillary forces draw it into the recessed areas of the mold. Once the channels in the PDMS are entirely filled by PEG-DMA (confirmed by checking under a microscope), the whole sample is exposed to UV irradiation for 15 min by irradiation with a UV-ozone cleaning system (UVOH 150

LAB, FHR, Ottendorf, Germany) to crosslink the structuring polymer, turning it solid. Structures are stored overnight in a 50 °C drying oven.

The PDMS stamp is left on the completed structures while cells are seeded, so that they adhere outside of the channel area. Only after cells have grown confluent is the PDMS mold gently peeled off, exposing the channel entrances and allowing the cells to migrate into the channels in a collective fashion.

In some instances, reference measurements with cells seeded uniformly over the channel are of interest (in particular to distinguish effects of the presence of a boundary from effects resulting from the directional migration). For these cases, the PDMS mold is simply removed before the cell seeding step was performed, and cells are seeded uniformly across the channels.

For the project of collective cell migration through constricted channels (see chapter 3.3), this microstructuring process was improved (see Fig. A.2). As changing a variety of geometric parameters relating to the constriction significantly increases the amount of measurements that need to be performed, an increase in measurement throughput was desirable. To this end, the geometry of the silicon master wafer is adjusted to display fourfold symmetry, so that cells can migrate into channels from four directions at once. The PDMS mold is trimmed down to the appropriate size (leaving a slight edge on all four sides so the channels do not penetrate to the end of the PDMS) and a hole is punched into the middle (ensuring that all channels are cut into and exposed). After treatment with argon plasma to render the structures hydrophilic, the PDMS is placed on the dish face down, as before. Immediately, a frame, which has been 3D printed to have the correct size, is placed on the PDMS, with the hole in the middle remaining open. Before the hydrophilic treatment wears off, a large drop of 4 % (v/v) solution of the photoinitiator 2-hydrody-2-methylpropiophenone in PEG-DMA is placed in the middle of the PDMS, where capillary forces draw it into the recessed areas of the mold. A weight is quickly placed on to the frame so that pressure is exerted on the mold, ensuring its proper adhesion to the substrate. This prevents leaks of the polymer from the area that will later become the walls into the area that will later become the actual channel and needs to remain free from it in order to remain adhesive for cells. Once the channels in the PDMS are entirely filled by PEG-DMA (confirmed by checking under a microscope), the whole sample is exposed to UV irradiation for 60 min to crosslink the structuring polymer, turning it solid. Structures are stored overnight in a 50 °C drying oven.

As before, the PDMS stamp is left on the completed structures while cells are seeded,

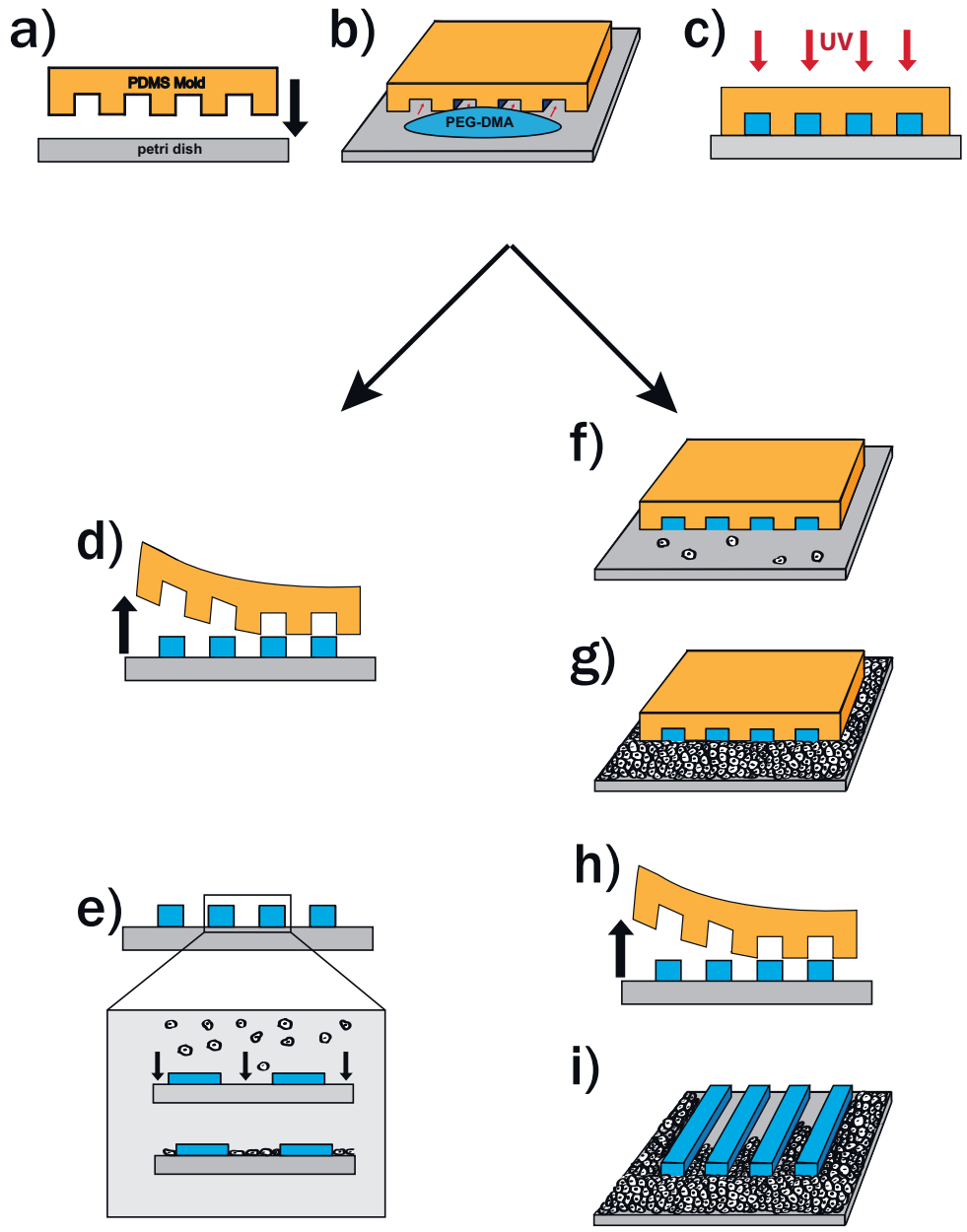

Figure A.1: Original microstructuring method for creation of channels for guided cell migration and control samples of resting confluent cell sheets. **a)** A PDMS mold formed from a master is placed onto a petri dish after plasma activation. **b)** A drop of PEG-DMA is placed in front of the mold. Capillary forces are sufficient to draw the second polymer into the channels of the mold. **c)** PEG-DMA is cross-linked by exposure to UV irradiation. **d)** To create the resting confluent cell sheets as references, the PDMS stamp is peeled off at this step of the microstructuring process. **e)** Cells are then seeded uniformly onto the sample, where they adhere and grow confluent, filling up the channels. **f)** Alternatively, to create channels that are initially free of cells and thus make a flow possible, cells are seeded before removal of the PDMS stamp. **g)** Cells are allowed to grow to confluence around the still protected channels. **h)** The PDMS mold is removed in the same manner as for the resting case. **i)** The channels become accessible and cells begin migrating into them. Adapted from reference[65] within the framework of Creative Commons Attribution 3.0 license.

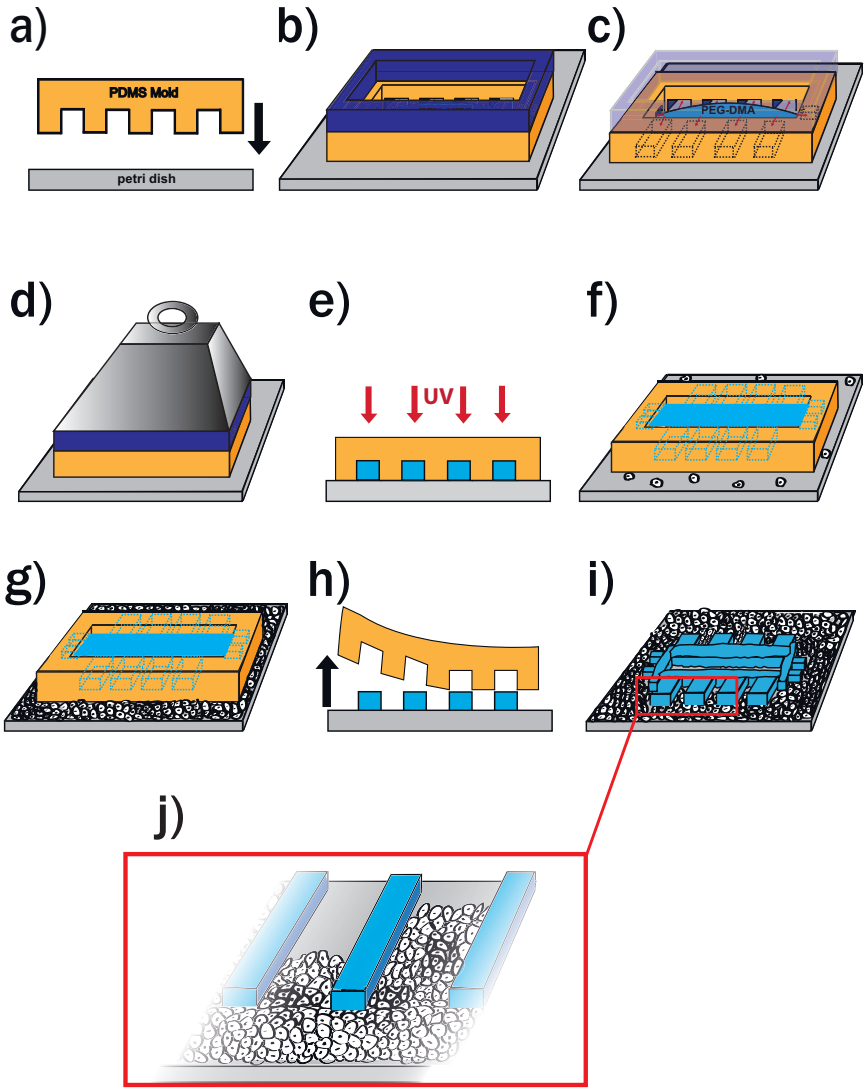

Figure A.2: Schematic of improved microstructuring method for creation of channels for guided cell migration. **a)** A PDMS mold made from a master and cut into the shape of a hollow frame is activated by plasma and placed on a petri dish. **b)** A 3D printed frame is placed on the PDMS master so that pressure can be exerted on it without blocking access to the middle. **c)** A drop of PEG-DMA is placed in the middle of the mold, where capillary forces draw the polymer into the channels of the mold. **d)** A weight is placed on the frame immediately after addition of the PEG-DMA, ensuring a tight connection between PDMS and dish so there is no leakage of PEG-DMA to the sides. **e)** Once the PEG-DMA has entirely filled the channels, UV irradiation is used to cross link it. **f)** Without removing the PDMS, cells are seeded on the dish, where they are allowed to grow for several days. **g)** The mold protects the actual channels from cell adhesion, so cells grow to confluence around it. **h)** The PDMS is then peeled off the dish very carefully. **i)** Collective cell migration into the now accessible channels begins from all directions. **j)** Zoom in on two channels on one side of stamp for enlarged view.

so that they adhere outside of the channel area. Only after cells have grown confluent is the PDMS mold gently peeled off, exposing the channel entrances and allowing the cells to migrate into the channels in a collective fashion.

A.1.2 Microcontact printing of ECM proteins

Microcontact printing was adapted to cell biology by Singhvi et al., who in 1994 stamped islands of hexadecanethiol $[HS(CH_2)_{15}CH_3]$ in self-assembled monolayers onto gold substrates. These islands support protein adsorption, whereas the remaining substrate, passivated with polyethylene glycol (PEG)-terminated alkanethiol $[HS(CH_2)_{11} - (OCH_2CH_2)_6OH]$, does not. Through exposure to purified ECM protein (specifically laminin), cell-friendly and cell-repellent areas were created [200]. Due to its power as a tool to study individual cells, in a predetermined shape that is consistent between all cells, and to find those same cells again later in the measurement, microcontact printing has found widespread use in the community since its original adaption. In particular, Théry et al. showed the orientation of the cell division axis depends on the geometry that cells are confined to [201]. Furthermore they showed the geometry of the adhesive environment influences the cells' stress fiber distribution [202] and polarization axis [203].

In addition to being very useful in the study of individual cells, microcontact printing and other similar micropatterning techniques that create defined cell-adhesive and cell repellent areas can be expanded to study systems of multiple cells. For instance, Tseng et al. used such patterns to show that the spatial organization of the ECM plays an important role in positioning of cell-cell junctions [182]. Expanding the use to dynamic phenomena, Huang et al. showed how two endothelial cells on a micropattern turn around each other in a very regular fashion [204]. Work by Segerer et al. expanded this to hold true for between two and eight epithelial cells on a pattern, though a discontinuity in the regularity of rotation occurs between four and five cells where there is a change in the general geometric arrangement of the cells [60].

In this work, microcontact printing was used to create patterns for the study of geometrical arrangement of four cells together on a micropattern. Both large squares and cloverleaf (four small islands connected by a cross) patterns were created following the same protocol (see Fig. A.3). A PDMS stamp with either the square or cloverleaf structures as protrusions is made from a silicon master wafer produced by laser direct imaging photolithography under cleanroom conditions. After 5 min UV treatment, this stamp is

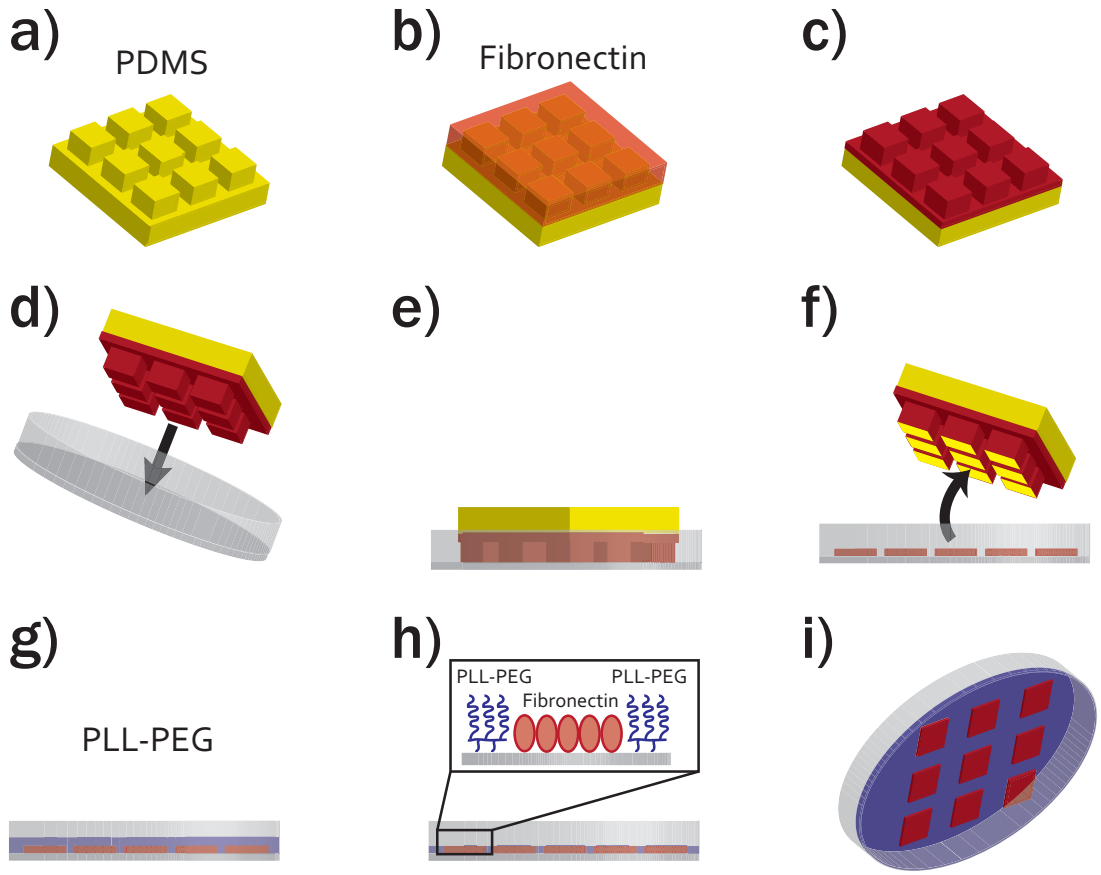

Figure A.3: Schematic of procedure for microcontact printing. **a)** A PDMS stamp with protrusion in the shape of the desired micropattern is prepared from a silicon master wafer. **b)** The stamp is incubated in a fibronectin solution. **c)** Only a thin film of protein remains on the stamp after removing the excess solution and rinsing the stamp. **d)** The stamp is brought into contact with a UV treated dish. **e)** Smoothing out the stamp (e.g. with tweezers) ensures all of its protrusions are fully in contact with the substrate for even protein transfer. **f)** The stamp is gently removed, leaving behind a protein pattern in the desired shape. **g)** The dish is incubated with a PLL-PEG solution. **h)** After removal of excess PLL-PEG and rinsing of the sample, only a layer of the PEG copolymer remains. **i)** The substrate is now covered in a pattern of fibronectin in the shape predetermined by the initial stamp, with intermittent areas passivated by PLL-PEG. These intermittent areas act cell repellent, whereas cells can adhere to the islands of ECM protein.

incubated with a 50 $\frac{\mu g}{ml}$ fibronectin (YO Proteins AB, Huddinge, Sweden) solution for 60 min. To remove excess protein, the stamp is washed with a drop of Milli-Q water, before being brought into a contact with an uncoated ibidi dish (ibidi, Martinsried, Germany) and smoothed by wiping over the surface with a pair of tweezers. A Poly(L-Lysine)-Poly(Ethylene-Glycol) (PLL-PEG, SuSoS AG, Dübendorf, Switzerland) solution is added to the edge of the stamp with a pipette, so that capillary forces pull it underneath the PDMS, before the stamp is removed. This can make the stamp easier to remove and improves protein transfer. After 30 min incubation with PLL-PEG, the sample is rinsed several times with PBS to remove any unbound polymer. This should ideally result in a sample covered in islands of a protein monolayer in the shape determined by the initial stamp, with intermittent areas covered by a monolayer of PLL-PEG. If cells are now seeded onto this sample, they will predominantly adhere to the fibronectin patches, not however to the passivated area in between. In this way, the cells can successfully be confined to the desired shapes of large squares or cloverleafs to study their arrangement.

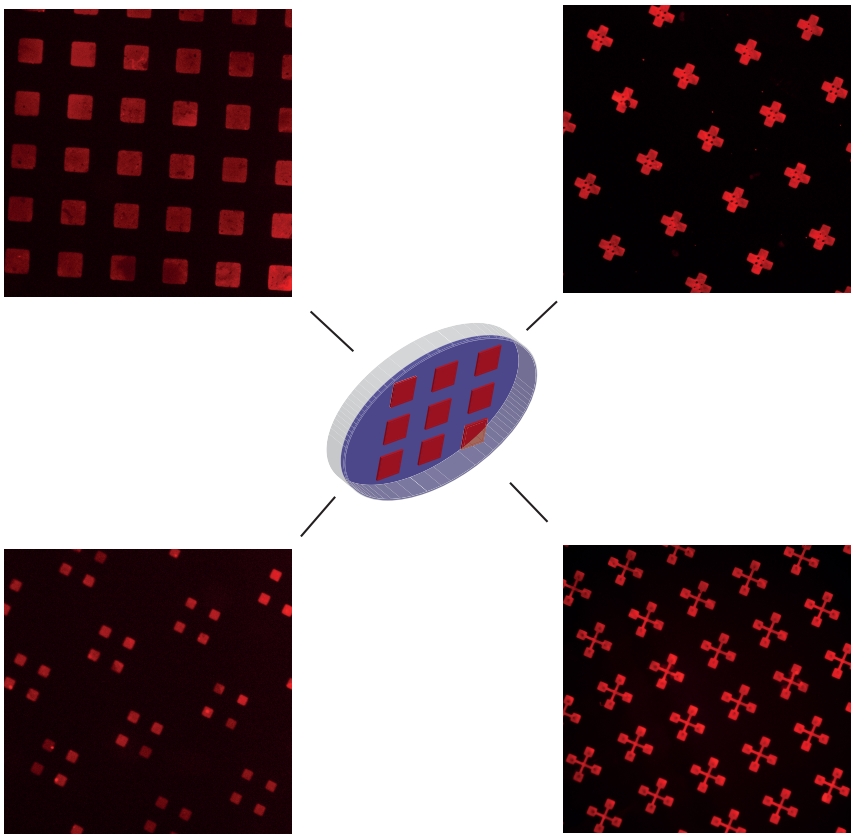

Figure A.4: Fluorescence images of subregions of fibronectin patterns for various geometries, produced by microcontact printing. Depending on the shape of the used master, the resulting pattern in the dish can take various shapes. 20% fibronectin labeled with Alexa 647 is mixed into the regular fibronectin to allow visualization.

For control of the patterning procedure, about 20% of the fibronectin can be replaced by fluorescently labeled protein. In this work, fibronectin labeled with Alexa 647 was used. In this concentration the adhesion behavior of cells on the pattern should be nearly identical to that on pure unlabeled fibronectin. At the same time, it is sufficient to visualize the pattern very easily and the fluorescence spectrum does not overlap with any of those of the fluorophores used to mark the cell (see Fig. A.4).

A.2 Evaluation tools for data analysis

A.2.1 Particle image velocimetry extracts cellular flow fields

An important tool for the study of collective cell behavior in the experiments of this thesis is PIV. Stemming originally from classical hydrodynamics, PIV has now become a prominent tool in the cell dynamics community [28, 38, 70, 82]. In its initial form, PIV was performed to visualize flows and currents in liquids by seeding them with tracer particles. Given the similarities between the migration of epithelial cell sheets and flowing liquids, it is unsurprising that the technique has been adapted to visualize the flow in such cells. While the time scale of flows is typically very different in epithelia as compared to Newtonian liquids, the only major difference in the application of the technique is the fact that tracer particles can be eschewed. Instead, the shapes of individual cells, as well as intracellular compartments, that are easy to see under a microscope provide the necessary patterns that visualize the flow.

PIV analysis is an intensity cross-correlation technique, typically performed on phase-contrast microscopy images. Pictures of the studied sample are taken at the same position at successive time points. The interval between two frames is set so that the typical displacement of shape patterns is small in a single time step. In this work, and frequently in PIV analysis on migrating cell layers in general, a time step of 10 min between frames was used. Pairs of successive images are then correlated with each other (second with first image, third with second image, etc.): to start off, the images are broken down into equally sized, rectangular subwindows (see Fig. A.5). The size of these windows can be chosen freely, with a smaller subwindow size increasing the resolution of the resulting PIV analysis. Arbitrarily small windows do not work well, however, as a lower boundary for the size is set by the fact that the typical length scale of patterns in the studied image

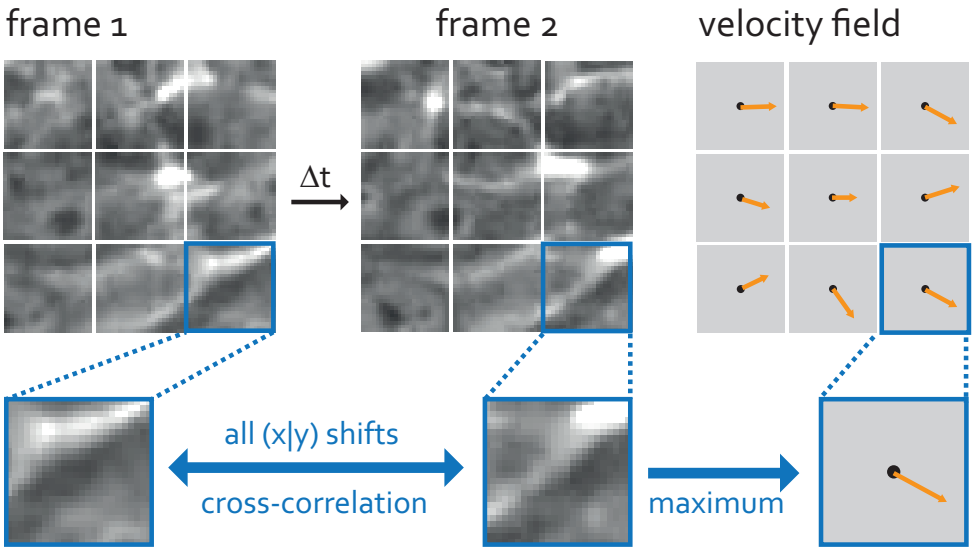

Figure A.5: Particle image velocimetry extracts the velocity fields of cellular motion. Two consecutive time frames (Δt = 10 min apart) are compared. Each individual frame is divided into multiple interrogation windows (approx. $8 \times 8 \mu m$ in size). The interrogation window in the first is then shifted in x- and y-direction and the pixelwise cross-correlation with the unshifted identical interrogation window from the second frame calculated. The shift leading to a maximum in the correlation is chosen as the correct displacement vector for this particular interrogation window. Taking the displacement vectors of all interrogation fields, together with the known time difference between the frames results in the velocity field describing the collective motion of the cell sheet.

must easily fit inside of it. Thus, in this work interrogation windows were set to 32×32 pixels (which corresponds to about 20 µm × 20 µm, or roughly the size of one cell). One way to increase the spatial resolution past a reasonable lower limit for the window size is by introducing an overlap between the interrogation windows. In this case, the original image is not broken down into a perfect lattice of smaller images for interrogation, but rather each subwindow is a snapshot of a small area of the original picture that also is identical to a certain extent with its surrounding subwindows (see Fig. A.6). Due to the redundantly used image information in this case the resulting velocity vectors are no longer entirely independent, and there are diminishing returns in continually increasing the overlap. Thus, values around 50% are typically used. In this work, an overlap of 62.5% was chosen.

After decomposition of the original image, the pixel-wise intensity I of all subwindows i, j of the first frame ($I_1^{i,j}$) are compared to the identical subwindows' intensities $I_2^{i,j}$ in the second frame. The intensity pattern of the first image is cross-correlated in a pixel-wise manner with the intensity pattern of the second image, not only directly but also after applying all possible pixel shifts (s,t) to it. The resulting cross-correlation function

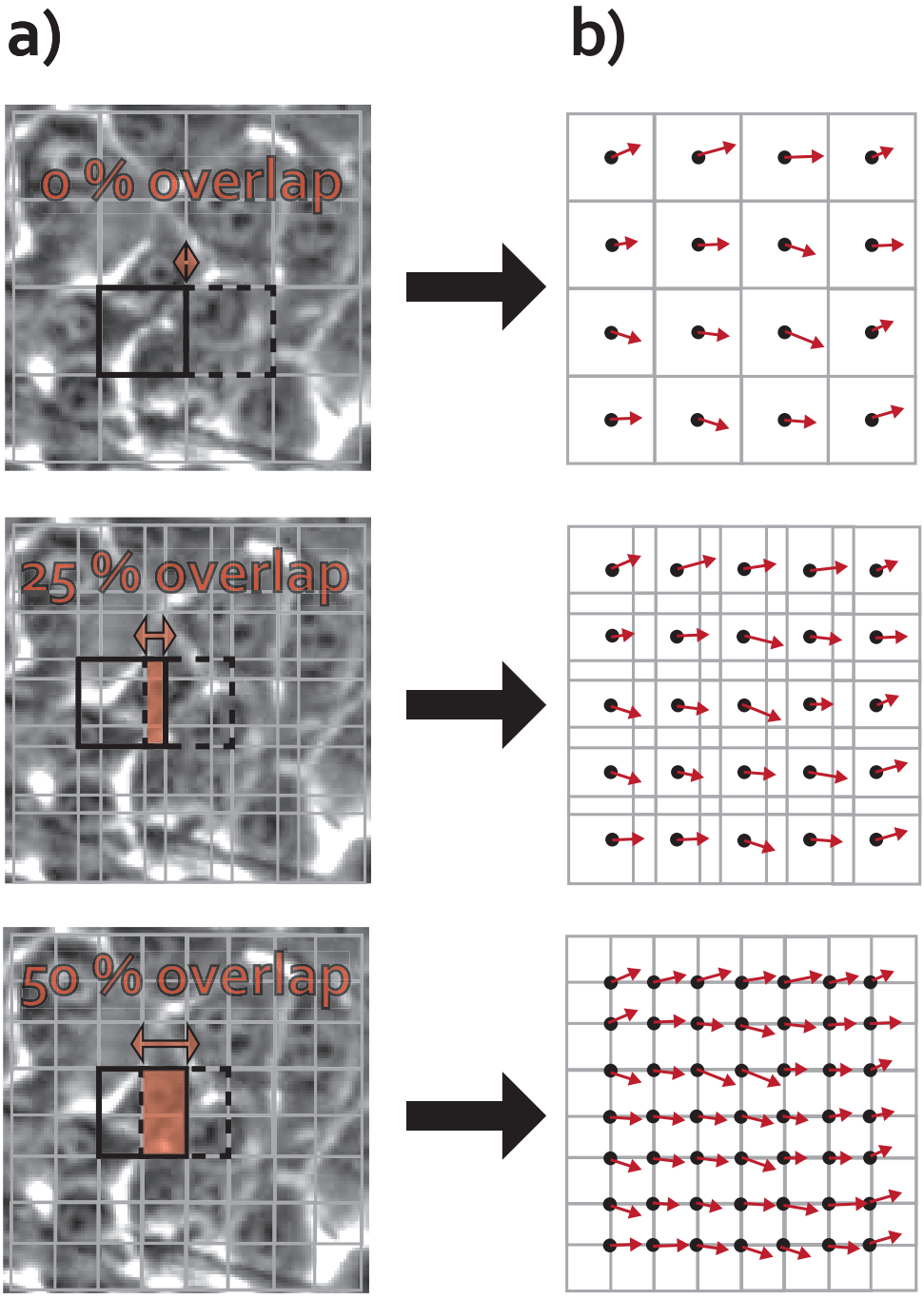

Figure A.6: Illustration of different degrees of overlap between the subwindows and the resulting PIV analysis. **a)** Image of section of an MCF10A cell sheet with schematic PIV interrogation windows overlayed for 0%, 25% and 50% overlap. All interrogation windows for this section of the image are depicted in gray, with two neighboring windows highlighted in black (one solid line, one dashed for easier differentiation). The overlap of the two highlighted windows is marked in red. **b)** Schematic velocity fields resulting from the different overlaps in a). Higher overlaps result in a more finely resolved grid of velocity vectors.

described by Eq. A.1 (with m and n specifying the pixels in the interrogation window) will display a peak when the examined shift (s,t) matches the actual shift of the pattern in the image between successive time points.

$$R(s,t) = \sum_{m=0}^{M-1} \sum_{n=0}^{N-1} \cdot I_1^{i,j}(m,n) \cdot I_2^{i,j}(m-s, n-t) \tag{A.1}$$

Thus, PIV is in essence a pattern-matching technique that determines how the shapes in an image (in this case the cells in an epithelium) have moved compared to a previous picture. The result for each interrogated subwindow is a vector designating the most likely displacement, yielding a vector field of local displacements throughout the entire image. With the known time-interval between successive frames, this can easily be used to calculate a velocity field instead.

While this completes the actual PIV analysis, it is customary to perform some post-processing steps on the calculated flow field (see Fig. A.7). Filtering of outliers and interpolation of missing values from surrounding values can help smooth out the initially noisy results. As the whole tissue in the experiment is connected, it is unlikely for a subregion to move in the opposite direction from its surroundings. If anything, entire cells or groups of cells could move contrary to the rest of the surrounding tissue. In this case, however, the sub-cellular resolution of the PIV grid would result in clusters of velocities with a different sign than the rest of the tissue, as opposed to only individual grid points with velocities of different sign than the surrounding points. Thus, such individual outliers are almost certainly errors in the analysis algorithm (typically noise or accidentally matched patterns) that can justifiably be filtered out. This does not only hold true for contrary directions of velocities, however, but also for velocities with absolute values deviating significantly from the surrounding grid points. Aside from the comparison to the immediate surrounding, it is also possible to filter by comparing to all globally calculated values, and to implement filters based on the heights of the correlation peaks that resulted in an (x,y)-shift being chosen as the correct one. In this latter case, the assumption is that correctly identified shifts will lead to larger peaks, whereas grid points with incorrect values will be the result of low peaks that were only slightly higher than all of their surroundings.

Taking all this into account, in this work four filters were used. In the first step, a signal-to-noise-ratio filter compares the the height of the correlation peak for each grid point with the mean correlation level. The value for this filter is chosen very generously, so that the correlation peak must be only slightly higher than the mean in order for the value

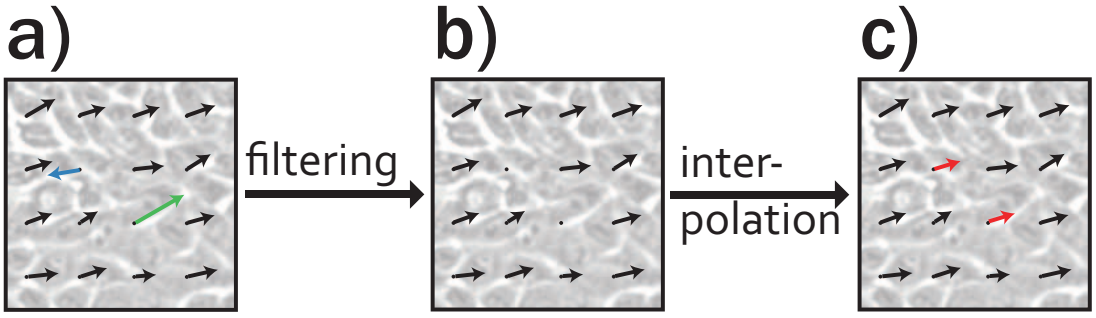

Figure A.7: Illustration of postprocessing steps of PIV data. **a)** Schematic of a velocity field with two outliers, one with absolute value significantly different than all surrounding vectors (green) and one with a similar absolute value but different sign (blue). **b)** In the filtering process, one of the four successively applied filters excludes the outliers and replaces their values by 'not a number' (NaN). **c)** In the interpolation step, new values for these grid points are interpolated from their neighbors.

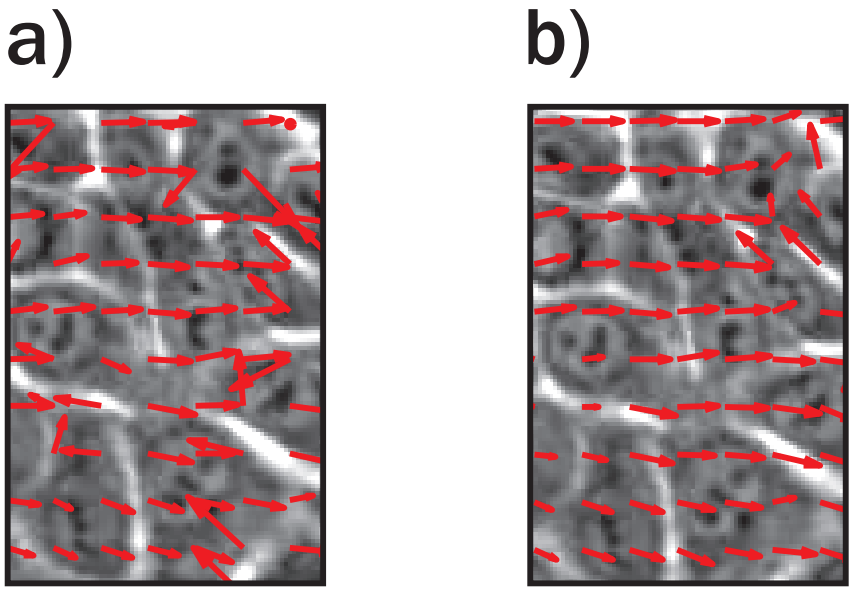

Figure A.8: Comparison of unfiltered and filtered PIV results. **a)** Phase-contrast image of a section of a sheet of MCF10A cells with the corresponding velocity field overlayed in red. The values calculated by the PIV analysis are depicted in their unfiltered form. **b)** Identical phase-contrast image with the corrected PIV data overlayed in red. Application of four different filters and subsequent interpolation of resulting missing values significantly cleans up the initially very noisy vector field. Collective migration with a preferential direction towards the right becomes much more pronounced. At the same time, the upper right corner highlights that regions that do move against the stream of the rest of the sheet are captured correctly and not eliminated by the filters.

to be kept. More strict rules would potentially make the use of this filter questionable, as mismatched features and stationary background can produce misleadingly high levels of correlation [205]. Following this, a global filter throws out all values outside of three standard deviations around the global mean for the velocity. Then, a peak height filter

removes all values that resulted from correlation peaks below a normalized value of 0.3. Finally, a local filter excludes all vectors that deviate by more than a factor of two from the mean of their surroundings.

To close the holes created in the velocity field by application of these filters, the final postprocessing step of the PIV analysis interpolates missing values from their surrounding neighbors. In this work, the interpolation algorithm was modified so that it only calculated a value if there were at least five of eight surrounding neighbors where a value had been calculated and not been excluded by the filtering steps. In this way, interpolation of values past the leading front of the cell sheet and into the empty area is prevented. Fig. A.8 shows the results of these postprocessing steps compared to the original PIV data.

A.2.2 Coarse-graining and time averaging

In order to smooth out short scale noise in the velocity fields resulting from the PIV analysis, space and time averaging steps were performed with custom Matlab algorithms. Coarse-graining steps were performed by calculating the average velocity vectors over between 2×2 and 8×8 neighboring vectors. The resulting vector is associated with a grid point at the center of the averaging region. Each velocity is calculated from distinct sets of vectors without overlap.
Time averaging is performed by gridpoint, with the mean of all velocity vectors on that grid point over the average interval taken and associated with that same grid point. A time average was only calculated if a velocity vector existed at all time points on this grid point, whereas grid points that had no velocity value during any frame are completely excluded. While this can lead to regions that are excluded only because the filtering and interpolation step resulted in a missing velocity vector in one of many time steps, it ensures that averages are only calculated when the resulting time average would really be based on the amount of points it is supposed to be based on. This is of particular importance at the leading edge of migrating cell sheets, as this front might spread into areas originally not covered by cells over the averaging period.

A.2.3 Determination of cell density

Local cell densities for chapters 3.1 and 3.2 were determined from fluorescence images of cell nuclei, where cells are easy to differentiate. Cells were counted with the standard

ImageJ [206] function "Find Maxima", which finds all peaks in the intensity of the current image. The noise tolerance was set individually for each measured position to give the most accurate match with the cell nuclei, but kept at the same value throughout each time point of the measurement. Manual counting for comparison revealed that the error seems to be only about 6% over the whole channel.
Detected cells are grouped into 50 µm wide bins, and the cell density calculated by dividing the number of cells in each bin by its area (50 µm × channel width).

A.2.4 Flux calculation

The flux calculation for chapter 3.1.2 is performed by taking the density data and the data from the PIV analysis, averaged in 50 µm bins. Coordinates are transformed into a moving frame of reference by calculating all coordinates as distances from the leading edge. The density gradient over the analyzed bins (3-6, 4-7 and 5-8, measured from the front, respectively) is determined by a linear fit to their four respective density values. The corresponding flux is calculated by multiplying the density and the velocity from the PIV analysis ($J = \rho v$) obtained for the outer two bins. These values are then averaged over all time points, resulting in three pairs of values (one for each set of bins) for each measured channel.

A.2.5 Vorticity calculation

The rotational component of velocity fields is studied by calculation of the vorticity. For each grid point i of the PIV analysis, the average perpendicular component of the relative velocities of the eight neighboring grid points j is calculated. A coarse-graining of $21 \times 21\,\mu m^2$ is chosen so that each grid point roughly represents the area of one cell.

Perpendicular components of the relative velocity vector $\mathbf{v}_{i,j} = v_j - v_i$ are extracted according to Eq. A.2 by performing a scalar product with $\mathbf{r}^{\perp}_{i,j}$, a vector orthogonal to the relative position vector $\mathbf{r}_{i,j} = \mathbf{r}_j - \mathbf{r}_i$, calculated by Eq. A.3.

$$c_{i,j} = \frac{\mathbf{r}^{\perp}_{i,j} \cdot \mathbf{v}_{i,j}}{r^2_{i,j}} \tag{A.2}$$

$$\mathbf{r}_{i,j}^{\perp} = \mathbf{e}_z \times \mathbf{r}_{i,j} = (\mathbf{e}_x \times \mathbf{e}_y) \times \mathbf{r}_{i,j} \tag{A.3}$$

Finally, the obtained value $c_{i,j}$ is averaged over all eight neighboring grid points j. This entire vorticity calculation can be condensed into Eq. A.4.

$$\Omega_i = \mathbf{e}_z \cdot (\mathbf{curl}\ \mathbf{v})_i \tag{A.4}$$

Due to the fact that the vortex formation found in cell sheets is a highly localized phenomenon, the determined vorticity will depend on the coarse-graining of the PIV grid and on the amount of neighbors it is calculated over. Averaging over too many neighbors carries the risk of smoothing out rotations. Averaging over too few neighbors on the other hand is likely to produce error prone results by weighting potential outliers in the PIV analysis too strongly. Eight neighbors is thus chosen as a compromise and should encompass about two rows of cells around a center cell.

A.2.6 Equivalent angle approximation for vorticity

To better visualize how much rotation calculated vorticity values actually correspond to, the equivalent vorticity value corresponding to different rotation angles per time step are calculated. An idealized grid is assumed, where each grid point corresponds perfectly to a cell (see Fig. A.9). The central cell positioned at $\mathbf{r}_{\text{center}}$ is taken to be at rest relative to its neighbors. Each of the eight neighboring cells is assumed to rotate around the central cell on perfect circles. For each neighboring grid point i, the velocity $\mathbf{v}_{\text{shift,i}}$ that would result from the PIV analysis is calculated according to Eq. A.5

$$\mathbf{v}_{\text{shift,i}} = \mathbf{r}_{\text{start,i}} - \mathbf{r}_{\text{end,i}} \tag{A.5}$$

Here, $\mathbf{r}_{\text{start,i}}$ is the coordinate the grid point i starts out on and $\mathbf{r}_{\text{end,i}}$ is the point it has rotated to after one time step. As rotation is assumed to be on a perfect circle, $\mathbf{r}_{\text{end,i}}$ can be calculated by simple trigonometric equations of the form of Eq. A.6.

$$\mathbf{r}_{\text{end,i}} = \begin{pmatrix} r \cdot \cos\alpha \\ r \cdot \sin\alpha \end{pmatrix} \tag{A.6}$$

Here, r is the magnitude of $\mathbf{r} = \mathbf{r}_{\text{start,i}} - \mathbf{r}_{\text{center}}$. The exact form of Eq. A.6 varies for each grid point and depends on whether the angle pushes the end point into the next quadrant of the coordinate system, but the general form always remains the same.

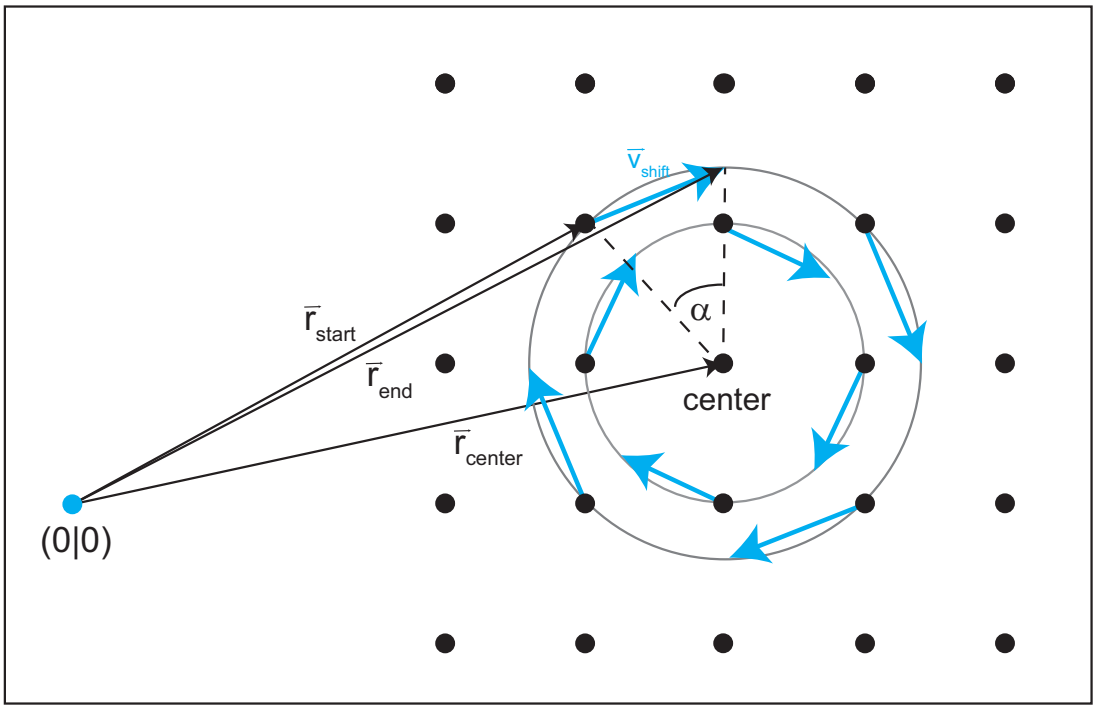

Figure A.9: Schematic representation of the angle to vorticity conversion approximation. Each cell sits on one grid point. One central grid point is at rest, while the eight surrounding cells rotate collectively around it on perfect circles. Grid points are calculated relative to an arbitrary origin. The velocities $\mathbf{v}_{\text{shift}}$ define the directest route corresponding to each cell's movement in a time step. They can be calculated from $\mathbf{r}_{\text{start}}$ and $\mathbf{r}_{\text{end}}$.

A.2.7 Quantitative orientation analysis

A second key tool in the study of the cellular flow in this thesis is quantitative analysis of the orientation in the cell sheets. The detection of orientation in image analysis has grown in relevance and today there is a wide range of applications from astrophysics [207] to biological and medical topics [208].

In the framework of this thesis, the analysis of alignment of cells within the cell sheet is of particular relevance, as the orientation field is a second observable for direct comparison with the active isotropic-nematic mixture model (in addition to the flow field). Given the key role orientation plays in liquid crystals, studying it quantitatively is invaluable when attempting to capture collective cell migration with such a model. In this work

a combination of Matlab and ImageJ algorithms was used to achieve this, the core of which is the OrientationJ plugin for ImageJ. OrientationJ implements a gradient-based orientation estimator, a class of tools frequently used to study orientation due to the fact that they are relatively simple to discretize and implement [209].

To this end, the directional derivative D_{u_θ} of the intensity f of an image along direction $\mathbf{u}_\theta$ is considered (the entire theoretical derivation of how the local orientation is calculated mathematically follows the book chapter ***Transforms and Operator for Directional Bioimage Analysis: A Survey*** by Püspöki et al. [209]):

$$D_{\mathbf{u}_\theta} f(x,y) = \langle \mathbf{u}_\theta, \nabla f(x,y) \rangle \tag{A.7}$$

Here, $\nabla f(x,y)$ is the gradient vector of the intensity evaluated at (x,y), $\mathbf{u}_\theta$ is the unit vector in direction θ and the angle brackets represent the inner product. The local directionality of an image can be estimated using $\mathbf{u}_\theta$ ($D_{\mathbf{u}_\theta}$ vanishes when $\mathbf{u}_\theta$ is perpendicular to ∇f and is maximized when $\mathbf{u}_\theta$ is collinear to ∇f), however, this method is very sensitive to noise [209].

Robustness to noise in gradient-based orientation estimators is improved by examining the so called structure tensor $\mathbf{J}(\mathbf{x})$ [210], a matrix that can be derived from the gradient of an image (Eq. A.8).

$$\mathbf{J}(\mathbf{x}_0) = \iint_{\mathbb{R}^2} w(\mathbf{x} - \mathbf{x}_0)(\nabla f(\mathbf{x}))\nabla^T f(\mathbf{x}) dx_1 dx_2 \tag{A.8}$$

Here, $w(x,y) \geq 0$ is a weighting function that defines the observation window (typically a square centered on (x_0, y_0)). Written out, Eq. A.8 becomes:

$$\mathbf{J}(\mathbf{x}_0) = \begin{pmatrix} (w * f_x^2)(\mathbf{x}_0) & (w * f_x f_y)(\mathbf{x}_0) \\ (w * f_y f_x)(\mathbf{x}_0) & (w * f_y^2)(\mathbf{x}_0) \end{pmatrix} \tag{A.9}$$

Here, $w * f$ designates the convolution of w and f, while f_x represents the partial derivative of f with respect to x. The structure tensor's eigenvalues are designated as λ_{max} and λ_{min} and they contain information about the predominant orientation within the observation window. Two measures, the energy E (Eq. A.10) and coherency C (Eq.

A.11), are defined in order to easily characterize this information.

$$E = |\lambda_{max}| + |\lambda_{min}| \tag{A.10}$$

$$C = \frac{\lambda_{max} - \lambda_{min}}{\lambda_{max} + \lambda_{min}} = \frac{\sqrt{(J_{22} - J_{11})^2 + 4J_{12}^2}}{J_{22} + J_{11}} \tag{A.11}$$

Here, J_{ij} refers to the ij-th element of the structure ternsor. If $E \approx 0$ (or in other words $\lambda_{max} = \lambda_{min} \approx 0$) the region is homogeneous. If $C \approx 0$ (or in other words $\lambda_{max} \approx \lambda_{min}$) then the region has no predominant direction and is rotational symmetric. If $C \approx 1$ (or in other words $\lambda_{max} > 0$, $\lambda_{min} \approx 0$ or $\lambda_{max} >> \lambda_{min}$), the eigenvector and one of the gradient directions are well-aligned.

The direction $\mathbf{u}_\theta$ along which the directional derivative in the observation window is maximized is given by:

$$\mathbf{u}_\theta = arg \max_{||\mathbf{u}||=1} ||D_{\mathbf{u}} f||_w^2 \tag{A.12}$$

The relevant function $||D_{\mathbf{u}_\theta} f||_w^2$ can be interpreted as the average energy in the observation window w (which is centered at (x_0, y_0)) and is given by:

$$||D_{\mathbf{u}_\theta} f||_w^2 = \langle \mathbf{u}^T \nabla f, \mathbf{u}^T \nabla f \rangle_w = \mathbf{u}^T \langle \nabla f, \nabla f \rangle_w \mathbf{u} = \mathbf{u}^T \mathbf{J} \mathbf{u} \tag{A.13}$$

The structure tensor's eigenvector corresponding to the largest eigenvector at $\mathbf{x}_0$ maximizes Eq. A.13. Thus, the dominant (local) orientation of the pattern is calculated by:

$$\mathbf{u}_\theta = (cos\theta, sin\theta) \tag{A.14}$$

Here, the angle θ is given by:

$$\theta = \frac{1}{2} arctan \left(\frac{2J_{12}}{J_{22} - J_{11}} \right) \tag{A.15}$$

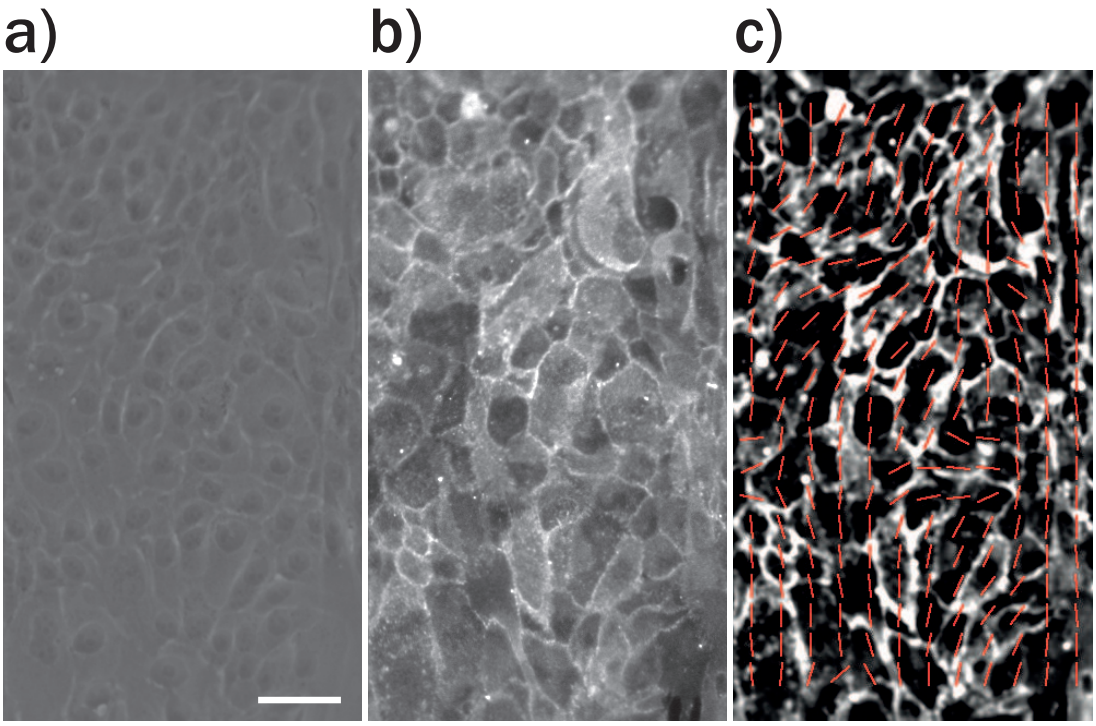

Figure A.10: Result of the orientation analysis compared to an E-cadherin antibody stain **a)** Phase-contrast image used as input for the orientation analysis. **b)** Fluorescence image of E-cadherin-eGFP stain of the same cells for better visualization of cell orientation. **c)** Result of the orientation analysis (red lines) overlayed on a preprocessed version of the image from b). Generally, good agreement seems to exist between the orientation analysis and the orientation seen in the image. All three images have been rotated by 90° compared to the usual orientation. Scale bar corresponds to 50 µm.

It is important to keep in mind that this calculation will always return a dominant direction for the orientation, independent of how strongly oriented or homogeneous the underlying image actually is. Only the coherency gives information about this, with values close to 1 indicating local alignment and values close to 0 indicating the absence of any preferred direction.

Further disadvantages, generally speaking, of the structure tensor method that OrientationJ uses for orientation estimation is low accuracy for corner detection and the fact that it only takes into account one scale [209]. For the quantification of orientation of cells in migrating sheets, however, the corner detection is of little interest. The fact that only one length scale is considered is less of an issue as well, as long as this length scale is correctly set to the size of the cells, though if there are large variations in the cell sizes throughout the same sheet, this would become more of an issue again.

Robustness to noise can further be increased by application of a bandpass filter prior

to processing the image. In this thesis, this preprocessing step was performed in ImageJ with a large filter size of 60 pixels, a small filter size of 9 pixels and a tolerance of 5.

In order to confirm the orientation detection algorithm worked on the input data, an MCF10A cell sheet that had invaded a straight channel was fixed and stained with an antibody to E-cadherin. Fig. A.10 shows the result of orientation detection applied to the phase-contrast images overlayed on the E-cadherin image, where orientation can be seen more clearly. In general, good agreement is found, though in areas where cells are less elongated and do not really have a preferred orientation, the algorithm still returns a clear result. Thus, the orientation analysis is deemed suitable for the experimental data, but results must be taken with care and not overinterpreted.

A.2.8 Single cell tracking and drift correction

Trajectories of individual cells for MSD analysis are traced automatically with the software openbox (Informationssysteme Schilling, Munich, Germany). A median filter (3×3 square) is applied to each image prior to nuclei localization with a Gaussian correlation algorithm. Using a reasonable maximum velocity estimated from the PIV analysis, images are correlated with the previous frame to ensure cells are not mapped incorrectly between time frames. Tracking is performed one cell at a time under supervision in case of issues. Cell tracks are ended when cells divided.

For cells tracked in cell sheets spreading in a preferential direction, a centering step is performed by subtracting a drift speed from each step of movement. This velocity is chosen individually for each cell so that the average displacement of all track points from the initial track point in x-direction is zero for the corrected track.

A.2.9 Automated cell front detection

Spreading of cell sheets into channels is followed via automated detection of the leading edge (see Fig. A.11). The algorithm is based on the intensities of the brightfield images. Specifically, plotting the intensities along the x-axis (summed over all y-values corresponding to that position along the channel) reveals a noisy profile with many peaks. In the region the cell sheet has not yet reached, however, the intensity profile is flat. This transition from fluctuation to plateau is used to detect the leading edge. A custom Matlab

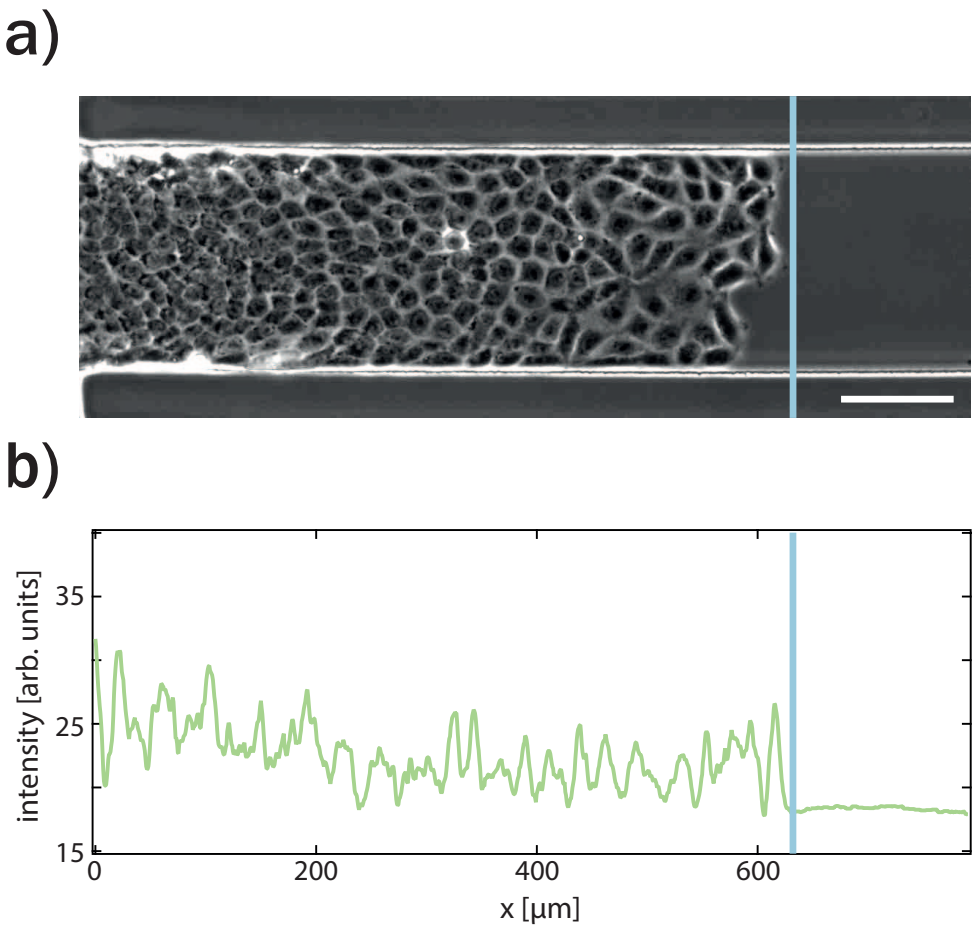

Figure A.11: Automated detection of the leading edge. **a)** Brightfield image of a channel with an invading cell sheet. The blue line marks the position of the front as detected by the algorithm, showing good agreement with the actual leading edge. **b)** Intensity profile over the channel depicted in a). The intensity values are summed up over all y-values for each x-value. The graph shows a plateau on the right hand side corresponding to the area the cells have not migrated into yet. Correspondingly, when coming from the right, a sharp increase is detected at the position of the leading edge. The algorithm uses this slope to detect the cell front.

script computes a rolling "coarse-grained" derivative coming from the right and moving to the left until its value surpasses a predefined threshold. The location where this occurred is defined as the cell front. This derivative is calculated by summing over ten adjacent intensity values and subtracting this by the sum over then adjacent intensity values shifted one pixel to the left (i.e. towards the leading edge). Finally, the quotient of this difference between the two sums and the first of the sums is calculated. Results are manually compared to the actual position of the cell front, and the few occurring outliers are removed. Time points where no position of the cell front was calculated due to this are interpolated linearly from the prior and succeeding time points.

A.2.10 Image stitching

In order to achieve the large fields of view necessary for following cell sheets invading the channels to a large depth, as described in chapter 3.3, several of the microscope field of views need to be stitched together. To this end, images were recorded with some overlap. Prior to stitching, the individual images were rotated so they all have the same orientation (in this thesis horizontal orientation of the channels parallel to the image border was chosen, with cells invading from the left) and trimmed down so the overlap between images is roughly 200 µm. Pairwise stitching is performed with the freely available "Image Stitching" plugin for ImageJ, linearly blending the overlap region and using subpixel accuracy [211]. Depending on the length of the channels, either two or three fields of view were stitched together to cover the necessary dimensions. To save computation time, only the last time points of each image series were registered against each other and the results applied to all other time points in that series.

A.2.11 Machine learning algorithms for cell-cell junction identification

In order to automatically readout the positions of cell-cell junctions from lifeact-eGFP images for systems of four cells on a cloverleaf pattern (see chapter 3.4), two different machine learning algorithms were used. One was based on the freely available software Ilastik [185], the other on a custom Matlab algorithm. Prior to the actual machine learning algorithms, images were preprocessed in the freely available software ImageJ. To this end, a Gaussian blur with a radius of $\sigma = 2.0\,\mathrm{px}$ is applied, followed by a bandpass filter with a lower limit of roughly 3 px and an upper limit of roughly 20 px. The result of this preprocessing step can be seen in Fig. A.12.

The preprocessed image is turned over to the actual machine learning programs. Both algorithms are random forest classification algorithms (see chapter 2.6 for details), but use different features to perform the classification. The Ilastik algorithm uses a broad number of features, specifically relating to intensity, edge and texture of the input image. For intensity, the used feature was Gaussian smoothing. For the edges, the Laplacian of a Gaussian was taken, as well as the Gaussian gradient magnitude, and the difference of the Gaussians. For texture, the structure tensor eigenvalues as well as the Hessian of Gaussian eigenvalues are used. All features are examined on scales of $\sigma = 0.7\,\mathrm{px}$, $1.0\,\mathrm{px}$,

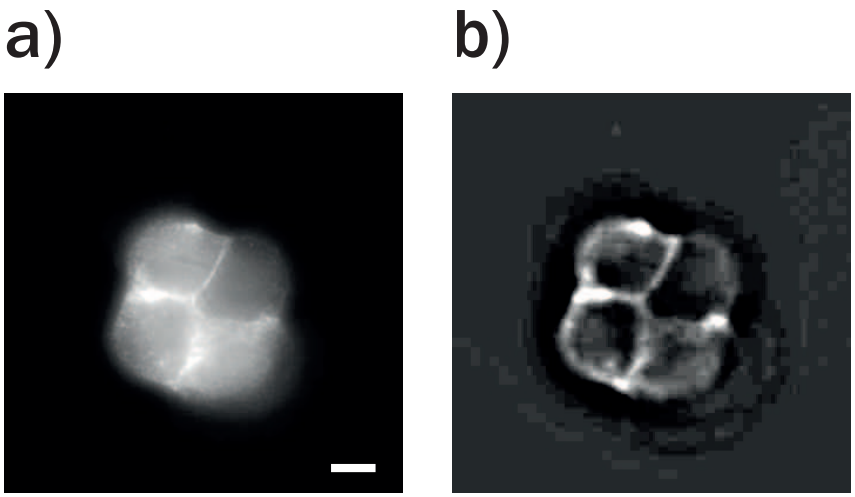

Figure A.12: Illustration of the preprocessing step. **a)** Original fluorescence input image (lifeact-eGFP). **b)** Preprocessed image after application of Gaussian blur and bandpass filter. Scale bar corresponds to 25 µm.

1.6 px and 3.5 px, with the exception of the Gaussian smoothing, which was examined at 0.3 px in addition to all the above scales. This multitude of intensity, edge and texture based input features should result in a high sensitivity of the Ilastik algorithm.

In contrast, the less efficient custom Matlab algorithm uses fewer of these sorts of features. It works solely on a pixel's actual intensity value, as well as the local intensity variance, calculated over $3 \times 3\,\mathrm{px}^2$ and $7 \times 7\,\mathrm{px}^2$. This is expected to result in a lower sensitivity for cell junction detection. To compensate, the custom algorithm uses three input features based on location, specifically the x-coordinate, the y-coordinate, and the deviation of the current pixel from a Voronoi construction based off of the cells' nuclei (see Fig. A.13). This *a priori* knowledge of where the cell junctions are expected to be should help prevent falsely identifying pixels far from the actual cell-cell junctions as being part of them.

Both algorithms were trained on 25 % of the evaluated data. These image frames were labeled manually. Due to differences in the algorithms, training data for the custom Matlab algorithm was labeled by tracing the contours of the cell-cell junctions and defining all points within that contour as being part of the junctions, while everything else is labeled as not being part of the border. For the Ilastik algorithm, only parts of the cell-cell junctions as well as parts of the non-border areas were traced and labeled, but the software's live-update and uncertainty displaying functions were used to choose regions the algorithm would benefit most from.

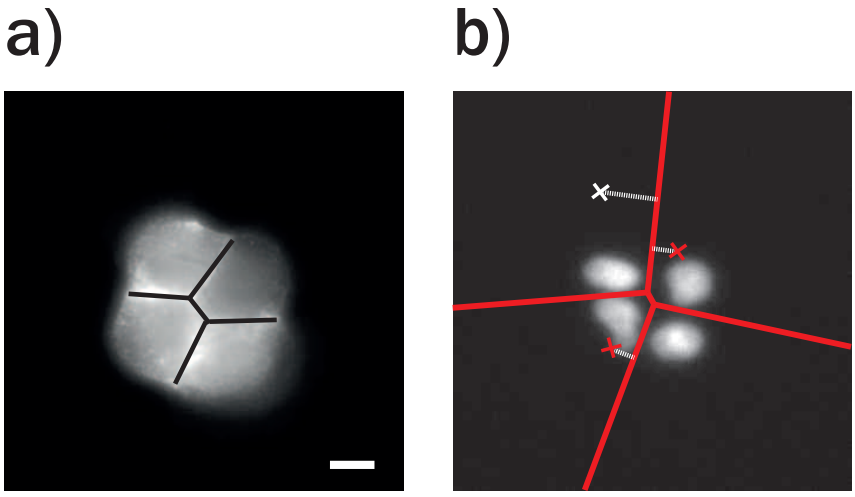

Figure A.13: Illustration of the parameter "distance to Voronoi construction" **a)** The lifeact-eGFP input image for a given frame is shown for reference, with the cell-cell junctions traced very roughly as straight black lines for easier visibility. **b)** Voronoi construction resulting from the position of the nuclei (automatically determined from the H2B mCherry fluorescence image). The resulting lines very roughly capture the cell-cell junctions as seen in a), but are too inexact to do more than serve as approximations. Three sample pixels are shown (small crosses) and their distance to the Voronoi construction indicated by the white dashed line. Distance is always calculated to whichever line is closest. When this distance is used as input parameter in the machine learning algorithm, pixels with low values (such as those indicated in red) should be more likely to be classified as belonging to the junction, whereas those at greater distances (such as the one indicated in white) will be less likely to be classified. Exact cutoffs will depend on the values the training data displays for this parameter. Scale bar corresponds to 25 µm.

A.3 Experimental protocols

A.3.1 Cell culture

All cells were grown in supplemented medium at 37 °C under 5 % CO_2 in a humidified atmosphere.

Doubly transfected Madin Darby canine kidney (MDCK) cells stably expressing mCherry-labeled H2B and eGFP-labeled Lifeact were cultured in Dulbecco's Modified Eagle Medium (cc pro, Oderorla, Germany), supplemented with 10 % fetal bovine serum (FBS), 20 mM L-glutamine and high glucose (4.5 $\frac{g}{l}$). Cells were grown to about 80 to 90 % confluence before trypsinization and centrifuged at 1000 rcf for 3 min. The cell pellet was resuspended in cell medium and cells were seeded in a fresh flask or on samples for experiments. For measurements, standard culture medium was replaced by CO_2 independent Leibovitz's L15 medium without phenol red, supplemented with 10 % FBS immediately prior to measurement. Measurements were performed at 37 °C with 0 % CO_2.

Wild type human mammary epithelial cells (MCF10A) were cultured in Dulbecco's Modified Eagle Medium: Nutrient Mixture F-12 (DMEM F-12, gibco, Fisher Scientific GmBH, Schwerte, Germany). This basal medium was supplemented with 2.5 mM GlutaMAX (L-Alanyl-L-Glutamine), 5 % horse serum, 20 $\frac{ng}{ml}$ hEGF (Sigma-Aldrich Chemie GmbH, Munich, Germany), 0.5 $\frac{\mu g}{ml}$ hydrocortisone (Sigma-Aldrich Chemie GmbH, Munich, Germany), 100 $\frac{ng}{ml}$ cholera toxin (Sigma-Aldrich Chemie GmbH, Munich, Germany) and 10 $\frac{\mu g}{ml}$ insulin (Sigma-Aldrich Chemie GmbH, Munich, Germany). For passaging, once cells had reached roughly 80 % confluency, the supernatant is collected and centrifuged at 300 rcf for 8 to 9 min, to retain floating, viable cells. The cell pellet is resuspended in fresh medium and added back to the adherent population at the end of the process. The adherent cell population is treated with accutase until cells dissociate (roughly 10 to 15 min), before being centrifuged at 500 rcf for 6 min. The cell pellet is resuspended in fresh medium and the cells seeded in a fresh flask or on samples for measurements. Measurements with MCF10A cells are performed in regular culture medium at 37 °C under humidified atmosphere, with 10 % CO_2. The 10 % CO_2 is chosen based on the fact that DMEM-F12 uses a sodium bicarbonate buffer system that maintains physiological pH value in the range of 5 and 10 % and that the actual CO_2 concentration that reaches the sample in most microscopy setups is typically lower than the preset concentration. Maintenance of physiological pH was confirmed by measurement with indicator paper

after a 48 h time-lapse study.

A.3.2 Microscopy

Phase-contrast and fluorescence scanning time-lapse measurements were performed using inverted TI Eclipse (Nikon) microscopes equipped with 10x and 20x Nikon phase-contrast objectives and either a mercury fibre illuminator (Intensilight, Nikon) or a solid state based light engine (Lumencor Spectra X, Lumencor Inc., Beaverton, OR, USA) as fluorescence excitation sources for the projects in chapters 3.1 and 3.2 (Intensilight) and the projects in chapter 3.3 and 3.4 (Spectra X), respectively. The microscopes were equipped with a CCD camera (Clara E, Andor Technology, Belfast, United Kingdom) and an sCMOS camera (pco.edge 4.2 LT, PCO AG, Kelheim, Germany), respectively for the projects in chapters 3.1 and 3.2 and the projects in chapter 3.3 and 3.4. Microscopes were equipped with a temperature-controlled heating stage (ibidi GmbH, Martinsried, Germany) or a large incubation box with a small gas mixer (Okolab10, Okolab, Naples, Italy), respectively for the projects in chapters 3.1 and 3.2 and the projects in chapter 3.3 and 3.4. Phase-contrast and fluorescent images were acquired in intervals of $\Delta t = 10\,\text{min}$.

List of Abbreviations

AP	Anterio-posterior
DOS	Density of states
DPD	Dissipative particle dynamics
ECM	Extracellular matrix
E-cadherin	Epithelial cadherin
eGFP	Enhanced green fluorescent protein
EMT	Epithelial-mesenchymal transition
H2B	Histone H2B
MCF10A	Michigan Cancer Foundation-10A
MDCK	Madin-Darby Canine Kidney
MIMIC	Micromolding in capillaries
mRNA	Messenger ribonucleic acid
MSD	Mean squared displacement
PBS	Phosphate buffered saline
PEG-DMA	poly(ethylene glycol)-dimethacrylate
PIV	Particle image velocimetry
PDMS	Polydemthylsiloxane
PD	Proximal-distal

PEG	Poly(Ethylene-Glycol)
PLL	Poly(L-Lysine)
Rac1	Ras-related C3 botulinum toxin substrate 1
RhoA	Ras homolog gene family, member A
siRNA	Small interfering ribonucleic acid

List of figures

2.1 Schematic of a T1 transition 14
2.2 Tissue deformation by T1 transition 14
2.3 Flocks of birds as samples of active matter 16
2.4 Flow of a Newtonian fluid through a pipe 27
2.5 Flow of a Newtonian fluid through a constriction 28
2.6 Theoretical population curve for ideal logistic growth 36
2.7 Traveling wave propagating in x-direction 37
2.8 Illustration of orientation of liquid crystals in different mesophases 39
2.9 Orientations of liquid crystals 41
2.10 Illustration of the dissipative particle dynamics simulation 44
2.11 Mechanism for aligning the motility force in DPD simulation 47
2.12 Cell shapes in an epithelial cell layer 49
2.13 Illustration of the cellular Potts model 52
2.14 Simple decision tree for categorizing e-mails 59
2.15 Exemplary random forest for categorizing e-mails 65

3.1 Overview of channel-guided cell migration study 69
3.2 Time series showing invasion of channels by cell sheets 71
3.3 Average front displacement and velocities for invading cell sheets 72
3.4 PIV analysis of channel invading cell sheets 73
3.5 Smoothing of the velocity field by spatial and temporal averaging 74
3.6 Profile of the velocity component v_x along the channel 75
3.7 Average profile of v_x velocity perpendicular to channel 76
3.8 Variance of the v_y component of a velocity field 76
3.9 Cell density flux in a migrating monolayer 79
3.10 Traveling wave analysis of the cell density profile 82
3.11 Fit of the traveling wave for several time points 83
3.12 Vortex formation in confined cell sheets 85
3.13 Effect of density on vorticity in confluent cell layers 86

3.14 Heatmaps depicting the influence of density and flow on vorticity 87
3.15 Quantification of the influence of flow on vorticity 88
3.16 Directionality of vorticity 89
3.17 Decay time of vortices in confluent cell layers 90
3.18 Motion of individual cells within the sheet with and without flow 92
3.19 MSD of cells under flow and in confluent layers 93
3.20 MSD analysis split parallel and perpendicular to flow 94
3.21 Collective migration into channels in experiment and DPD simulation . . . 100
3.22 Flow and density profiles in experiment and DPD simulation 101
3.23 Order of the division axis in invading cell sheets 103
3.24 Order of the division axis in resting sheets 105
3.25 Alignment of cell divisions with local flow gradients 108
3.26 MCF10A cells migrating through a constriction 115
3.27 Evolution of the position of the cell front passing through constriction . . . 116
3.28 Evolution of the shape of the cell front passing through constriction 118
3.29 Influx of cells into the channel 120
3.30 PIV analysis of collective migration through constriction 122
3.31 Heatmap corresponding to velocity field 123
3.32 Smoothing of velocity field through time averaging 125
3.33 Smoothing of velocity field through coarse-graining 127
3.34 Velocity profile in straight channels in dependence of width 129
3.35 Profile of the velocity in dependence on constriction diameter 131
3.36 Evolution of flow through a constricted channel over time 133
3.37 Velocity profile for different constriction lengths 135
3.38 Velocity profile for different steepness of constrictions 136
3.39 Comparison of velocity with active isotropic-nematic mixture model 138
3.40 Velocity orientation compared with active isotropic-nematic mixture model 139
3.41 Comparison of orientation with active isotropic-nematic mixture model . . 140
3.42 Schematic of a T1 transition 147
3.43 Arrangement of cells on large square micropatterns 152
3.44 Representation of cells with abstracted cell-cell junctions 153
3.45 Rotation of two-cell system 154
3.46 Pinning of cells by choice of adhesion geometry 159
3.47 Machine learning algorithm results for cell-cell junction recognition 162
3.48 Quantification of classification rates for the various algorithms 164
3.49 T1 transitions in minimal four cell system 166

3.50 Schematic energy landscape for four cell systems undergoing T1 transitions 167
3.51 Fluctuation of junction length in a four cell system 168
3.52 Artificial stretching/compressing of cell arrangement 169

4.1 Possible experimental setup for future cellular hydrodynamics studies . . . 179

A.1 Original microstructuring method for creation of channels 185
A.2 Improved microstructuring method for creation of channels 186
A.3 Schematic of procedure for microcontact printing 188
A.4 Fluorescence images of various microcontact printed geometries 189
A.5 Particle image velocimetry 191
A.6 Illustration of different subwindow overlap for PIV 192
A.7 Illustration of postprocessing steps for PIV 194
A.8 Comparison of unfiltered and filtered PIV results 194
A.9 Schematic representation of the angle to vorticity conversion approximation 198
A.10 Orientation analysis compared to an E-cadherin antibody stain 201
A.11 Automated detection of the leading edge 203
A.12 Illustration of the preprocessing step for machine learning 205
A.13 Illustration of the parameter “distance to Voronoi construction” 206

Bibliography

[1] Chepizhko, Oleksandr ; Giampietro, Costanza ; Mastrapasqua, Eleonora ; Nourazar, Mehdi ; Ascagni, Miriam ; Sugni, Michela ; Fascio, Umberto ; Leggio, Livio ; Malinverno, Chiara ; Scita, Giorgio ; Santucci, Stéphane ; Alava, Mikko J. ; Zapperi, Stefano ; La Porta, Caterina A. M.: Bursts of activity in collective cell migration. In: Proceedings of the National Academy of Sciences of the United States of America 113 (2016), Nr. 41. – DOI 10.1073/pnas.1600503113

[2] Plutoni, Cédric ; Bazellieres, Elsa ; Le Borgne-Rochet, Malïys ; Comunale, Franck ; Brugues, Augusti ; Séveno, Martial ; Planchon, Damien ; Thuault, Sylvie ; Morin, Nathalie ; Bodin, Stéphane ; Trepat, Xavier ; Gauthier-Rouvière, Cécile: Pcadherin promotes collective cell migration via a Cdc42mediated increase in mechanical forces. In: Journal of Cell Biology 212 (2016), Nr. 2

[3] Ladoux, Benoit ; Mège, René Marc ; Trepat, Xavier: Front-Rear Polarization by Mechanical Cues: From Single Cells to Tissues. In: Trends in Cell Biology 26 (2016), Nr. 6. – DOI 10.1016/j.tcb.2016.02.002

[4] Hakim, Vincent ; Silberzan, Pascal: Collective cell migration : A physics perspective. In: Reports on Progress in Physics 80 (2017). – DOI 10.1088/1361–6633/aa65ef

[5] Schweitzer, Frank: Brownian agents and active particles: Collective dynamics in the natural and social sciences. 2007

[6] Marchetti, M. C. ; Joanny, Jean-François ; Ramaswamy, Sriram ; Liverpool, Tanniemola B. ; Prost, Jacques ; Rao, Madan ; Simha, R. A.: Hydrodynamics of soft active matter. In: Reviews of Modern Physics 85 (2013), Nr. 3. – DOI 10.1103/RevModPhys.85.1143

[7] Jones, Daniel P. ; True, Harry D. ; Patel, Jyoti: Leukocyte trafficking in cardiovascular disease: insights from experimental models. In: Mediators of Inflammation 2017 (2017). – DOI 10.1155/2017/9746169

[8] Ransohoff, Richard M. ; Kivisäkk, Pia ; Kidd, Grahame: Three or more routes for leukocyte migration into the central nervous system. In: Nature Reviews Immunology 3 (2003), Nr. 7. – DOI 10.1038/nri1130

[9] Madri, Joseph A. ; Graesser, Donnasue: Cell migration in the immune system: the evolving inter-related roles of adhesion molecules and proteinases. In: Developmental Immunology 7 (2000), Nr. 2-4. – DOI 10.1155/2000/79045

[10] Ayala, Ramsés ; Shu, Tianzhi ; Tsai, Li H.: Trekking across the brain: The journey of neuronal migration. In: Cell 128 (2007), Nr. 1. – DOI 10.1016/j.cell.2006.12.021

[11] Valiente, Manuel ; Marín, Oscar: Neuronal migration mechanisms in development and disease. In: Current Opinion in Neurobiology 20 (2010), Nr. 1. – DOI 10.1016/j.conb.2009.12.003

[12] Friedl, Peter ; Hegerfeldt, Yael ; Tusch, Miriam: Collective cell migration in morphogenesis and cancer. In: International Journal of Developmental Biology 48 (2004). – DOI 10.1387/ijdb.041821pf

[13] Ewald, Andrew J. ; Brenot, Audrey ; Duong, Myhanh ; Chan, Bianca S. ; Werb, Zena: Collective epithelial migration and cell rearrangements drive mammary branching morphogenesis. In: Developmental Cell 14 (2008), Nr. 4. – DOI 10.1016/j.devcel.2008.03.003

[14] Aman, Andy ; Piotrowski, Tatjana: Cell migration during morphogenesis. In: Developmental Biology 341 (2010), Nr. 1. – DOI 10.1016/j.ydbio.2009.11.014

[15] Vasilyev, Aleksandr ; Liu, Yan ; Mudumana, Sudha ; Mangos, Steve ; Lam, Pui Y. ; Majumdar, Arindam ; Zhao, Jinhua ; Poon, Kar L. ; Kondrychyn, Igor ; Korzh, Vladimir ; Drummond, Iain A.: Collective cell migration drives morphogenesis of the kidney nephron. In: PLoS Biology 7 (2009), Nr. 1. – DOI 10.1371/journal.pbio.1000009

[16] Weijer, Cornelis J.: Collective cell migration in development. In: Journal of Cell Science 122 (2009). – DOI 10.1242/jcs.036517

[17] Poujade, Mathieu ; Grasland-Mongrain, Erwan ; Hertzog, A ; Jouanneau, J ; Chavrier, Philippe ; Ladoux, Benoît ; Buguin, Axel ; Silberzan, Pascal: Collective migration of an epithelial monolayer in response to a model wound. In: Proceedings of the National Academy of Sciences of the United States of America 104 (2007), Nr. 41. – DOI 10.1073/pnas.0705062104

[18] Brugués, Agustí ; Anon, Ester ; Conte, Vito ; Veldhuis, Jim H. ; Gupta, Mukund ; Colombelli, Julien ; Muñoz, José J. ; Brodland, G. W. ; Ladoux, Benoit ; Trepat, Xavier: Forces driving epithelial wound healing. In: Nature Physics 10 (2014). – DOI 10.1038/nphys3040

[19] Friedl, Peter ; Gilmour, Darren: Collective cell migration in morphogenesis, regeneration and cancer. In: Nature Reviews. Molecular Cell Biology 10 (2009), Nr. 7. – DOI 10.1038/nrm2720

[20] Friedl, Peter ; Locker, Joseph ; Sahai, Erik ; Segall, Jeffrey E.: Classifying collective cancer cell invasion. In: Nature Cell Biology 14 (2012), Nr. 8. – DOI 10.1038/ncb2548

[21] Deisboeck, Thomas S. ; Couzin, Iain D.: Collective behavior in cancer cell populations. In: BioEssays 31 (2009), Nr. 2. – DOI 10.1002/bies.200800084

[22] Haeger, Anna ; Krause, Marina ; Wolf, Katarina ; Friedl, Peter: Cell jamming: Collective invasion of mesenchymal tumor cells imposed by tissue confinement. In: Biochimica et Biophysica Acta - General Subjects 1840 (2014), Nr. 8. – DOI 10.1016/j.bbagen.2014.03.020

[23] Maiuri, Paolo ; Terriac, Emmanuel ; Paul-Gilloteaux, Perrine ; Vignaud, Timothée ; McNally, Krista ; Onuffer, James ; Thorn, Kurt ; Nguyen, Phuong A. ; Georgoulia, Nefeli ; Soong, Daniel ; Jayo, Asier ; Beil, Nina ; Beneke, Jürgen ; Hong Lim, Joleen C. ; Pei-Ying Sim, Chloe ; Chu, Yeh S. ; Jiménez-Dalmaroni, Andrea ; Joanny, Jean F. ; Thiery, Jean P. ; Erfle, Holger ; Parsons, Maddy ; Mitchison, Timothy J. ; Lim, Wendell A. ; Lennon-Duménil, Ana M. ; Piel, Matthieu ; Théry, Manuel: The first world cell race. In: Current Biology 22 (2012), Nr. 17. – DOI 10.1016/j.cub.2012.07.052

[24] Lo, Chun M. ; Wang, Hong B. ; Dembo, Micah ; Wang, Yu L.: Cell movement is guided by the rigidity of the substrate. In: Biophysical Journal 79 (2000), Nr. 1. – DOI 10.1016/S0006–3495(00)76279–5

[25] Charras, Guillaume ; Sahai, Erik: Physical influences of the extracellular environment on cell migration. In: Nature Reviews Molecular Cell Biology 15 (2014), Nr. 12. – DOI 10.1038/nrm3897

[26] Yilmaz, Mahmut ; Christofori, Gerhard: EMT, the cytoskeleton, and cancer cell invasion. In: Cancer and Metastasis Reviews 28 (2009), Nr. 1-2. – DOI 10.1007/s10555–008–9169–0

[27] Angelini, Thomas E. ; Hannezo, Edouard ; Trepat, Xavier ; Fredberg, Jeffrey J. ; Weitz, David A.: Cell migration driven by cooperative substrate deformation patterns. In: Physical Review Letters 104 (2010), Nr. 16. – DOI 10.1103/PhysRevLett.104.168104

[28] Petitjean, Laurence ; Reffay, Myriam ; Grasland-Mongrain, E. ; Poujade, Mathieu ; Ladoux, Benoît ; Buguin, Axel ; Silberzan, Pascal: Velocity fields in a collectively migrating epithelium. In: Biophysical Journal 98 (2010), Nr. 9. – DOI 10.1016/j.bpj.2010.01.030

[29] Lee, Rachel M. ; Stuelten, Christina H. ; Parent, Carole A. ; Losert, Wolfgang: Collective cell migration over long time scales reveals distinct phenotypes. In: Convergent Science Physical Oncology 2 (2016). – DOI 10.1088/2057–1739/2/2/025001

[30] Douezan, S. ; Guevorkian, K. ; Naouar, R. ; Dufour, S. ; Cuvelier, D. ; Brochard-Wyart, F.: Spreading dynamics and wetting transition of cellular aggregates. In: Proceedings of the National Academy of Sciences 108 (2011), Nr. 18. – DOI 10.1073/pnas.1018057108

[31] Rolli, Claudio G. ; Nakayama, Hidekazu ; Yamaguchi, Kazuo ; Spatz, Joachim P. ; Kemkemer, Ralf ; Nakanishi, Jun: Switchable adhesive substrates: Revealing geometry dependence in collective cell behavior. In: Biomaterials 33 (2012), Nr. 8. – DOI 10.1016/j.biomaterials.2011.12.012

[32] Marel, Anna-Kristina ; Piera Alberola, Alicia ; Rädler, Joachim O.: Proliferation and collective migration of small cell groups released from circular patches. In: Biophysical Reviews and Letters 07 (2012), Nr. 01n02. – DOI 10.1142/S1793048012500026

[33] Shaw, Tanya. J. ; Martin, Paul: Wound repair at a glance. In: Journal of Cell Science 122 (2009), Nr. 18. – DOI 10.1242/jcs.031187

[34] Liang, Chun-Chi ; Park, Ann Y. ; Guan, Jun-Lin: In vitro scratch assay: a convenient and inexpensive method for analysis of cell migration in vitro. In: Nature Protocols 2 (2007), Nr. 2. – DOI 10.1038/nprot.2007.30

[35] Zordan, Michael D. ; Mill, Christopher P. ; Riese, David J. ; Leary, James F.: A high throughput, interactive imaging, bright-field wound healing assay. In: Cytometry Part A 79 A (2011), Nr. 6. – DOI 10.1002/cyto.a.21029

[36] Friedl, Peter ; Alexander, Stephanie: Cancer invasion and the microenvironment: Plasticity and reciprocity. In: Cell 147 (2011), Nr. 5. – DOI 10.1016/j.cell.2011.11.016

[37] Vedula, Sri Ram K. ; Leong, Man C. ; Lai, Tan L. ; Hersen, Pascal ; Kabla, Alexandre J. ; Lim, Chwee T. ; Ladoux, Benoît: Emerging modes of collective cell migration induced by geometrical constraints. In: Proceedings of the National Academy of Sciences of the United States of America 109 (2012), Nr. 32. – DOI 10.1073/pnas.1119313109

[38] Angelini, Thomas E. ; Hannezo, Edouard ; Trepat, Xavier ; Marquez, Manuel ; Fredberg, Jeffrey J. ; Weitz, David A.: Glass-like dynamics of collective cell migration. In: Proceedings of the National Academy of Sciences of the United States of America 108 (2011), Nr. 12. – DOI 10.1073/pnas.1010059108

[39] Tambe, Dhananjay T. ; Hardin, C C. ; Angelini, Thomas E. ; Rajendran, Kavitha ; Park, Chan Y. ; Serra-Picamal, Xavier ; Zhou, Enhua H. ; Zaman, Muhammad H. ; Butler, James P. ; Weitz, David A. ; Fredberg, Jeffrey J. ; Trepat, Xavier: Collective cell guidance by cooperative intercellular forces. In: Nature Materials 10 (2011), Nr. 6. – DOI 10.1038/nmat3025

[40] Garrahan, J. P.: Dynamic heterogeneity comes to life. In: Proceedings of the National Academy of Sciences 108 (2011), Nr. 12. – DOI 10.1073/pnas.1101436108

[41] Sadati, Monirosadat ; Taheri Qazvini, Nader ; Krishnan, Ramaswamy ; Park, Chan Y. ; Fredberg, Jeffrey J.: Collective migration and cell jamming. In: Differentiation 86 (2013), Nr. 3. – DOI 10.1016/j.diff.2013.02.005

[42] Trepat, Xavier ; Fredberg, Jeffrey J.: Plithotaxis and emergent dynamics in collective cellular migration. In: Trends in Cell Biology 21 (2011), Nr. 11. – DOI 10.1016/j.tcb.2011.06.006

[43] Liu, Andrea J. ; Nagel, Sidney R.: The Jamming Transition and the Marginally Jammed Solid. In: Annual Review of Condensed Matter Physics 1 (2010). – DOI 10.1146/annurev–conmatphys–070909–104045

[44] Park, Jin A. ; Kim, Jae H. ; Bi, Dapeng ; Mitchel, Jennifer A. ; Qazvini, Nader T. ; Tantisira, Kelan ; Park, Chan Y. ; McGill, Maureen ; Kim, Sae H. ; Gweon, Bomi ; Notbohm, Jacob ; Steward, Robert ; Burger, Stephanie ; Randell, Scott H. ; Kho, Alvin T. ; Tambe, Dhananjay T. ; Hardin, Corey ; Shore, Stephanie A. ; Israel, Elliot ; Weitz, David A. ; Tschumperlin, Daniel J. ; Henske, Elizabeth P. ; Weiss, Scott T. ; Manning, M. L. ; Butler, James P. ; Drazen, Jeffrey M. ; Fredberg, Jeffrey J.: Unjamming and cell shape in the asthmatic airway epithelium. In: Nature Materials 14 (2015), Nr. 10. – DOI 10.1038/nmat4357

[45] Nnetu, Kenechukwu D. ; Knorr, Melanie ; Strehle, Dan ; Zink, Mareike ; Käs, Josef A.: Directed persistent motion maintains sheet integrity during multicellular spreading and migration. In: Soft Matter 8 (2012), Nr. 26. – DOI 10.1039/c2sm07208d

[46] Chepizhko, Oleksandr ; Lionetti, Maria C. ; Malinverno, Chiara ; Scita, Giorgio ; Zapperi, Stefano ; La Porta, Caterina A. M.: From jamming to collective cell migration through a boundary induced transition. (2018)

[47] Cisneros, Luis H. ; Kessler, John O. ; Ganguly, Sujoy ; Goldstein, Raymond E.: Dynamics of swimming bacteria: Transition to directional order at high concentration. In: Physical Review E 83 (2011), Nr. 6. – DOI 10.1103/PhysRevE.83.061907

[48] Baskaran, Aparna ; Marchetti, M. C.: Statistical mechanics and hydrodynamics of bacterial suspensions. In: Proceedings of the National Academy of Sciences of the United States of America 106 (2009), Nr. 37. – DOI 10.1073/pnas.0906586106

[49] Surrey, Thomas ; Nédélec, François ; Leibler, Stanislas ; Karsenti, Eric: Physical properties determining self-organization of motors and microtubules. In: Science 292 (2001), Nr. 5519. – DOI 10.1126/science.1059758

[50] Kemkemer, Ralf ; Kling, D ; Kaufmann, D. ; Gruler, Hans: Elastic properties of nematoid arrangements formed by amoeboid cells. In: The European Physical Journal E 1 (2000), Nr. 2-3. – DOI 10.1007/s101890050024

[51] Toner, John ; Tu, Yuhai: Long-Range Order in a Two-Dimensional Dynamical XY Model: How Birds Fly Together. In: Physical Review Letters 75 (1995), dec, Nr. 23. – DOI 10.1103/PhysRevLett.75.4326

[52] Paxton, Walter F. ; Kistler, Kevin C. ; Olmeda, Christine C. ; Sen, Ayusman ; St. Angelo, Sarah K. ; Cao, Yanyan ; Mallouk, Thomas E. ; Lammert, Paul E. ; Crespi, Vincent H.: Catalytic Nanomotors: Autonomous Movement of Striped Nanorods. In: Journal of the American Chemical Society 126 (2004), Nr. 41. – DOI 10.1021/ja047697z

[53] Cao, Y.Uny ; Fukunaga, Alex.S. ; Kahng, Andrew.B.: Cooperative mobile robotics: antecedents and directions. In: Proceedings 1995 IEEE/RSJ International Conference on Intelligent Robots and Systems. Human Robot Interaction and Cooperative Robots 1 (1997). – DOI 10.1109/IROS.1995.525801

[54] Ramaswamy, Sriram: The mechanics and statistics of active matter. In: Annual Review of Condensed Matter Physics 1 (2010). – DOI 10.1146/annurev–conmatphys–070909–104101

[55] Nagatani, Takashi: The physics of traffic jams. In: Reports on Progress in Physics 65 (2002). – DOI 10.1088/0034–4885/65/9/203

[56] Chung, Koohong ; Rudjanakanoknad, Jittichai ; Cassidy, Michael J.: Relation between traffic density and capacity drop at three freeway bottlenecks. In: Transportation Research Part B: Methodological 41 (2007), Nr. 1. – DOI 10.1016/j.trb.2006.02.011

[57] Bi, Dapeng ; Yang, Xingbo ; Marchetti, M. C. ; Manning, M. L.: Motility-driven glass and jamming transitions in biological tissues. In: Physical Review X 6 (2016), Nr. 2. – DOI 10.1103/PhysRevX.6.021011

[58] Bi, Dapeng ; Lopez, Jorge H. ; Schwarz, J. M. ; Manning, M. L.: Energy barriers and cell migration in densely packed tissues. In: Soft Matter 10 (2014), Nr. 12. – DOI 10.1039/c3sm52893f

[59] Etournay, Raphaël ; Popović, Marko ; Merkel, Matthias ; Nandi, Amitabha ; Blasse, Corinna ; Aigouy, Benoît ; Brandl, Holger ; Myers, Gene ; Salbreux, Guillaume ; Jülicher, Frank ; Eaton, Suzanne: Interplay of cell dynamics and epithelial tension during morphogenesis of the Drosophila pupal wing. In: eLife 4 (2015). – DOI 10.7554/eLife.07090

[60] Segerer, Felix J. ; Thüroff, Florian ; Piera Alberola, Alicia ; Frey, Erwin ; Rädler, Joachim O.: Emergence and persistence of collective cell migration on small circular micropatterns. In: Physical Review Letters 114 (2015), Nr. 22. – DOI 10.1103/PhysRevLett.114.228102

[61] Adrian, Ronald J.: Scattering particle characteristincs and their effect on pulsed laser measurements of fluid flow: speckle velocimetry vs particle image velocimetry. In: Applied Optics 23 (1984), Nr. 11. – DOI 10.1364/AO.23.001690

[62] Adrian, Ronald J.: Twenty years of particle image velocimetry. In: Experiments in Fluids 39 (2005), Nr. 2. – DOI 10.1007/s00348–005–0991–7

[63] Marel, Anna-Kristina ; Zorn, Matthias ; Klingner, Christoph ; Wedlich-Söldner, Roland ; Frey, Erwin ; Rädler, Joachim O.: Flow and diffusion in channel-guided cell migration. In: Biophysical Journal 107 (2014). – DOI 10.1016/j.bpj.2014.07.017

[64] Zorn, Matthias L. ; Marel, Anna K. ; Segerer, Felix J. ; Rädler, Joachim O.: Phenomenological approaches to collective behavior in epithelial cell migration. In: Biochimica et Biophysica Acta - Molecular Cell Research 1853 (2015), Nr. 11. – DOI 10.1016/j.bbamcr.2015.05.021

[65] Anna-Kristina Marel ; Nils Podewitz ; Zorn, Matthias ; Rädler, Joachim O. ; Elgeti, Jens: Alignment of cell division axes in directed epithelial cell migration. In: New Journal of Physics 16 (2014). – DOI 10.1088/1367–2630/16/11/115005

[66] Rørth, Pernille: Collective cell migration. In: Annual review of cell and developmental biology 25 (2009). – DOI 10.1146/annurev.cellbio.042308.113231

[67] Khalil, Antoine A. ; Friedl, Peter: Determinants of leader cells in collective cell migration. In: Integrative biology : quantitative biosciences from nano to macro 2 (2010). – DOI 10.1039/c0ib00052c

[68] Lauffenburger, Douglas A. ; Horwitz, Alan F.: Cell migration: A physically integrated molecular process. In: Cell 84 (1996), Nr. 3. – DOI 10.1016/S0092–8674(00)81280–5

[69] Bindschadler, Michael ; McGrath, James L.: Sheet migration by wounded monolayers as an emergent property of single-cell dynamics. In: Journal of cell science 120 (2007). – DOI 10.1242/jcs.03395

[70] Trepat, Xavier ; Wasserman, Michael R. ; Angelini, Thomas E. ; Millet, Emil ; Weitz, David A. ; Butler, James P. ; Fredberg, Jeffrey J.: Physical forces during collective cell migration. In: Nature Physics 5 (2009), Nr. 6. – DOI 10.1038/nphys1269

[71] Vitorino, Philip ; Meyer, Tobias: Modular control of endothelial sheet migration. In: Genes & Development 22 (2008). – DOI 10.1101/gad.1725808.tracheal

[72] Ouaknin, Gaddiel Y. ; Bar-Yoseph, Pinhas Z.: Stochastic collective movement of cells and fingering morphology: No maverick cells. In: Biophysical Journal 97 (2009), Nr. 7. – DOI 10.1016/j.bpj.2009.05.064

[73] Mark, Shirley ; Shlomovitz, Roie ; Gov, Nir S. ; Poujade, Mathieu ; Grasland-Mongrain, Erwan ; Silberzan, Pascal: Physical model of the dynamic instability in an expanding cell culture. In: Biophysical Journal 98 (2010), Nr. 3. – DOI 10.1016/j.bpj.2009.10.022

[74] Vishwakarma, Medhavi: Group decisions influence emergence and regulation of leaders during collective migration of epithelial cells. Lausanne, EPFL, Diss., 2017

[75] Aman, Andy ; Piotrowski, Tatjana: Wnt/β-catenin and Fgf signaling control collective cell migration by restricting chemokine receptor expression. In: Developmental Cell 15 (2008), Nr. 5. – DOI 10.1016/j.devcel.2008.10.002

[76] Friedl, P. ; Noble, P. B. ; Walton, P. A. ; Laird, D. W. ; Chauvin, P. J. ; Tabah, R. J. ; Black, M. ; Zanker, K. S.: Migration of coordinated cell clusters in mesenchymal and epithelial cancer explants in vitro. In: Cancer Research 55 (1995)

[77] Reffay, M. ; Petitjean, L. ; Coscoy, S. ; Grasland-Mongrain, E. ; Amblard, F. ; Buguin, a. ; Silberzan, P.: Orientation and polarity in collectively migrating cell structures: Statics and dynamics. In: Biophysical Journal 100 (2011), Nr. 11. – DOI 10.1016/j.bpj.2011.04.047

[78] Rodriguez, LuisG. ; Wu, Xiaoyang ; Guan, Jun-Lin: Wound-Healing Assay. In: Guan, Jun-Lin (Hrsg.): Cell Migration SE - 3 Bd. 294. Humana Press, 2005. – ISBN 978–1–58829–382–4

[79] Wong, M. K K. ; Gotlieb, A. I.: The reorganization of microfilaments, centrosomes, and microtubules during in vitro small wound reendothelialization. In: Journal of Cell Biology 107 (1988). – DOI 10.1083/jcb.107.5.1777

[80] Coomber, Brenda L. ; Gotlieb, Avrum I.: In vitro endothelial wound repair - Interaction of cell migration and proliferation. In: Arteriosclerosis, Thrombosis, and Vascular Biology 10 (1990)

[81] Zahm, J M. ; Kaplan, H ; Hérard, A L. ; Doriot, F ; Pierrot, D ; Somelette, P ; Puchelle, E: Cell migration and proliferation during the in vitro wound repair of the respiratory epithelium. In: Cell motility and the cytoskeleton 37 (1997). – DOI 10.1002/(SICI)1097–0169(1997)37:1¡33::AID–CM4¿3.0.CO;2–I

[82] Serra-Picamal, Xavier ; Conte, Vito ; Vincent, Romaric ; Anon, Ester ; Tambe, Dhananjay T. ; Bazellieres, Elsa ; Butler, James P. ; Fredberg, Jeffrey J. ; Trepat, Xavier: Mechanical waves during tissue expansion. In: Nature Physics 8 (2012), Nr. 8. – DOI 10.1038/nphys2355

[83] Dye, Natalie A. ; Popović, Marko ; Spannl, Stephanie ; Etournay, Raphaël ; Kainmüller, Dagmar ; Ghosh, Suhrid ; Myers, Eugene W. ; Jülicher, Frank ; Eaton, Suzanne: Cell dynamics underlying oriented growth of the Drosophila wing imaginal disc. In: Development (2017). – DOI 10.1242/dev.155069

[84] Walck-Shannon, Elise ; Hardin, Jeff: Cell intercalation from top to bottom. In: Nature Reviews Molecular Cell Biology 15 (2014), Nr. 1. – DOI 10.1038/nrm3723

[85] Sugimura, Kaoru ; Ishihara, Shuji: The mechanical anisotropy in a tissue promotes ordering in hexagonal cell packing. In: Development 140 (2013), Nr. 19. – DOI 10.1242/dev.094060

[86] Etournay, Raphaël ; Merkel, Matthias ; Popović, Marko ; Brandl, Holger ; Dye, Natalie A. ; Aigouy, Benoît ; Salbreux, Guillaume ; Eaton, Suzanne ; Jülicher, Frank: TissueMiner: A multiscale analysis toolkit to quantify how cellular processes create tissue dynamics. In: eLife 5 (2016). – DOI 10.7554/eLife.14334

[87] Weairet, D. ; Rivier, N.: Soap, cells and statistics-random patterns in two dimensions. In: Contemporary Physics 25 (1984), Nr. 1. – DOI 10.1080/00107518408210979

[88] Stavans, Joel: The evolution of cellular structures. In: Reports on Progress in Physics 56 (1993). – DOI 10.1088/0034–4885/56/6/002

[89] Farhadifar, Reza ; Röper, Jens C. ; Aigouy, Benoit ; Eaton, Suzanne ; Jülicher, Frank: The influence of cell mechanics, cell-cell interactions, and proliferation on epithelial packing. In: Current Biology 17 (2007). – DOI 10.1016/j.cub.2007.11.049

[90] Jones, Richard A. L.: Soft Condensed Matter. Oxford University Press, 2004

[91] Zafeiris, Anna ; Viscek, Tamás: Collective motion. In: Physics Reports 517 (2012)

[92] Yamada, Daizou ; Hondou, Tsuyoshi ; Sano, Masaki: Coherent dynamics of an asymmetric particle in a vertically vibrating bed. In: Physical Review E 67 (2003), Nr. 4. – DOI 10.1103/PhysRevE.67.040301

[93] Tritton, David J.: Physical fluid dynamics. Springer Science & Business Media, 2012

[94] Zierep, Jürgen ; Bühler, Karl: Grundzüge der Strömungslehre: Grundlagen, Statik und Dynamik der Fluide. Springer-Verlag, 2010

[95] Bruus, Henrik: Theoretical microfluidics. Oxford University Press, 2008

[96] Batchelor, George K.: An introduction to fluid dynamics. Cambridge University Press, 2000

[97] Kollmannsberger, Philip ; Fabry, Ben: Linear and nonlinear rheology of living cells. In: Annual Review of Materials Research 41 (2011), Nr. 1. – DOI 10.1146/annurev–matsci–062910–100351

[98] Landau, L D. ; Lifschitz, E M.: Lehrbuch der theoretischen Physik Band VI. In: Hydrodynamik (Akademie–Verlag) (1980)

[99] Panton, Ronald L.: Incompressible flow. John Wiley & Sons, 2006

[100] Saw, Thuan B. ; Doostmohammadi, Amin ; Nier, Vincent ; Kocgozlu, Leyla ; Thampi, Sumesh ; Toyama, Yusuke ; Marcq, Philippe ; Lim, Chwee T. ; Yeomans, Julia M. ; Ladoux, Benoit: Topological defects in epithelia govern cell death and extrusion. In: Nature 544 (2017), Nr. 7649. – DOI 10.1038/nature21718

[101] Joos, Georg: Lehrbuch der theoretischen Physik, 13., unveränderter Nachdruck der 12. Auflage. In: Aulaverlag, Wiesbaden (1977)

[102] Avila, K. ; Moxey, D. ; Lozar, A. de ; Avila, M. ; Barkley, D. ; Hof, B.: The onset of turbulence in pipe flow. In: Science 333 (2011), Nr. 6039. – DOI 10.1126/science.1203223

[103] Kirby, Brian J.: Micro-and nanoscale fluid mechanics: transport in microfluidic devices. Cambridge University Press, 2010

[104] Laufer, John: The structure of turbulence in fully developed pipe flow / National Advisory Committee for Aeronautics. Version: 1954. `https://ntrs.nasa.gov/search.jsp?R=19930092199`. Washington DC, 1954. – Forschungsbericht

[105] Ranft, Jonas ; Basan, Markus ; Elgeti, Jens ; Joanny, Jean-François ; Prost, Jacques ; Jülicher, Frank: Fluidization of tissues by cell division and apoptosis. In: Proceedings of the National Academy of Sciences of the United States of America 107 (2010), dec, Nr. 49. – DOI 10.1073/pnas.1011086107

[106] Bartumeus, Frederic ; Luz, M. G. E. ; Viswanathan, G. M. ; Catalan, J.: Animal Search Strategies: A Quantitative Random-Walk Analysis. In: Ecology 86 (2005), Nr. 11. – DOI 10.1890/04–1806

[107] Haber, C. ; Ruiz, S. A. ; Wirtz, D.: Shape anisotropy of a single random-walk polymer. In: Proceedings of the National Academy of Sciences of the United States of America 97 (2000), Nr. 20. – DOI 10.1073/pnas.190320097

[108] Gail, Mitchell H. ; Boone, Charles W.: The locomotion of mouse fibroblasts in tissue culture. In: Biophysical Journal 10 (1970), Nr. 10. – DOI 10.1016/S0006–3495(70)86347–0

[109] Codling, Edward A. ; Plank, Michael J. ; Benhamou, Simon: Random walk models in biology. In: Journal of the Royal Society, Interface / the Royal Society 5 (2008), Nr. 25. – DOI 10.1098/rsif.2008.0014

[110] Viswanathan, G. M. ; Afanasyev, V. ; Buldyrev, Sergey V. ; Stanley, H. E.: Lévy flights in random searches. In: Physica A 282 (2000). – DOI 10.1016/S0378–4371(00)00071–6

[111] Edwards, Andrew M. ; Phillips, Richard A. ; Watkins, Nicholas W. ; Freeman, Mervyn P. ; Murphy, Eugene J. ; Afanasyev, Vsevolod ; Buldyrev, Sergey V. ; Luz, M. G. E. ; Raposo, E. P. ; Stanley, H. E. ; Viswanathan, Gandhimohan M.: Revisiting Lévy flight search patterns of wandering albatrosses, bumblebees and deer. In: Nature 449 (2007), Nr. 7165. – DOI 10.1038/nature06199

[112] Benhamou, Simon: How many animals really do the Lévy walk? In: Ecology 88 (2007), Nr. 8. – DOI 10.1890/06–1769.1

[113] Méhes, Elod ; Mones, Enys ; Németh, Valéria ; Vicsek, Tamás: Collective motion of cells mediates segregation and pattern formation in co-cultures. In: PloS one 7 (2012), Nr. 2. – DOI 10.1371/journal.pone.0031711

[114] Szabó, A. ; Unnep, R. ; Méhes, E. ; Twal, W O. ; Argraves, W. S. ; Cao, Y. ; Czirók, A.: Collective cell motion in endothelial monolayers. In: Physical Biology 7 (2010), Nr. 4. – DOI 10.1088/1478–3975/7/4/046007

[115] Murray, J. D.: Mathematical Biology : I . An Introduction , Third Edition. Springer, 2002. – ISBN 0387952233

[116] Debenedetti, Pablo G. ; Stillinger, Frank H.: Supercooled liquids and the glass transition. In: Nature 410 (2001). – DOI 10.1038/35065704

[117] Ediger, M. D. ; Angell, C. A. ; Nagel, Sidney R.: Supercooled liquids and glasses. In: Journal of Physical Chemistry 100 (1996), Nr. 31. – DOI 10.1021/jp953538d

[118] Avramov, I: Viscosity of glassforming melts. In: Journal of Non-Crystalline Solids 238 (1998). – DOI 10.1016/S0022–3093(98)00672–3

[119] Mayer, P. ; Bissig, H. ; Berthier, L. ; Cipelletti, L. ; Garrahan, J. P. ; Sollich, P. ; Trappe, V.: Heterogeneous dynamics of coarsening systems. In: Physical Review Letters 93 (2004), Nr. 11. – DOI 10.1103/PhysRevLett.93.115701

[120] Griffiths, Graham ; Schiesser, William E.: Traveling wave analysis of partial differential equations: numerical and analytical methods with MATLAB and Maple. Academic Press, 2010. – ISBN 978–0–12–384652–5

[121] Gennes, Pierre-Gilles de ; Prost, Jacques: The physics of liquid crystals. Bd. 83. Oxford University Press, 1995. – ISBN 0 19 851785 6

[122] Marenduzzo, D. ; Orlandini, E. ; Cates, M. E. ; Yeomans, J. M.: Steady-state hydrodynamic instabilities of active liquid crystals: Hybrid lattice Boltzmann simulations. In: Physical Review E - Statistical, Nonlinear, and Soft Matter Physics 76 (2007), Nr. 3. – DOI 10.1103/PhysRevE.76.031921

[123] Vicsek, Tams ; Czirk, Andrs ; Ben-Jacob, Eshel ; Cohen, Inon ; Shochet, Ofer: Novel type of phase transition in a system of self-driven particles. In: Physical Review Letters 75 (1995), Nr. 6. – DOI 10.1103/PhysRevLett.75.1226

[124] Basan, Markus ; Prost, Jacques ; Joanny, Jean-François ; Elgeti, Jens: Dissipative particle dynamics simulations for biological tissues: rheology and competition. In: Physical Biology 8 (2011). – DOI 10.1088/1478–3975/8/2/026014

[125] Basan, Markus ; Elgeti, Jens ; Hannezo, Edouard ; Rappel, Wouter-Jan ; Levine, Herbert: Alignment of cellular motility forces with tissue flow as a mechanism for efficient wound healing. In: Proceedings of the National Academy of Sciences of the United States of America 110 (2013), Nr. 7. – DOI 10.1073/pnas.1219937110

[126] Nikunen, P. ; Karttunen, M. ; Vattulainen, I.: How would you integrate the equations of motion in dissipative particle dynamics simulations? In: Computer Physics Communications 153 (2003), Nr. 3. – DOI 10.1016/S0010–4655(03)00202–9

[127] Puliafito, Alberto ; Hufnagel, Lars ; Neveu, Pierre ; Streichan, Sebastian ; Sigal, Alex ; Fygenson, D K. ; Shraiman, Boris I.: Collective and single cell behavior in epithelial contact inhibition. In: Proceedings of the National Academy of Sciences of the United States of America 109 (2012), Nr. 3. – DOI 10.1073/pnas.1007809109

[128] Graner, Francois ; Glazier, James A.: Simulation of biological cell sorting using a two-dimensional extended Potts model. In: Phys. Rev. Lett. 69 (1992), Nr. 13. – DOI 10.1103/PhysRevLett.69.2013

[129] Glazier, James A. ; Graner, Francois: Simulation of the differential adhesion driven rearrangement of biological cells. In: Phys. Rev. E 47 (1993), Nr. 3. – DOI 10.1103/PhysRevE.47.2128

[130] Thüroff, Florian P.: Collective motion in active matter - from microscopic models to maroscopic dynamics, Ludwig-Maximilians-Universität München, Diss., 2014

[131] Michie, D ; Spiegelhalter, D J. ; Taylor, C C. ; Michie, Editors D. ; Spiegelhalter, D J. ; Taylor, C C.: Machine learning, neural and statistical classification. In: Ellis Horwood series in artificial intelligence 37 (1994), Nr. 4. – DOI 10.2307/1269742

[132] Guzella, Thiago S. ; Caminhas, Walmir M.: A review of machine learning approaches to spam filtering. In: Expert Systems with Applications 36 (2009), Nr. 7. – DOI https://doi.org/10.1016/j.eswa.2009.02.037

[133] Amodei, Dario ; Anubhai, Rishita ; Battenberg, Eric ; Case, Carl ; Casper, Jared ; Catanzaro, Bryan ; Chen, Jingdong ; Chrzanowski, Mike ; Coates, Adam ; Diamos, Greg ; Elsen, Erich ; Engel, Jesse ; Fan, Linxi ; Fougner, Christopher ; Han, Tony ; Hannun, Awni ; Jun, Billy ; LeGresley, Patrick ; Lin, Libby ; Narang, Sharan ; Ng, Andrew ; Ozair, Sherjil ; Prenger, Ryan ; Raiman, Jonathan ; Satheesh, Sanjeev ; Seetapun, David ; Sengupta, Shubho ; Wang, Yi ; Wang, Zhiqian ; Wang, Chong ; Xiao, Bo ; Yogatama, Dani ; Zhan, Jun ; Zhu, Zhenyao: Deep Speech 2: End-to-End Speech Recognition in English and Mandarin. In: Proceedings of the 33rd International Conference on Machine Learning 48 (2015). – DOI 10.1145/1143844.1143891

[134] LeCun, Y A. ; Jackel, L D. ; Bottou, L ; Brunot, A ; Cortes, C ; Denker, J S. ; Drucker, H ; Guyon, I ; Müller, U A. ; Säckinger, E ; Simard, P Y. ; Vapnik, V N.: Learning algorithms for classification: A comparison on handwritten digit recognition. In: Neural Networks (1995)

[135] Wieland, Marc ; Pittore, Massimiliano: Performance evaluation of machine learning algorithms for urban pattern recognition from multi-spectral satellite images. In: Remote Sensing 6 (2014), Nr. 4. – DOI 10.3390/rs6042912

[136] Kubat, Miroslav ; Holte, Robert C. ; Matwin, Stan: Machine learning for the detection of oil spills in satellite radar images. In: Machine Learning 30 (1998), Nr. 2-3. – DOI 10.1023/A:1007452223027

[137] Gong, Yihong ; Xu, Wei: Machine learning for multimedia content analysis. Bd. 30. Springer Science & Business Media, 2007. – ISBN 9780387699424

[138] Mohri, Mehryar ; Rostamizadeh, Afshin ; Talwalkar, Ameet: Foundations of machine learning. MIT press, 2012. – ISBN 9780262018258

[139] Gareth, James ; Witten, Daniela ; Hastie, Trevor ; Tibshirani, Robert: An introduction to statistical learning with applications in R. In: Springer (2013). – DOI 10.1016/j.peva.2007.06.006

[140] Tu, Jack V.: Advantages and disadvantages of using artificial neural networks versus logistic regression for predicting medical outcomes. In: Journal of Clinical Epidemiology 49 (1996), Nr. 11. – DOI 10.1016/S0895–4356(96)00002–9

[141] Maiuri, Paolo ; Rupprecht, Jean F. ; Wieser, Stefan ; Ruprecht, Verena ; Bénichou, Olivier ; Carpi, Nicolas ; Coppey, Mathieu ; De Beco, Simon ; Gov, Nir ; Heisenberg, Carl P. ; Lage Crespo, Carolina ; Lautenschlaeger, Franziska ; Le Berre, Maël ; Lennon-Dumenil, Ana M. ; Raab, Matthew ; Thiam, Hawa R. ; Piel, Matthieu ; Sixt, Michael ; Voituriez, Raphaël: Actin flows mediate a universal coupling between cell speed and cell persistence. In: Cell 161 (2015), Nr. 2. – DOI 10.1016/j.cell.2015.01.056

[142] Doxzen, Kevin ; Vedula, Sri Ram K. ; Leong, Man C. ; Hirata, Hiroaki ; Gov, Nir S. ; Kabla, Alexandre J. ; Ladoux, Benoit ; Lim, Chwee T.: Guidance of collective cell migration by substrate geometry. In: Integrative Biology 5 (2013), Nr. 8. – DOI 10.1039/c3ib40054a

[143] Rosen, P ; Misfeldt, D S.: Cell density determines epithelial migration in culture. In: Proceedings of the National Academy of Sciences of the United States of America 77 (1980), Nr. 8. – DOI 10.1073/pnas.77.8.4760

[144] Wan, L. Q. ; Ronaldson, K. ; Park, M. ; Taylor, G. ; Zhang, Y. ; Gimble, J. M. ; Vunjak-Novakovic, G.: Micropatterned mammalian cells exhibit phenotype-specific left-right asymmetry. In: Proceedings of the National Academy of Sciences 108 (2011), Nr. 30. – DOI 10.1073/pnas.1103834108

[145] Schreiber, Christoph ; Segerer, Felix J. ; Wagner, Ernst ; Roidl, Andreas ; Rädler, Joachim O.: Ring-shaped microlanes and chemical barriers as a platform for probing single-cell migration. In: Scientific Reports 6 (2016). – DOI 10.1038/srep26858

[146] Potdar, Alka A. ; Lu, Jenny ; Jeon, Junhwan ; Weaver, Alissa M. ; Cummings, Peter T.: Bimodal analysis of mammary epithelial cell migration in two dimensions. In: Annals of Biomedical Engineering 37 (2009), Nr. 1. – DOI 10.1007/s10439–008–9592–y

[147] Selmeczi, D. ; Li, L. ; Pedersen, L. I I. ; Nrrelykke, S. F. ; Hagedorn, P. H. ; Mosler, S. ; Larsen, N. B. ; Cox, E. C. ; Flyvbjerg, H.: Cell motility as random motion: A review. In: European Physical Journal: Special Topics 157 (2008), Nr. 1. – DOI 10.1140/epjst/e2008–00626–x

[148] Li, Liang ; Nørrelkke, Simon F. ; Cox, Edward C.: Persistent cell motion in the absence of external signals: A search strategy for eukaryotic cells. In: PLoS ONE 3 (2008), Nr. 5. – DOI 10.1371/journal.pone.0002093

[149] Maini, Philip K. ; McElwain, D. L. S. ; Leavesley, David I.: Traveling wave model to interpret a wound-healing cell migration assay for human peritoneal mesothelial cells. In: Tissue Engineering 10 (2004), Nr. 3-4. – DOI 10.1089/107632704323061834

[150] Sengers, Bram G. ; Please, Colin P. ; Oreffo, Richard O C.: Experimental characterization and computational modelling of two-dimensional cell spreading for skeletal regeneration. In: Journal of the Royal Society, Interface / the Royal Society 4 (2007), Nr. 17. – DOI 10.1098/rsif.2007.0233

[151] Sengers, B G. ; Please, C P. ; Taylor, M ; Oreffo, R O C.: Experimental-computational evaluation of human bone marrow stromal cell spreading on trabecular bone structures. In: Annals of Biomedical engineering 37 (2009), Nr. 6. – DOI 10.1007/s10439–009–9676–3

[152] Eisenmann, Christoph ; Kim, Chanjoong ; Mattsson, Johan ; Weitz, David A.: Shear melting of a colloidal glass. In: Physical Review Letters 104 (2010), Nr. 3. – DOI 10.1103/PhysRevLett.104.035502

[153] Sethna, James P. ; Dahmen, Karin A. ; Myers, Christopher R.: Crackling noise. In: Nature 410 (2001), Nr. 6825. – DOI 10.1038/35065675

[154] Bittig, Thomas ; Wartlick, Ortrud ; Kicheva, Anna ; González-Gaitárr, Marcos ; Jülicher, Frank: Dynamics of anisotropic tissue growth. In: New Journal of Physics 10 (2008). – DOI 10.1088/1367–2630/10/6/063001

[155] LeGoff, Loïc ; Rouault, Hervé ; Lecuit, Thomas: A global pattern of mechanical stress polarizes cell divisions and cell shape in the growing Drosophila wing disc. In: Development 140 (2013), Nr. 19. – DOI 10.1242/dev.090878

[156] Montel, Fabien ; Delarue, Morgan ; Elgeti, Jens ; Malaquin, Laurent ; Basan, Markus ; Risler, Thomas ; Cabane, Bernard ; Vignjevic, Danijela ; Prost, Jacques ; Cappello, Giovanni ; Joanny, Jean-François: Stress clamp experiments on multicellular tumor spheroids. In: Physical Review Letters 107 (2011), Nr. 18. – DOI 10.1103/PhysRevLett.107.188102

[157] Montel, Fabien ; Delarue, Morgan ; Elgeti, Jens ; Vignjevic, Danijela ; Cappello, Giovanni ; Prost, Jacques: Isotropic stress reduces cell proliferation in tumor spheroids. In: New Journal of Physics 14 (2012). – DOI 10.1088/1367–2630/14/5/055008

[158] Day, C. L. ; Harrist, T. J. ; Gorstein, F. ; Sober, A. J. ; Lew, R. A. ; Friedman, R. J. ; Pasternack, B. S. ; Kopf, A. W. ; Fitzpatrick, T. B. ; Mihm, M. C.: Malignant melanoma. Prognostic significance of 'microscopic satellites' in the reticular dermis and subcutaneous fat. In: Annals of Surgery 194 (1981), Nr. 1. – DOI 10.1097/00000658–198107000–00019

[159] Lange, Janina R. ; Fabry, Ben: Cell and tissue mechanics in cell migration. In: Experimental Cell Research 319 (2013), Nr. 16. – DOI 10.1016/j.yexcr.2013.04.023

[160] Wolf, Katarina ; Wu, Yi I. ; Liu, Yueying ; Geiger, Jörg ; Tam, Eric ; Overall, Christopher ; Stack, M S. ; Friedl, Peter: Multi-step pericellular proteolysis controls the transition from individual to collective cancer cell invasion. In: Nature Cell Biology 9 (2007), Nr. 8. – DOI 10.1038/ncb1616

[161] Gaggioli, Cedric ; Hooper, Steven ; Hidalgo-Carcedo, Cristina ; Grosse, Robert ; Marshall, John F. ; Harrington, Kevin ; Sahai, Erik: Fibroblast-led collective invasion of carcinoma cells with differing roles for RhoGTPases in leading and following cells. In: Nature Cell Biology 9 (2007), Nr. 12. – DOI 10.1038/ncb1658

[162] Alexander, Stephanie ; Koehl, Gudrun E. ; Hirschberg, Markus ; Geissler, Edward K. ; Friedl, Peter: Dynamic imaging of cancer growth and invasion: A modified skinfold chamber model. In: Histochemistry and Cell Biology 130 (2008), Nr. 6. – DOI 10.1007/s00418–008–0529–1

[163] Weigelin, Bettina ; Bakker, Gert-Jan ; Friedl, Peter: Intravital third harmonic generation microscopy of collective melanoma cell invasion. In: IntraVital 1 (2012), Nr. 1. – DOI 10.4161/intv.21223

[164] Yang, Yongliang ; Jamilpour, Nima ; Yao, Baoyin ; Dean, Zachary S. ; Riahi, Reza ; Wong, Pak K.: Probing leader cells in endothelial collective migration by plasma lithography geometric confinement. In: Scientific Reports 6 (2016). – DOI 10.1038/srep22707

[165] Tarle, Victoria ; Gauquelin, Estelle ; Vedula, S R K. ; Alessandro, Joseph D. ; Lim, C T. ; Ladoux, Benoit ; Gov, Nir S.: Modeling collective cell migration in geometric confinement. In: Physical Biology (2017)

[166] Tarle, Victoria ; Ravasio, Andrea ; Hakim, Vincent ; Gov, Nir S.: Modeling the finger instability in an expanding cell monolayer. In: Integrative Biology 7 (2015), Nr. 10. – DOI 10.1039/C5IB00092K

[167] Glenn, Honor L. ; Messner, Jacob ; Meldrum, Deirdre R.: A simple non-perturbing cell migration assay insensitive to proliferation effects. In: Scientific Reports 6 (2016). – DOI 10.1038/srep31694

[168] Nnetu, Kenechukwu D. ; Knorr, Melanie ; Käs, Josef ; Zink, Mareike: The impact of jamming on boundaries of collectively moving weak-interacting cells. In: New Journal of Physics 14 (2012). – DOI 10.1088/1367–2630/14/11/115012

[169] Schoetz, Eva-Maria ; Lanio, Marcos ; Talbot, Jared A. ; Manning, M. L.: Glassy dynamics in three-dimensional embryonic tissues. In: Journal of The Royal Society Interface 10 (2013). – DOI 10.1098/rsif.2013.0726

[170] Bertet, Claire ; Sulak, Lawrence ; Lecuit, Thomas: Myosin-dependent junction remodelling controls planar cell intercalation and axis elongation. In: Nature 429 (2004). – DOI 10.1038/nature02581.1.

[171] Lecuit, Thomas ; Lenne, Pierre-françois: Cell surface mechanics and the control of cell shape , tissue patterns and morphogenesis. In: Nature Reviews Molecular Cell Biology 8 (2007). – DOI 10.1038/nrm2222

[172] Krieg, M. ; Arboleda-Estudillo, Y. ; Puech, P. H. ; Käfer, J. ; Graner, F. ; Müller, D. J. ; Heisenberg, C. P.: Tensile forces govern germ-layer organization in zebrafish. In: Nature Cell Biology 10 (2008), Nr. 4. – DOI 10.1038/ncb1705

[173] Blanchard, Guy B. ; Kabla, Alexandre J. ; Schultz, Nora L. ; Butler, Lucy C. ; Sanson, Benedicte ; Gorfinkiel, Nicole ; Mahadevan, L. ; Adams, Richard J.: Tissue tectonics: Morphogenetic strain rates, cell shape change and intercalation. In: Nature Methods 6 (2009), Nr. 6. – DOI 10.1038/nmeth.1327

[174] Guillot, Charlène ; Lecuit, Thomas: Mechanics of epithelial tissue. In: Science 340 (2013). – DOI 10.1126/science.1235249

[175] Spencer, Meryl A. ; Jabeen, Zahera ; Lubensky, David K.: Vertex stability and topological transitions in vertex models of foams and epithelia. In: European Physical Journal E 40 (2017), Nr. 1. – DOI 10.1140/epje/i2017–11489–4

[176] Bi, Dapeng ; Lopez, J. H. ; Schwarz, J. M. ; Manning, M. L.: A density-independent rigidity transition in biological tissues. In: Nature Physics 11 (2015)

[177] Rauzi, Matteo ; Verant, Pascale ; Lecuit, Thomas ; Lenne, Pierre F.: Nature and anisotropy of cortical forces orienting Drosophila tissue morphogenesis. In: Nature Cell Biology 10 (2008), Nr. 12. – DOI 10.1038/ncb1798

[178] Lee, Rachel M. ; Kelley, Douglas H. ; Nordstrom, Kerstin N. ; Ouellette, Nicholas T. ; Losert, Wolfgang: Quantifying stretching and rearrangement in epithelial sheet migration. In: New Journal of Physics 15 (2013). – DOI 10.1088/1367–2630/15/2/025036

[179] Hufnagel, Lars ; Teleman, Aurelio A. ; Rouault, Hervé ; Cohen, Stephen M. ; Shraiman, Boris I.: On the mechanism of wing size determination in fly development. In: Proceedings of the National Academy of Sciences of the United States of America 104 (2007), Nr. 10. – DOI 10.1073/pnas.0607134104

[180] Hilgenfeldt, Sascha ; Erisken, Sinem ; Carthew, Richard W.: Physical modeling of cell geometric order in an epithelial tissue. In: Proceedings of the National Academy of Sciences of the United States of America 105 (2008), Nr. 3. – DOI 10.1073/pnas.0711077105

[181] Manning, M L. ; Foty, Ramsey A. ; Steinberg, Malcolm S. ; Schoetz, Eva-Maria: Coaction of intercellular adhesion and cortical tension specifies tissue surface tension. In: Proceedings of the National Academy of Sciences of the United States of America 107 (2010), Nr. 28. – DOI 10.1073/pnas.1003743107

[182] Tseng, Q. ; Duchemin-Pelletier, E. ; Deshiere, A. ; Balland, M. ; Guillou, H. ; Filhol, O. ; Thery, M.: Spatial organization of the extracellular matrix regulates cell-cell junction positioning. In: Proceedings of the National Academy of Sciences 109 (2012), Nr. 5. – DOI 10.1073/pnas.1106377109

[183] Alberola, Alicia P.: Quantitative cell assays and reduction of cell-to-cell variability in defined microenvironments, LMU München, PhD thesis, 2010

[184] Albert, Philipp J. ; Schwarz, Ulrich S.: Dynamics of cell shape and forces on micropatterned substrates predicted by a cellular Potts model. In: Biophysical Journal 106 (2014), Nr. 11. – DOI 10.1016/j.bpj.2014.04.036

[185] Sommer, C ; Straehle, C ; Köthe, U ; Hamprecht, F A.: Ilastik: Interactive learning and segmentation toolkit. In: 2011 IEEE International Symposium on Biomedical Imaging: From Nano to Macro, 2011. – ISSN 1945–7928

[186] Kaliman, Sara ; Jayachandran, Christina ; Rehfeldt, Florian ; Smith, Ana S.: Limits of applicability of the voronoi tessellation determined by centers of cell nuclei to epithelium morphology. In: Frontiers in Physiology 7 (2016). – DOI 10.3389/fphys.2016.00551

[187] Trichas, Georgios ; Smith, Aaron M. ; White, Natalia ; Wilkins, Vivienne ; Watanabe, Tomoko ; Moore, Abigail ; Joyce, Bradley ; Sugnaseelan, Jacintha ; Rodriguez, Tristan A. ; Kay, David ; Baker, Ruth E. ; Maini, Philip K. ; Srinivas, Shankar: Multi-cellular rosettes in the mouse visceral endoderm facilitate the ordered migration of anterior visceral endoderm cells. In: PLoS Biology 10 (2012), Nr. 2. – DOI 10.1371/journal.pbio.1001256

[188] Bardet, Pierre L. ; Guirao, Boris ; Paoletti, Camille ; Serman, Fanny ; Léopold, Valentine ; Bosveld, Floris ; Goya, YÛki ; Mirouse, Vincent ; Graner, François ; Bellaïche, Yohanns: PTEN controls junction lengthening and stability during cell rearrangement in epithelial tissue. In: Developmental Cell 25 (2013), Nr. 5. – DOI 10.1016/j.devcel.2013.04.020

[189] Tamada, Masako ; Zallen, Jennifer A.: Square cell packing in the Drosophila embryo through spatiotemporally regulated EGF receptor signaling. In: Developmental Cell 35 (2015), Nr. 2. – DOI 10.1016/j.devcel.2015.09.015

[190] Merkel, Matthias ; Etournay, Raphaël ; Popović, Marko ; Salbreux, Guillaume ; Eaton, Suzanne ; Jülicher, Frank: Triangles bridge the scales: Quantifying cellular contributions to tissue deformation. In: Physical Review E 95 (2017), Nr. 3. – DOI 10.1103/PhysRevE.95.032401

[191] McBeath, Rowena ; Pirone, Dana M. ; Nelson, Celeste M. ; Bhadriraju, Kiran ; Chen, Christopher S.: Cell shape, cytoskeletal tension, and RhoA regulate stem cell lineage commitment. In: Developmental Cell 6 (2004), Nr. 4. – DOI 10.1016/S1534–5807(04)00075–9

[192] Desai, Ravi A. ; Gao, Lin ; Raghavan, Srivatsan ; Liu, Wendy F. ; Chen, Christopher S.: Cell polarity triggered by cell-cell adhesion via E-cadherin. In: Journal of Cell Science 122 (2009). – DOI 10.1242/jcs.028183

[193] Chabner, Bruce A. ; Roberts, Thomas G.: Timeline: Chemotherapy and the war on cancer. In: Nature Reviews Cancer 5 (2005), Nr. 1, 65–72. – DOI 10.1038/nrc1529

[194] Singh, A. ; Settleman, J.: EMT, cancer stem cells and drug resistance: An emerging axis of evil in the war on cancer. In: Oncogene 29 (2010), Nr. 34. – DOI 10.1038/onc.2010.215

[195] Hanahan, Douglas: Rethinking the war on cancer. In: The Lancet 383 (2014), Nr. 9916. – DOI 10.1016/S0140–6736(13)62226–6

[196] Kim, Enoch ; Xia, Younan ; Whitesides, George M.: Polymer microstructures formed by moulding in capillaries. In: Nature 376 (1995). – DOI 10.1038/376581a0

[197] Shim, Hyun W. ; Lee, Ji H. ; Hwang, Taek S. ; Rhee, Young W. ; Bae, Yun M. ; Choi, Joon S. ; Han, Jongyoon ; Lee, Chang S.: Patterning of proteins and cells on functionalized surfaces prepared by polyelectrolyte multilayers and micromolding in capillaries. In: Biosensors and Bioelectronics 22 (2007), Nr. 12. – DOI 10.1016/j.bios.2007.02.016

[198] Song, Hwan M. ; Lee, Chang S.: Simple fabrication of functionalized surface with polyethylene glycol microstructure and glycidyl methacrylate moiety for the selective immobilization of proteins and cells. In: Korean Journal of Chemical Engineering 25 (2008), Nr. 6. – DOI 10.1007/s11814–008–0241–9

[199] Marel, Anna-Kristina ; Rappl, Susanne ; Piera Alberola, Alicia ; Rädler, Joachim O.: Arraying cell cultures using PEG-DMA micromolding in standard culture dishes. In: Macromolecular Bioscience 13 (2013), Nr. 5. – DOI 10.1002/mabi.201200400

[200] Singhvi, Rahul ; Kumar, Amit ; Lopez, Gabriel P. ; Stephanopoulos, Gregory N. ; Wang, Daniel I. C. ; Whitesides, George M. ; Ingber, Donald E.: Engineering cell shape and function. In: Science 264 (1994). – DOI 10.1126/science.8171320

[201] Théry, Manuel ; Racine, Victor ; Pépin, Anne ; Piel, Matthieu ; Chen, Yong ; Sibarita, Jean-Baptiste ; Bornens, Michel: The extracellular matrix guides the orientation of the cell division axis. In: Nature Cell Biology 7 (2005), Nr. 10. – DOI 10.1038/ncb1307

[202] Théry, Manuel ; Pépin, Anne ; Dressaire, Emilie ; Chen, Yong ; Bornens, Michel: Cell distribution of stress fibres in response to the geometry of the adhesive environment. In: Cell Motility and the Cytoskeleton 63 (2006), Nr. 6. – DOI 10.1002/cm.20126

[203] Théry, Manuel ; Racine, Victor ; Piel, Matthieu ; Pépin, Anne ; Dimitrov, Ariane ; Chen, Yong ; Sibarita, Jean-Baptiste ; Bornens, Michel: Anisotropy of cell adhesive microenvironment governs cell internal organization and orientation of polarity. In: Proceedings of the National Academy of Sciences of the United States of America 103 (2006). – DOI 10.1073/pnas.0609267103

[204] Huang, S. ; Brangwynne, C. P. ; Parker, K. K. ; Ingber, Donald E.: Symmetry-breaking in mammalian cell cohort migration during tissue pattern formation: Role of random-walk persistence. In: Cell Motility and the Cytoskeleton 61 (2005). – DOI 10.1002/cm.20077

[205] Raffel, Markus ; Willert, Christian E. ; Wereley, Steven ; Kompenhans, Jürgen: Particle image velocimetry: a practical guide. Springer, 2013

[206] NIH: ImageJ Image Processing Software. `https://imagej.nih.gov/ij/`

[207] Bernasconi, Pietro N. ; Rust, David M. ; Hakim, Daniel: Advanced automated solar filament detection and characterization code: Description, performance, and results. In: Solar Physics 228 (2005), Nr. 1-2. – DOI 10.1007/s11207–005–2766–y

[208] Agam, G ; Armato, S G. ; Wu, Changhua: Vessel tree reconstruction in thoracic CT scans with application to nodule detection. In: IEEE Transactions on Medical Imaging 24 (2005), Nr. 4. – DOI 10.1109/TMI.2005.844167

[209] Püspöki, Zsuzsanna ; Storath, Martin ; Sage, Daniel ; Unser, Michael: Transforms and operators for directional bioimage analysis: A survey. In: Focus on Bio-Image Informatics Bd. 219. 2016. – ISBN 978–3–319–28547–4

[210] Kapitel Adaptive R. In: Nath, Sumit K. ; Palaniappan, Kannappan: Adaptive robust structure tensors for orientation estimation and image segmentation. Berlin, Heidelberg : Springer Berlin Heidelberg, 2005. – ISBN 978–3–540–32284–9

[211] Preibisch, Stephan ; Saalfeld, Stephan ; Tomancak, Pavel: Globally optimal stitching of tiled 3D microscopic image acquisitions. In: Bioinformatics 25 (2009), Nr. 11. – DOI 10.1093/bioinformatics/btp184